



HAL
open science

Développement et optimisation des diagnostics des faisceaux du LHC et du SPS basé sur le suivi de la lumière synchrotron

Georges Trad

► **To cite this version:**

Georges Trad. Développement et optimisation des diagnostics des faisceaux du LHC et du SPS basé sur le suivi de la lumière synchrotron. Physique des accélérateurs [physics.acc-ph]. Université Grenoble Alpes, 2015. Français. NNT : 2015GREAY005 . tel-01157800

HAL Id: tel-01157800

<https://theses.hal.science/tel-01157800>

Submitted on 28 May 2015

HAL is a multi-disciplinary open access archive for the deposit and dissemination of scientific research documents, whether they are published or not. The documents may come from teaching and research institutions in France or abroad, or from public or private research centers.

L'archive ouverte pluridisciplinaire **HAL**, est destinée au dépôt et à la diffusion de documents scientifiques de niveau recherche, publiés ou non, émanant des établissements d'enseignement et de recherche français ou étrangers, des laboratoires publics ou privés.



UNIVERSITÉ DE
GRENOBLE

THÈSE

Pour obtenir le grade de

DOCTEUR DE L'UNIVERSITÉ DE GRENOBLE

Spécialité : **Physique Subatomique et Astroparticules**

Arrêté ministériel : 7 août 2006

Présentée par

Georges TRAD

Thèse dirigée par **Jean Marie DE CONTO**
codirigée par **Federico RONCAROLO**

préparée au sein du **Laboratoire de l'Organisation Européenne
de Recherche Nucléaire - CERN**
dans l'**École Doctorale de Physique - Grenoble**

Développement et optimisation des diagnostics des faisceaux du LHC et du SPS basé sur le suivi de la lumière synchrotron

Thèse soutenue publiquement le **22 Janvier 2015**,
devant le jury composé de :

M. Philip BAMBADE

Rapporteur

M. Johann COLLOT

Président

M. Jean Marie DE CONTO

Membre

M. Mauro MIGLIORATI

Rapporteur

M. Dominique REBREYEND

Membre

M. Federico RONCAROLO

Membre

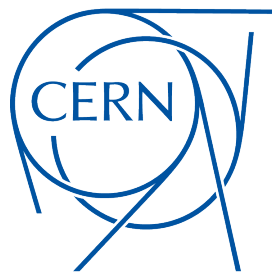
M. Enrico BRAVIN

Invité

*Université Joseph Fourier / Université Pierre Mendès France /
Université Stendhal / Université de Savoie / Grenoble INP*



Development and Optimisation of the
SPS and LHC beam diagnostics
based on Synchrotron Radiation monitors



UNIVERSITÉ DE GRENOBLE

Georges TRAD

European Organisation
for Nuclear Research
CERN

Ecole doctorale de Physique
LPSC
Université de Grenoble

A thesis submitted for the degree of

Doctor of Philosophy

January 22nd, 2015

Contents

Contents	i
List of Figures	v
Introduction	1
1 Overview	5
1.1 CERN accelerators complex	5
1.2 Introduction to beam dynamics	9
1.2.1 Lorentz force	9
1.2.2 Betatronic oscillations	10
1.2.3 Dispersion	14
1.2.4 Transport matrix	15
1.2.5 Luminosity	16
1.3 Profile measurements techniques at CERN	17
2 Synchrotron Light Theory and Its Use in Diagnostics	21
2.1 Fields emitted by moving relativistic charges	22
2.2 Various SR sources	29
2.2.1 Bending magnets	29
2.2.2 Short magnets and dipole edge radiation	31
2.2.3 Undulators and wigglers	33
2.3 SR application for transverse diagnostic	35
2.3.1 SR imaging technique	35
2.3.2 SR interferometry technique	39

3	Synchrotron Light Monitors at CERN	41
3.1	LHC	41
3.1.1	Source description	42
3.1.2	Light extraction system	46
3.1.3	Optical system	47
3.1.4	Detector	52
3.2	SPS	55
3.2.1	Source description	55
3.2.2	Light extraction system	57
3.2.3	Optical and detection systems	57
4	Simulation of the SR Monitors' Performance	59
4.1	SR simulation tools	59
4.1.1	Synchrotron Radiation Workshop (SRW)	60
4.1.2	Zemax	61
4.1.3	Combined approach	62
4.2	LHC source characterisation	65
4.3	Performance of the LHC SR imaging monitors	69
4.3.1	Analysis of the original reflective optics system	69
4.3.2	Analysis of the new refractive optics system	76
4.4	New telescope design and characterization	77
4.4.1	Resolution improvement	77
4.4.2	Imaging throughout the LHC ramp	85
4.4.3	Limitation of the SR imaging in LHC	86
4.5	SR interferometry for the LHC	89
4.5.1	Simulated performance	93
4.5.2	Error sources and corrections	100
4.6	SPS source characterisation	104
4.7	Performance of the SPS SR imaging system	106
5	Beam Measurements	109
5.1	SR source observations	109
5.1.1	SPS	109

5.1.2	LHC	114
5.2	Characterization of the LHC imaging system	116
5.2.1	Magnification measurements	116
5.2.2	Cross-calibration with Wire Scanners (WS)	121
5.2.3	Cross-calibration with luminosity measurements	129
5.2.4	LHC SR imaging summary	132
5.3	Interferometry at ALBA	133
5.3.1	Corrections	137
6	RF Heating in the LHC Light Extraction System	143
6.1	Longitudinal wake fields, potentials and coupling impedance	144
6.2	Beam observations	148
6.2.1	SR steering drift	148
6.2.2	Extraction mirror support failure and coating deterioration . .	150
6.2.3	Temperature monitoring	153
6.3	Light extraction system re-design	155
6.4	Coupling impedance laboratory measurements	157
6.4.1	Stretched wire technique	157
6.4.2	Experimental results	159
7	From Beam Size to Beam Emittance: Optical Functions	169
7.1	K-modulation	171
7.1.1	Measurement technique	171
7.1.2	Experimental results	173
7.2	β transport to beam size monitors	179
7.2.1	Analytical transport	179
7.2.2	Mad-X transport	181
7.2.3	Results	183
8	New SR Optical System for the LHC	186
	Conclusions	196

Appendix	i
A Derivation of the SR spatial distribution emitted by relativistic charges on circular orbit	i
References	v

List of Figures

1.1	CERN accelerators chain [1].	6
1.2	Schematic layout of the <i>LHC</i> . Beam 1 (blue) circulates clockwise and Beam 2 (red) counter-clockwise.	8
1.3	Frenet-Serret coordinate system.	10
1.4	Particle trajectory describing an ellipse in the transverse phase space.	13
1.5	Off-momentum particle trajectory describing a shifted ellipse in the transverse phase space.	15
1.6	Beam Gas Ionisation monitors working principle.	17
1.7	Wire Scanners working principle.	18
2.1	Position vectors r and r' used in the calculation of the retarded potentials, quantifying the time delay effect of the finite propagation speed of the SR.	22
2.2	The geometry used for the treatment of synchrotron radiation, featuring K^* as coordinate system moving along the trajectory.	26
2.3	The total radiated power by the charged particle in K^* reference frame [2].	27
2.4	Lorentz transformation for the relativistic case, shapes the emitted SR angular distribution in a forward narrow cone [2].	30
2.5	Frequency distribution of SR radiated intensity (in a.u.) in a bending magnet [2].	31
2.6	SR light pulse duration seen by an observer [2].	32
2.7	Undulator working principle as an SR source.	33
2.8	SR imaging system working principle.	36
2.9	SR interferometry working principle.	39

LIST OF FIGURES

3.1	Sketch of the BSRT Synchrotron light sources.	42
3.2	Dipole D3 critical wavelength λ_c shift with energy.	43
3.3	Vertical profile of the emitted SR fan for $\lambda = 400\text{ nm}$ at different energies, compared to the $1/\gamma$ Gaussian profile approximation.	44
3.4	Opening angle of the SR cone for different wavelengths (200, 400 and 600 nm) with the energy ramp up to 7 TeV.	44
3.5	Characteristics of the undulator radiation. Top plot: peak on-axis emission wavelength vs. proton energy. Bottom plot: proton emission spectrum on axis versus wavelength (log scale).	45
3.6	Sketch of the SR extraction tank in the LHC.	47
3.7	Transmission of the BSRT fused-silica vacuum window [3].	48
3.8	LHC optical bench housing the BSRT in IR 4 in the shielded enclave under the beam line.	48
3.9	Sketch of the BSRT in the reflective optics (focusing mirrors F1, F2) version, showing the calibration line occupying the right part of the optical table complementary to the imaging line. The trombone delay line (formed by mirrors M1, . . . , M7) is shown in both configurations: "Short" for focusing on the undulator radiation and "Long" for compensating for the source shift at high energy and focusing in the D3 core.	50
3.10	Sketch of the BSRT in the refractive optics (lenses F1, F2) version, showing the calibration line occupying the right part of the optical table complementary to the imaging line. The version features only on movable element, the zoom lens F2, used for moving the focus from the undulator radiation to the D3 core.	52
3.11	Low light Intensifier working principle.	53
3.12	The spectral response characteristic of the Proxicam for different photocathode types used in the intensifier [4].	54
3.13	SPS dipole MBB critical wavelength λ_c shift with energy ramp up to 450 GeV.	56
3.14	Schematics of the SPS SR light sources.	57
3.15	Sketch of the Synchrotron light extraction tank of the SPS BSR.	58
3.16	Optical system of the SPS BSR, based on two focusing lenses.	58

4.1	Code flow of the new simulation tool developed during this thesis work.	62
4.2	Simulation of the LHC SR power (in units of $W \cdot mm^{-2}$ per proton) at the extraction mirror, for different beam energies.	66
4.3	Total LHC SR power per proton, integrated over the extraction mirror area, in the 200 . . . 800 nm wavelength range.	67
4.4	SR power density as function of beam energy, as calculated for the LHC systems.	68
4.5	Sensitivity of the LHC imaging system based on reflective optics (left) obtained as a convolution of the detector's sensitivity and the transmission of the optical system (right).	70
4.6	LSF of the LHC reflective optics based imaging system at injection energy (450 GeV) at the wavelength of 600 nm.	70
4.7	Effective width of the LSF at 450 GeV integrated over the detectable range (200 nm–800 nm) for the reflective optics based imaging system case.	71
4.8	LSF of the LHC reflective optics based imaging system at flattop energy (7 TeV) at the wavelength of 400 nm.	72
4.9	Effective LSF width at the flattop energy (7 TeV) and 400 nm for the reflective optics based imaging system case.	73
4.10	Schematics of the unfolded optical delay line showing eventual light cutting caused by small mirrors tilts β_i along the line.	74
4.11	Light cutting at the last mirror M8 of the trombone line (right plot, shown in logarithmic scale), simulated by displacing the nominal position of M8 (central plot, shown in logarithmic scale) by the corresponding 9 mm.	74
4.12	Effective LSF width at the energy of 4 TeV and 400 nm for the reflective optics based imaging system case.	75
4.13	The nominal LSF of the LHC reflective optics imaging system, at 4 TeV and 400 nm focusing on the rising edge D3, compared to the case of a misaligned system.	75
4.14	Effective LSF width for the LHC refractive optics based imaging system, shown for injection energy (450 GeV integrated over the range 200–800 nm) and the energies 4 and 7 TeV (at 400 nm).	76

4.15 Slit selection technique for reducing the DOF effect by limiting the imaged light to a fraction of the total SR (selecting a short path within the bending dipole).	78
4.16 Tracking of an arbitrary photon phase space (position and angle) taken as a source, in a simplified optical system based on a single focusing element. Results denote that an angular selection at the source (black area in (a)) corresponds to a position selection at 1 focal length from the lens (black area in (c)).	79
4.17 Probing the horizontal slit effect in terms of σ_{LSF} at 7 TeV and 400 nm.	80
4.18 Sensitivity of the upgraded LHC imaging system based on refractive optics optimized from 250 nm operation (left) obtained as a convolution of the detector's sensitivity and the transmission of the optical system (right).	81
4.19 Effective LSF width at 7 TeV for the refractive optics based imaging system, compared at two wavelengths 400 and 250 nm.	82
4.20 SR intensity distribution (H, V and total polarization) at the LHC extraction mirror at 7 TeV and 250 nm.	82
4.21 Comparing σ_{LSF} at 7 TeV and 250 nm for different SR polarization (horizontal, vertical and total) at different focus within the dipole. . .	83
4.22 LHC extraction mirror flatness, measured via the “Fiserau interferometer” technique by WZWOPTICAG®.	84
4.23 Spot diagram of the LHC refractive based imaging system at 250 nm for the ideal (left) and real (right) extraction mirror.	84
4.24 Comparing LSF at 7 TeV and 250 nm for the ideal (blue) and real (green) extraction mirror.	85
4.25 Extracted SR energy per proton per wavelength (in the detectable range 200–800 nm) as function of beam energy.	86
4.26 The horizontal resolution is studied along the LHC ramp for different focusing settings (left plot), to find the minimum σ_{LSF} (lower right plot) and the optimum focusing plane (top right plot) at every energy.	87
4.27 Relative error on the emittance determination in function of the uncertainty on the system's resolution for different emittances.	88

4.28	Visibility variation corresponding to emittance range to be measured in the LHC (at 450 GeV and 7 TeV) for different slit separations and wavelengths.	90
4.29	Relative error on the beam size determination in function of the visibility, calculated for different values of error on the measured pixel intensity.	91
4.30	Interferometry fringe visibility as function of the beam size for various slit separation, shown for beam sizes corresponding to the emittance range of 2 to 5 μm at 450 GeV and 7 TeV.	92
4.31	Typical optical system used for SR interferometry measurements. . .	93
4.32	Interferometer LSF at 450 GeV at 550 nm, simulated for a slit separation 5 mm and 1 mm width.	94
4.33	Reference macro-particles chosen from the horizontal phase space of the proton beam at 450 GeV.	95
4.34	Interferogram of 7 reference particles at 450 GeV (top plot) showing a qualitative dependency of the pattern centroid with the position and angle of the macro-particle. A numerical model is found describing such a relation via a linear and a parabolic dependency as shown in the bottom plots.	96
4.35	Interference fringes corresponding to different beam normalized emittances at 450 GeV in the LHC.	97
4.36	Comparison of the simulated visibility variation in function of the beam size with respect to the theoretic predictions (left plot). The absolute discrepancy is calculated (upper right plot) to be < 0.01 leading to an error in terms of beam size determination $< 2\%$	97
4.37	Interferometer LSF at 7 TeV at 550 nm, simulated for a slit separation 9 mm and 1 mm width.	98
4.38	Interference fringes corresponding to different beam normalized emittances at 7 TeV in the LHC (for a slit separation 11 mm and width 2 mm) are shown in the left plot. The obtained curve mapping the visibility change in function of the emittance is given in the right plot.	99

4.39	Relative error on beam size determination in function of the beam size (for different slits separation) when neglecting the finite spectral width of the color filter.	101
4.40	Visibility variation in function of beam size when assuming monochromatic light (solid line) or a quasi-monochromatic light (dashed line). . .	101
4.41	Sketch showing the effect of the extraction mirror surface deformation (Φ_1, Φ_2) on the apparent slit separation.	102
4.42	Relative error on the slit separation determination (and respectively on the beam size inferred value) for different separations, plotted for various deformations of the extraction mirror surface.	103
4.43	SR intensity distribution (a.u.) on the SPS extraction mirror at top energy (450 GeV) for several wavelengths covering the detectable range (200– 800 nm).	105
4.44	On one hand SR power spectrum, integrated over the extraction mirror area, is shown for 3 energies (270, 405, 450 GeV). Additionally, the LHC power spectrum emitted by the undulator is shown for comparison (left). On the other hand, the integrated energy per turn over the detectable range in function of the beam energy is shown in the right plot.	106
4.45	SR intensity distribution on the extraction mirror emitted by a filament beam in the range of 200– 800 nm.	107
4.46	Sensitivity of the SPS imaging system obtained as a convolution of the detector’s sensitivity and the transmission of the optical system. . . .	107
4.47	Total LSF of the SPS imaging system at 450 GeV integrated over the detectable range, convoluted with the system sensitivity.	108
4.48	SPS horizontal and vertical effective σ_{LSF} in function of the beam size at 450 GeV.	108
5.1	Imaged SPS SR light for a bunch of $\sim 10^{11}$ protons over 4 SPS turns along the energy ramp.	111
5.2	Calibration of the SPS imaging system.	112
5.3	Measured SR intensity emitted by a bunch of 10^{11} protons over 4 turns during the SPS energy ramp.	113

5.4	Imaged SPS SR light of 24 bunches at the Energy of 290 GeV integrated over 4 SPS turns.	113
5.5	Spectral sensitivity of the LHC extraction mirror monitoring CCD [5].	114
5.6	Measured SR light distribution (left plots) at the extraction mirror (delimited by the red rectangle) compared to the simulated SR intensity (right plots).	115
5.7	Beam 1 (right) and Beam 2 (left) resolution targets used for magnification measurement.	117
5.8	Beam orbit as measured by the Beam Position Monitors (BPMs) at the location of different profile monitors while applying closed orbit bumps of different amplitudes [6].	118
5.9	Schematic of the BSRT optical system, where at each bump amplitude the camera has been moved from end of the translation stage to the other to measure the magnification at every camera position.	119
5.10	SR centroid on the CCD shift with respect to the beam transverse displacement at different camera positions (0, 40, 60 and 100 mm). . .	119
5.11	Horizontal and vertical measured magnifications at different CCD position.	120
5.12	Bunch by bunch normalized emittances measured by WS (red) and BSRT (grey histogram) during the cross calibration period at injection energy (450 GeV) and 3.5 TeV.	122
5.13	Induced error on the LSF width determination by error on the magnification measurement (blue). The black curve is a first order approximation of $\frac{\partial \epsilon_{\sigma_c}}{\partial \epsilon_K}$	123
5.14	Beam-based calibration technique to obtain experimentally the magnification and the LSF width of the BSRT optical system through a cross calibration with the WS measurements. The regression coefficients obtained in the top plot are applied in the bottom plot obtaining the normalized emittance evolution as measured by the BSRT and WS. .	125

5.15	Normalized emittance evolution for 3 different bunches in the LHC fill 3215 as measured by BSRT (line) and WS (square). The measurements are carried out at 450 GeV (left of the grey vertical band) and 4 TeV (right of the vertical grey band). The additional black curves represent the increase of the optical function at the collision point (a.u.) and is not of interest to our studies.	127
5.16	Normalized emittance evolution for 3 different bunches in the LHC fill 3216 as measured by BSRT (line) and WS (square). The measurements are carried out at 450 GeV (left of the grey vertical band) and 4 TeV (right of the vertical grey band). The additional black curves represent the increase of the optical function at the collision point (a.u.) and is not of interest to our studies.	128
5.17	Normalized emittances evolution during the BSRT-WS cross calibration for the LHC Fill 2201.	130
5.18	Evolution of the measured instantaneous luminosity measured by ATLAS and CMS compared to the computed luminosity computed from the measured beam parameters. The red dotted curve is obtained by scaling the black curve to be compared with the luminosity measurements.	130
5.19	Normalized emittance evolution as measured by the BSRT during a luminosity calibration fill in the LHC.	131
5.20	Sketch of SR optical path at ALBA from its source (bending dipole <i>BM01</i>) to the optical bench.	134
5.21	Color bandpass filter used in the interferometry setup at ALBA. . . .	134
5.22	Vertical projection of the interference fringes of the ALBA beam size interferometer for different slit separations, ranging from 8 to 32 mm. Experimental data is shown in blue, while the fit according to Eq. 2.48 is shown in red.	136
5.23	Measured fringe visibility during the slits separation scan from 9 to 28 mm, fitted by Gaussian distribution.	137
5.24	Relative error introduced by neglecting the finite bandpass of the color filter assuming monochromatic light for different beam size and slit separation.	138

5.25	Visibility reduction due to chromatic effects for different beam sizes and slit separations.	138
5.26	Incoherent depth of field effect on the interference fringes visibility for different slit separations and beam sizes.	139
5.27	Interferometer double slit calibration to be applied to the physically measured slit separation $D_{physical}$ to obtain the effective separation $D_{effective}$	140
5.28	An example of visibility corrections (chromatic correction and DOF) to be applied for a given set of beam sizes ranging from 45 μm to 59 μm	141
5.29	Fringe visibility change with respect to the slit separation before (red) and after (green) applying the correction algorithm.	142
6.1	RLC circuit.	146
6.2	Real and imaginary parts of impedance Z of a resonator [7].	147
6.3	Correlation between the horizontal steering mirror motor position that was set for centering the SR on the camera (green) and the peak beam intensity per fill (blue).	149
6.4	Sketch to explain the conversion of the steering mirror motor steps into the corresponding displacement of the light source (see text).	149
6.5	Schematics showing the steering mirror as a tool to compensate beam displacements and extraction mirror tilts for the case the LHC BSRT optical system parameters.	150
6.6	Estimated extraction mirror (blue) tilt with respect to the steering mirror tilt (green) deduced from the motor steps.	151
6.7	Outcome of the visual and microscopic inspection of the light extraction system after its removal in August 2012.	152
6.8	(a) Location of the six in-vacuum temperature probes (square markers with color code corresponding to the plot below) as installed in one of the light extraction systems and (b) temperature profiles during a dedicated machine development period with varying beam intensity and longitudinal bunch length.	154
6.9	3D models of the old and new light extraction systems (courtesy of W. Andreazza).	156

6.10	Simulated Longitudinal impedance by the mean of CST comparing different combinations of mirror holder materials [8].	156
6.11	Stretched Wire technique for coupling impedance measurement.	158
6.12	Laboratory setup for wire measurements.	159
6.13	New Design of the extraction mirror, on the measurement bench. To be noted the absence of the cavity-like shape created by the mirror holder in the old design.	160
6.14	Alternative holder design, based on the initial metallic holder, except that all the parts seen by the beam were replaced by ceramic.	160
6.15	Matching Network for the "stretched wire" technique composed of attenuators, matching resistor and absorbing foam.	161
6.16	Empty Tank reference S_{21} measurement with (red) and without (black) the absorbing foam used for matching at high frequencies.	162
6.17	Transmission measurement compared to simulations for the metallic holder with no mirror installed and no ferrites, at different distances from the beam (60 mm being the nominal position).	163
6.18	Measured scattering parameter S_{21} via stretched wire technique comparing, at the nominal distance (20 mm from wire/beam), the effect of inserting the metallic mirror holder with no mirror mounted and no ferrites installed (black) with the configuration with three different types of mirrors.	164
6.19	Measured scattering Parameter S_{21} for different mirror holders via the stretched wire technique were compared. The glass mirror with dielectric coating was mounted on the three mirror holders (old metallic in black, new ceramic in blue and the new modified metallic in red) and positioned at the nominal distance (20 mm from wire/beam).	165
6.20	Measured scattering Parameter S_{21} via stretched wire technique, comparing original BSRT extraction system (silicon bulk mirror mounted on metallic holder with ferrites) in black and the new design for after LS1 operation (glass mirror with dielectric coating mounted on a modified metallic holder without ferrites) in red.	166

6.21	Calculated coupling impedance Z_L of the initially installed extraction system (2012 in black) and the newly designed and installed system (2015 in red).	166
6.22	LHC beam spectra measured during proton fill 2261 at injection energy (blue). The green dots reveal the peaks and used only for visual purpose. The red line is an envelope of the lobes higher peaks [9]. . .	167
6.23	Power lost in the two versions of the SR extraction system (2012 (pre-LS1) in blue and 2015n (post-LS1) in green. The upper plot shows the cumulative power lost in Watt, while the lower plot shows the power loss spectrum in Watt/Hz.	167
7.1	K-modulation working principle.	171
7.2	Schematics of IR4 showing the qudrupoles IP4	173
7.3	K-modulation applied for RQ5.R4.B2; the blue curve denotes the current trims applied to the quadrupole and the green and red curve shows respectively the horizontal and vertical resulting tune changes.	174
7.4	Validation of the approximation in Eq. 7.13 for the LHC parametrs. The blue and red curves denote respectively the relative error introduced by the approximation in function on the induced tune change for the horizontal and vertical tune working points (0.28 and 0.31) . .	175
7.5	Correlation between the current steps set to the quadrupole RQ5.R4.B2 and the measured tune in the horizontal plane for Beam 2. A Linear regression is applied (red curve) and summarized by the line equation on the top.	176
7.6	IR4 optical Layout for Beam 1 showing β_x in blue and β_y in red and the measured β s via K-modulation in black (horizontal) and green (vertical). The green and purple vertical bands denote the beam size monitors (WS and BSRT source) while the yellow ones represent the modulated quadrupoles.	178
7.7	Schematics explaining the analytical transport of the measured β s at the quadrupoles via K-modulation to the beam size monitors.	180

LIST OF FIGURES

7.8	Schematics explaining the transport of the measured β s at the quadrupoles via K-modulation to the beam size monitors via the matching module in Mad-X.	181
7.9	LHC beam 1 mean normalized horizontal emittance evolution, in fill 2778, calculated using the model predicted β (blue) and the measured β via K-modulation at the SR monitors location.	185
8.1	New external calibration line installed in the LHC (Courtesy: A. Goldblatt).	187
8.2	New optical bench layout for post-LS1 operation, featuring the imaging line, the interferometry line and the wavefront distortion measurement line.	188
8.3	Sketch of the interferometry line to be installed in the LHC (Courtesy: A. Goldblatt).	189
8.4	Motorized double slits system to be used for the interferometry line in the LHC (Courtesy: A. Goldblatt).	190
8.5	LSF of two double slits system at $D_1 = D_2 = 11$ mm at $\lambda = 550$ nm, with the corresponding horizontal and vertical projections.	190
8.6	Comparing 2D interferometer LSF with separate 1D interferometer respectively in the horizontal and vertical plane.	191
8.7	LSF of various 2D interferometers obtained by varying the drift space between the single sets of double slits.	191
8.8	Hartmann-mask Setup.	192
8.9	Hartmann-mask working principle.	194
8.10	Diffraction pattern of the SR light passing through different Hartmann-mask hole diameter at different distances from the extraction mirror.	195
11	The geometry used for the treatment of synchrotron radiation, featuring K^* as coordinate system moving along the trajectory.	ii

Introduction

Measuring the beam transverse emittance is fundamental in every accelerator and, for colliders in particular, the precise determination of the beam emittance is essential to maximize the luminosity and thus the performance of the colliding beams.

In high energy machines, where the emittance is not a directly accessible quantity, it is often inferred from the measurement of the transverse beam sizes and the knowledge of the accelerator optics.

Beam size measurement methods can be split into two families: destructive and non-destructive techniques.

Synchrotron Radiation (SR) is a versatile tool for non-destructive beam diagnostics, since its characteristics are closely related to those of the source beam, thus representing an eye into the accelerator. SR is widely used in electron accelerators and storage rings and less often in hadron machines, because the amount of emitted radiation decreases with the increase of the accelerated particle mass.

Since the SR power also increases with energy, at the European Center for Nuclear Research (CERN) SR monitors can be exploited as the proton beam size monitor of the two higher energy machines, the Super Proton Synchrotron (SPS) and the Large Hadron Collider (LHC). When these two accelerators are operated with nominal parameters the total beam intensity and energy rule out invasive beam size measurement techniques and SR measurements result in the only available diagnostics.

This thesis focuses on the development and the optimisation of the transverse beam diagnostics based on SR monitors in the SPS and the LHC and it is structured in four main parts.

The introductory part, covered by the first two chapters, provides the basic concepts of transverse beam dynamics and presents the properties of the radiation emitted by accelerated charges explaining how it can be used in diagnostics.

Chapter 1 offers an overview of the CERN accelerators complex introducing the SPS, the LHC and their beams. In addition it recalls the main beam dynamics concepts used throughout this thesis: the machine optical functions derived from the beam transverse motion described by the betatronic oscillations, the Twiss parameters and its transport matrix. Moreover, the beam transverse emittance and the collider luminosity are defined. Lastly, the different techniques employed at CERN to measure the beam profile in the different accelerators are presented.

Chapter 2 describes the synchrotron light emission by relativistic accelerated particles calculated from the generalisation of the radiation emitted by non-relativistic charges. The properties of the light are given for different sources: bending magnet and undulators. Additionally, visible-SR based monitors used for the beams transverse diagnostics, such as the direct imaging and SR interferometry, are described.

The second part, covered by the following two chapters, is dedicated to the SR monitors performance definition, and simulation.

Chapter 3 presents the existing beam size monitors in the LHC: the full chain is described, from the SR source to the extraction mechanism, successively to the optical system and finally to the detector. However, aiming for its reactivation, also the historic monitor in the SPS installed in the late 70's is described.

Conventional simulation packages treat SR sources, optical transport and photon detection separately. Chapter 4 includes the development and validation of a new simulation tool that, combining the available codes, allowed providing a comprehensive study of the CERN SR systems from source to detector. Such a study resulted in the design of the new LHC SR imaging monitor.

The same chapter includes the description, characterization and design of the interferometer technique as an alternative method to the direct imaging for the beam size

determination via SR. Taking into account the LHC machine and beam parameters, a feasibility study demonstrated its applicability and its expected performance was assessed.

The experimental part of the thesis work comprises laboratory and beam-based measurements, discussed in detail in Chapters 5, 6 and 7.

Chapter 5 describes the beam experiments carried out on different accelerators to validate the simulations reported in Chapter 4. This includes several studies in the LHC, aimed at characterizing the installed imaging system. In addition, the first beams circulating in the SPS after the CERN Long Shutdown (LS1) were used to verify the alignment, the magnification and the transmission of the recently installed SR monitor. Finally, in the frame of the collaboration with the ALBA synchrotron light source in Barcelona, the beam tests scheduled during the commissioning of the ALBA interferometer allowed gaining operative experience with the system and validating the studies of the LHC interferometer.

Chapter 6, is dedicated to laboratory studies carried out at CERN to characterize the electro-magnetic coupling between the LHC SR extraction tank and the LHC beams. These tests were motivated by the reliability problems of the LHC SR extraction mirror arisen in 2012, that originated from beam induced heating and became the main source of aberrations in the LHC SR monitors. The concept of longitudinal impedance is presented and the “stretched wire” technique, as a method to measure it, is described and applied.

The results were mainly used to validate the available radio frequency simulations and to choose the best modification to the extraction system to be implemented, which is meant to reduce the mirror heating, and, consequently its deformation and the resulting worsening of the SR monitor resolution.

Since the beam emittance is the physical quantity of interest in the performance analysis of the LHC, determining the optical functions at the SR monitors is as relevant as measuring the beam size. Moreover, an accurate knowledge of the beam optics at the SR monitors is crucial for the characterisation of the monitors’ performance, in particular for the magnification measurement, as discussed in Chapter 5. Therefore,

the description of the “K-modulation” method for the optical function determination and its application in a dedicated measurement campaign are reported in Chapter 7.

Chapter 8, the concluding part, presents the final layout of the SR monitors and the description of the various optical elements to be installed in the LHC. The upgrades of the system proposed on the basis of this thesis work are highlighted, including the new system for the on line monitoring of the extraction mirror deformation caused by the beam induced heating.

Chapter 1

Overview

1.1 CERN accelerators complex

Founded in 1954, the European Organisation for Nuclear Research (CERN) laboratory sits astride the Franco-Swiss border near Geneva. CERN's main function is to provide the particle accelerators and other infrastructure needed for high-energy physics research; as a result, numerous experiments have been constructed following international collaborations since it was one of Europe's first joint ventures that now has 21 member states [1].

Nowadays, the most known accelerator at CERN is the Large Hadron Collider (LHC), in which proton beams are accelerated to the highest energy in the world and then put in collision to probe into the heart of matter. However, this top energy is gradually built up in a chain of accelerators of equal importance. Each machine boosts the energy of the particles beam, before injecting it into the next machine in the sequence. A full scheme of the CERN accelerator chain is shown in Fig.1.1, denoting the various properties and type of the circulating beams in the different experiments. Since this work is mainly treating the proton beams colliding in the LHC, the following contains a brief description of the different accelerators the beam passes through, focusing more on the LHC and its last injector.

The proton source consists of hydrogen gas that is injected in a plasma chamber, where strong electromagnetic fields ionize the atoms and protons are extracted at 100 KeV towards *LINAC 2*.

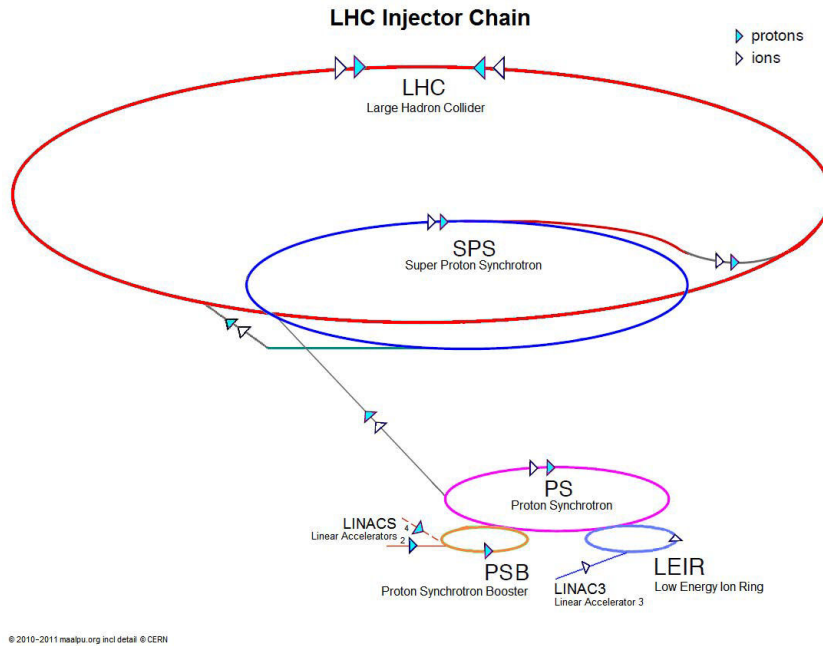


Figure 1.1: CERN accelerators chain [1].

The *LINAC 2* is a linear accelerator in which the protons are captured in bunches, accelerated to the energy of 50 MeV and sent to the first circular accelerator in the chain.

The Proton Synchrotron Booster (*PSB*) consists of four superimposed synchrotron rings that accelerate the protons from 50 MeV/c to 1.4 GeV/c for injection into the Proton Synchrotron (*PS*). It is important to know that the LHC-type beams transverse quality is defined in the *PSB*, since multi-turn injection is employed to accumulate the beam coming from *LINAC 2*. By contrast, in the accelerator chain downstream, the beam is always transferred in a single-turn, so that the transverse emittances are basically unchanged apart from residual mismatch or high-intensity effects.

In the *PS* the protons are accelerated up to a momentum of 26 GeV/c; this accelerator determines the *LHC* protons longitudinal structure (bunch spacing) as the result of a sophisticated series of Radio Frequency (RF) gymnastics done throughout the *PS* cycle. Finally the beam is extracted toward the Super Proton Synchrotron

(*SPS*).

The *SPS* accelerates the proton beams up to 450 GeV/c (the injection energy of the *LHC*). It is a 7 Km circumference synchrotron divided in 6 sectors interleaved by long straight sections (LSS 1-6) of almost 130 m each. The revolution period in this machine is 23 μ s. In the past, the *SPS* was used as protons/anti-protons collider (allowing the discovery of the *W* and *Z* bosons in 1981-1984 [10]) and as electrons/positrons injector for the Large Electron Positron collider (*LEP*). Nowadays it is used as well for fixed targets experiments and for testing innovative acceleration schemes based on plasma wakefields [11].

Finally the last energy boost is given in the *LHC* itself, where the injected beams of 450 GeV/c are brought up by design report to 7 TeV/c, making it the worlds highest energy particle accelerator. The *LHC* is installed in the same underground tunnel that was built for the Large Electron Positron collider (*LEP*), with a circumference of 27 Km long, laying at about 100 m underground. The *LHC* is divided into 8 octants [12], where two counter rotating beams circulate in two separated rings designed to be filled with protons (p) or ions (Pb). In four Interaction Points (IP 1, 2, 5, 8) distributed around the ring, the detectors of *ATLAS*, *ALICE*, *CMS* and *LHCb* experiments are respectively installed, where the beams collide in common vacuum chambers as shown in Fig. 1.2.

The *LHC* was operated at half of its design beam energy in 2010 (3.5 TeV) and 2011 and at 4 TeV in 2012, as shown in Tab. 1.1. In 2013 it went into a long shutdown (LS1) [13] planned for maintenance and consolidation in order to increase beam energy to 6.5 TeV per beam, with beam operation restart planned for early 2015. By 2013, the *LHC* had achieved many milestones setting new records for maximum beam intensity and energy stored and highest luminosity reached in a collider [14]. Moreover, it recorded the first observations of the very rare decay of the *B_s* meson into two muons ($B_s^0 \rightarrow \mu^+ \mu^-$) (a major test of super-symmetry), created a quark-gluon plasma, and discovered two previously unobserved particles, i.e. the $\chi_b(3P)$ bottomonium state and a massive 125 GeV boson which has been confirmed to be the long-sought Higgs boson [15, 16]. Following this, the 2013 Nobel Prize was awarded to Peter Higgs and Francois Englert who theorized the existence of this particle in 1964 [17].

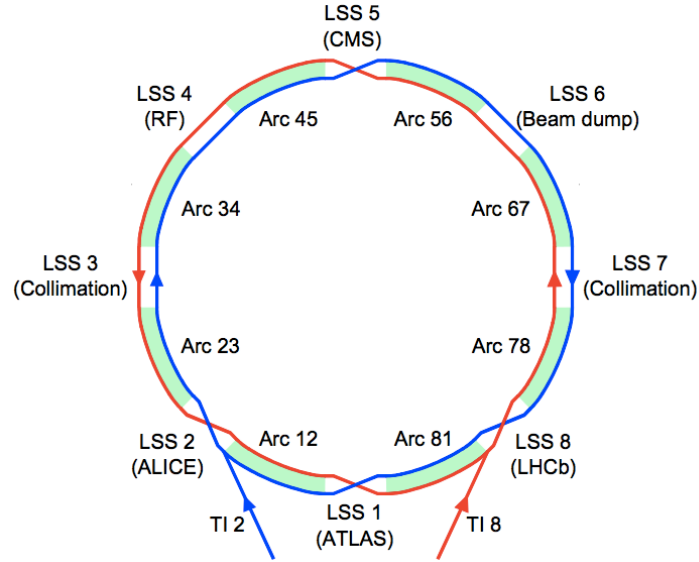


Figure 1.2: Schematic layout of the *LHC*. Beam 1 (blue) circulates clockwise and Beam 2 (red) counter-clockwise.

Parameter		2010	2011	2012	Design
Beam Energy	[TeV]	3.5	3.5	4	7
β^* in IP 1 and 5	[m]	2.0/3.5	1.5/1.0	0.6	0.55
Bunch Spacing	[ns]	150	75/50	50	25
Max num of bunches		368	1380	1380	2808
Max protons per bunch		$1.2 \cdot 10^{11}$	$1.45 \cdot 10^{11}$	$1.7 \cdot 10^{11}$	$1.15 \cdot 10^{11}$
Normalized emittance at injection	[mm.mrad]	2	2.4	2.5	3.75
Peak Luminosity	[$cm^{-2} \cdot s^{-1}$]	$2.1 \cdot 10^{32}$	$3.7 \cdot 10^{33}$	$7.7 \cdot 10^{33}$	10^{34}
Stored Beam Energy	[MJ]	28	110	140	362

Table 1.1: An overview of performance-related parameters during the LHC Run I.

1.2 Introduction to beam dynamics

This section is meant to give an overview of the basic equations governing the motion of the particles in an accelerator. To accomplish this, the concepts of optical functions, tune, transport matrix and beam parameters such as transverse emittance and luminosity are introduced. A comprehensive introduction to beam dynamics can be found in [18].

1.2.1 Lorentz force

In an accelerator the charged particles are guided and accelerated by means of electromagnetic fields, based on the relativistic form of the Lorentz equation:

$$\vec{F} = \gamma q \left(\vec{E} + c\vec{\beta} \times \vec{B} \right) \quad (1.1)$$

where \vec{F} is the force acting on a particle of electric charge q moving at a relativistic velocity $\vec{v} = \vec{\beta}c$, due to an external electromagnetic fields \vec{E} and \vec{B} . The Lorentz factor is defined as $\gamma = \frac{1}{\sqrt{1-\beta^2}}$, with c being the speed of light.

The electric field is supplied using the Radio Frequency (RF) cavities, providing the particles with the needed energy for the acceleration and to compensate for the one lost in the accelerator. The node of the RF sinusoidal wave is synchronised with the passage of particles with the nominal momentum. Therefore it creates stationary trap regions for these synchronous particles called buckets. The particles “clumped” around a synchronous particle in the center of the bucket create the bunch. In the case of the SPS, in operational conditions, the bucket length is 5 ns while in the LHC it is the half.

The magnetic fields are responsible of the bending and the focusing of the particles around the design trajectory for the nominal momentum particles, the closed orbit. The bending is generated by dipoles applying a magnetic field perpendicular to the plane of the trajectory, while the focusing is generated by quadrupoles. The sign and the value of the deflection that a particle undergoes in the quadrupoles varies with its momentum and its transverse offset with respect to the magnet’s center. Hence different focusing and defocusing are applied to the particles in the bunch; these “chromatic” effects are corrected with higher order corrections using sextupole and

octupole magnets.

1.2.2 Betatronic oscillations

For the beam dynamics description, we consider the Frenet-Serret coordinate system $(\vec{s}, \vec{x}, \vec{y})$, presented in Fig. 1.3, moving with the particle on a trajectory where the local curvature is ρ . Accordingly, the position of a particle in the transverse plane $(x,$

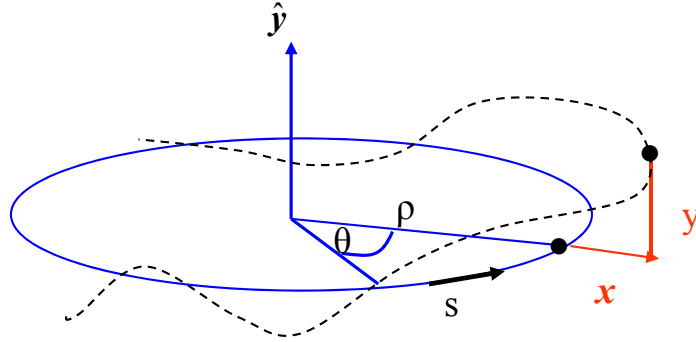


Figure 1.3: Frenet-Serret coordinate system.

y) is given by:

$$\vec{R} = (\rho + x)\vec{x} + y\vec{y} \quad (1.2)$$

The transverse motion is calculated assuming the magnetic field components being only transverse and symmetric with respect to the horizontal plane ($\partial B_x/\partial x = -\partial B_y/\partial y = 0$ and $\partial B_y/\partial x = \partial B_x/\partial y$) and $\gamma = \text{constant}$ (the particle does not radiate energy). The magnetic field near the origin can then be expressed as:

$$B_y(x) = B_{y0} + \frac{dB_y}{dx}x + \frac{1}{2!} \frac{d^2 B_y}{dx^2} x^2 + \frac{1}{3!} \frac{d^3 B_y}{dx^3} x^3 + \dots \quad (1.3)$$

Normalizing B_y to the beam momentum, one gets:

$$\frac{B_y(x)}{p/e} = \frac{1}{\rho} + kx + \frac{1}{2!} mx^2 + \dots \quad (1.4)$$

that is the expression of an infinite sum of multipolar elements: dipole, quadrupole, etc. The expansion parameters, $1/\rho$, k and m , are responsible for the beam bending,

focusing and chromaticity correction respectively.

Taking into account a charged particle ($q = e$) crossing a magnetic field under the aforementioned assumption and considering only its linear terms in x, y , the Lorentz force has to be equal to the centripetal force:

$$e(\vec{v} \times \vec{B}) = m_0 \gamma \ddot{\vec{R}} \quad (1.5)$$

where the acceleration $\ddot{\vec{R}}$ is:

$$\ddot{\vec{R}} = (\ddot{r} - r\dot{\theta}^2)\vec{x} + (2\dot{r}\dot{\theta} + r\ddot{\theta})\vec{s} + y\ddot{y} \quad (1.6)$$

Therefore considering only the radial component (along x):

$$\ddot{r} - r\dot{\theta}^2 = \frac{d^2}{dt^2}(\rho + x) - \frac{v_s^2}{\rho + x} \quad (1.7)$$

$$-\frac{ev_s B_y}{\gamma m_0} = -\frac{ev_s^2 B_y}{v_s \gamma m_0} = -\frac{B_y}{p/e} v_s^2 \quad (1.8)$$

Changing the independent variable from t to s and since $x \ll \rho$:

$$v_s^2 x'' - \frac{1}{\rho} \left(1 - \frac{x}{\rho}\right) v_s^2 = -\left(\frac{1}{\rho} + kx\right) v_s^2 \quad (1.9)$$

$$x'' + \left[\frac{1}{\rho^2} + k(s) \right] x = 0 \quad (1.10)$$

Similarly, since there is no bending in the vertical plane:

$$y'' - k(s)y = 0 \quad (1.11)$$

The derived equation of motion is the Hill's equation [19], that describes a pseudo-harmonic oscillator in which the spring constant k depends on the ring position (s). Its solution along x for a given s (identical for y) can be expressed by:

$$x(s) = A\sqrt{\beta_x(s)} \sin(\phi_x(s) + \phi_0) \quad (1.12)$$

where $\beta_x(s)$ is the amplitude modulation, ϕ_0 an arbitrary phase, $\phi_x(s)$ the phase advance along the trajectory and A a constant that will be defined in the following. By inserting Eq. 1.12 in the equation of motion (Eq. 1.10):

$$\phi(s) = \int_0^s \frac{ds'}{\beta(s')} \quad (1.13)$$

the phase advance of the oscillation from the origin to the point s in the lattice is defined. The tune Q , is closely correlated with the phase advance per turn and is defined as the number of oscillations in one revolution (full turn of the machine of circumference C):

$$Q = \frac{1}{2\pi} \phi(C) = \frac{1}{2\pi} \int_{s_0}^{s_0+C} \frac{ds}{\beta(s)} \quad (1.14)$$

Finally, the constant A can be expressed through $x(s)$ and $x'(s)$:

$$A^2 = \gamma(s)x^2(s) + 2\alpha(s)x(s)x'(s) + \beta(s)x'^2(s) \quad (1.15)$$

where α, β, γ are called the Twiss parameters, related as:

$$\alpha(s) = -\frac{\beta'(s)}{2}, \quad \gamma(s) = \frac{1 + \alpha(s)^2}{\beta(s)} \quad (1.16)$$

Equation 1.15 leads to a parametric representation of an ellipse in the transverse phase space (x, x') , depicted in Fig. 1.4, while the particle moves around the accelerator. In addition, there is a whole family of similar ellipses mapping every particle in the beam. These skew ellipses are all centered around the origin and have the same orientation. A particle which is contained inside an ellipse returns to a point inside the ellipse after one turn in accelerator.

In addition, $\epsilon = A^2$ is defined as the Courant-Snyder invariant, called emittance, with $\epsilon = \text{Ellipse Area}/\pi$. Indeed, according to Liouville theorem, the emittance is a constant of the motion in the presence of only conservative forces and no energy dissipation.

Then a bunch could be represented statistically as a Gaussian distribution of particles in the transverse phase plane and defines the beam size $\sigma_{x,y}$ and divergence

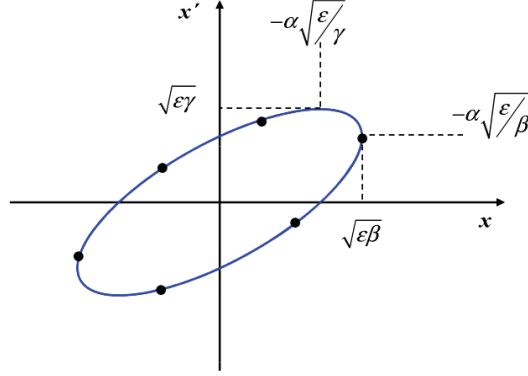


Figure 1.4: Particle trajectory describing an ellipse in the transverse phase space.

$\sigma_{x',y'}$ as following:

$$\sigma_{x,y}(s) = \sqrt{\epsilon_{x,y}\beta_{x,y}(s)} \quad (1.17)$$

$$\sigma_{x',y'}(s) = \sqrt{\epsilon_{x,y}\gamma_{x,y}(s)} \quad (1.18)$$

As the emittance is constant, a shrinking of the beam size is observed when the beam is accelerated: the beam size reduction is inversely proportional to the momentum increase. However, since the acceleration process consists in increasing only the longitudinal momentum, it should preserve the transverse distributions. This phenomenon is often called adiabatic damping which is somewhat misleading since no dissipative effects are involved. Therefore the concept of the normalized emittance defined as the enclosing area of a fraction of the particles in the $(x, \gamma\beta x')$ phase space becomes useful to use.

$$\epsilon_{n_{x,y}} = (\gamma\beta) \epsilon_{x,y} \quad (1.19)$$

Hence the normalized emittance is constant at every location and independent from the particles energy. This provides a great advantage: beam diagnostics, despite its location, can evaluate the beam emittance at collision energy and estimates its impact on the luminosity as described later in this chapter.

1.2.3 Dispersion

Up to now, only the behaviour of a particle with nominal momentum has been considered; in the following, the case of an off-momentum particle is studied and the contribution to the betatronic motion is investigated. By defining δ as:

$$\delta = \frac{p - p_0}{p_0} \quad (1.20)$$

the momentum deviation, Eq. 1.10, becomes:

$$x'' + \left[\frac{1 - \delta}{\rho(s)^2 (1 + \delta)} - \frac{B_1(s)}{B\rho(1 + \delta)} \right] x = \frac{\delta}{\rho(s) (1 + \delta)} \quad (1.21)$$

By searching solutions of the type:

$$x(s) = x_\beta(s) + D(s) \cdot \delta \quad (1.22)$$

where x_β is the solution previously obtained for nominal momentum particles in Eq. 1.12, and $D(s)$ is the *dispersion function*. The latter is defined as:

$$D(s) = \int_0^s \frac{\sqrt{\beta(s)\beta(s')}}{\rho(s')} \sin(\varphi(s') - \varphi(s)) ds' \quad (1.23)$$

As shown in Fig. 1.5, the modified solution results in an additional motion on top of the betatronic one:

$$\begin{cases} x_s(s) = D(s) \delta \\ x'_s(s) = D'(s) \delta \end{cases} \quad (1.24)$$

so that the solution of Eq. 1.21 is expressed by:

$$\begin{cases} x(s) = x_\beta(s) + x_s(s) \\ x'(s) = x'_\beta(s) + x'_s(s) \end{cases} \quad (1.25)$$

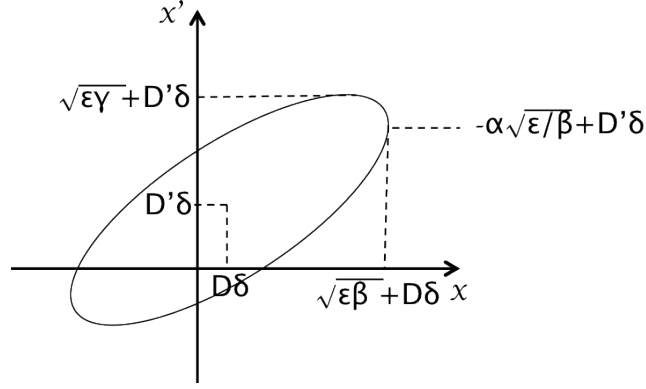


Figure 1.5: Off-momentum particle trajectory describing a shifted ellipse in the transverse phase space.

1.2.4 Transport matrix

The *transport matrix* is defined as the matrix that allows to calculate the evolution of a known position and angle of a particle (x_0, x'_0) around the full circumference of the accelerator. Some manipulations [20] allow to rewrite the equation of motion (1.12) as follows:

$$x(s) = a\sqrt{\beta(s)}\sin(\varphi(s)) + b\sqrt{\beta(s)}\cos(\varphi(s)) \quad (1.26)$$

where a and b can be obtained in function of x and x' at a given position s_1 :

$$\begin{cases} a = x(s_1) \left[\frac{\sin(\varphi(s_1)) + \alpha(s_1)\cos(\varphi(s_1))}{\sqrt{\beta(s_1)}} \right] + x'(s_1) \sqrt{\beta(s_1)}\cos(\varphi(s_1)) \\ b = x(s_1) \left[\frac{\cos(\varphi(s_1)) - \alpha(s_1)\sin(\varphi(s_1))}{\sqrt{\beta(s_1)}} \right] - x'(s_1) \sqrt{\beta(s_1)}\sin(\varphi(s_1)) \end{cases} \quad (1.27)$$

Substituting Eq.1.27 in Eq. 1.26, the solution of $x(s_2)$ and $x'(s_2)$ in a matrix formalism can be written as follows:

$$\begin{pmatrix} x(s_2) \\ x'(s_2) \end{pmatrix} = M(s_1|s_2) \begin{pmatrix} x(s_1) \\ x'(s_1) \end{pmatrix} \quad (1.28)$$

where:

$$M(s_1|s_2) = \begin{pmatrix} \sqrt{\frac{\beta_2}{\beta_1}} (\cos\varphi_{21} + \alpha_1 \sin\varphi_{21}) & \sqrt{\beta_2\beta_1} \sin\varphi_{21} \\ -\frac{1+\alpha_1\alpha_2}{\sqrt{\beta_2\beta_1}} \sin\varphi_{21} + \frac{\alpha_1-\alpha_2}{\sqrt{\beta_2\beta_1}} \cos\varphi_{21} & \sqrt{\frac{\beta_1}{\beta_2}} (\cos\varphi_{21} - \alpha_2 \sin\varphi_{21}) \end{pmatrix} \quad (1.29)$$

The subscripts 1 and 2 indicates the Twiss parameters in s_1 and s_2 , while φ_{21} is the phase advance between the two points of the machine. Using matrix properties, it is immediate to demonstrate:

$$M(s_3|s_1) = M(s_3|s_2) M(s_2|s_1) \quad (1.30)$$

1.2.5 Luminosity

Beside the center of mass energy of the colliding beams, the performance of a collider is usually quantified by the luminosity \mathcal{L} , defined as the proportionality factor between the observed events R rate and the interaction cross section σ_{int} :

$$\frac{dR}{dt} = \mathcal{L} \sigma_{int} \quad (1.31)$$

The luminosity of two Gaussian bunches colliding head-on (with no transverse offset) is given by:

$$\begin{aligned} \mathcal{L} &= f \frac{N_1 N_2}{2\pi \sqrt{\sigma_{1x}^2 + \sigma_{2x}^2} \sqrt{\sigma_{1y}^2 + \sigma_{2y}^2}} \\ &= f \frac{N_1 N_2}{4\sqrt{\epsilon_x \beta_x^* \epsilon_y \beta_y^*}} \end{aligned} \quad (1.32)$$

where N_i is the intensity of bunch i ($i=1, 2$), f is the revolution frequency of the collider, $\beta_{x,y}^*$ is the beta function in the collision point in the horizontal and vertical plane (x, y) and σ_x, σ_y are the bunch sizes. However different factors contribute to the reduction of this nominal luminosity such as the crossing angle, hourglass factor and the transverse offset between the colliding bunches [21].

1.3 Profile measurements techniques at CERN

In the SPS and the LHC, the beam emittance is not directly measurable, due to the extreme beam parameters and to the machine high energy. Therefore different measurements techniques are applied to measure the beam size from which the transverse emittance can be derived. The transverse diagnostic instruments used in the SPS and the LHC will be described in the following paragraphs.

The betatron matching monitor

The matching monitor [22] is an invasive measurement device and consists of imaging the Optical Transition Radiation (OTR) emitted by a thin radiator using asymmetric optics coupled to a fast linear CMOS imaging sensor. It can be used only to study the beam optics injection mismatch, by recording the beam images of low intensity beams during the first few hundreds turns after the injection into the ring.

The beam gas ionization monitor (BGI)

The BGI [23] is mainly designed to monitor lead ions transverse profiles and its

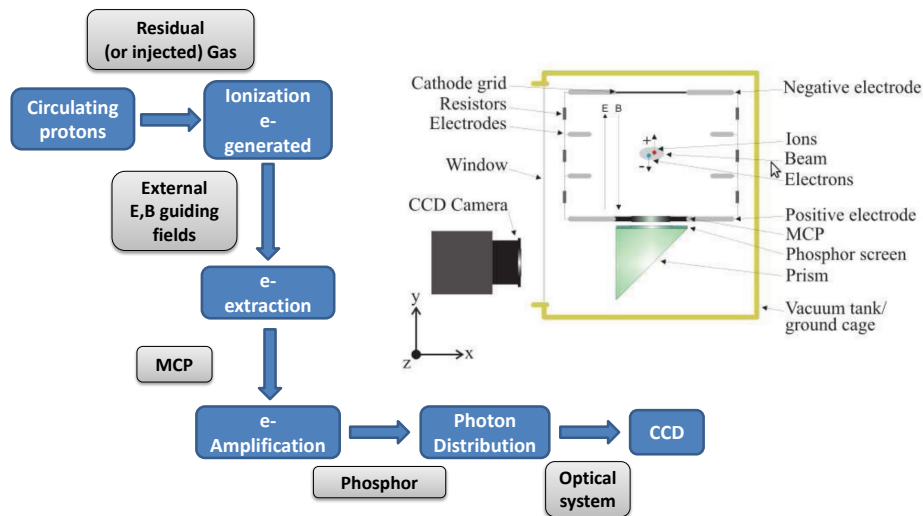


Figure 1.6: Beam Gas Ionisation monitors working principle.

working principle is shown in Fig. 1.6. It is based on collecting the electrons which are created when the beam ionizes the residual gas. These electrons are then driven

by an external electrical field to a Micro Channel Plate (MCP) in which the electrons number is amplified. The beam size is obtained by imaging the transverse distribution of the electrons after its conversion to photons on a deposited phosphor screen coupled to the Charge-Coupled Device (CCD). Lately some effort has been put into adapting the system to measure also proton beams profiles, but for the moment it is still not operational. This monitor is partially intercepting, since the beam-gas interactions cause proton multiple scattering that can increase the beam size, especially when gas is locally injected into the beam pipe in order to increase the detector signal.

The beam wire scanners (WS)

A WS [24] is an intercepting device consisting of a thin wire which is moved across

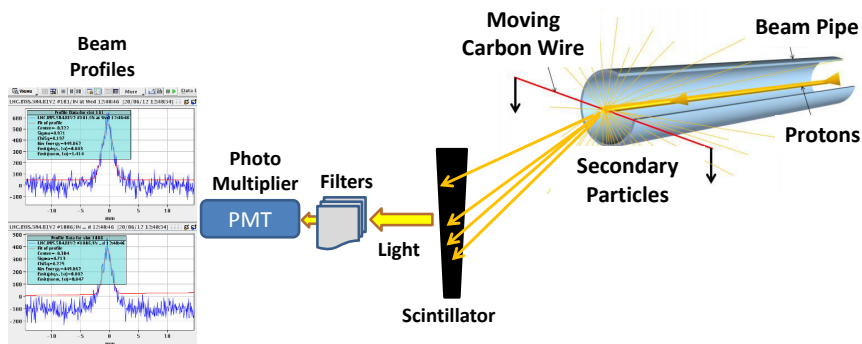


Figure 1.7: Wire Scanners working principle.

the beam; by doing so, the beam interacts with the wire material and a signal can be obtained by detecting the flux of secondary particles several meters downstream of the wire using a scintillator. This kind of WS are used in all CERN rings (in the linacs the amplitude signal is directly deduced by the secondary emission on the wire) and since they need to cover a large range of beam characteristics (size, energy and intensity), their design varies in terms of mechanics (wire movement in the pipe: linear vs. circular), but a similar acquisition systems is preserved and is described in Fig. 1.7. In the LHC, the devices are linear with a constant speed of 1 m/s . In the Super Proton Synchrotron (SPS), both linear scanners with a speed around 1 m/s and rotational ones with nominal speed of 6 m/s are used (new prototypes to be installed in 2015 will reach 10 m/s). By plotting the count rate of the detector

against the wire position a representation of the beam profile is obtained. However the maximum intensity measurable by the WS is limited [25]; it is defined by the Carbon wire breakage due to sublimation. The wire damage is not immediate above the new defined thresholds, but scanning such high intensity beams would speed up the wire deterioration. Table 1.2 presents the found threshold for both beams at injection and 6.5 TeV for two beam emittances. It has to be noted that the different thresholds per beam and per plane is due to the optical function β value at the scanner location, hence the beam size to be scanned.

Therefore, WS are considered the reference devices for beam emittance measurements in the LHC and the SPS. All the other profile monitors are calibrated to this reference.

		BEAM 1		BEAM 2	
		H	V	H	V
		ε (μm)			
450 GeV	2	164	118	204	106
	3.5	217	156	269	141
7 TeV	2	53.1	51.5	51.6	26.9
	3.5	70.3	68.1	68.2	35.6

Table 1.2: Maximum beam intensity limits for WS measurements (in 10^{11} protons).

The beam synchrotron light monitor (BSRT)

The BSRT is the only non-destructive instrument measuring the beam size in the LHC. It consists of imaging the visible synchrotron light emitted by the protons in IR 4 on a fast gated CCD camera, providing a beam 2D image from which the beam size in both planes (horizontal and vertical) can be extracted [26]. The measurements are non-invasive, continuous, automatic and compatible with high intensity operation. It measures bunch-by-bunch transverse profiles and is calibrated with respect to the WS during dedicated low beam intensity runs. The LHC has been equipped with one BSRT per beam from the beginning of Run I. More details about the installed monitors can be found in Section 3.1. Moreover, during LS1 an obsolete (not used)

installation in the SPS has been refurbished with a LHC-like BSRT monitor that has been commissioned at the same time of writing this report. A historical glance will be given on the old monitor in Section 3.2, and the 2014 commissioning results are presented in Section 5.1.1.

The synchrotron light monitors represent the main subject of this thesis work and will be widely described and discussed in the following chapters.

Chapter 2

Synchrotron Light Theory and Its Use in Diagnostics

Synchrotron Radiation (SR) has been investigated theoretically for over a century and experimentally for about half of this time. The basic theoretical considerations and investigations of the radiation emitted by relativistic charged particles in circular motion goes back to the work of Liénard (1898) followed by Schott, Jassinsky, Kerst, Ivanenko, Pomeranchuk and others; but the first observation of the visible SR accidentally took place on April 24, 1947 at the General Electric Research Laboratory in Schenectady, New York [27]. Nowadays SR is widely produced by the use of dedicated synchrotrons and is employed in a host of applications, ranging from solid-state physics to medicine. Synchrotron sources, producing X rays, offer unique probes of the semiconductors that lie at the heart of the electronics industry. Both ultraviolet radiation and X rays generated by synchrotrons are also employed in the treatment of diseases, especially certain forms of skin cancer [28].

More related to this thesis work, SR results as a very powerful tool for non-invasive beam diagnostics and is therefore a valuable tool for accelerators operation.

In this chapter, the general formulas describing the SR are derived together with the expressions of the EM fields emitted by a moving charge, that will be generalized for the ultra-relativistic case. Furthermore, emitted radiation from bending magnets in circular accelerators and from periodic magnetic structures such as the undulators will be studied. Finally two techniques for exploiting the SR for beam diagnostics are

discussed: imaging and interferometry.

2.1 Fields emitted by moving relativistic charges

The general solution of Maxwell's equations, for the case of a time varying charge ρ and current density \vec{j} , in the Lorentz gauge is described by the following scalar and vector *retarded potentials* [29]:

$$\phi(\vec{r}, t) = \frac{1}{4\pi\epsilon_0} \int_V \frac{\rho(\vec{r}', t_{ret})}{|\vec{r} - \vec{r}'|} dV \quad (2.1)$$

$$\vec{A}(\vec{r}, t) = \frac{\mu_0}{4\pi} \int_V \frac{\vec{j}(\vec{r}', t_{ret})}{|\vec{r} - \vec{r}'|} dV \quad (2.2)$$

where r and r' are respectively the position vector at the time of observation t and the retarded time t_{ret} .

The solution at time t , is determined by the characteristic of the charge motion at t_{ret} , where the retardation effect derives from the finite EM propagation speed c . The relation between the two times is described in Fig. 2.1.

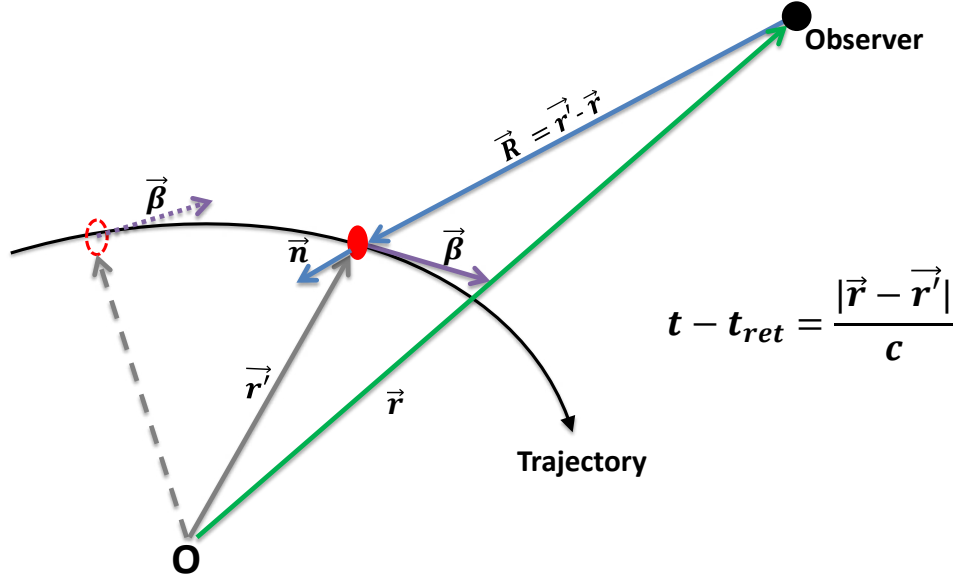


Figure 2.1: Position vectors r and r' used in the calculation of the retarded potentials, quantifying the time delay effect of the finite propagation speed of the SR.

By substituting

$$t_{ret} = t - \frac{|\vec{r} - \vec{r}'|}{c} \quad (2.3)$$

in Eqs. 2.1 and 2.2, one obtains the so-called *Liénard-Wiechert potentials*:

$$\phi(\vec{r}, t) = \frac{1}{4\pi\epsilon_0} \int_V \frac{\rho\left(\vec{r}', t - \frac{|\vec{r} - \vec{r}'|}{c}\right)}{|\vec{r} - \vec{r}'|} dV \quad (2.4)$$

$$\vec{A}(\vec{r}, t) = \frac{\mu_0}{4\pi} \int_V \frac{\vec{j}\left(\vec{r}', t - \frac{|\vec{r} - \vec{r}'|}{c}\right)}{|\vec{r} - \vec{r}'|} dV \quad (2.5)$$

If Eqs.2.4 and 2.5 are evaluated for a point charge q with instantaneous velocity $\vec{\beta}$, at a distance \vec{R} from the observer, with \vec{n} the corresponding unit vector (see Fig. 2.1) and using the properties of the Dirac deltas of the charge, the potentials reduce to:

$$\phi(\vec{r}, t) = \left\{ \frac{1}{4\pi\epsilon_0} \frac{q}{R} \frac{1}{(1 + \vec{n}\vec{\beta})} \right\}_{ret} \quad (2.6)$$

$$\vec{A}(\vec{r}, t) = \left\{ \frac{c\mu_0}{4\pi} \frac{q}{R} \frac{\vec{\beta}}{(1 + \vec{n}\vec{\beta})} \right\}_{ret} \quad (2.7)$$

Since by construction:

$$\begin{cases} \vec{E} = -\left(\nabla'\phi + \frac{\partial\vec{A}}{\partial t}\right) \\ \vec{B} = \nabla' \times \vec{A} \end{cases} \quad (2.8)$$

then the Liénard-Wiechert electric and magnetic fields are derived, obtaining:

$$\begin{aligned}
\vec{E} &= -\frac{q}{4\pi\epsilon_0} \nabla' \frac{1}{R(1+\vec{n}\vec{\beta})} - \frac{c\mu_0 q}{4\pi} \frac{\partial}{\partial t} \frac{\vec{\beta}}{R(1+\vec{n}\vec{\beta})} \\
\vec{B} &= \frac{c\mu_0 q}{4\pi} \times \left(\frac{\vec{\beta}}{[R(1+\vec{n}\vec{\beta})]} \right) \\
&= \frac{c\mu_0 q}{4\pi} \left(\frac{1}{[R(1+\vec{n}\vec{\beta})]} \nabla' \times \vec{\beta} - \frac{1}{[R(1+\vec{n}\vec{\beta})]^2} (\nabla' [R(1+\vec{n}\vec{\beta})]) \times \vec{\beta} \right)
\end{aligned} \tag{2.9}$$

Finally, by defining $\dot{\vec{\beta}}$ as the instantaneous acceleration and introducing $a = R(1+\vec{n}\vec{\beta})$, the fields expression become:

$$\vec{E} = \frac{q}{4\pi\epsilon_0} \left\{ -\frac{1-\beta^2}{a^3} (\vec{R} + \vec{\beta}R) + \frac{1}{ca^3} \vec{R} \times [(\vec{R} + \vec{\beta}R) \times \dot{\vec{\beta}}] \right\}_{ret} \tag{2.10}$$

$$\vec{B} = \frac{c\mu_0 q}{4\pi} \left\{ -\frac{[\vec{\beta} \times \vec{n}]}{a^2} - \frac{R}{ca^2} [\dot{\vec{\beta}} \times \vec{n}] + \frac{R}{a^3} \left(\vec{n}\vec{\beta} + \beta^2 + \frac{\vec{R}}{c} \dot{\vec{\beta}} \right) [\vec{\beta} \times \vec{n}] \right\}_{ret} \tag{2.11}$$

It could be noted that for static conditions, $\vec{\beta} = \dot{\vec{\beta}} = 0$, the electric field expression goes back to the Coulomb law of a point charge.

The electric field equation consists of two terms having different dependence on the distance between the source and the observation point:

- the first term decreases with the square of R and depends only on the velocity and the position of the charge. Since a Lorentz transformation would reduce this term to an electrostatic field, it does not lead to an emitted radiation;
- the second term is proportional to the acceleration $\dot{\vec{\beta}}$ and decreases with the first power of R .

Therefore, in the far field conditions (keeping only the term proportional to $1/R$), the field expressions become:

$$\vec{E} = \frac{q}{4\pi\epsilon_0} \frac{1}{ca^3} \left\{ \vec{R} \times \left[\left(\vec{R} + \vec{\beta}R \right) \times \dot{\vec{\beta}} \right] \right\}_{ret} \quad (2.12)$$

$$\vec{B} = \frac{c\mu_0 q}{4\pi} \left\{ -\frac{[\dot{\vec{\beta}} \times \vec{n}]}{cR(1 + \vec{n}\vec{\beta})^2} + \frac{(\dot{\vec{\beta}}\vec{n}) [\vec{\beta} \times \vec{n}]}{cR(1 + \vec{n}\vec{\beta})^3} \right\}_{ret} \quad (2.13)$$

By computing $\vec{E} \times \vec{n}$ in the far field approximation, it is shown [2] that the magnetic field can also be expressed by:

$$\vec{B} = \frac{1}{c} [\vec{E} \times \vec{n}] \quad (2.14)$$

Hence the Poynting vector, the directional energy flux density of the Liénard-Wiechert fields, can be written as:

$$\begin{aligned} \vec{S} &= \frac{1}{\mu_0} [\vec{E} \times \vec{B}] = \frac{1}{c\mu_0} [\vec{E} \times (\vec{E} \times \vec{n})] = \\ &= \frac{1}{c\mu_0} [\vec{E} (\vec{E}\vec{n}) - \vec{n}\vec{E}^2] = -\frac{1}{c\mu_0} \vec{E}^2 \vec{n} \end{aligned} \quad (2.15)$$

Then, one can choose a suitable coordinate system K^* in the particle frame, as shown in Fig. 11, which moves with the particle of charge $q = e$ and can define:

- Θ as the angle between the direction of the particle acceleration and the direction of observation;
- ϕ as the azimuth angle with respect to the direction of acceleration.

In this coordinate system the electric field expression is reduced to:

$$\begin{aligned} \vec{E}^* &= \frac{e}{4\pi\epsilon_0} \frac{1}{cR^3} \left(\vec{R} \times \left[\vec{R} \times \dot{\vec{\beta}}^* \right] \right) = \\ &= \frac{e}{4\pi\epsilon_0} \frac{1}{cR} \left(\vec{n} \times \left[\vec{n} \times \dot{\vec{\beta}}^* \right] \right) \end{aligned} \quad (2.16)$$

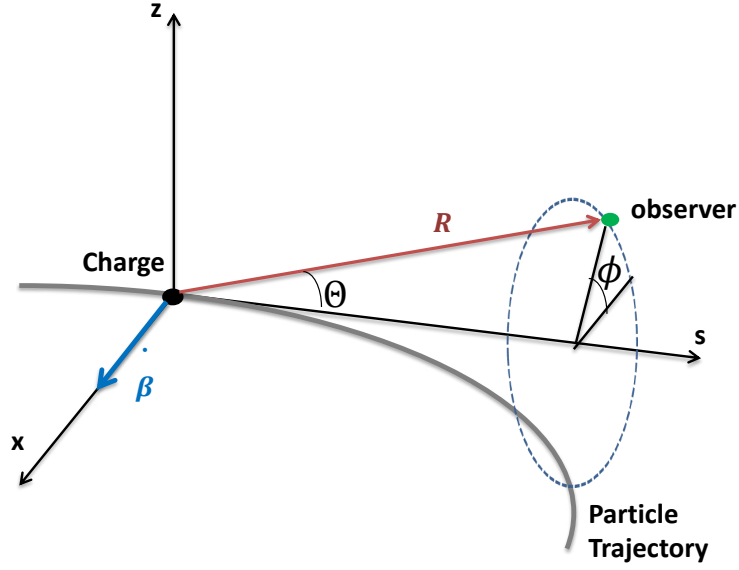


Figure 2.2: The geometry used for the treatment of synchrotron radiation, featuring K^* as coordinate system moving along the trajectory.

since $\vec{v}^* = 0 \Rightarrow \dot{\vec{\beta}}^* = 0$ and $a = R\ddot{\vec{\beta}} \neq 0$. Therefore, the radiated power per unit solid angle $d\Omega$, at the distance R from the generating charge, calculated as the flux of the pointing vector (Eq. 2.15) is:

$$\begin{aligned} \frac{dP}{d\Omega} &= -\vec{n}\vec{S}R^2 = \frac{1}{c\mu_0} \frac{e^2}{(4\pi\epsilon_0)^2} \frac{1}{c^2} \left(\vec{n} \times \left[\vec{n} \times \dot{\vec{\beta}}^* \right] \right)^2 = \\ &= \frac{e^2}{(4\pi)^2 c\epsilon_0} \left(\vec{n} \times \left[\vec{n} \times \dot{\vec{\beta}}^* \right] \right)^2 \end{aligned} \quad (2.17)$$

Using the following vector relations:

$$\begin{aligned} \left(\vec{n} \times \left[\vec{n} \times \dot{\vec{\beta}}^* \right] \right)^2 &= \left(\vec{n} \left(\vec{n} \dot{\vec{\beta}}^* \right) - \dot{\vec{\beta}}^* \left(\vec{n} \vec{n} \right) \right)^2 = \\ &= \left(\dot{\vec{\beta}}^* \right)^2 - \left(\vec{n} \dot{\vec{\beta}}^* \right)^2 = \left(\dot{\vec{\beta}}^* \right)^2 \sin^2 \Theta \end{aligned} \quad (2.18)$$

with

$$\vec{n} \cdot \dot{\vec{\beta}}^* = |\vec{n}| |\dot{\vec{\beta}}^*| \cos \Theta = |\dot{\vec{\beta}}^*| \cos \Theta \quad (2.19)$$

then the the radiation's spatial power distribution results to be:

$$\frac{dP}{d\Omega} = \frac{e^2}{(4\pi)^2 c \epsilon_0} \left(\dot{\vec{\beta}}^* \right)^2 \sin^2 \Theta \quad (2.20)$$

that corresponds to the power distribution of a Hertz dipole [29].

The total radiated power by the charged particle is obtained by integrating Eq. 2.20 over the full solid angle:

$$\begin{aligned} P_{TOT} &= \int_0^{4\pi} \frac{dP}{d\Omega} d\Omega \\ &= \frac{e^2}{(4\pi)^2 c \epsilon_0} \left(\dot{\vec{\beta}}^* \right)^2 \int_0^{2\pi} \int_0^\pi \sin^3 \Theta d\Theta d\phi \\ &= \frac{e^2}{6\pi \epsilon_0 c} \left(\dot{\vec{\beta}}^* \right)^2 \end{aligned} \quad (2.21)$$

Fig. 2.3 graphically shows the hertz dipole radiation distribution described in Eq. 2.21,

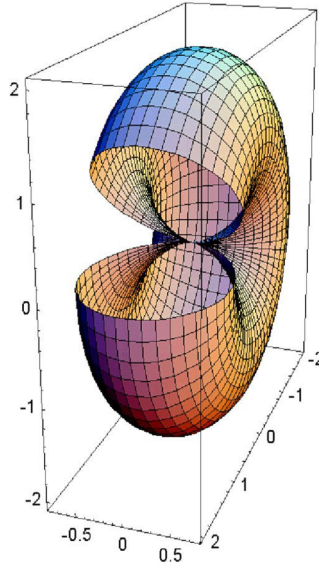


Figure 2.3: The total radiated power by the charged particle in K^* reference frame [2].

known as *Larmor's Formula* since it was first derived by J.J. Larmor in 1897, in the context of the wave theory of light [30].

Knowing that:

$$\vec{\beta}^* = \frac{\dot{\vec{v}}^*}{c} = \frac{\dot{\vec{p}}}{m_0 c} \quad (2.22)$$

Eq. 2.21 can be written in terms of non relativistic particle momentum:

$$P_{TOT} = \frac{e^2}{6\pi\epsilon_0 m_0^2 c^3} \left(\frac{d\vec{p}}{dt} \right)^2 \quad (2.23)$$

Since the total radiated power is a Lorentz invariant quantity, in order to find a valid expression of P_{TOT} for an arbitrary particle speed $\vec{\beta}$, including the relativistic case, a Lorentz invariant can be derived as a generalisation of Eq. 2.23 that for $\beta \ll 1$ it reduces to the classical Larmor's equation.

The generalisation [29] is unique since it contains only up to the first derivative of $\vec{\beta}$ and it is obtained by replacing the time t with the charge proper time element τ (where $d\tau = \frac{1}{\gamma} dt$) and the classical momentum \vec{p} with the momentum-energy-4-vector p^μ .

The resulting generalized expression is:

$$P_{TOT} = -\frac{e^2}{6\pi\epsilon_0 m_0^2 c^3} \left(\frac{dp_\mu^\vec{}}{d\tau} \cdot \frac{dp^\mu^\vec{}}{d\tau} \right) \quad (2.24)$$

where by definition of the scalar product of the 4-vector:

$$-\left(\frac{dp_\mu^\vec{}}{d\tau} \cdot \frac{dp^\mu^\vec{}}{d\tau} \right) = \left(\frac{d\vec{p}}{d\tau} \right)^2 - \frac{1}{c^2} \left(\frac{dE}{d\tau} \right)^2 = \left(\frac{d\vec{p}}{d\tau} \right)^2 - \beta^2 \left(\frac{d\vec{p}^2}{d\tau} \right) \quad (2.25)$$

Hence the final expression of the instantaneous emitted power in the case a of relativistic particle becomes:

$$P_{TOT} = \frac{e^2 c}{6\pi\epsilon_0 (m_0 c^2)^2} \left[\left(\frac{d\vec{p}}{d\tau} \right)^2 - \frac{1}{c^2} \left(\frac{dE}{d\tau} \right)^2 \right] \quad (2.26)$$

2.2 Various SR sources

2.2.1 Bending magnets

The spatial relationship between $\vec{\beta}$ and $\dot{\vec{\beta}}$ in Eq. 2.26, determines the detailed SR angular power distribution. When the charge is in instantaneous circular motion (the case of bending magnets), its acceleration $\dot{\vec{\beta}}$ is perpendicular to its velocity $\vec{\beta}$ and its energy is constant. Consequently, the total SR radiated power in a long dipole reduces to:

$$\begin{aligned}
 P_{TOT} &= \frac{e^2 c}{6\pi\epsilon_0(m_0c^2)^2} \left[\left(\frac{d\vec{p}}{d\tau} \right)^2 \right] \\
 &= \frac{e^2 c}{6\pi\epsilon_0(m_0c^2)^2} \cdot \gamma^2 \cdot \left[\left(\frac{d\vec{p}}{dt} \right)^2 \right] \\
 &= \frac{e^2 c}{6\pi\epsilon_0(m_0c^2)^4} \frac{E^4}{\rho^2}
 \end{aligned} \tag{2.27}$$

Its angular distribution can be derived based on [31, 32] as in Appendix A and results to be:

$$\frac{dP}{d\Omega} = \frac{1}{c^3\mu_0} \frac{e^4}{(4\pi\epsilon_0)^2} \frac{\beta^4 (\beta^2 - 1) \sin^2 \Theta \cos^2 \phi + (1 - \beta \cos \Theta)^2}{\rho^2 (1 - \beta \cos \Theta)^5} \tag{2.28}$$

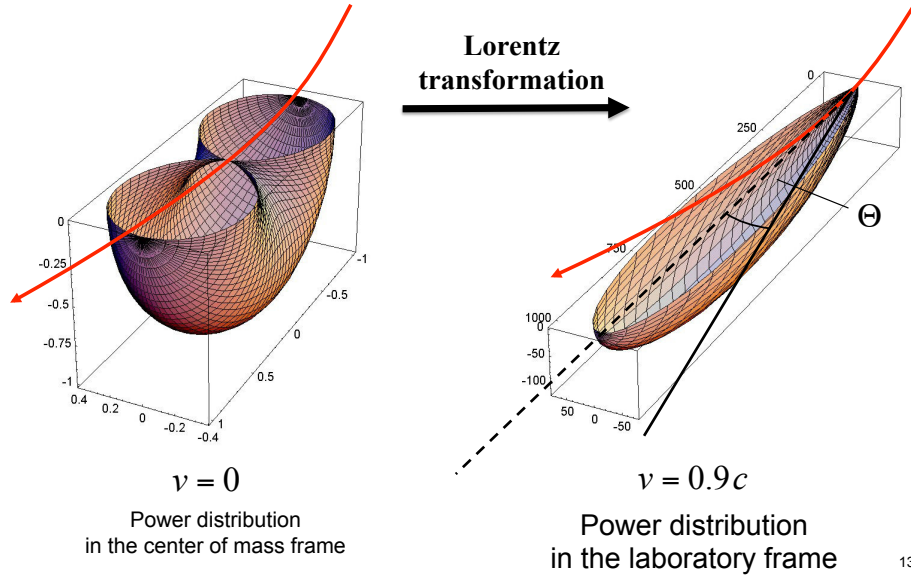
Figure 2.4 shows that, for the relativistic case, the synchrotron radiation occurs in a narrow cone of nominal angular width $\sim 1/\gamma$.

By integrating Eq. 2.28 over time, the energy received by an observer (per unit solid angle at the source) is obtained from:

$$\frac{d^2W}{d\Omega} = \int_{-\infty}^{\infty} \frac{d^2P}{d\Omega} dt = c\epsilon_0 \int_{-\infty}^{\infty} \left| R\vec{E}(t) \right|^2 dt \tag{2.29}$$

Then applying the Parseval theorem, by the mean of the Fourier transform, Eq. 2.29 can be expressed in the frequency domain as:

$$\frac{d^2W}{d\Omega} = 2c\epsilon_0 \int_0^{\infty} \left| R\vec{E}(\omega) \right|^2 d\omega \tag{2.30}$$



13

Figure 2.4: Lorentz transformation for the relativistic case, shapes the emitted SR angular distribution in a forward narrow cone [2].

The angular and the frequency distribution of the energy W received by an observer are expressed by:

$$\begin{aligned} \frac{dW}{d\Omega d\omega} &= 2c\epsilon_0 R^2 \left| \vec{E}(\omega) \right|^2 \\ &= \frac{e^2}{4\pi\epsilon_0 4\pi^2 c} \left| \int_{-\infty}^{\infty} \vec{E}(t) e^{i\omega(t - \hat{n} \cdot \vec{r}(t)/c)} dt \right|^2 \end{aligned} \quad (2.31)$$

Furthermore, from the calculations in Appendix A, it could be expressed as well by:

$$\frac{dW}{d\Omega d\omega} = \frac{e^2}{16\pi^3 \epsilon_0 c} \left(\frac{2\omega\rho}{3c\gamma^2} \right)^2 (1 + \gamma^2\theta^2)^2 \left[K_{2/3}^2(\xi) + \frac{\gamma^2\theta^2}{1 + \gamma^2\theta^2} K_{1/3}^2(\xi) \right] \quad (2.32)$$

where K is a modified Bessel function of the second kind, and ξ is defined as $\xi = \frac{\rho\omega}{3c\gamma^3} (1 + \gamma^2\theta^2)^{3/2}$. Radiation emitted in a bending magnet is linearly polarized when observed in the bending plane. Out of this plane, the polarization is elliptical and can be decomposed into its horizontal and vertical components, respectively the first and second terms in the last bracket of Eq. 2.32.

By integrating over all angles, the frequency distribution of the radiated energy is

obtained:

$$\frac{dW}{d\omega} = \oint \frac{dW}{d\omega d\Omega} d\Omega = \frac{\sqrt{3}e^2}{4\pi\epsilon_0 c} \gamma F\left(\frac{\omega}{\omega_c}\right) \quad (2.33)$$

where

$$F(y) = y \cdot \int_y^\infty K_{5/3}(t') dt', \quad \omega_c = \frac{3c}{2\rho} \gamma^3 \quad (2.34)$$

represent the function shaping the spectral distribution of the SR energy, plotted in Fig. 2.5, and the critical frequency respectively. The critical frequency is defined as the frequency dividing the spectrum into two halves, that is, equal power is radiated above and below ω_c . It is also worth pointing out that the maximum of the emission spectrum is at $\omega_{max} = 0.29\omega_c$.

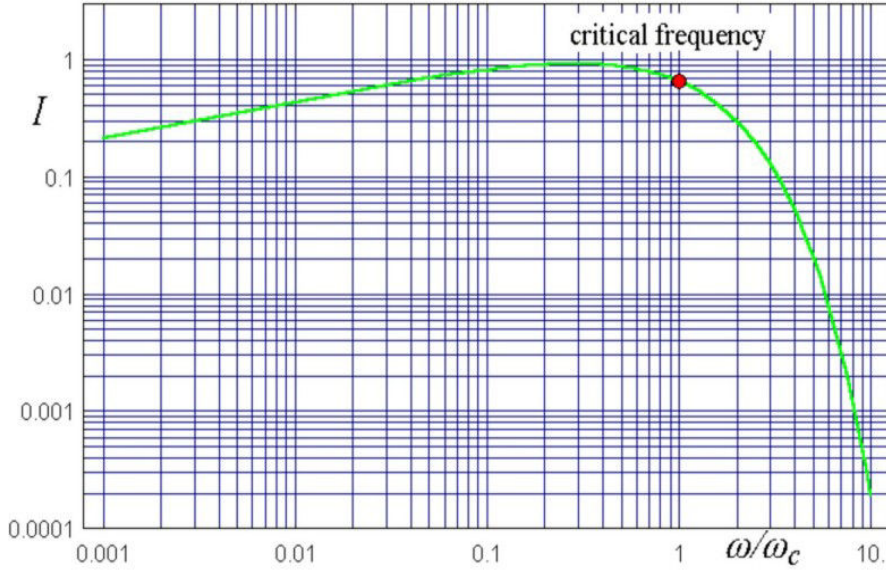


Figure 2.5: Frequency distribution of SR radiated intensity (in a.u.) in a bending magnet [2].

2.2.2 Short magnets and dipole edge radiation

Since the SR synchrotron radiation emitted by ultra-relativistic particles ($\gamma \gg 1$) is focused within a forward cone of an angle $\Theta = 1/\gamma$, an observer will detect the electromagnetic fields only when the tangent to the particle trajectory makes an angle smaller than $1/\gamma$ on either side of the straight line joining the particle to the

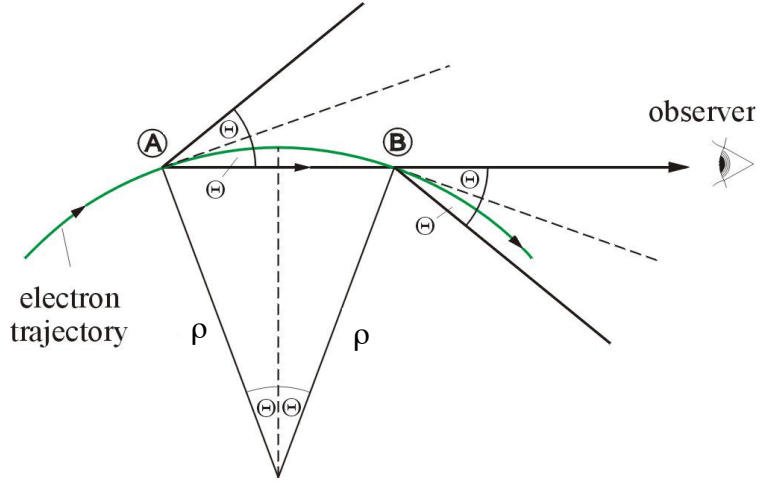


Figure 2.6: SR light pulse duration seen by an observer [2].

observation point. Referring to Fig. 2.6, the duration of the light pulse Δt is the difference of the time needed by the charge and the photon moving from point A to point B:

$$\begin{aligned} \Delta t &= t_{charge} - t_{photon} \\ &= \frac{2\rho\Theta}{c\beta} - \frac{2\rho \sin \Theta}{c} \simeq \frac{4\rho}{3c\gamma^3} \end{aligned} \quad (2.35)$$

and the corresponding SR spectrum extends up to $\omega_{typ} = 2\pi/\Delta t = \pi\omega_c$, before decreasing following the law $(\omega/\omega_{typ}) \cdot \exp(-4\pi\omega/3\omega_{typ})$. However, the dipole field is not sharply contained inside the magnet core. Along the longitudinal axis of the magnet a moving particle undergoes a field strength change from zero to the nominal value over some length (generally of the order of a few mm). The length and shape of this “edge field” varies depending on the magnet construction. If this rapid field variation occurs within a length L such as the deflection of the particle $\alpha \ll 1/\gamma$ (definition of a short magnet), the observer sees a light pulse with a rise time $\tau_d \approx (1/2\gamma^2) \cdot L/c$ [33, 34]. Therefore the previous spectrum is extended up to $\sim 1/\tau_d$, and the critical frequency is shifted to a higher value. Although the total power of

the edge radiation is negligible compared to the SR from the body of the dipole, the spectral brightness of edge radiation can be much higher in some wavelength regions far from the dipole core critical wavelength.

2.2.3 Undulators and wigglers

In addition to the SR unavoidably emitted in the bending magnets main components of a synchrotron, dedicated “insertion devices” are used to generate brighter SR beams. These generally are formed by a sequence of short dipole fields of alternating polarity. The beam is therefore deflected in alternate directions to give an undulating trajectory [35, 36].

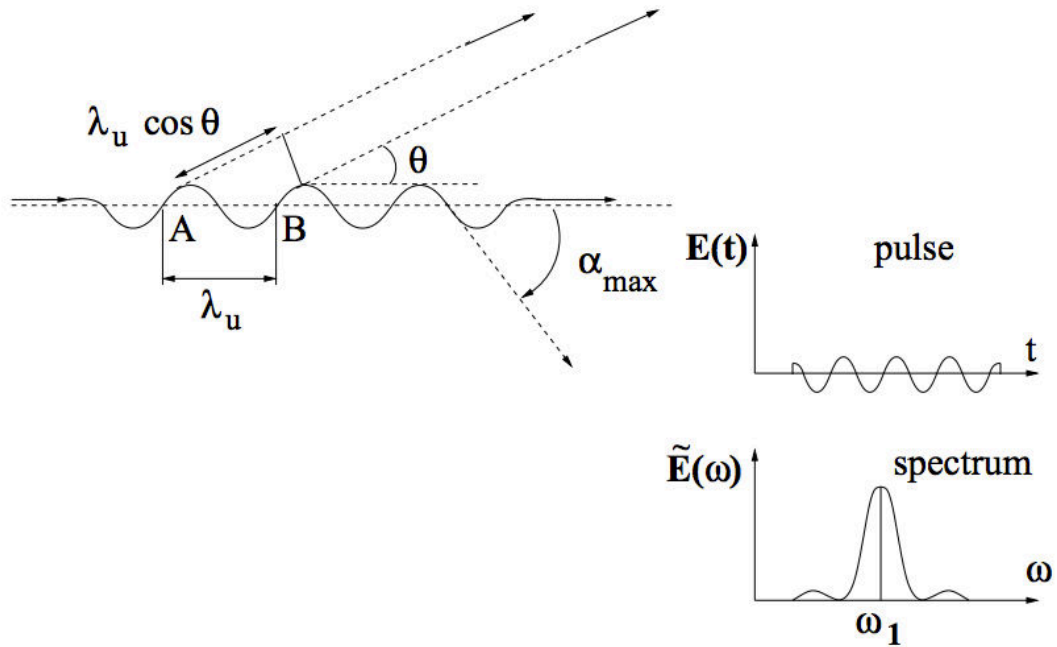


Figure 2.7: Undulator working principle as an SR source.

If the integrated field strength in the two directions is equal, then the total bending angle will be zero. Furthermore, if the magnetic structure is arranged so that the field sections at each end are of half the length of the others, the traversing beam will exit the undulator with no transverse displacement. The insertion device is then described as matched and can be inserted into the beam line without affecting the beam orbit.

If the magnetic field B varies sinusoidally and is in the vertical direction:

$$B(z) = B_0 \cos(2\pi z \lambda_u) \quad (2.36)$$

where B_0 is the peak of the magnetic field, z the distance along its axis and λ_u its period.

An important parameter characterizing the sinusoidal charge motion lying in the horizontal plane is the deflection parameter K given by:

$$K = \frac{e B_0 \lambda_u}{2\pi m_0 c} \quad (2.37)$$

Such a parameter relates the maximum deflection angle, α_{max} , and the natural opening of the synchrotron radiation $1/\gamma$:

- when $K > 1$, the opening of the light cone is small compared to the α_{max} , and the observed radiation comes mainly from the tops of the sine-like trajectory. The received electric field consists of a series of peaks whose Fourier transform contains a series of harmonics. One speaks in this case of a "wiggler";
- when $K < 1$, the radiation from the various periods can exhibit strong interference phenomena, because the angular excursions of the electrons are within the nominal $1/\gamma$ radiation cone. One speaks then of an "undulator".

If the coherence condition for the undulator radiation, defined as:

$$\lambda_{coh} = \frac{\lambda_u}{2\gamma^2} \left(1 + \frac{K^2}{2} + \gamma^2 \Theta_{obs}^2 \right) \quad (2.38)$$

is verified, then at the observation angle Θ_{obs} , the SR emitted by successive undulator periods will interfere constructively. In addition to the wavelength given by Eq. 2.38, SR is also emitted at the harmonics $\lambda = \lambda_{coh}/n$.

The width of the undulator spectral peak is inversely proportional to its number of periods N_u . Hence, in an undulator with few periods the SR is not monochromatic but has a broad spectrum centred at λ_{coh} . Contrarily, if $N_U \gg 1$, interference effects dominate and near-monochromatic SR will be emitted.

The angular spectral energy density emitted in an undulator observed in the direction (θ, φ) , found in [37, 35], is:

$$\frac{dW}{d\Omega d\omega} = \frac{r_0 e^2 B_0^2 N_u \lambda^u \gamma^4}{\pi m^0} \frac{N_u}{\omega_1} \left[\text{sinc} \left(\frac{\pi (\omega - \omega_1) N_u}{w_1} \right) + \text{sinc} \left(\frac{\pi (\omega + \omega_1) N_u}{w_1} \right) \right]^2 \left[\frac{(1 - \gamma^2 \theta^2 \cos(2\varphi))^2}{(1 + \gamma^2 \theta^2)^5} + \frac{(\gamma^2 \theta^2 \sin(2\varphi))^2}{(1 + \gamma^2 \theta^2)^5} \right] \quad (2.39)$$

where the first and second terms in the last brackets refer to the horizontal and vertical polarization of the emitted SR electric field.

Finally, the total power emitted in the forward cone by a particle traversing a weak undulator (where $K \ll 1$) is:

$$P = \frac{\pi e^2 c \gamma^2}{\epsilon_0 \lambda_u^2 N_u} \frac{K^2}{(1 + K^2/2)^2} \quad (2.40)$$

2.3 SR application for transverse diagnostic

SR is considered a versatile tool for non-destructive beam diagnostics, since its characteristics are closely related to those of the source beam. It is widely used in accelerators and storage rings. On one hand, by studying the pulsed nature of SR, originated from the bunched structure of the beam, the longitudinal profiling of the entire ring can be performed. On the other hand, since the SR brilliance is dominated by transverse size and angular divergence of the beam, probing its intensity distribution gives a direct information of the beam transverse profiles.

In [38] and [39], an overview of the methods presently applied to exploit SR for transverse beam diagnostic purposes is given.

However, since this thesis treats only the diagnostics using the visible spectrum of SR, in the following the most diffused transverse diagnostic techniques using visible SR will be briefly presented: imaging and interferometry.

2.3.1 SR imaging technique

SR imaging consists in the determination of the photon beam size emitted by bending magnets or dedicated insertion devices, that allows retrieving the charged beam

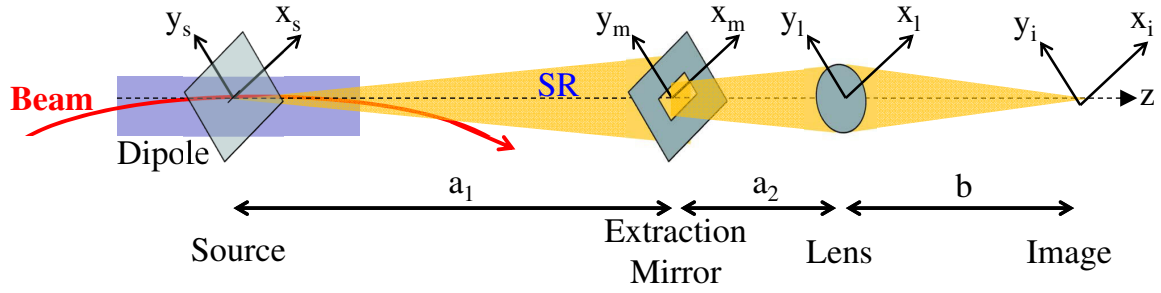


Figure 2.8: SR imaging system working principle.

transverse size at the SR source. With knowledge of the machine optics (β , D) at the location of the SR source and the relative energy spread, the beam emittance can also be obtained.

Every imaging system is characterized by its resolution and its ability to resolve details, that is strictly limited by fundamental effects such as chromatic aberrations, geometric aberrations, depth of field effects and diffraction [40]. This resolution is often approximated by the width of the Point Spread Function (PSF), the response of the imaging system to a point source, since the degree of spreading (blurring) of the point object is a measure of the quality of the system.

While monochromatic aberrations (i.e. spherical aberrations) are generally sufficiently small when aplanatic combination lenses are used [41], chromatic effects can be avoided by observing monochromatic radiation (i.e. filtering the radiation with narrow bandpass filters). Consequently, the resolution of a SR monitor is generally limited by the light diffraction and depth of field effects.

The resolution, of a such diffraction-limited instruments, is proportional to the size of the system aperture, and inversely proportional to the wavelength of the light being observed. In case of circular apertures, the diffraction limited PSF is approximated by the Airy disc, whose width is:

$$\Delta x \approx 1.22\lambda f_{\#} \quad (2.41)$$

where λ is the observed wavelength and $f_{\#}$ is the F-number of the optical system defined as the ratio between the lens focal length and the effective aperture.

The resolution of a typical SR imaging system sketched in Fig. 2.8 is deeply discussed in [42, 43, 44, 45, 46] and mainly obtained by successively propagating and diffracting the emitted light over the optical elements (lenses, slits,...) from the source to the detector.

The emitted SR (in this case from a bending magnet) is diffracted by several apertures (extraction mirror and lens) before being imaged by an ideal thin lens on a CCD.

The following presents the calculations for an SR monitor resolution by calculating the image of a single charge (imaging system resolution) observed by a detector.

According to Rayleigh-Sommerfield diffraction propagation [47], the SR field E^s emitted from the charge and propagated to the extraction mirror plane is:

$$E_{x_m, y_m}^m(\vec{r}_m, \omega) = -i \frac{e^{ika_1}}{\lambda a_1} \cdot e^{i \frac{k}{2a_1}(x_m^2 + y_m^2)} \int_{-\infty}^{+\infty} \int_{-\infty}^{+\infty} dx_s dy_s E_{x_s, y_s}^s(\vec{r}_s, \omega) e^{i \frac{k}{2a_1}(x_s^2 + y_s^2)} e^{-ik \frac{x_s x_m + y_s y_m}{a_1}} \quad (2.42)$$

Where $k = 2\pi/\lambda$, $\omega = 2c\pi/\lambda$ and λ is the wavelength of the light. E^m is then diffracted up to the lens plane by the mirror restricted aperture according to:

$$E_{x_l, y_l}^{lin}(\vec{r}_l, \omega) = -i \frac{e^{ika_2}}{\lambda a_2} \cdot e^{i \frac{k}{2a_2}(x_l^2 + y_l^2)} \int_{-x_m/2}^{+x_m/2} dx_m \int_{-\infty}^{+\infty} dy_m E_{x_m, y_m}^m(\vec{r}_m, \omega) e^{i \frac{k}{2a_2}(x_m^2 + y_m^2)} e^{-ik \frac{x_m x_l + y_m y_l}{a_2}} \quad (2.43)$$

The light is then imaged by an ideal thin lens, which transforms the phase of the light as:

$$E_{x_l, y_l}^{lout}(\vec{r}_l, \omega) = E_{x_l, y_l}^{lin}(\vec{r}_l, \omega) \cdot e^{-i \frac{k}{2f}(x_l^2 + y_l^2)} \quad (2.44)$$

where f is the focus of the lens:

$$f = \frac{1}{(a_1 + a_2)^{-1} + b^{-1}} \quad (2.45)$$

The physical interpretation of the phase shift is a transformation of the spherical wave diverging from a point at a distance $(a_1 + a_2)$ in front of the lens to a spherical wave converging toward a point at a distance b behind it. The electric field in the image plane E^i is then expressed by:

$$E_{x_i, y_i}^i(\vec{r}_i, \omega) = -i \frac{e^{ikb}}{\lambda b} \cdot e^{i \frac{k}{2b}(x_i^2 + y_i^2)} \int_{-x_l/2}^{+x_l/2} dx_m \int_{-x_l/2}^{+x_l/2} dy_l E_{x_l, y_l}^{l_{out}}(\vec{r}_l, \omega) e^{i \frac{k}{2b}(x_l^2 + y_l^2)} e^{-ik \frac{x_l x_i + y_l y_i}{b}} \quad (2.46)$$

The spatial intensity distribution on the detector, PSF, is given by:

$$\frac{d^2 W}{d\omega d\Omega} = \frac{c}{4\pi^2} \left(\left| \vec{E}_{x_i}^i(\vec{r}_i, \omega) \right|^2 + \left| \vec{E}_{y_i}^i(\vec{r}_i, \omega) \right|^2 \right) \quad (2.47)$$

However, the acceptance of SR monitors is such as the incoming light is emitted spontaneously over a beam trajectory and not a point source. Therefore a generalization of the concept of the PSF is introduced, the Line Spread Function (LSF).

The LSF is an important quantity since the image of any finite beam size can be calculated as the 2-dimensional convolution¹ of the source intensity distribution and the LSF.

The performance analysis of the SR imaging systems of the LHC and SPS will be discussed in details in 4.3, 4.4.3, and 4.7. Furthermore, an exhaustive analysis of experimental data taken during LHC run I is carried out for the LSF determination, and presented in 5.2.

¹For the visible SR, emitted by bunch having a length $\gg \lambda$ (the observed wavelength), the image formation process is linear in power and described by linear system theory. This means that when two objects A and B are imaged simultaneously, the result is equal to the sum of the independently imaged objects.

2.3.2 SR interferometry technique

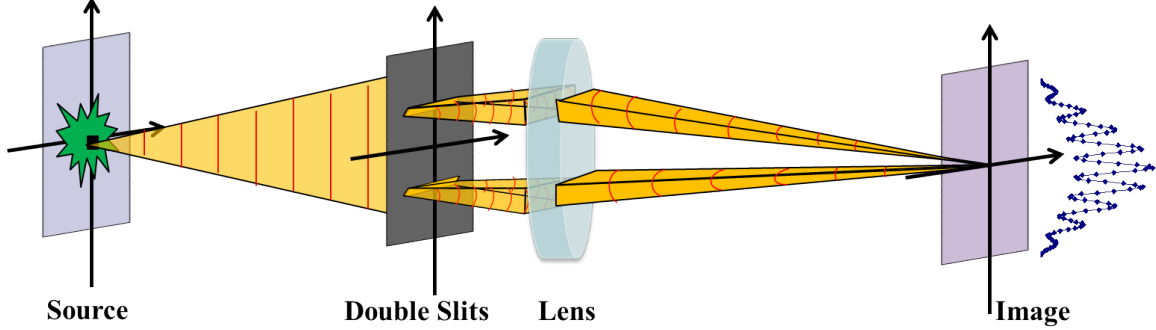


Figure 2.9: SR interferometry working principle.

An alternative technique to SR imaging, for non-destructive beam diagnostics, is the SR interferometry. Rigorous derivation of the principle can be found in [48, 40]. In the following a brief overview of the technique is given.

The instrument is a wavefront-division-type two-beam SR interferometer using polarized, quasi-monochromatic light. Its principle is based on the investigation of the spatial coherence of the emitted light, in particular on the measurement of the first order degree of mutual spatial coherence Γ . SR interferometers use a double slit to sample the incoming wavefront and to obtain the one-dimensional interference pattern along the vertical or horizontal axis. A schematic setup is shown in Fig. 2.9. The intensity of the interference pattern measured on the detector plane depends on Γ , and is expressed by:

$$I(x) = I_0 \left[\text{sinc} \left(\frac{2\pi a}{\lambda_0 R} x \right) \right]^2 \cdot \left\{ 1 + |\Gamma| \cos \left(\frac{2\pi D}{\lambda_0 R} x + \phi \right) \right\} \quad (2.48)$$

with a the half of the single slit width, D the separation between the two slits, λ_0 the wavelength of observation, I_0 the sum of the incoherent intensities from both slits, ϕ an arbitrary phase and R the distance from the lens to the detector plane.

According to Van Cittert-Zernike theorem [48], the degree of coherence Γ is the Fourier

transform of the intensity distribution of the source:

$$\Gamma(D) = \int f(x) \exp(-i \frac{2\pi D}{\lambda_0 R_0}) dx \quad (2.49)$$

with R_0 being the distance from the source to the double slits and $f(x)$ the intensity shape of the source.

There are two operational modes for the SR interferometry:

- *Fixed Slit Separation:*

this mode relies on the hypothesis of a Gaussian distribution of $f(x)$. Therefore by acquiring and fitting the interference pattern to obtain the spatial coherence $|\Gamma|$, the beam size σ_x can be measured using:

$$\sigma_x = \frac{\lambda_0 R_0}{\pi D} \sqrt{\frac{1}{2} \ln \frac{1}{|\Gamma|}} \quad (2.50)$$

- *Slit Separation Scanning Mode:*

In this mode, the intensity pattern is recorded for varying slit separation D and the beam shape $f(x)$ is obtained by applying a Fourier back transform of the resulting curve $\Gamma(D)$.

The proposed SR interferometer for the LHC is presented in [4.5.1](#) where its expected performance and limitations are deeply discussed, while its physical implementation in the LHC BSRT is presented in [Chapter 8](#).

Chapter 3

Synchrotron Light Monitors at CERN

This chapter is meant to give a comprehensive description of the CERN beam size monitors based on visible synchrotron radiation imaging. Such instruments are installed only in the SPS and the LHC, since visible SR is not detectable earlier in the accelerators chain. The LHC and SPS SR sources, the extraction systems, the optical lines and the detectors will be presented.

3.1 LHC

The LHC is equipped with two SR monitors (one per beam) used to characterise the transverse and longitudinal beam distributions. The light emitted by a superconducting undulator and/or by a dipole magnet (depending on the beam energy) is intercepted by an extraction mirror in vacuum and sent through a vacuum window (viewport) to the imaging Beam Synchrotron Radiation Telescope (BSRT).

Given the minimum and the maximum values of the design optical functions at the location of the SR source ¹, $\beta_{min} = 127$ m and $\beta_{max} = 334$ m, and the range of normalized beam emittances circulating in the LHC, (1.5...8 μm), Table 3.1 summarizes

¹It is worth noting that the undulator and the D3 dipole are installed in a dispersion free region next to the RF cavities. In any case, the momentum spread is $\sim 10^{-4}$, therefore eventual spurious dispersion would not have an important impact on the beam size broadening.

the beam sizes the instrument is meant to measure.

	σ_{min} [mm]	σ_{max} [mm]
450 GeV	0.63	2.35
7 TeV	0.16	0.6

Table 3.1: Range of the beam sizes to be measured by the BSRT at injection energy 450 GeV and flattop energy 7 TeV.

Compatibly with high intensity and high energy operation, the BSRT is the only instrument offering non-invasive, continuous and single bunch measurements of the LHC beams.

3.1.1 Source description

As mentioned above, the BSRT SR source is represented by a dedicated undulator and a separation dipole of the D3 type used to increase the beams separation at the RF cavities location in IR4 [12], as sketched in Fig. 3.1. Such a SR source shifts gradually with energy from the undulator (at injection energy, 450 GeV) to the D3 that dominates from 1.2 TeV onwards as will be explained below.

D3 dipole

The D3 is one of a set of four 9.45 m long superconducting dipoles that separate the beams on either sides of IR4 to accommodate the RF cavities. It is ramped

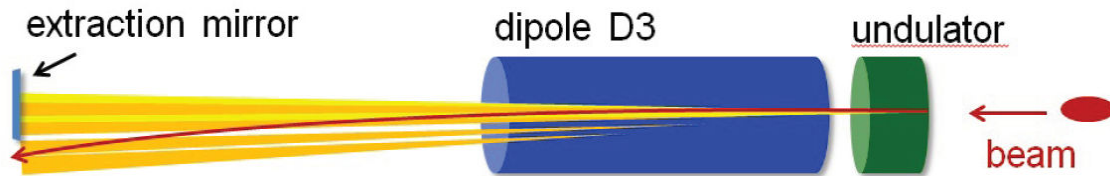


Figure 3.1: Sketch of the BSRT Synchrotron light sources.

to a maximum field of 3.9 T guiding the protons at 7 TeV, giving a bend angle of 1.58 mrad and a radius of curvature $\rho = 6013$ m. The D3 is considered as the primary source of visible SR for the diagnostic; in fact, Fig. 3.2 presenting the SR critical wavelength (introduced in 2.2.1) as function of energy, shows that the light from the dipole core from energies $> \sim 1.8$ TeV is emitted within the visible region delimited by the horizontal red lines (200 and 800 nm).

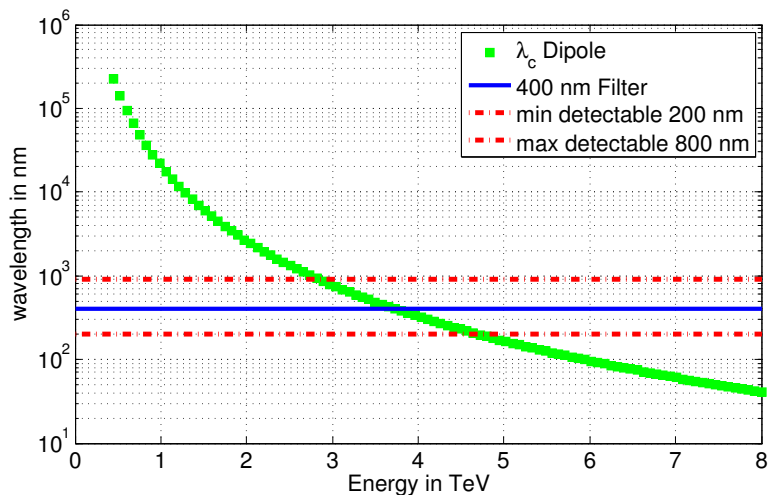


Figure 3.2: Dipole D3 critical wavelength λ_c shift with energy.

The SR from the dipole core is emitted in a narrow cone centred on the tangent to the protons trajectory. A commonly used approximation consists in assuming a Gaussian light intensity distribution inside a cone aperture of $1/\gamma$ and it is often forgotten that this approximation is valid only for observations in the vicinity of the critical wavelength. In fact, Fig. 3.3 evidences the difference between the real SR intensity distribution (as calculated with Eq. 2.32) and a $1/\gamma$ Gaussian distribution at a chosen wavelength (400 nm, used in operation), for different beam energies.

Nevertheless, since the rough approximation of the SR profile by a Gaussian distribution is very convenient for many studies, Fig. 3.4 presents the $1/\gamma$ approximation of the cone angle aperture for different wavelengths within the visible region, as function of beam energy.

Finally, it is important to note that the dipole field is not sharply contained inside the magnet core and the effect of the field strength changing from zero to the nominal

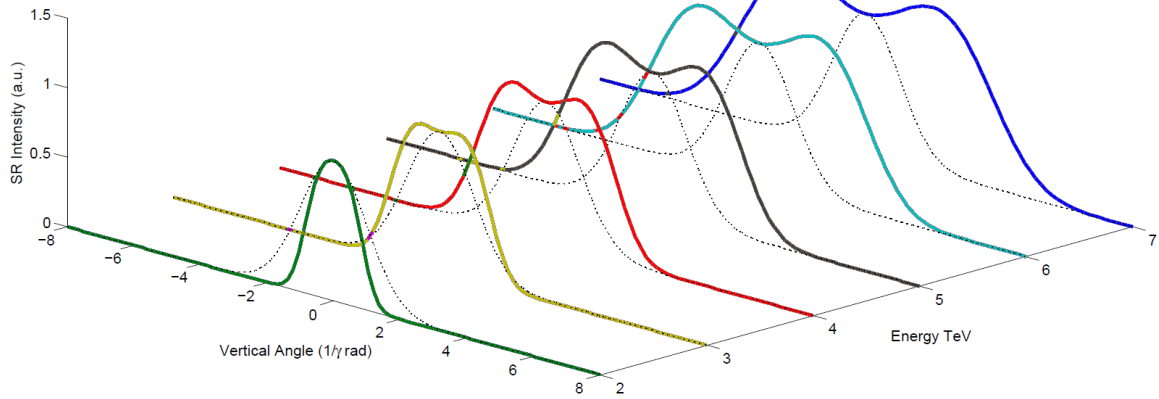


Figure 3.3: Vertical profile of the emitted SR fan for $\lambda = 400 \text{ nm}$ at different energies, compared to the $1/\gamma$ Gaussian profile approximation.

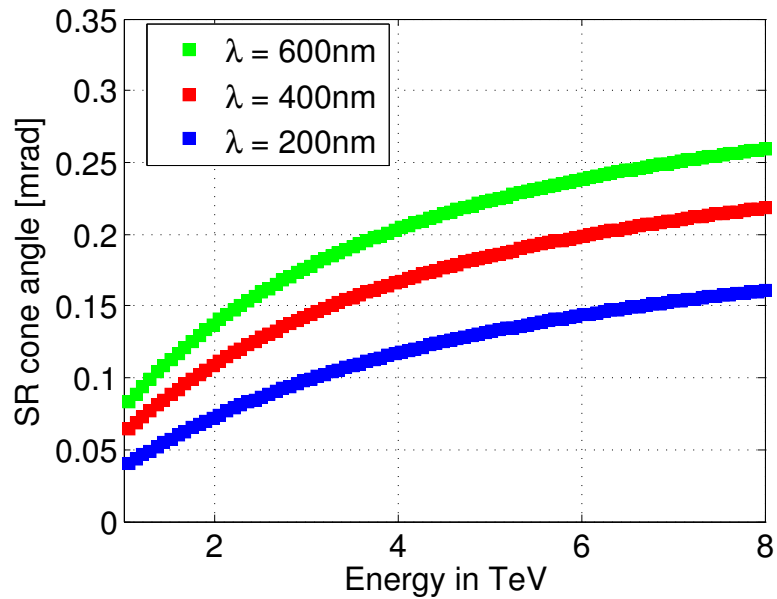


Figure 3.4: Opening angle of the SR cone for different wavelengths (200, 400 and 600 nm) with the energy ramp up to 7 TeV.

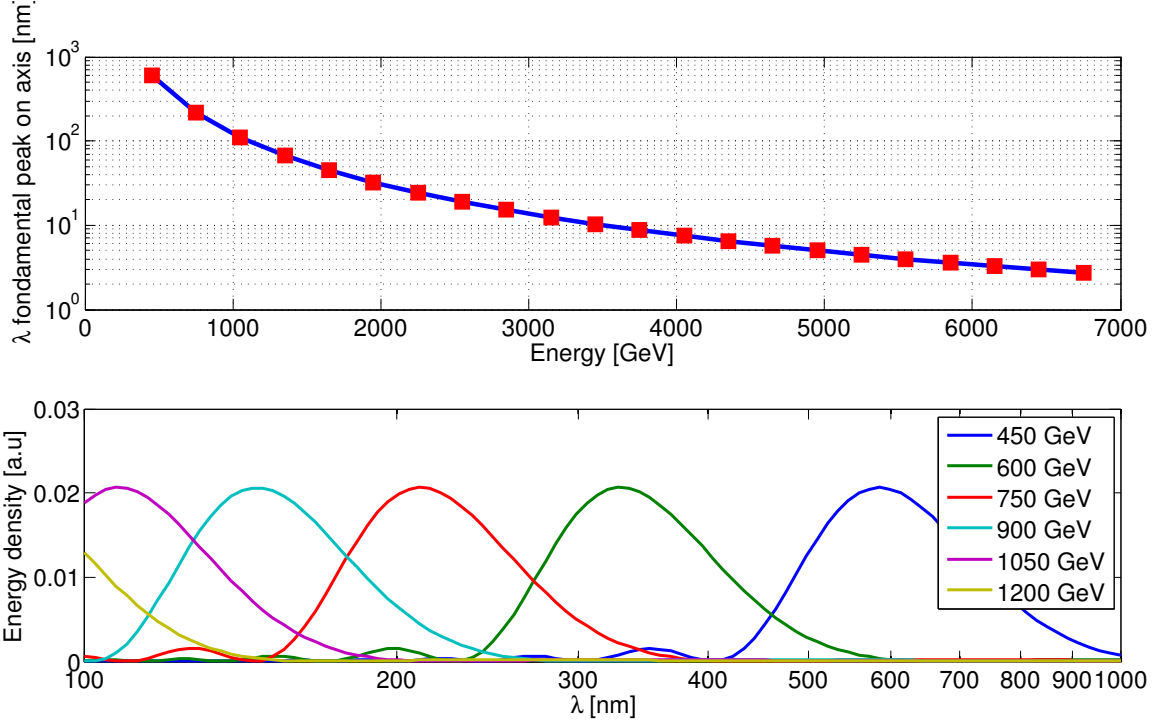


Figure 3.5: Characteristics of the undulator radiation. Top plot: peak on-axis emission wavelength vs. proton energy. Bottom plot: proton emission spectrum on axis versus wavelength (log scale).

value, denominated as “the edge effect” (described in 2.2.2), results in an enhancement of the SR at lower wavelength. The edge effect is observable from ~ 1.2 TeV onward, and is quantified through the extensive simulations presented in 4.2.

Undulator

A dedicated undulator was designed [37, 49] to enhance the SR visible component from the injection energy of 450 GeV up to about 1.2 TeV, when the D3 visible SR contribution becomes detectable. The undulator is installed 937 mm upstream of D3, with which shares the cryostat. It is made of two 28 cm periods with a peak field of 5 T, thus resulting in the “undulator parameter” $K \sim 0.0712$.

Figure 3.5 shows the peak wavelength of the “on-axis” emitted SR: for instance, at

450 GeV its spectrum peaks in the red (607 nm), and since it only has two periods, its spectrum is rather large. Therefore, even when its spectrum is centred outside the visible, there is still substantial light available for energy up to ~ 1 TeV.

It is relevant to note that at 7 TeV the peak emission λ_{peak} is strongly shifted to shorter wavelengths (~ 2 nm). These short wavelengths are absorbed by the in vacuum extraction mirror and cause a local heating of the mirror. The heating could cause the mirror surface to expand unevenly and thus bend, leading to a movement and/or distortion of the image. Moreover, if the heating mechanism is sufficiently fast it could cause permanent damage to the mirror coating.

For this reason, simulations were carried out to check whether the undulator should be turned off once its spectrum peaks outside of the visible region. The SR power hitting the extraction mirror was simulated with only the D3 field present and then with only the undulator. The undulator contribution resulted in about 31 mW, in line with the analytical power estimation based on Eq. 2.39, that yields to ~ 23 mW [50]. This corresponds to about 10-15% of the total power and no need was found to routinely ramp the undulator down during operation at high energies.

3.1.2 Light extraction system

In order to describe the SR extraction geometry, the origin of the $(x y z)$ coordinate system, adopted throughout this work, is placed at the undulator center. The particles travel in the $+z$ direction, the $+y$ direction is vertically upward and the radially outward direction is $+x$. This forms a right-handed coordinate system for Beam 1, travelling clockwise around the ring. At $z = 27.24$ m, the protons are sufficiently separated from the photons to provide room for a rectangular mirror (50 mm x 70 mm), rotated by 45° about the x axis, that extracts the light directing it downward to a shielded enclave below the beam line where the optical table lies. As sketched in Fig. 3.6, the transverse offset (toward $+x$) between the mirror edge and the proton beam is around 20 mm, satisfying the minimum clearance distance required by machine protection [51] corresponding to $\sim 17 \sigma_{BEAM}$ ¹. As described above, the dipole's

¹Due to the emittance adiabatic damping, along the energy ramp the beam size σ_{BEAM} decreases. Therefore, the clearance distance is calculated taking into account the beam size at injection energy of the nominal normalized emittance (3.75 μm) and the highest β function in the horizontal plane.

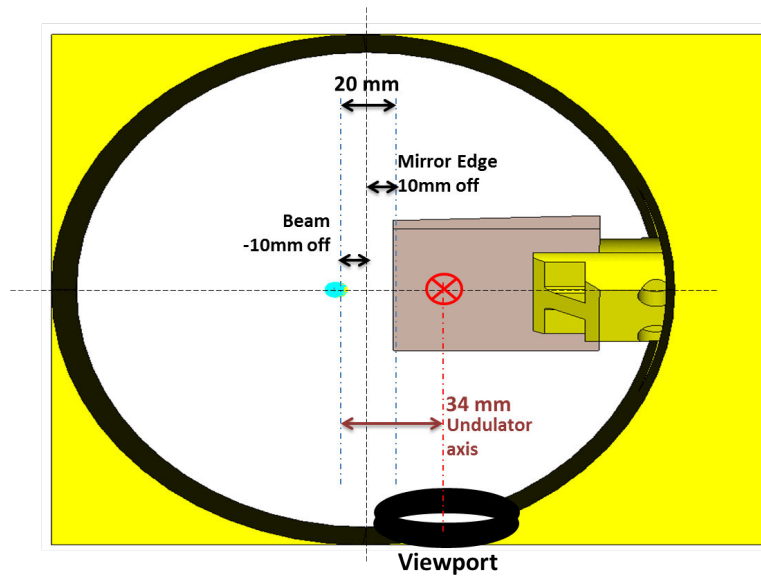


Figure 3.6: Sketch of the SR extraction tank in the LHC.

core (uniform field region) radiation follows the tangent to the orbit. As the particle enters the dipole, at $z = 1.217$ m, the light first strikes the extraction mirror at $x = 0$ m and then sweeps towards x until the tangent misses the mirror edge ($x = -12.9$ mm) when the particle passes $z = 4.55$ m (~ 3.34 m inside the D3). The installed view port is made of HPFS[®], a high purity synthetic amorphous silicon dioxide manufactured by flame hydrolysis [3]. The noncrystalline, colorless, silica glass combines a very low thermal expansion coefficient with excellent optical qualities and exceptional transmittance in ultraviolet. This view port is certified to meet transmittance $> 80\%$ /cm from 185 nm to ~ 2.2 μm . A typical internal transmittance curve for HPFS[®] Standard Grade fused silica is shown in Fig. 3.7.

3.1.3 Optical system

The imaging system is installed on an optical bench ($4.8\text{ m} \times 0.8\text{ m}$) below the beam line, depicted in Fig. 3.8. Given the large distance (~ 28 m) from the SR sources to the extraction mirror, a “two-focusing element” system is necessary to reach a suitable magnification (dictated by the detector resolution) on such a reasonably short table. In addition, the optical system has to cope with the shift of the SR source from

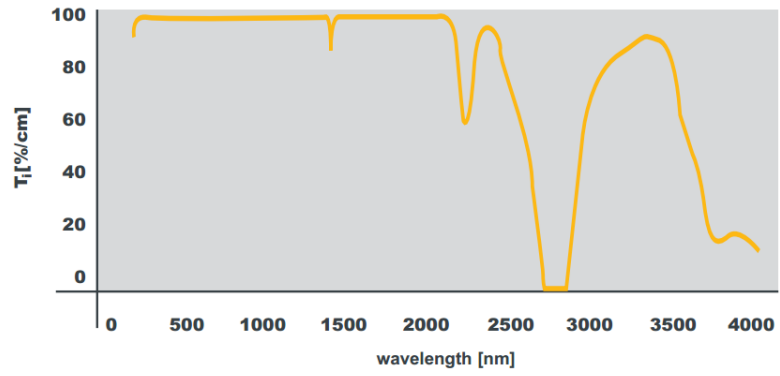


Figure 3.7: Transmission of the BSRT fused-silica vacuum window [3].

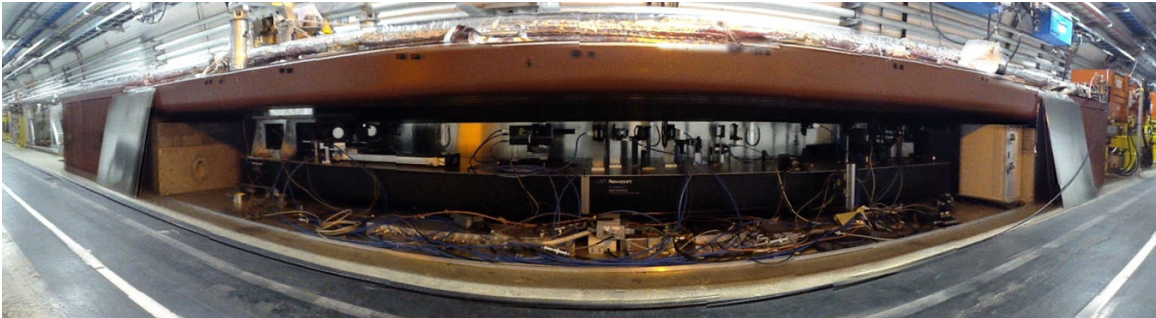


Figure 3.8: LHC optical bench housing the BSRT in IR 4 in the shielded enclave under the beam line.

the undulator to the D3 edge and core (~ 3 m). For the LHC operation, two optical systems have been tested up to now: the first is based on reflective optics where the two focusing elements are spherical mirrors and the second one, proposed after the studies presented in Chapter 4, is based on refractive optics where the focusing is made using achromat lenses.

Reflective optics

In order to keep the systematic error on the beam size determination by Gaussian fitting below the 1% level, the width of the imaged beam $\sigma_{meas} = M_{TOT} \cdot \sigma_{BEAM}$ (with M_{TOT} being the total magnification of the optical system) should occupy a minimum of 3 pixels on the detector [52].

Assuming a typical value at 7 TeV of $\sigma_{BEAM} = 180 \mu\text{m}$ that the system is supposed to image and a detector resolution res_{det} of $16.5 \mu\text{m}$, the minimum magnification of the optical system should be:

$$M_{TOT_{min}} = \frac{3 \cdot res_{det}}{\sigma_{BEAM_{min}}} \sim 0.275 \quad (3.1)$$

For the reflective optical system used from the start of the LHC operation until the end of 2012, a conservative value of $M_{TOT} = 0.3$ was chosen.

Such a system is sketched in Fig. 3.9. The first mirror receiving the SR from the extraction mirror on this table is the ‘‘Steering’’ motorized mirror, used to adjust the light steering for the following elements in order to cope with beam position drifts and any fluctuation/vibration of the table. A set of seven mirrors (M1...M7) create a variable light delay line, the trombone [53]. By moving M1 and M6, the optical path could be lengthened by adding the chicane (M2, M3, M4, M5). This was used to compensate the SR source shift from the undulator to the D3 core, thus keeping fixed the distance from the source to the first focusing element, F1.

F1 and F2 are two spherical concave mirrors with radii curvatures of 8000 and 1500 mm respectively, corresponding to focal lengths of 4 and 0.75 mm. Therefore, F1 forms an intermediate image with an approximate magnification $MAG_1 \sim 0.15$, while F2 magnifies it by a factor of 2 ($MAG_2 \sim 2$) reaching the sought $MAG_{TOT} \sim 0.3$ in a fixed image plane for both configuration: SR source being the undulator combined to the short delay line and SR source being the D3 core combined with the long delay

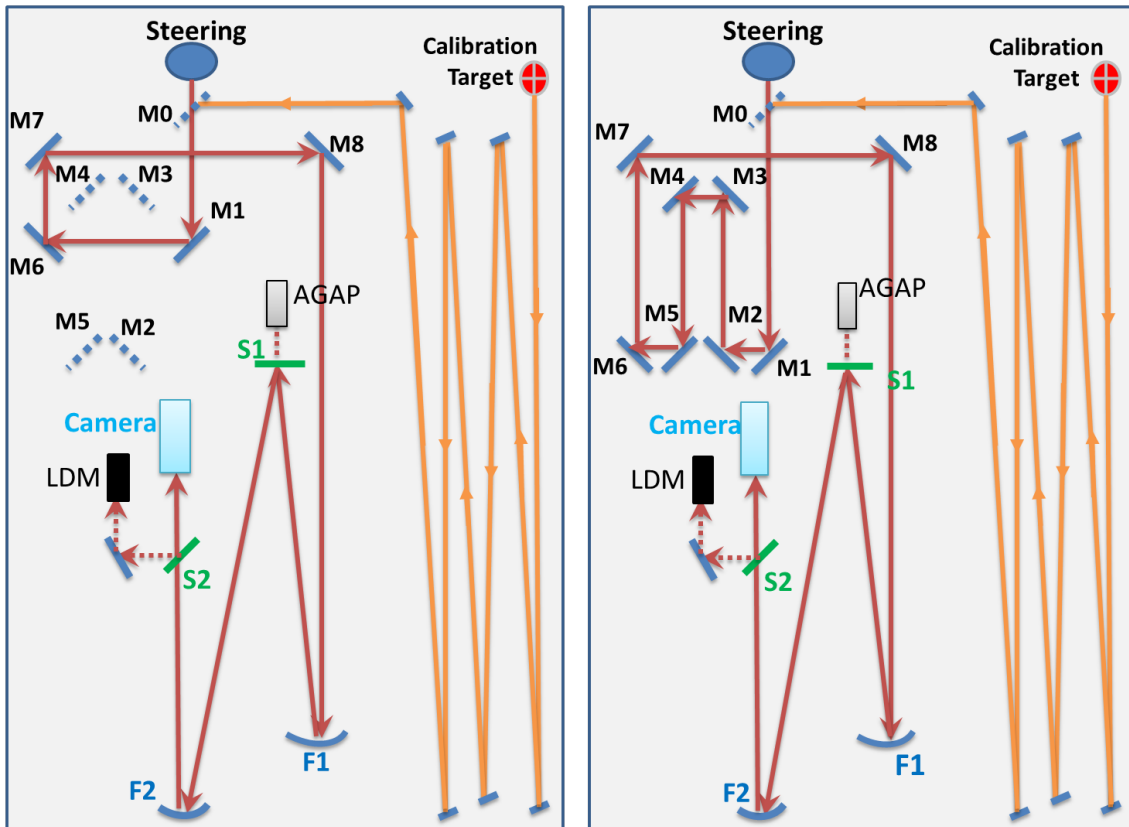


Figure 3.9: Sketch of the BSRT in the reflective optics (focusing mirrors F1, F2) version, showing the calibration line occupying the right part of the optical table complementary to the imaging line. The trombone delay line (formed by mirrors M1, . . . , M7) is shown in both configurations: "Short" for focusing on the undulator radiation and "Long" for compensating for the source shift at high energy and focusing in the D3 core.

line.

By design, the choice of reflective rather than refractive optics was constrained by the varying SR spectrum with the different sources and beam energies (as will be shown in Chapter 4.2). However, the use of spherical mirrors introduces astigmatism in the optical system. This is minimized by setting the light incidence angles on F1 and F2 to small values (only 1° to the normal in the horizontal plane).

A large portion of the optical table is occupied by a calibration line (used to measure the system magnification, as will be discussed in Chapter 5.2.1), where an incoher-

ently illuminated resolution target is imaged through a multiple passes path across the table up to the camera (inserted in the imaging line through the M0 mirror) giving this line the same length as the optical path from the undulator.

Finally, even though not being the direct object of these studies, it is worth mentioning that the optical table houses the Abort GAP monitor (AGAP) [54] and the Longitudinal Density Monitor (LDM) [55], two instruments for longitudinal diagnostics of the LHC beams. Such devices are coupled to the imaging line through two light splitters (S1 and S2), picking up about 8% of the extracted light.

Refractive optics

The extreme difficulty of the aforementioned reflective system alignment, and its complexity due to the high number of motorized elements, posed some problems in the operation and in the interpretation of its measurements, as will be discussed in Sections 4.3.1 and 5.2.2.

Therefore, an alternative system was conceived, developed and installed. The system, sketched in Fig. 3.10, is still based on two focusing stages but using lenses rather than focusing mirrors [56]. In particular, the two lenses (F1 and F2) are custom designed achromats, optimized for 400-600 nm operation. The first focusing element (F1) is placed immediately after the steering mirror, removing the delay trombone and reducing the optical length from the source by ~ 3.5 m with respect to the old design, thus avoiding any light cutting on the folding mirrors. The F2 lens is installed on a movable stage in order to change the focusing according to the beam energy (and source shift).

The respective focal lengths of F1 and F2 are 4.81 m and 0.3 m. Hence the total magnification of the optical systems is 0.6 at injection energy (focusing on the undulator) and 0.5 at higher energy (focusing on the D3 dipole).

The choice of the magnification was a trade off between Eq. 3.1 setting its minimum value and avoiding an excessive magnification (> 0.9) [53, 37] that for big beam sizes such as the injected beam could spread the available light over too many pixels, thus decreasing the signal to noise ratio.

The balance between the much simpler optical line of the new system and eventual drawbacks on the monitors resolutions with respect to the previous system are investi-

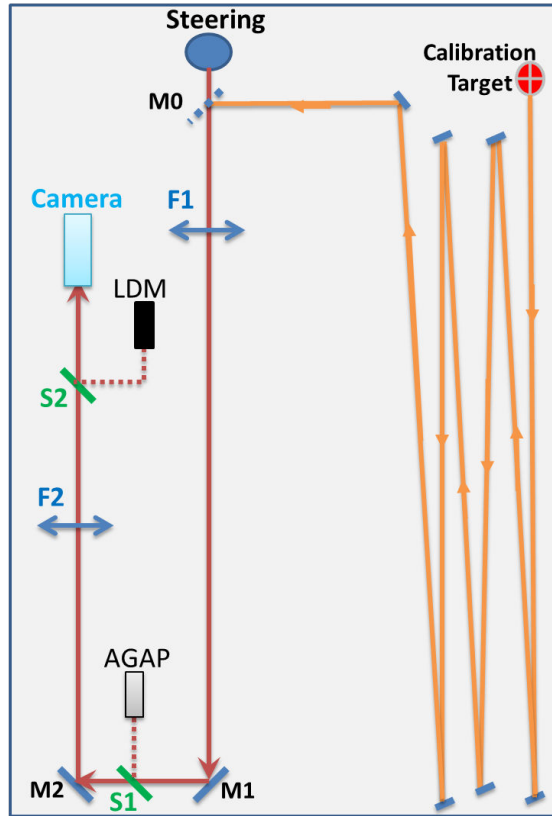


Figure 3.10: Sketch of the BSRT in the refractive optics (lenses F1, F2) version, showing the calibration line occupying the right part of the optical table complementary to the imaging line. The version features only on movable element, the zoom lens F2, used for moving the focus from the undulator radiation to the D3 core.

gated in detail in Chapter 4. The performance of these two systems will be compared in terms of resolution using dedicated developed simulation tools.

3.1.4 Detector

The detector used for the BSRT is a Proxicam type HL4 S NIR camera with a red enhanced S25 photocathode (type N) [4]. It has a built-in image intensifier used for gating and amplifying the SR light: gating can be achieved down to 20 ns, thus

selecting only 1 circulating bunch for a single turn¹. The intensifier working principle is described in Fig. 3.11. The incoming photons hit the photocathode, a very thin light

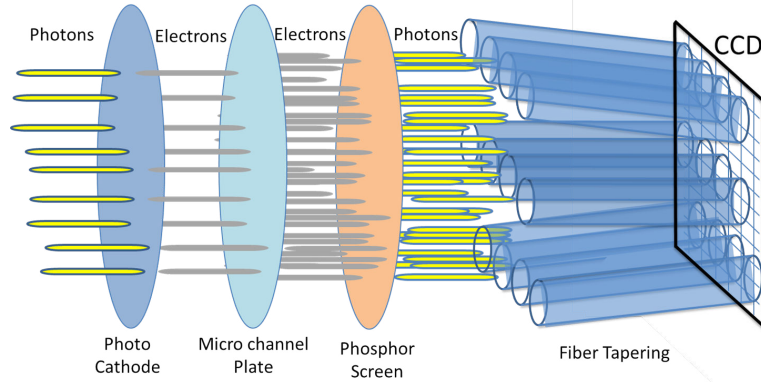


Figure 3.11: Low light Intensifier working principle.

sensitive layer deposited on the input window, then converts the photons into electrons and releases them into the vacuum of the tube. Once released by the photocathode, these photo-electrons are accelerated and focused by a high electrical field towards the Multi Channel Plate (MCP). By acting on the polarization of this high voltage, gating is possible, and only the desired photo-electrons reach the MCP. The MCP is a thin glass disc which contains millions of small channels. When an electron coming from the photocathode strikes the inner wall of one channel, several secondary electrons are generated by the impact and each of these secondary generates more secondary electrons. This process is repeated along the depth of the MCP channels. For each electron that enters the MCP, thousands of electrons are generated and subsequently accelerated towards the phosphor screen. The phosphor screen is a thin phosphorous light emitting layer deposited on the inside of the output window of the intensifier tube which converts the electrons back into photons. When the multiplied electrons flow out of the MCP and strike that layer, tens of thousands of photons will be generated for every single photon that was initially converted by the photocathode [57]. The output of the intensifier is often coupled through an optical fiber bundle to the CCD. The final spatial resolution of the system (intensifier + CCD) is limited by the space

¹The intensifier maximum speed is limited to 200 Hz, therefore turn by turn measurements are not available, but only 1 measurement every 55 turns.

between the fibers.

For the Proxicam, the image area on the photocathode is 12.8 mm by 9.6 mm. The intensifier output is fibre-coupled with an 18:11 reducing taper to the CCD, which has 756 by 581 pixels. Imaged back to the cathode, the pixels are almost square, 16.9 μm by 16.5 μm . The photocathode spectral sensitivity is shown in Fig. 3.12.

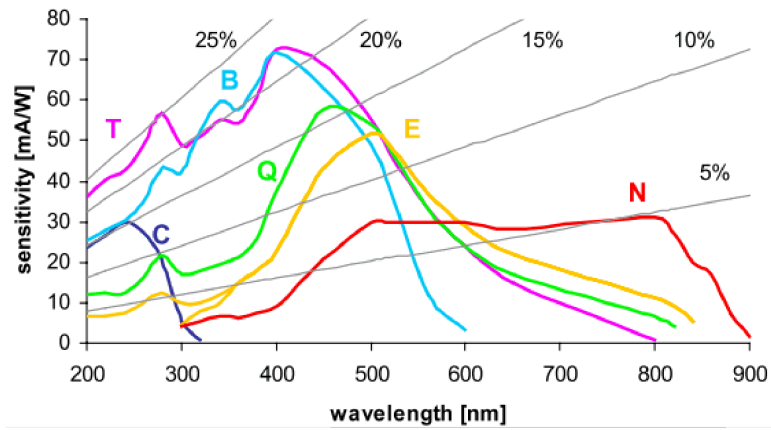


Figure 3.12: The spectral response characteristic of the Proxicam for different photocathode types used in the intensifier [4].

3.2 SPS

Visible SR was measured for the first time in the SPS in late 1979 [58, 59]. During an experiment, light intensity measurement was carried out using a photomultiplier and images were acquired using a VIDICON camera with a silicon target [60]. Signals on the photomultiplier were detected from a proton beam as weak as 10^{11} particles, while images were captured for energies greater than 350 GeV and proton intensity higher than $6 \cdot 10^{12}$. Following this experiment, visible SR was used during $p\bar{p}$ operation to monitor the beam size evolution whilst in store. Since then the system was only used periodically for testing and is, since several years, no longer operational.

In order to continually monitor the brightness of the SPS beams to the LHC, a monitor capable of measuring the beam size at extraction is required. Up to now the SPS has relied on the use of wire scanners, but this has two drawbacks. Firstly the instrument lifetime is compromised if used systematically on each SPS pulse, and secondly wire damage is possible when used with high brightness beams. Since a profile monitor based on synchrotron light, *BSR*, could solve both of these issues, it was planned to refurbish the SR monitor of the SPS as part of the LHC Injectors Upgrade (LIU) project [61].

3.2.1 Source description

No dedicated insertion devices are installed in the SPS to generate SR. Therefore SR diagnostics should be based on the light emitted from the bending dipoles. The bends in the SPS are of two types, MBA and MBB, having the same magnetic properties but different aperture. Each magnet is 6.2 m long, has a bending radius of 743.08 m and reaches a maximum magnetic field of ~ 2.02 T corresponding to a circulating proton beam of 450 GeV.

As Fig. 3.13 shows, the critical wavelength of the SPS bending magnets is far from the visible range (300– 800 nm), even at flattop energy of 450 GeV, where its minimum value amounts to 28 μm ; hence, eventual visible SR does not correspond to the classical SR from a constant magnetic field.

At this point, it is worth mentioning the historical importance of the detected SR,

since it served as a proof of the existence of the dipole edge radiation emitted by relativistic protons theorized by Coisson in [33] and described in Chapter 2.2.2. In

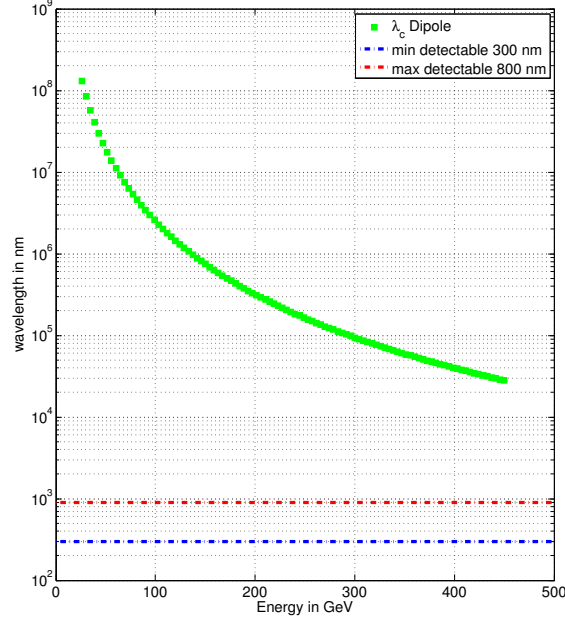


Figure 3.13: SPS dipole MBB critical wavelength λ_c shift with energy ramp up to 450 GeV.

the following, the light used for the diagnostics is emitted from the edges of two consecutive MBBs. Moreover, since the distance between the two dipoles is ~ 50 cm, an interference phenomenon is observed between the SR emitted in the falling edge of the dipole 52130 and in the rising edge of the dipole 52150, as sketched in Fig. 3.14. As summarized in Tab. 3.2, the machine optics parameters at the location of the SPS BSRT and considering normalized beam emittances in the range $1 \dots 3 \mu m$ result in beam sizes at the BSRT location of $534 - 644 \mu m$ in the horizontal plane and $394 - 682 \mu m$ in the vertical plane.

	Horizontal	Vertical
Beta function β [m]	31.147	74.55
Dispersion function D [m]	1.5634	0

Table 3.2: Optics parameters at the SPS BSR source location.

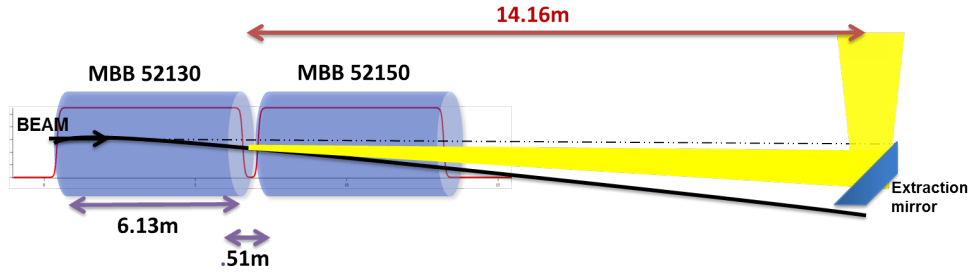


Figure 3.14: Schematics of the SPS SR light sources.

Unlike the LHC case, the horizontal dispersion at the SR source location is not negligible and increases the horizontal beam size by $\sim 109\%$ for normalized beam emittance of $1\ \mu\text{m}$ and by 46% for normalized beam emittance of $3\ \mu\text{m}$ at $450\ \text{GeV}$. This implies that precise horizontal beam size measurements are only possible if the momentum spread and the dispersion are known with high accuracy.

Further details and quantitative studies of the SPS source are given in Chapter 4.6.

3.2.2 Light extraction system

The SR extraction system is located in the SPS Long Straight Section LSS5, $14.16\ \text{m}$ downstream of the rising edge of MBB 52150. The light is extracted using an in vacuum rectangular mirror ($100\ \text{mm}$ by $80\ \text{mm}$) rotated by 45° about the y axis, that extracts the light directing it sideward to a $150\ \text{mm}$ diameter viewport. As shown in Fig. 3.15, the transverse offset (toward $+x$) between the mirror edge and the proton beam is about $67.7\ \text{mm}$, whereas the mirror's axis is aligned with the beam axis at the MBBs edges. The light is then bent downward by a fixed mirror to a shielded enclave where the optical system lies.

3.2.3 Optical and detection systems

The system refurbishment focuses mainly on re-designing and re-implementing the optical system, used to guide and focus the SR light, and the deployment of a new camera. The new optical system consists of a 2 stage imaging system using high

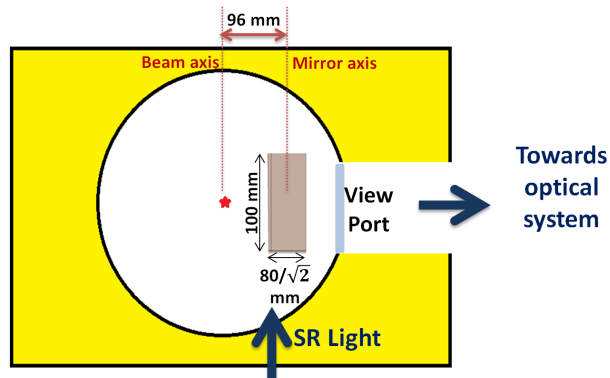


Figure 3.15: Sketch of the Synchrotron light extraction tank of the SPS BSR.

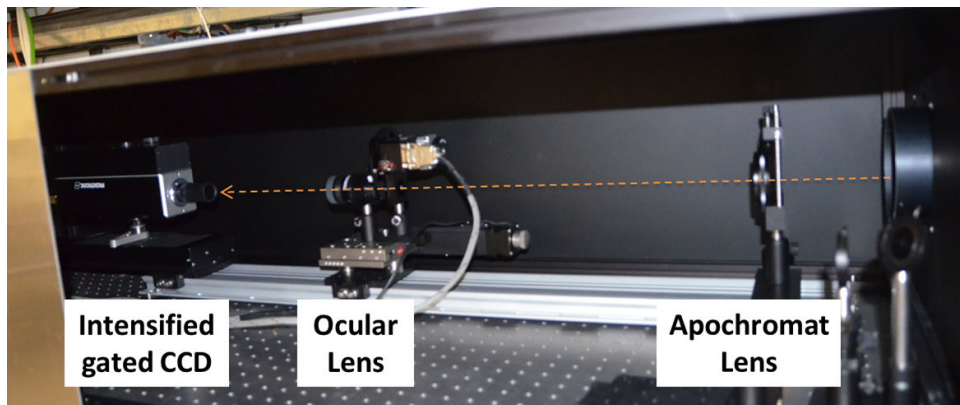


Figure 3.16: Optical system of the SPS BSR, based on two focusing lenses.

quality apochromatic lens with focal length of $f = 800$ mm and an ocular lens of focal length $f = 18$ mm, coupled to the gated, intensified, analogue camera used for the LHC and described above. The design magnification is 0.25, however since the ocular lens is mounted on a translation stage, it is used as a zoom allowing to change the magnification from 0.17 to 0.31.

Additionally, an in-vacuum calibration target (BSRF) is installed between the two dipoles, allowing for a better alignment accuracy of the optical system and to measure its magnification as discussed in Chapter 5.1.1. The performance of SPS SR beam size monitor will be investigated in Chapter 4.

Chapter 4

Simulation of the SR Monitors’ Performance

This chapter is dedicated to assess the accuracy and resolution of the SR-based beam size monitors by means of available and novel simulation codes. In particular, the new simulation tools developed during this thesis work allows characterizing the SR emitted by any source, its transport along an optical system and its imaging on a detector.

The particular case of the LHC and SPS SR imaging systems is considered, estimating its theoretical resolution. After discussing the imaging simulation results, a new proposal for a beam size monitor based on SR interferometry is studied, assessing its resolution and expected performance.

The summary of these studies was published as a part of the International Particle Accelerator Conference IPAC14 proceedings [62] and in this chapter the results will be presented in more detail.

4.1 SR simulation tools

Although the formulae presented in Chapter 2 for the SR intensity and spectrum calculations from a bending magnet and undulator are well known, analytical solutions for the radiation from the edge field and from a short undulator involve some approximations. These types of SR are better modelled by a simulation code such

as Synchrotron Radiation Workshop (SRW) [63, 64, 65], chosen as the SR source simulator, that separately treats each short segment of magnetic field. The magnetic field within these short segments is taken as constant and the SR emission from each segment is then modelled with no further approximations. Moreover, to take into account the interference effects, SR from all the segment are propagated together.

Even though SRW includes a wavefront propagation package based on near field calculations, it results being limited for the available optical elements and the transverse extent of the wavefront to be propagated. The commercial optical design software *Zemax* [66] was identified as a more suitable tool for transporting the wavefront obtained from SRW through the various optical elements, modeled including aberrations. A new tool developed in Matlab [67] was used as 'glue' code between SRW and *Zemax*. Matlab has also been used for simulating the SR emitted from a finite size beam, as described in Section 4.1.3.

4.1.1 Synchrotron Radiation Workshop (SRW)

SRW, developed by O. Chubar and P. Elleaume at the European Synchrotron Radiation Facility (ESRF), is a physical optics computer code for simulating SR generated by relativistic electrons¹ in magnetic fields of arbitrary configurations.

By applying a proper scaling to the proton energy E_{proton} and to the magnetic field B_{proton} guiding it:

$$\begin{aligned} E_{equivalent} &= E_{proton} \cdot \frac{m_e}{m_p} \\ B_{equivalent} &= B_{proton} \cdot \frac{m_e}{m_p} \end{aligned} \tag{4.1}$$

where m_e and m_p are respectively the rest masses of the electron and the proton, ($m_e/m_p \sim 1/1836$), SRW is able to simulate as well the SR emitted by protons.

SRW is integrated as a toolbox into the graphing and analysing software Igor Wave-metrics [68] to ease the pre and post processing via the powerful scripting environment

¹An upgraded version of SRW recently released features the ability of changing the type of the simulated particle github.com/ochubar/SRW

and the flexibility that Igor offers.

The SR radiation is calculated from a filament relativistic charged beam (i.e zero transverse size) travelling through an arbitrary magnetic field and observed in a plane located at a fixed distance from the source, as a function of the photon energy (monochromatic radiation) and polarization. The broadening of the intensity profile induced by the non zero transverse emittances is optionally computed on request, assuming that one can neglect the variations of the magnetic field of the source as a function of the transverse coordinates. This is done by performing a convolution over horizontal and vertical coordinates of the single-electron SR intensity with a 2D Gaussian function (with widths defined by the beam sizes).

4.1.2 Zemax

Zemax is an optical design program that is used to design and analyse optical systems. In its basic mode, named *geometrical optics mode*, it works by ray-tracing, i.e. modelling the propagation of rays through the optical elements. Even though, some ray based diffraction computations are implemented in this mode, such as the diffraction Merit Transfer Function (MTF), these computations are only an approximation and assume that the relevant diffraction effects only occur from the exit pupil to the image.

Zemax also includes the *Physical Optics Propagation (POP)* mode, using diffraction laws to propagate a wavefront sequentially through an optical system element by element. The POP mode is used for free space propagation: when a wavefront reaches an optical surface, it is decomposed into rays traced geometrically including aberrations and diffraction throughout the surface (i.e. the lens) and then recomposed into a wavefront at its exit. To propagate the field from one surface to the other different propagation algorithms are automatically chosen by Zemax in order to achieve the highest numerical accuracy (see [69, 70]).

The choice is based on the computation of the Fresnel number F_N , defined as:

$$F_N = \frac{2}{\lambda} \left[\sqrt{Z^2 + R^2} - Z \right] \quad (4.2)$$

with λ being the wavelength of the propagated wave, R the radius of the beam and

Z the propagation distance.

In the far field ($F_N \sim 0$) the Fraunhofer diffraction algorithm is used, while in near field ($0 < F_N < 1$) the Fresnel diffraction algorithm is chosen for the propagation. For large Fresnel numbers ($F_N > 1$), the very near field region, a propagation based on the angular spectrum of the light beam is adopted [71].

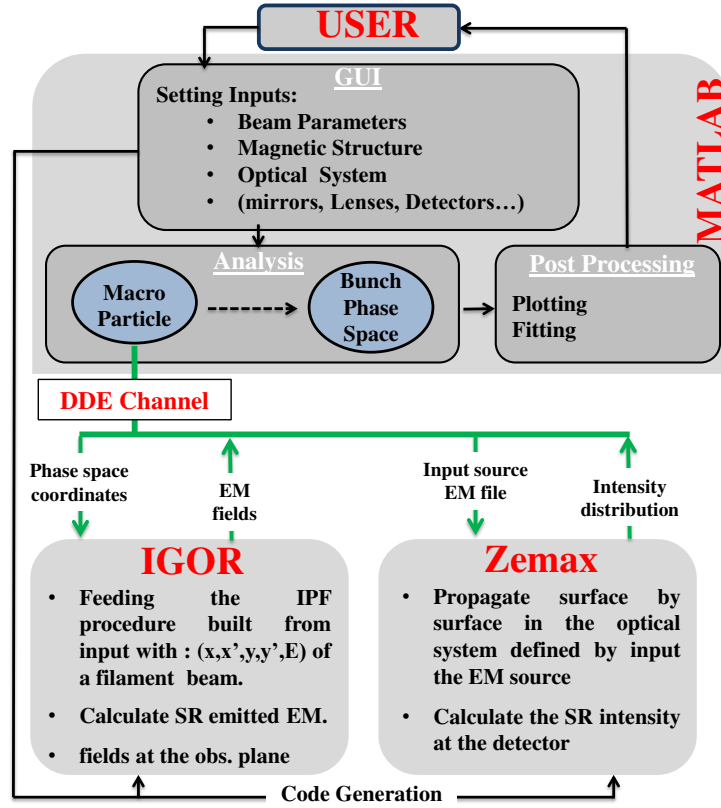


Figure 4.1: Code flow of the new simulation tool developed during this thesis work.

4.1.3 Combined approach

In computing, Dynamic Data Exchange [72] (DDE) is a method of inter-process communication under MS WindowsTM. It allows one program to subscribe to items made available by another program, enabling applications to exchange data.

For designing and characterizing the SR systems discussed in this thesis work, a new simulation suite based on a MATLAB DDE server to interface SRW and Zemax was

developed. The code flow, shown in Fig. 4.1, explains how the user, interfacing only with MATLAB via a Graphical User Interface (GUI), can generate the SRW and ZEMAX codes, transparently run them and analyse the results.

The GUI inputs are the beam energy, position, intensity, emittance (zero emittance beam or finite size beam), the magnetic structure (dipoles/undulators position and field) and the optical system description (lenses, mirrors, apertures, slits, filters and detector).

Considering the case of zero input beam size, the operations flow is:

- an Igor Procedure File (IPF) describing the SR source (magnetic elements) is created in Matlab;
- the IPF and its inputs (beam energy, SR wavelength and beam position) are pushed to SRW through the DDE channel;
- the IPF is executed;
- SR electromagnetic fields in the observation plane, defined as the surface of the first optical element of the imaging system (usually the in-vacuum extraction mirror), are calculated;
- the results are passed back to MATLAB using the same communication channel for normalization and phase correction;
- a Zemax File (ZMX), listing the optical elements (lenses, drifts, mirrors, apertures...) as surfaces, is generated and fed together with the input fields encapsulated in the format of Zemax Beam File (ZBF) to Zemax;
- after propagation in POP mode to the detectors plane, the light intensity distribution is extracted by Matlab, post-processed and delivered to the user.

The result is interpreted as the Line Spread Function (LSF) of the monitor, defined as the system response to a pencil beam (i.e. null emittance), and is also considered as the theoretical optical resolution of the SR imaging system.

The LSF is a necessary generalization of the concept of the PSF introduced in Chapter 2.3.1, since the acceptance of SR monitors is always such as the incoming light is emitted spontaneously over a beam trajectory and not a point source.

It is also worth mentioning that the LSF is always meant in the source plane, obtained by decoupling the optical system magnification (that is different for different focusing planes), and allows comparing different LSFs for different focusing positions.

A more realistic case implies a Finite Beam Size (FBS), involving the description of the real SR and its propagation to the detector. The final image is reconstructed by summing the intensities of individual emitters instead of the electric fields. This is possible, because only visible (200 nm – 800 nm) SR is considered, and the RMS bunch length is several hundreds of picoseconds, therefore the protons can be considered to emit SR incoherently.

The following will describe the two methods developed for simulating the FBS case.

Weighted uniform phase space sampling

This method consists in dividing the transverse phase spaces $((x, x')$ and (y, y')) into small areas of partial coherence, weighted accordingly to the 2D multivariate normal distribution fitting the beam emittance. From the SR emitted by a single macro particle, the LSF is calculated at the detector plane and the response of the finite size beam is obtained via the weighted sum of the LSFs over the sampled phase space.

The density of the phase sampling depends on the beam emittance and the optical system apertures. The choice of 10 macro particles per sigma of the Gaussian distributions per plane was found to be always a good compromise between under and over sampling.

Reconstruction by extrapolation

Since the computational load (proportional to the simulation time) required by the first method can easily become very demanding, an alternative approach is based on the simulation of only a few *reference* macro-particles. By fitting the results one can develop a numerical model predicting the SR intensity distribution of every particle in phase space.

Even though this method was found suitable for the LHC injection case (undulator radiation), the numerical model is often difficult to find, making this approach difficult to adapt to all situations.

4.2 LHC source characterisation

The developed GUI was at first ran with SRW alone to characterize the LHC BSRT source characteristics, by modelling the undulator and dipole magnets and setting an observation window at the position of the extraction mirror, perpendicular to the beam direction at the undulator. This simulation was performed with the following two approximations:

- a built-in sinusoidal function is used in SRW to reproduce the magnetic field of the undulator, anyhow well reproducing the measured field map;
- the D3 edge field is modelled using SRWs default edge field function, defined through a sigmoid function:

$$B(s) = \frac{B_{max}}{1 + e^{-s/k}} \quad (4.3)$$

where k is calculated knowing the distance over which the field is rising from 10% to 90% of the maximum. As suggested in [50], $k=56$ mm was used in this case.

During the acceleration of a proton beam in the LHC, the power distribution on the extraction mirror of the SR simulated and integrated over the spectral range of the monitors sensitivity (200 to 800 nm), is shown in Fig. 4.2. The power plots can be interpreted as in the following:

- at 450 GeV, the undulator is the dominant source and its SR peaks on the extraction mirror at $(x=0,y=0)$, that in the same coordinates system used in Chapter 3.1.2 corresponds to the undulator center;
- at 1 TeV the undulator is still the dominant source but the on-axis undulator radiation is in the Ultra Violet (UV). Since the wavelength is strongly dependent on the angle of observation, SR is emitted on-axis only at the undulator coherence wavelength, whereas other wavelengths are emitted in hollow cones with opening angle proportional to the difference between the observed wavelength and the coherence wavelength. Even if it is hardly visible on a linear intensity scale, on a logarithmic scale one could appreciate the appearance of D3 edge radiation as a spot at $(0,0)$;

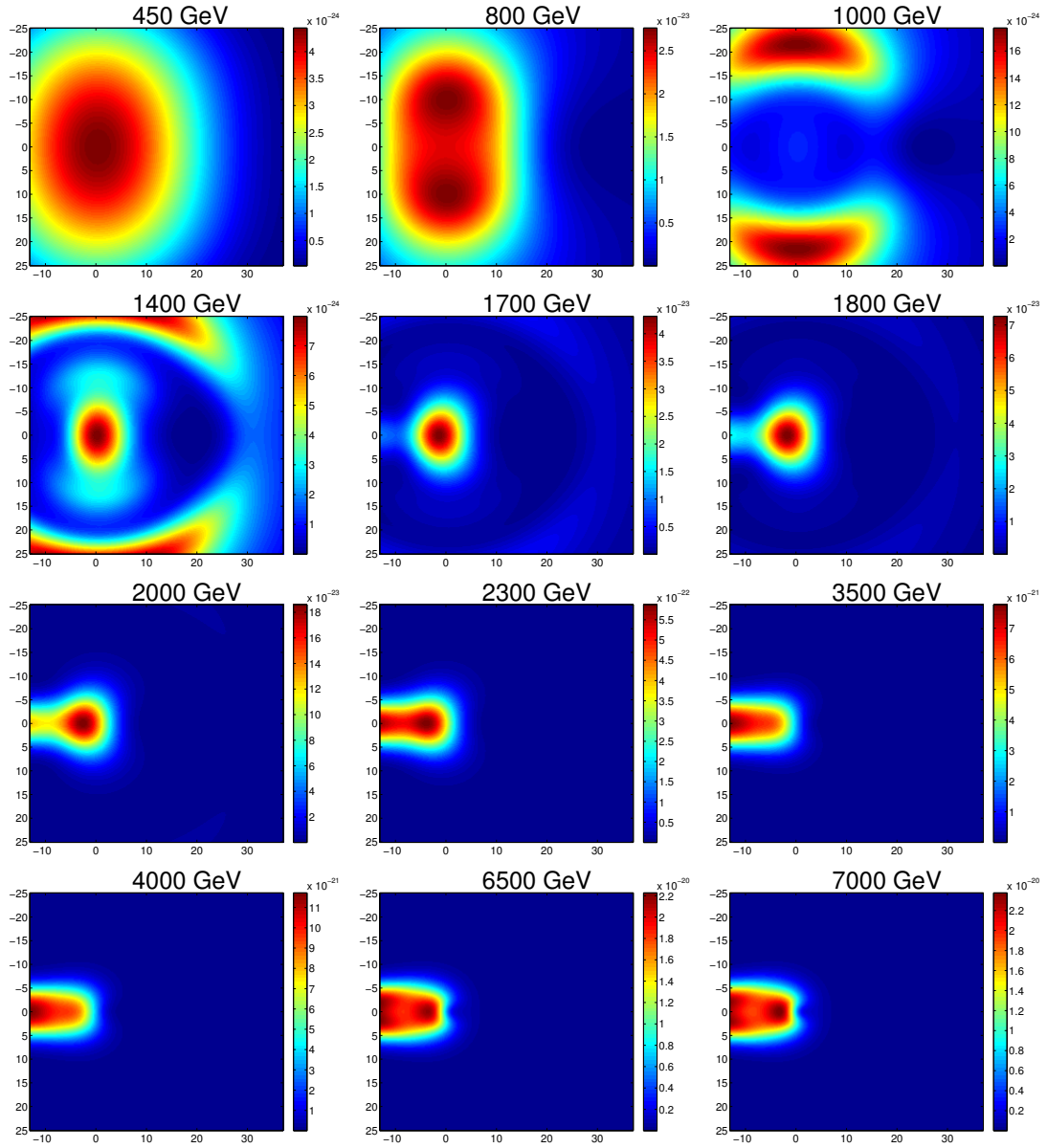


Figure 4.2: Simulation of the LHC SR power (in units of $W \cdot mm^{-2}$ per proton) at the extraction mirror, for different beam energies.

- although the total power radiated from the D3 edge is always much smaller than that from the dipole centre, at the energies where both the dipole and the undulator spectrum are centred outside the visible range, the radiation from the D3 edge field is significant. This is observed from ~ 1.2 TeV to ~ 1.8 TeV where the D3 edge radiation is the dominant source;
- above 2 TeV, the SR from the body of the dipole is dominant. SR from the dipole shows up as a streak from (0,0) to the inner edge of the mirror. This is the so called searchlight effect, where the photon beam of the particles bent in the dipole is swept across the extraction mirror. As already mentioned in Chapter 3.1.2 only the light emitted from the first 3.5 m of the D3 is intercepted by the extraction mirror;
- as also shown in Fig. 3.3, the opening angle of the emission cone gets wider with the energy ramp since the observed wavelength range becomes greater than λ_c ;
- from ~ 5 TeV onward, an important contribution to the SR originates again from the edge.

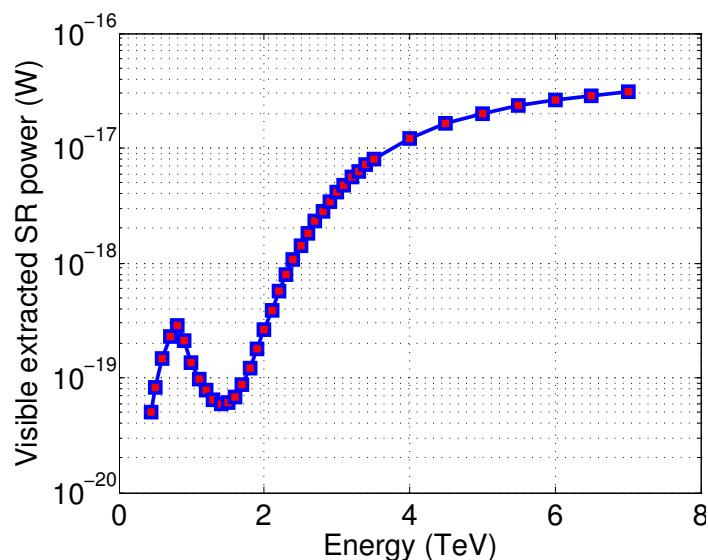


Figure 4.3: Total LHC SR power per proton, integrated over the extraction mirror area, in the 200 . . . 800 nm wavelength range.

By integrating the SR spectrum over the extraction mirror area, the LHC extracted SR power per proton (in the 200 nm–800 nm range) is shown in Fig. 4.3. The minimum observed at around 1.1 TeV corresponds to when the undulator is emitting SR mostly in the UV while the dipole is still mostly in the IR. Above 1.3 TeV the SR from the dipole edge starts to enter the visible region, hence the observed increase of the SR intensity.

Another interpretation of the results is given in Fig. 4.4, where the SR power density as function of radiation wavelength is shown for different beam energies. These curves were very useful for designing the BSRT telescope and understanding its performances all along the energy ramp.

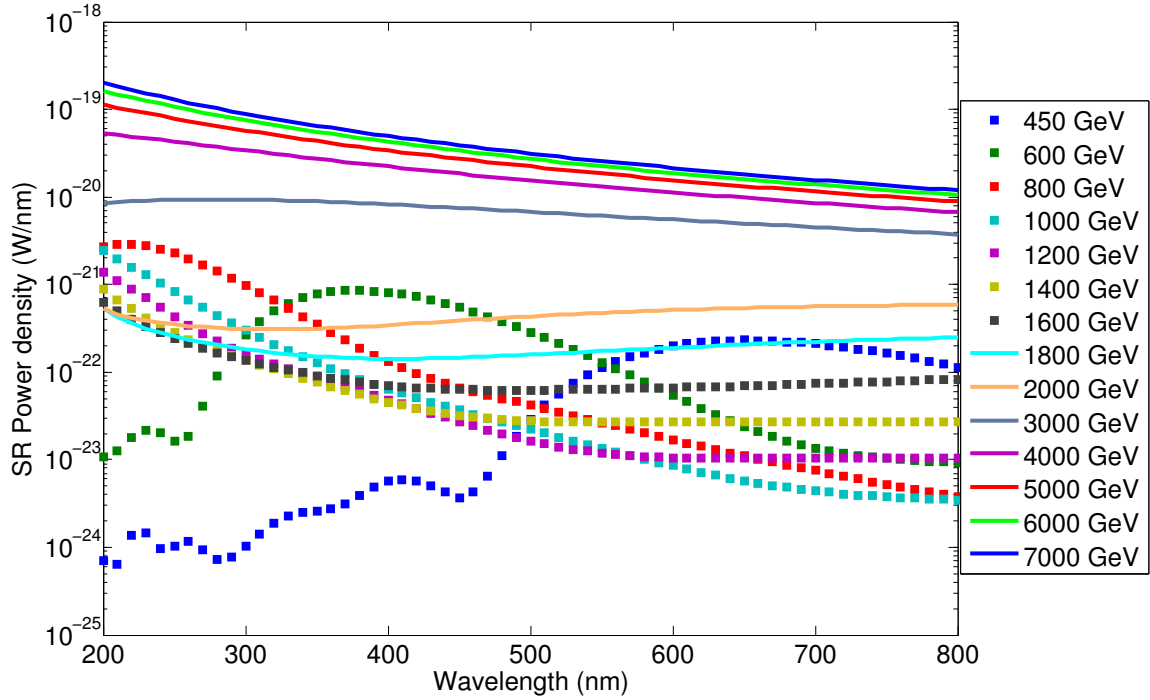


Figure 4.4: SR power density as function of beam energy, as calculated for the LHC systems.

4.3 Performance of the LHC SR imaging monitors

In the following the performance of the BSRT in terms of optical resolution, hence LSF, will be calculated for both the reflective and refractive optical systems, considering two scenarios used in pre-LS1 operation:

- injection energy with no bandpass filters;
- flattop energy using a bandpass filters centered around 400 nm.

In describing the simulation codes in Chapter 4.1.3, the example of a monochromatic LSF was considered. By iterating the same procedure over different wavelengths and performing a weighted sum of the obtained LSF according to the convolution between spectral acceptance of the optical and detector systems, the LSF expected in more realistic cases could be obtained.

4.3.1 Analysis of the original reflective optics system

The spectral sensitivity of the whole system could be obtained by accounting for the spectral transmission of the individual elements forming the reflective optics based imaging system (silver protected mirrors, focusing mirrors, splitters and the extraction mirror) and the detector sensitivity (described in Chapter 3.1.4). This is shown in Fig. 4.5.

For the injection energy scenario, the system sensitivity was used as a weight function for all the LSF calculated in the range of 200-800 nm¹. The resulting horizontal and vertical LSFs are shown in Fig. 4.6, for different positions of the camera corresponding to different focusing in the object plane: center of the undulator, rising edge of D3 and 1.5 m into the core of D3. Keeping in mind that the image formation is mathematically described as a convolution of the beam distribution with the BSRT LSF, under the assumption of Gaussian distributions, the measured beam size would be expressed

¹The wavelength range was uniformly sampled by 61 wavelength spaced by 10 nm.

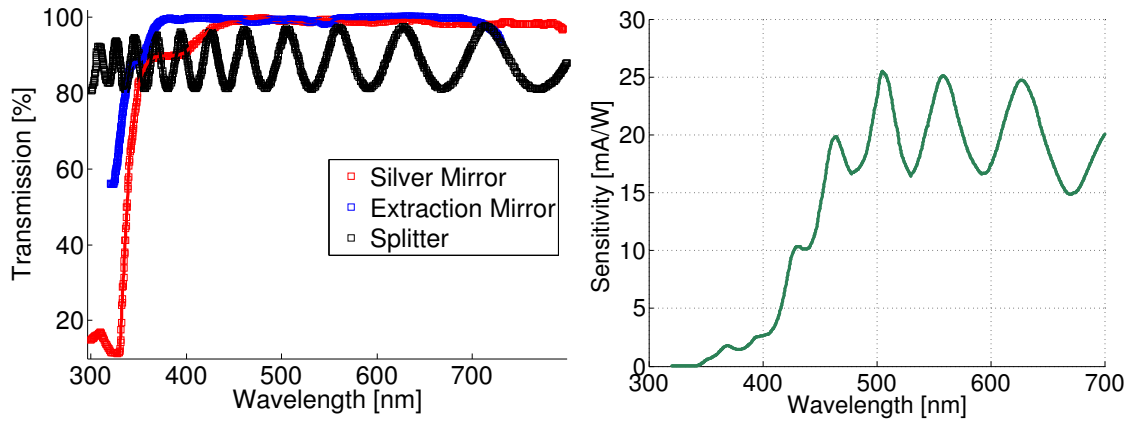


Figure 4.5: Sensitivity of the LHC imaging system based on reflective optics (left) obtained as a convolution of the detector's sensitivity and the transmission of the optical system (right).

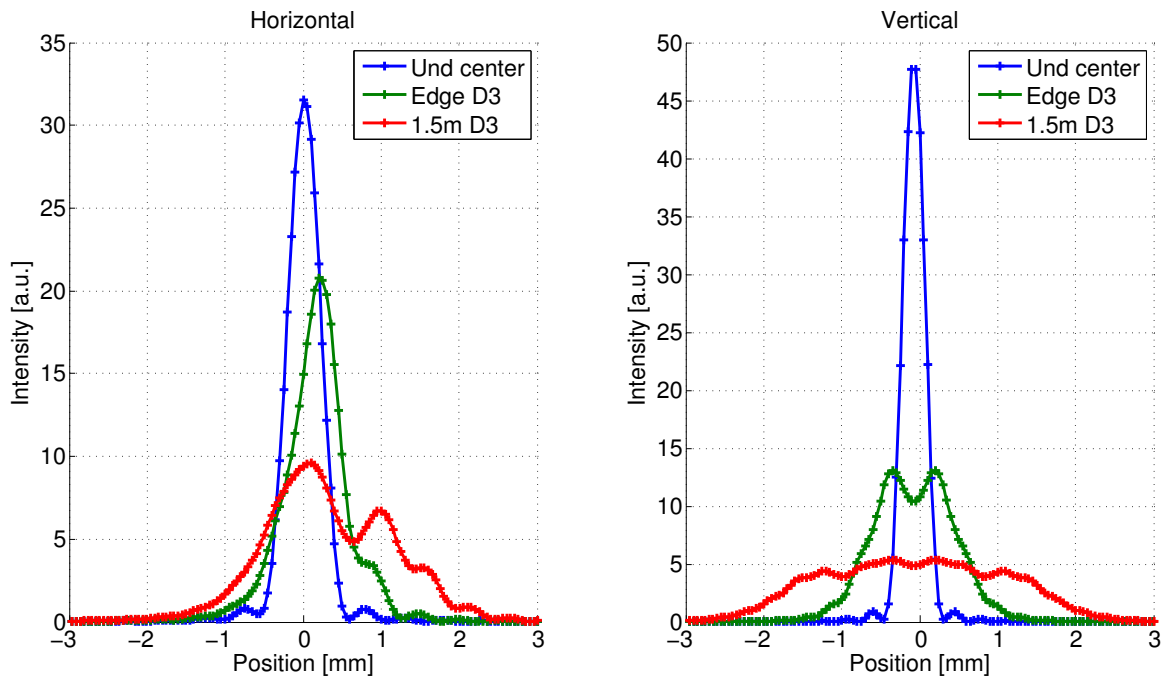


Figure 4.6: LSF of the LHC reflective optics based imaging system at injection energy (450 GeV) at the wavelength of 600 nm.

as¹:

$$\sigma_{BSRT_{meas}}^2 = \sigma_{BSRT}^2 + \sigma_{LSF}^2 \quad (4.4)$$

where σ_{BSRT} is the width of the beam distribution at the undulator (/D3) and (for this ‘Gaussian case’) σ_{LSF} is the LSF width.

However, the LSF is rarely approximated by a Gaussian distribution, therefore, to compare different LSF curves, the concept of the ”effective LSF width” is introduced. The effective width σ_{LSF} is obtained by applying a Gaussian fit to the result of the convolution of the real LSF (plotted in Fig. 4.6) with the typical beam size of ~ 1 mm in the LHC (corresponding to a normalized emittance of $2 \mu\text{m}$) at the SR source location.

The results are shown in Fig. 4.7, where for both planes the effective σ_{LSF} is plotted. Therefore, the resolution of the system, defined as the minimum σ_{LSF} achieved with the best focusing, can be estimated as $\sim 280 \mu\text{m}$ in the horizontal and $\sim 190 \mu\text{m}$ in the vertical plane, when focusing on the center of the undulator.

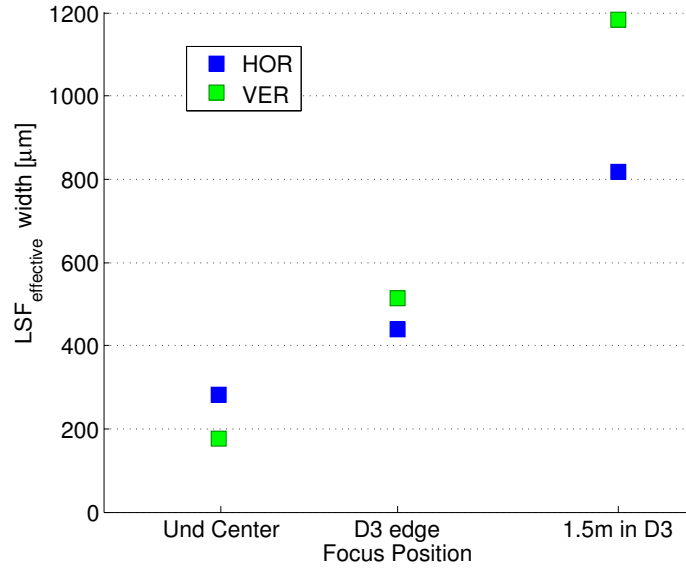


Figure 4.7: Effective width of the LSF at 450 GeV integrated over the detectable range (200 nm–800 nm) for the reflective optics based imaging system case.

¹The convolution of two uni-variate Gaussian distributions f and g having respectively the means μ_f, μ_g and standard deviations σ_f, σ_g is a Gaussian distribution with mean and standard deviation $\mu_{f*g} = \mu_f + \mu_g$ and $\sigma_{f*g} = \sqrt{\sigma_f^2 + \sigma_g^2}$

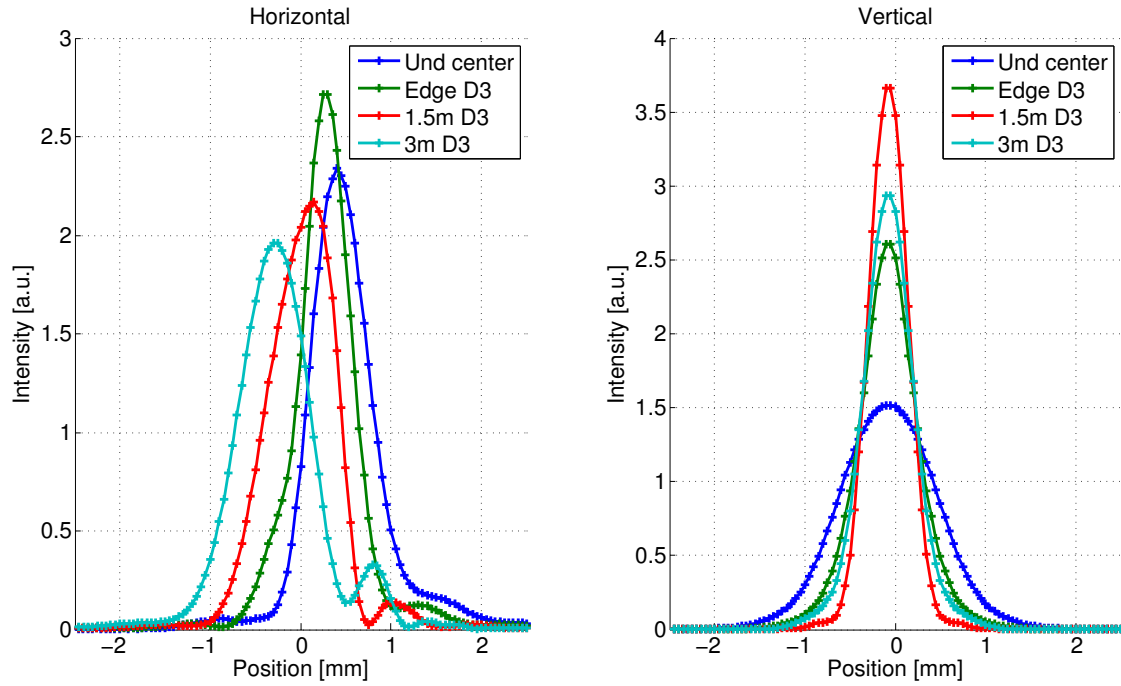


Figure 4.8: LSF of the LHC reflective optics based imaging system at flattop energy (7 TeV) at the wavelength of 400 nm.

Considering the second operational scenario, at the flattop energy of 7 TeV, SR imaging is performed through a narrow (width < 10 nm) band pass filter, therefore the LSF computed only at the wavelength of 400 nm is considered as a good approximation of the real case.

The LSF is plotted in Fig. 4.8, at different focusing planes. The displacement of the horizontal LSF peak for different focusing within the D3 corresponds directly (through the optical magnification) to the beam bending in the dipole. Then, as for the low energy case, the effective σ_{LSF} was calculated, this time using the typical beam size of ~ 0.2 mm in the convolution.

The results shown in Fig. 4.9 evidence the astigmatism in the reflective optical system, since the focus point is at different locations for the horizontal and vertical plane. This is unavoidable when using focusing mirrors.

The resolution of the system could be calculated as ~ 310 μm in the horizontal plane when focusing on the rising edge of the D3 and ~ 220 μm in the vertical plane when

focusing ~ 1.5 m inside the D3.

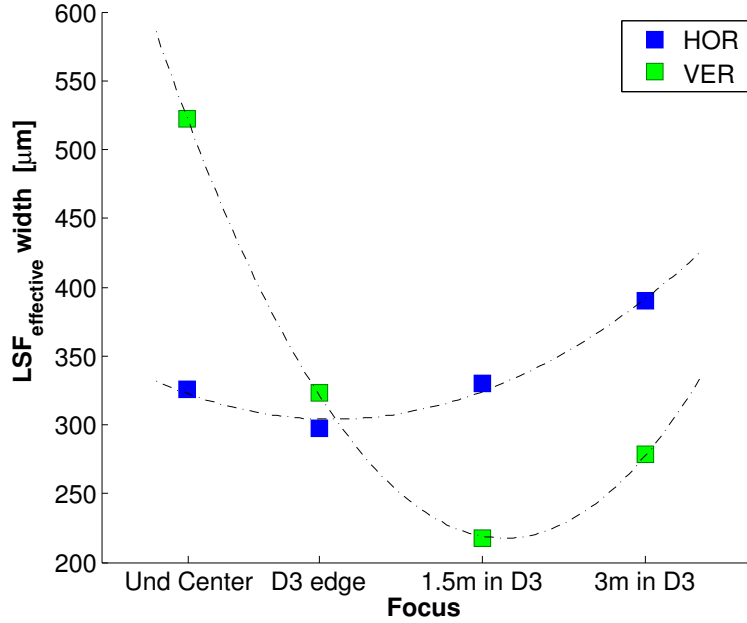


Figure 4.9: Effective LSF width at the flattop energy (7 TeV) and 400 nm for the reflective optics based imaging system case.

The operational experience gained in 2012, described in Chapter 5.2.2, motivated dedicated studies of the LSF dependency on any system misalignment. Indeed, with the old reflective system, avoiding light cutting at all energies resulted to be a very difficult task due to the delay line complexity.

A sketch of the unfolded optical line, up the first focusing element (F1), is shown in Fig. 4.10. The sketch evidences that sub-degree tilts β_i of the mirrors, amplified over the ~ 10 m distance from the extraction mirror to $M8$, result in a displacement Δx of the SR and can potentially induce a light cutting on some elements.

The impact of such misalignment was studied for the 2012 operational scenario (4 TeV, 400 nm color filter) as an attempt to explain the difference between the expected LSF and the measured one, that will be discussed in Chapter 5.2.2.

For example, the simulations showed that a light cutting on $M8$, as shown in Fig. 4.11, would induce a drastic change on the LSF. In particular, in the absence of misalign-

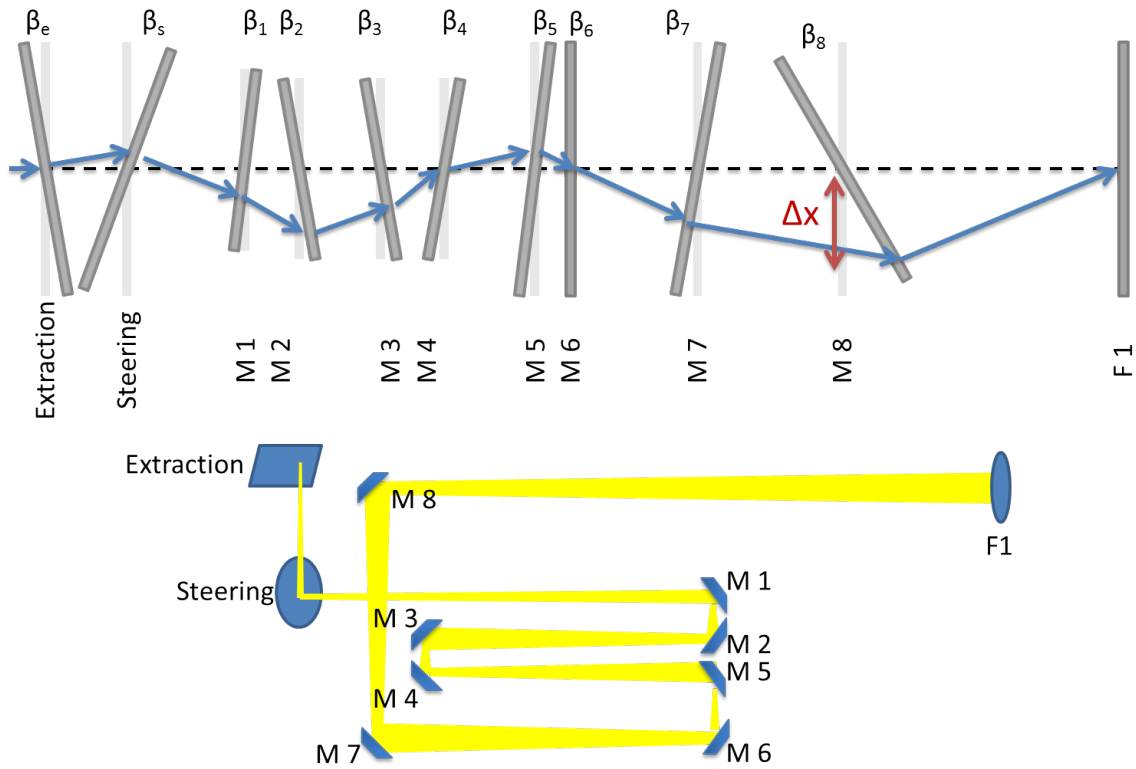


Figure 4.10: Schematics of the unfolded optical delay line showing eventual light cutting caused by small mirrors tilts β_i along the line.

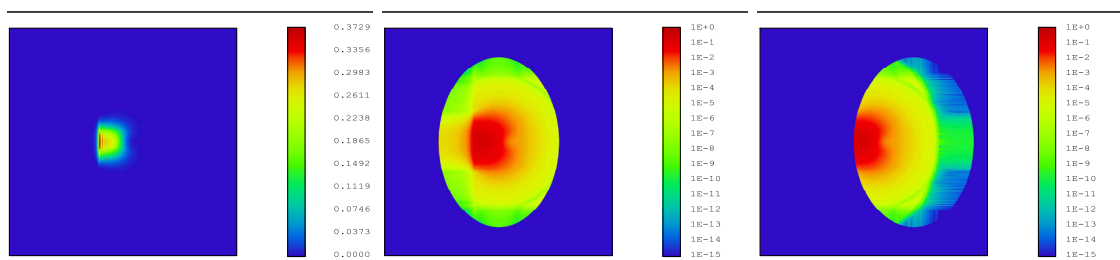


Figure 4.11: Light cutting at the last mirror M8 of the trombone line (right plot, shown in logarithmic scale), simulated by displacing the nominal position of M8 (central plot, shown in logarithmic scale) by the corresponding 9 mm.

ment and consequent light cutting, Fig. 4.12 identifies the minimum σ_{LSF} to be $\sim 300\mu\text{m}$ in the horizontal plane when focusing around the D3 edge. This LSF is then compared to the LSF obtained when a cut of $\sim 9\text{mm}$ is occurring on M8, as shown in Fig. 4.13. The misalignment and light cut on M8 yields an effective LSF width (as defined above) of $\sim 580\mu\text{m}$, i.e. a deterioration of the optical resolution of about +95%.

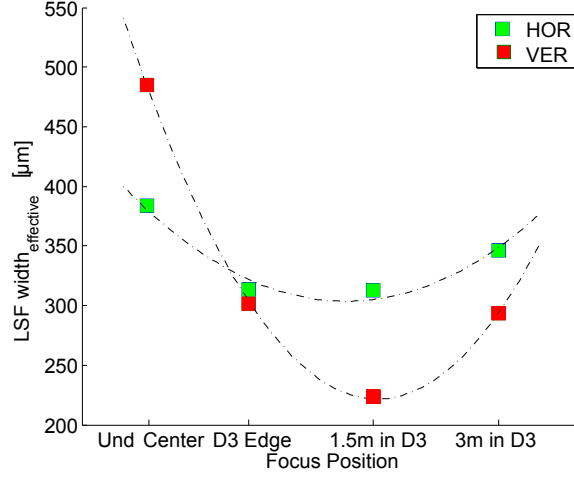


Figure 4.12: Effective LSF width at the energy of 4 TeV and 400 nm for the reflective optics based imaging system case.

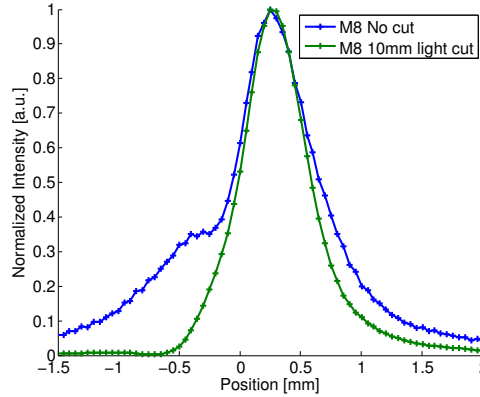


Figure 4.13: The nominal LSF of the LHC reflective optics imaging system, at 4 TeV and 400 nm focusing on the rising edge D3, compared to the case of a misaligned system.

4.3.2 Analysis of the new refractive optics system

The migration to this new optical system based on focusing lenses was conditioned by the trade-off between the simplification of the system, easing its operation, its stability and any possible degradation of the system resolution. In fact, by construction, additional broadening of the LSF is expected due to the chromatic and geometrical aberrations introduced by the lenses.

The simulated effective σ_{LSF} for the three beam energies is shown in Fig. 4.14. From these simulations it is possible to determine the horizontal and vertical minimum σ_{LSF} , that are compared to the ones of the old refractive system in Table 4.1.

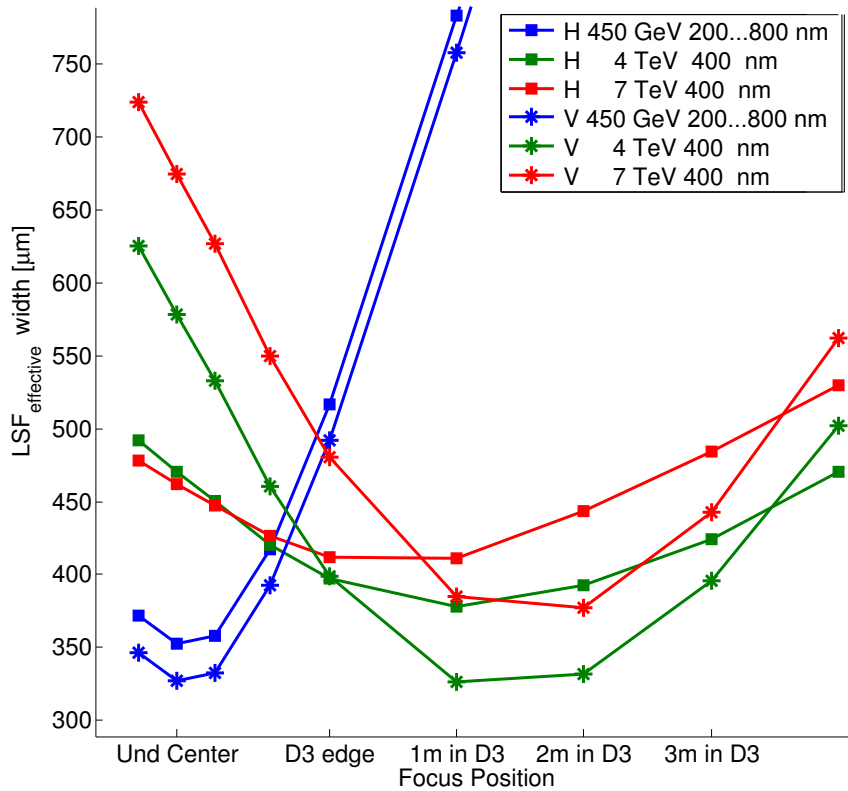


Figure 4.14: Effective LSF width for the LHC refractive optics based imaging system, shown for injection energy (450 GeV integrated over the range 200–800 nm) and the energies 4 and 7 TeV (at 400 nm).

	Reflective		Refractive	
	H	V	H	V
450 GeV	290	190	330	300
4 TeV	300	220	370	320
7 TeV	310	230	410	370

Table 4.1: Comparison σ_{LSF} [μm].

As expected, an increase is observed in all planes and for all the energies with respect to the theoretical σ_{LSF} of the original system. However, as will be discussed in Chapter 5, contrarily to the reflective optics, the newly proposed imaging system showed better stability and easier operation. For this system the agreement between the expected and the measured resolution is remarkable.

4.4 New telescope design and characterization

4.4.1 Resolution improvement

During the LHC long shutdown, an extensive set of simulations were dedicated to improve the performances of the SR imaging system. This implied studying in detail the different options for decreasing the theoretical LSF width and, where possible, implementing in the simulations realistic operational scenarios and all possible optical components and installation (e.g. alignment) imperfections.

Such studies, discussed throughout this section, resulted in the design and development of the an upgraded system that will be described in detail in Chapter 8.

Characterization and reduction of the depth of field effect

A significant contribution to the LSF broadening (at least in the horizontal plane) comes from the depth of field (DOF) effect, caused by the big bending radius of the dipole D3 (~ 6 km). The DOF effect can be reduced by the use of a horizontal slit selecting photons generated along a short path in the dipole. This technique is sketched in Fig. 4.15, where the slit blocks the un-desired (yellow) SR cones corresponding to the red proton beam path in the dipole, selecting only the light from the smaller green path.

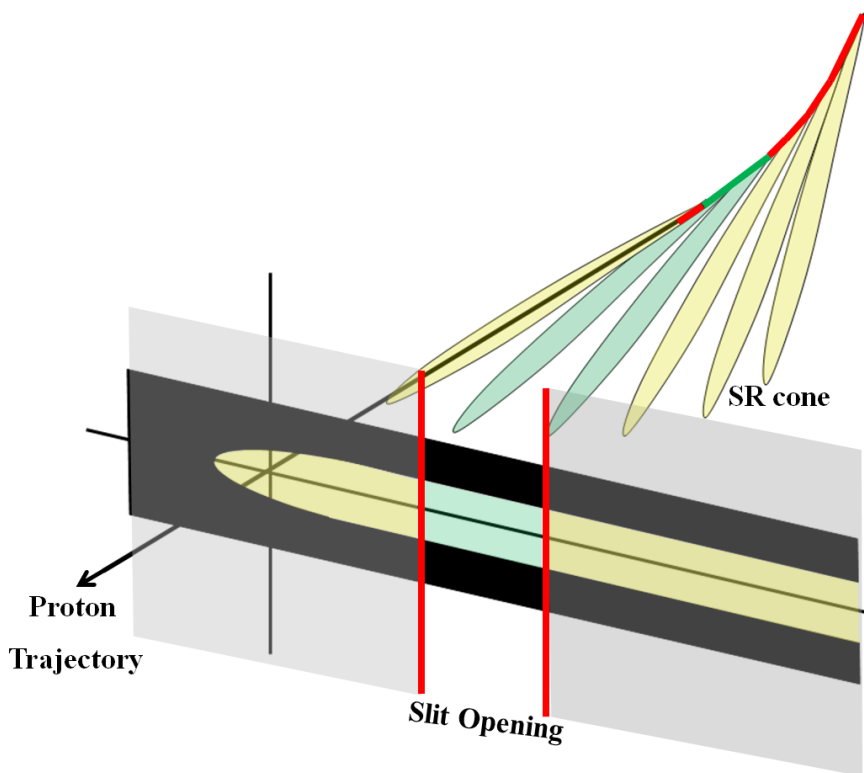


Figure 4.15: Slit selection technique for reducing the DOF effect by limiting the imaged light to a fraction of the total SR (selecting a short path within the bending dipole).

Since SR is emitted in narrow cones of opening angle $\sim 1/\gamma$ tangent to the beam trajectory, the SR cut corresponds to an angular cut in the photons phase space entering the telescope.

The optimum slit position is found by tracking ¹ an arbitrary photon phase space (position and angle) in a simplified optical system based on a single focusing element, as shown in Fig. 4.16. At the source (Fig. 4.16a), an angular selection within the blue 2D Gaussian phase space is shown in black. The latter is tracked up to the focusing lens after a drift D_1 , then to one focal length f after the lens and through a final drift $\frac{D_1 \cdot f}{D_1 - f} - f$ to the conjugated image plane of the source.

¹ The tracking was performed based on a matrix formalism where the drift space is represented by $\begin{pmatrix} 1 & D \\ 0 & 1 \end{pmatrix}$ and the lens of focus f is approximated using the thin lens formalism by $\begin{pmatrix} 1 & 0 \\ -\frac{1}{f} & 1 \end{pmatrix}$

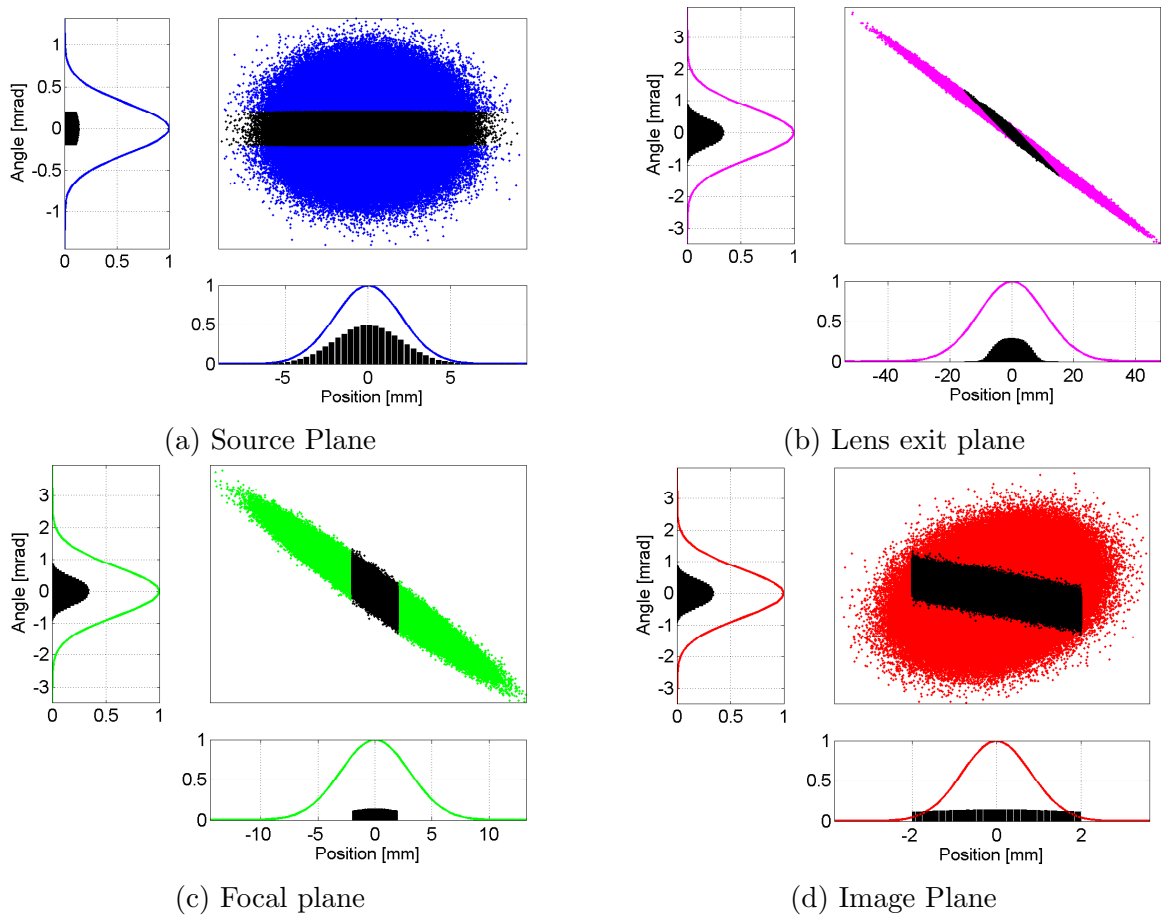


Figure 4.16: Tracking of an arbitrary photon phase space (position and angle) taken as a source, in a simplified optical system based on a single focusing element. Results denote that an angular selection at the source (black area in (a)) corresponds to a position selection at 1 focal length from the lens (black area in (c)).

Indeed, it is observed that, at a distance of one focal length from the focusing lens, the position selection (slit) corresponds to an angular selection at the source.

The LSF improves by reducing the slit opening, down to a slit aperture for which diffraction on the slit itself becomes dominant in the achievable resolution. This is evident from the simulation results of Fig. 4.17, where for different focus in the object plane (corresponding to different depths in the dipole) σ_{LSF} is plotted as function of the slit width. No difference is observed as the slit aperture decreases from 4 mm (no light cutting is taking place) down to ~ 2.5 mm implying a shorter source path. For smaller apertures, LSF broadening by diffraction dominates and results in the

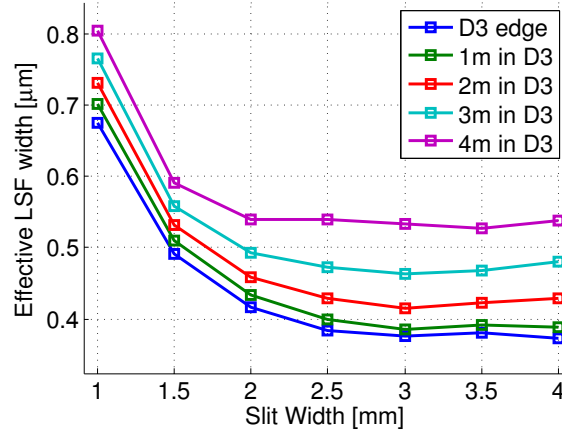


Figure 4.17: Probing the horizontal slit effect in terms of σ_{LSF} at 7 TeV and 400 nm.

increase of σ_{LSF} .

Therefore, no gain is expected in terms of the system resolution and the DOF will remain a limiting factor in the horizontal plane.

This is a very relevant result for assessing the ultimate system performances. Indeed, the analytical studies performed in the past for the BSRT design were suggesting the use of a slit [53] and only with these set of simulations including diffraction effects the slit usefulness could be assessed.

Reduction of diffraction by measuring at lower wavelengths

Since the diffraction¹ contribution to the LSF is wavelength dependent, reducing the imaging wavelength linearly reduces the width of the diffraction spot. The diffraction phenomena depends on the acceptance of the optical system and the light distribution within this aperture. The SR cone aperture is also wavelength dependent, thus motivating an extensive set of simulations to assess the effectiveness of shifting to a shorter wavelength.

Since SR is emitted in a broad spectrum, the choice of the new wavelength for imag-

¹ This section refers to the overall diffraction contribution on the imaging system, dominated by the SR small cone angle, i.e. it is totally independent of the diffraction on the slit discussed above. No slit is considered in these studies.

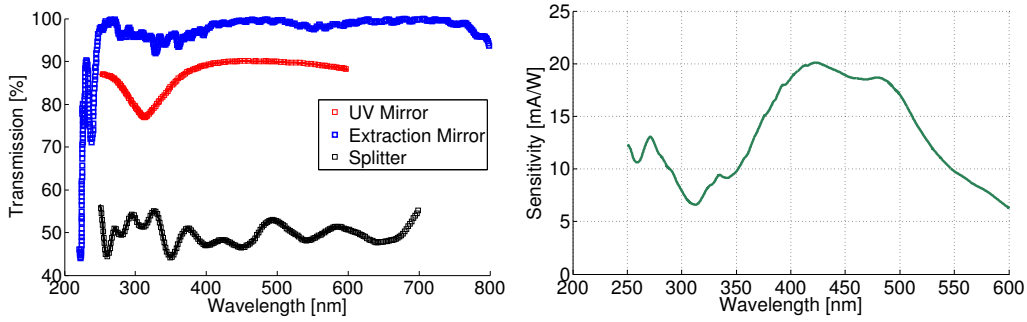


Figure 4.18: Sensitivity of the upgraded LHC imaging system based on refractive optics optimized from 250 nm operation (left) obtained as a convolution of the detector’s sensitivity and the transmission of the optical system (right).

ing at high energy was driven by the availability of the optical components (mirrors, lenses, splitters, filters, etc.).

After looking into literature and an extensive market survey, 250 nm was found to be the shortest wavelength available, therefore a new optical system was designed to cope with this change and will be described in details in Chapter 8. The spectral sensitivity of the new system, taking into account the transmission of the UV enhanced mirrors, splitters and the new intensifier photocathode, is shown in Fig. 4.18.

Compared to Fig. 4.5, a clear enhancement of the system response at 250 nm is observed allowing operation at such a low wavelength. A reduction of the system’s sensitivity, by a factor 4, is observed around 600 nm (central frequency of the emitted light from the undulator at 450 GeV). Such a reduction was judged acceptable and not limiting to the operation, since the intensity loss could be compensated by an additional gain of the intensifier.

Figure 4.19, compares the effective σ_{LSF} for the imaging system with lenses optimized for 400 nm with a similar one optimized for 250 nm. A clear benefit is obtained since a reduction of $\sim 15\%$ is observed for the lower wavelength scenario.

Reduction of diffraction by selecting the vertical polarization

As described in Chapter 2.2.1, SR from bending magnet is elliptically polarized outside the orbit plane. The horizontal and vertical polarization components are compared to the total polarization in Fig. 4.20. As it can be seen from the central plot,

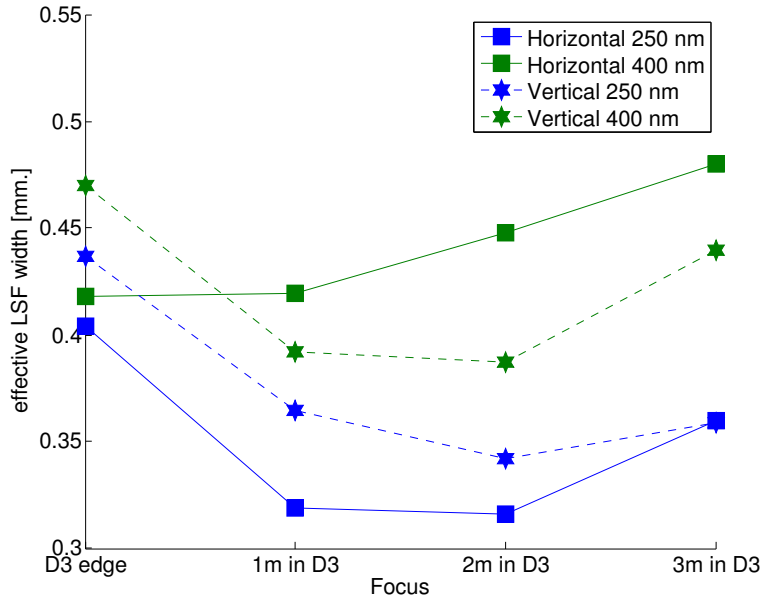


Figure 4.19: Effective LSF width at 7 TeV for the refractive optics based imaging system, compared at two wavelengths 400 and 250 nm.

selecting the vertical polarization results in imaging SR with an average wider angular distribution and an intensity drop to zero in the beam orbit plane. Therefore, a smaller contribution from diffraction is potentially expected, thus a narrower LSF.

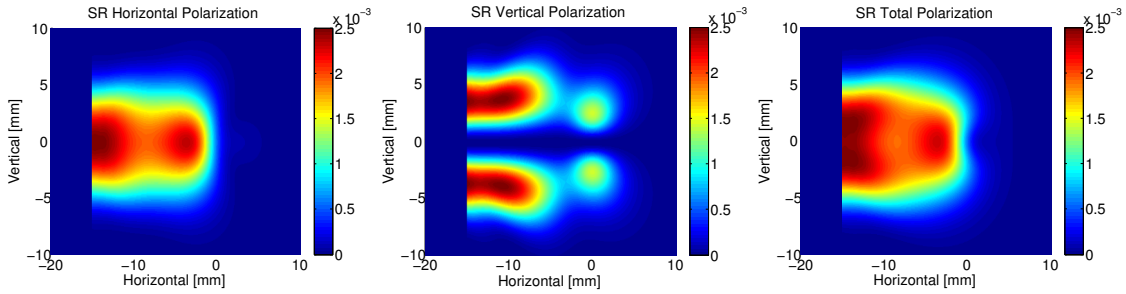


Figure 4.20: SR intensity distribution (H, V and total polarization) at the LHC extraction mirror at 7 TeV and 250 nm.

However, as shown in Fig. 4.21, the imaging simulation with the vertical polarization only resulted in a negligible improvement of less than $10 \mu\text{m}$ LSF width reduction. For this reason, also considering the complication of adding another optical element

(polarizer) with its imperfections, it was decided not to include such option in the new system.

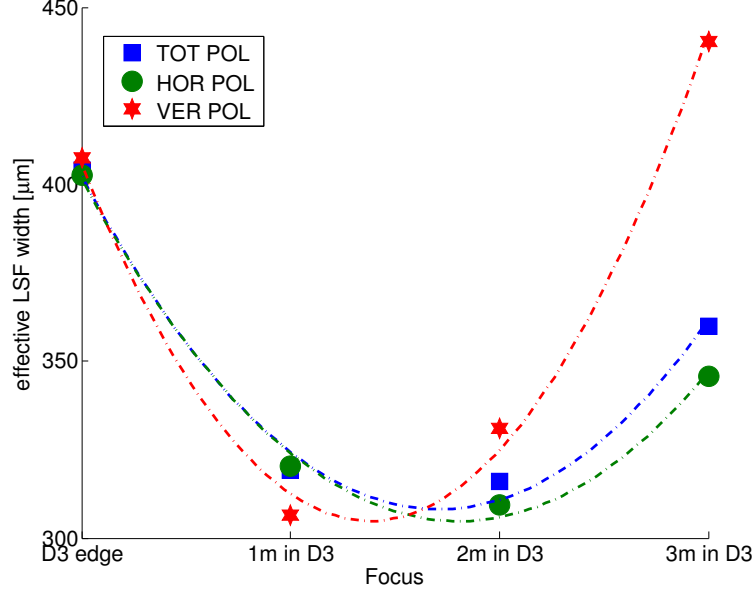


Figure 4.21: Comparing σ_{LSF} at 7 TeV and 250 nm for different SR polarization (horizontal, vertical and total) at different focus within the dipole.

Aberrations from optical surface imperfections

Shifting to lower wavelengths has the drawback of making the system more sensitive to the optical surface imperfections. Therefore, a special care must be taken in order to keep the aberrations contribution below the diffraction limit. This implies adopting optical elements (mirrors, lenses, splitters, filters) with high quality surface flatness. Since for the BSRT telescopes the extraction mirror (characterized by a special coating and subject to thermal cycles) has been identified as the most critical element, a set of simulations was performed by replacing its ideal reflective surface with the one that was measured via the “Fisau interferometer” [73] method (through measurement of the reflected wavefront error) for one of the mirrors, as shown in Fig. 4.22. The measured surface features a peak to valley deformation of ~ 170 nm ($\sim \lambda/2$ @250 nm).

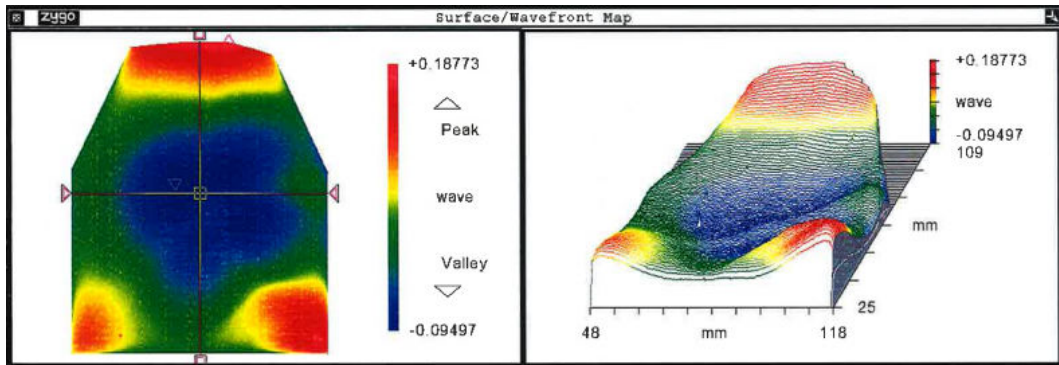


Figure 4.22: LHC extraction mirror flatness, measured via the “Fisau interferometer” technique by WZOPTICAG®.

The simulations were based on ray tracing and the results are shown in Fig. 4.23. As expected, passing from the ideal to the real mirror, the spot size increases from $10\mu\text{m}$ to $112\mu\text{m}$. Conversely, as shown in Fig. 4.24, no significant difference was

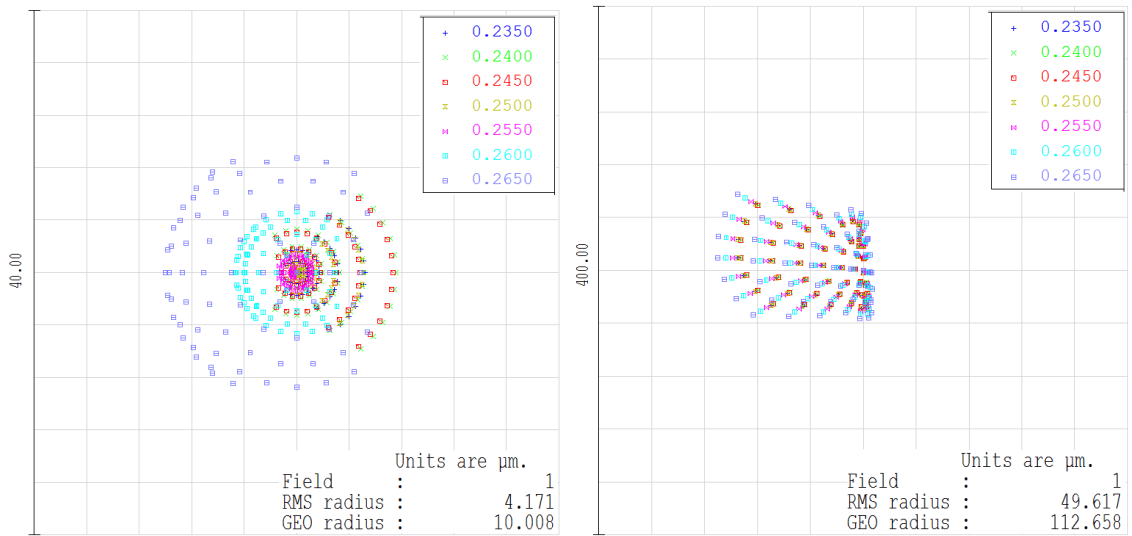


Figure 4.23: Spot diagram of the LHC refractive based imaging system at 250 nm for the ideal (left) and real (right) extraction mirror.

observed between the perfect and the real mirror in terms of LSF. This means that the aberrations, introduced by the not-perfect mirror, result in a LSF broadening that is in the shadow of the diffraction contribution.

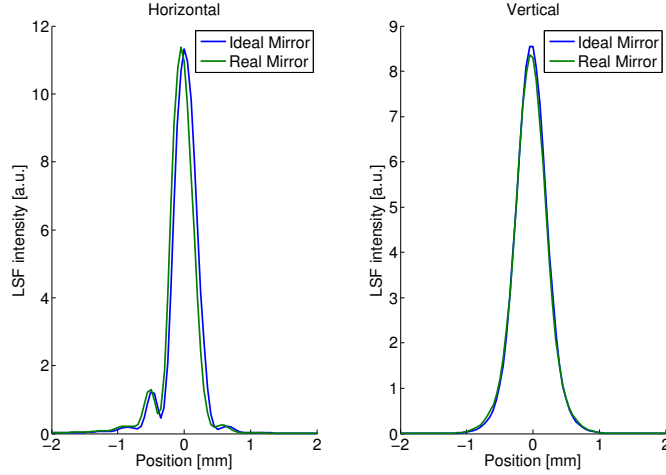


Figure 4.24: Comparing LSF at 7 TeV and 250 nm for the ideal (blue) and real (green) extraction mirror.

4.4.2 Imaging throughout the LHC ramp

For a continuous beam size monitoring during the LHC ramp, the knowledge of the LSF is needed at every energy. In addition, given the beneficial effect of shifting the imaging working point to lower wavelengths, one has to study the optimal beam energy, at which inserting the narrow band chromatic filter.

Figure 4.25 shows the energy of the extracted SR per proton per wavelength (in the detectable range 200-800 nm) as function of beam energy.

At injection energy, there is not enough light at low wavelengths and the imaging is performed over all the visible spectrum. Therefore, the total SR energy extracted to the telescope I_{INJ} (black dashed line in the figure) is obtained as a convolution of the system sensitivity (see Fig. 4.5) and the emitted SR energy spectrum.

Then, these simulations specify that the switching to a quasi-monochromatic imaging should take place around 2 TeV for 400 nm or 2.2 TeV for 250 nm, in order to have the amount of SR (in a narrow color filter of width ~ 15 nm) equal to I_{INJ} .

Accordingly, LSF calculations were performed along the energy ramp finding at each energy the minimum effective σ_{LSF} and the corresponding system focus. The energy of 2 TeV was taken as the transition energy for the color filter insertion.

A summary of the horizontal resolution as function of energy and focusing settings

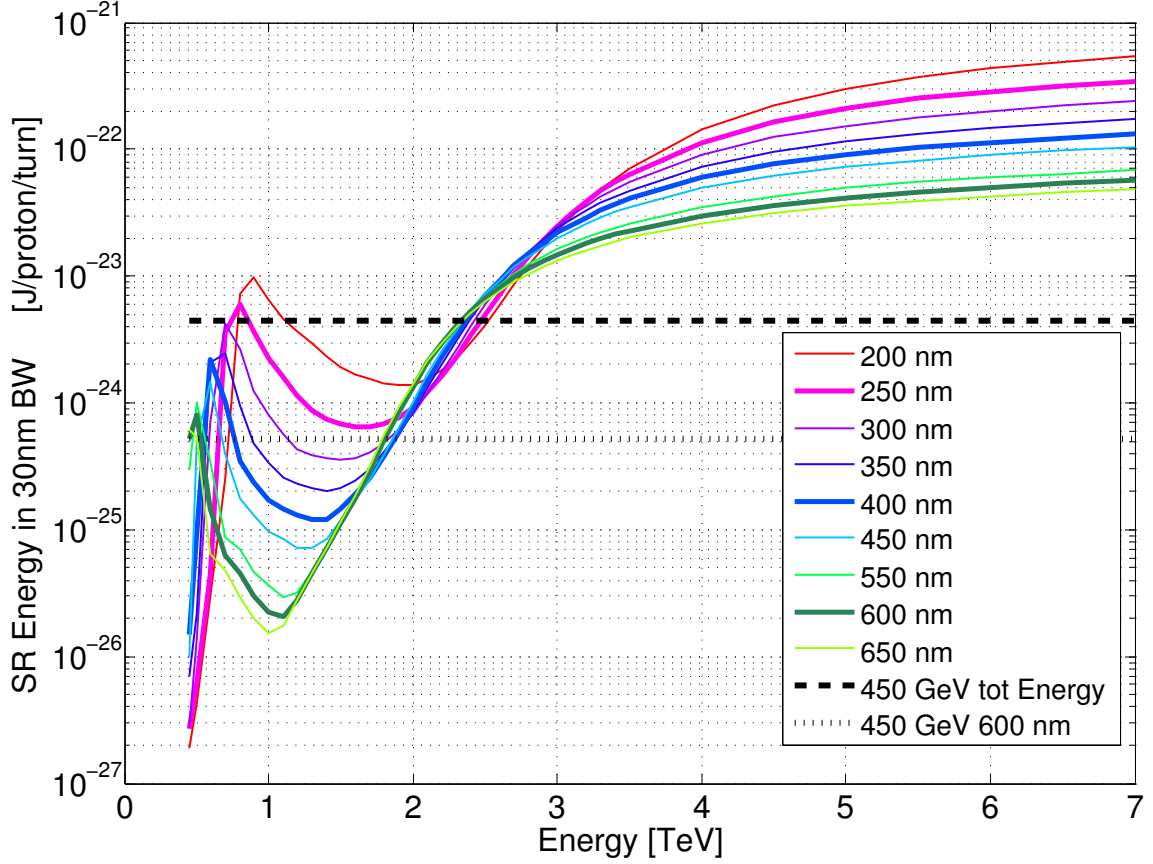


Figure 4.25: Extracted SR energy per proton per wavelength (in the detectable range 200–800 nm) as function of beam energy.

is shown in Fig. 4.26. These results will be fundamental for the re-commissioning, setting up and operation of the BSRT systems in 2015.

4.4.3 Limitation of the SR imaging in LHC

The most demanding challenge of the LHC SR monitors is to image beams with widths as low as $\sim 160\mu\text{m}$ at 7 TeV (see Table 3.1), in order to calculate the beam emittance with an error within 10%.

Recalling Eq. 4.4, the beam size at the BSRT is expressed as:

$$\sigma_{BSRT} = \sqrt{\sigma_{BSRT_{meas}}^2 - \sigma_{LSF}^2} \quad (4.5)$$

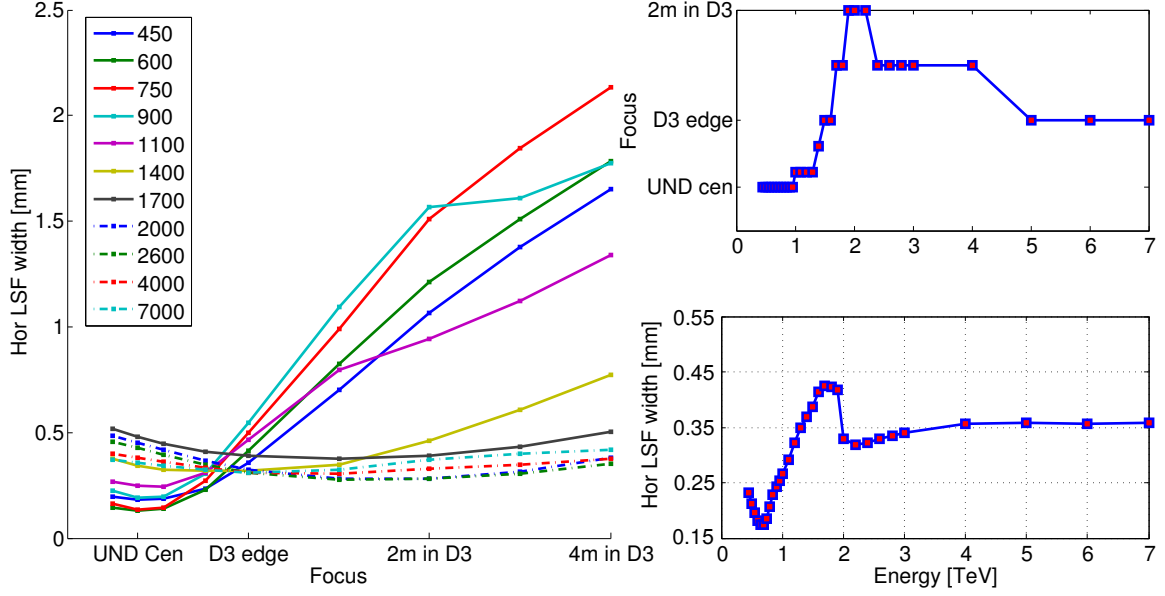


Figure 4.26: The horizontal resolution is studied along the LHC ramp for different focusing settings (left plot), to find the minimum σ_{LSF} (lower right plot) and the optimum focusing plane (top right plot) at every energy.

An intrinsic limitation originates from the error on the determination of σ_{LSF} (either experimentally or via simulations) and its impact on the emittance determination is obtained by the error propagation of Eq. 4.5:

$$\begin{aligned}
\epsilon_{\epsilon_{BSRT}} &= 2 \cdot \epsilon_{\sigma_{BSRT}} \\
&= 2 \cdot \frac{\Delta\sigma_{BSRT}}{\sigma_{BSRT}} \\
&= 2 \cdot \frac{1}{\sigma_{BSRT}} \left| \frac{\partial\sigma_{BSRT}}{\partial\sigma_{LSF}} \right| \Delta\sigma_{LSF} \\
&= 2 \cdot \frac{\sigma_{LSF}}{\sigma_{BSRT}} \left| \frac{\partial\sigma_{BSRT}}{\partial\sigma_{LSF}} \right| \epsilon_{\sigma_{LSF}} \\
&= 2 \cdot \frac{\sigma_{LSF}}{\sigma_{BSRT}} \frac{2\sigma_{LSF}}{2\sqrt{\sigma_{BSRT_{meas}}^2 - \sigma_{LSF}^2}} \epsilon_{\sigma_{LSF}} \\
&= 2 \cdot \left(\frac{\sigma_{LSF}}{\sigma_{BSRT}} \right)^2 \cdot \epsilon_{\sigma_{LSF}} \tag{4.6}
\end{aligned}$$

where $\epsilon_{\epsilon_{BSRT}}$ is the error on the emittance, σ_{BSRT} is the real beam size to be

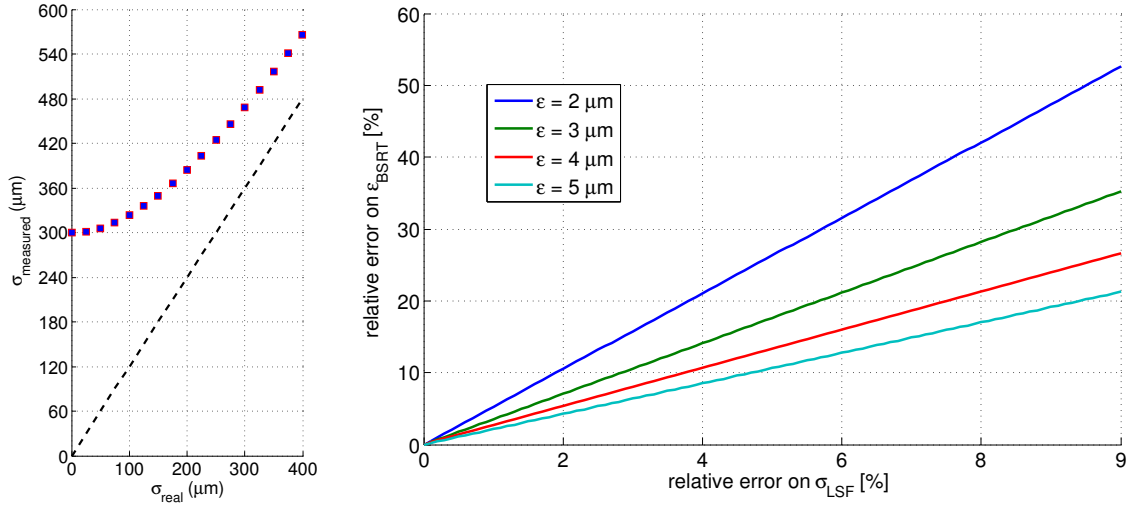


Figure 4.27: Relative error on the emittance determination in function of the uncertainty on the system's resolution for different emittances.

measured at the SR source and $\epsilon_{\sigma_{\text{LSF}}}$ is the error on the knowledge of the BSRT resolution. As shown in Fig. 4.27, the impact of the error amplification factor $\left(\frac{\sigma_{\text{LSF}}}{\sigma_{\text{BSRT}}}\right)^2$ is found very important and limiting for the small emittance case ($2 \mu\text{m}$), where the measurement uncertainty can reach $\sim 50\%$ for $\epsilon_{\sigma_{\text{LSF}}} = 10\%$.

Such an intrinsic limitation of the SR imaging system at 7 TeV, led us requesting a modification of the optical functions in IR4 at the profile monitors location. Even though the proposal was approved, an alternative (SR based) beam size measuring technique was studied and developed. It will be discussed in the next section.

4.5 SR interferometry for the LHC

The interferometry technique using visible SR for beam size measurement, described in 2.3.2, was found to be the best alternative to direct imaging. It allows the determination of the size of a spatially incoherent source by measuring the spatial distribution of the degree of coherence after propagation, with an achievable resolution of few μm . The method is based on the Van Cittert-Zernike theorem, which states that there is a Fourier transform relation between the intensity distribution of the incoherent object and the complex degree of coherence. The visibility of the interferogram fringes, using the intensities I_{max} at the peak of the interference fringe and I_{min} at its valley, is defined as:

$$V = \frac{I_{max} - I_{min}}{I_{max} + I_{min}} \quad (4.7)$$

It is convenient recalling Eq. 2.48, that describes the intensity of the interference pattern measured on the detector plane:

$$I(x) = I_0 \left[\text{sinc} \left(\frac{2\pi a}{\lambda_0 R} x \right) \right]^2 \cdot \left\{ 1 + |\Gamma| \cos \left(\frac{2\pi D}{\lambda_0 R} x + \phi \right) \right\} \quad (4.8)$$

where a is the half of the single slit width, D the separation between the two slits, λ_0 the wavelength of observation, I_0 the sum of the incoherent intensities from both slits, ϕ an arbitrary phase, R the distance from the lens to the detector plane and $|\Gamma|$ the modulus of the first order degree of mutual spatial coherence. The latter is strictly related to the beam size σ_{beam} , through:

$$\sigma_{beam} = \frac{\lambda_0 R_0}{\pi D} \sqrt{\frac{1}{2} \ln \frac{1}{|\Gamma|}} \quad (4.9)$$

Moreover, a good approximation of the fringe visibility is given by:

$$V = \frac{2\sqrt{I_1 \cdot I_2}}{I_1 + I_2} |\Gamma| \quad (4.10)$$

that reduces to $V = \Gamma$ when I_1 , the light passing through the first slit, and I_2 , the light passing through the second slit, are the same. Contrarily, any imbalance of the light intensities on the slit results in a decrease of visibility.

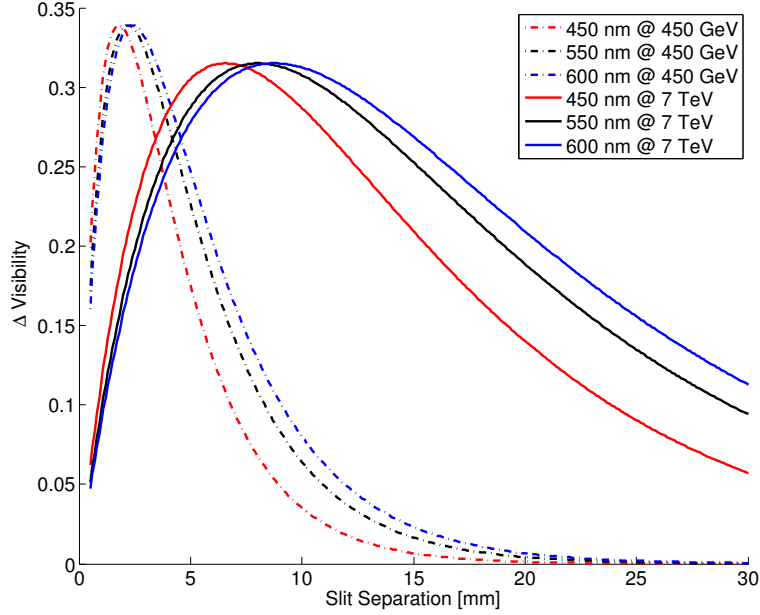


Figure 4.28: Visibility variation corresponding to emittance range to be measured in the LHC (at 450 GeV and 7 TeV) for different slit separations and wavelengths.

Taking into account the range of the beam sizes to be measured in the LHC at both energies (450 GeV and 7 TeV), corresponding to typical normalized emittances in the range $2\ \mu\text{m} \dots 0.5\ \mu\text{m}$, the combination of the wavelength λ_0 and the optimum slit separation D to be used in operation was chosen in order to maximize the variation of visibility ($V_{max}|_{\sigma_{min}} - V_{min}|_{\sigma_{max}}$).

As evident Fig. 4.28, the optimal working point at injection energy corresponds to a slit separation of few millimeters $\sim 2.5\ \text{mm}$, whereas at flattop energy, the optimal separation is $\sim 10\ \text{mm}$. Practically, the minimum slit separation achievable is dictated by mechanical limitations of the automated slit (described in Chapter 8) while the maximum separation value is limited by the available SR light at the slits plane (limited by the SR angular cut applied by the extraction mirror).

Recalling the SR power density versus energy (Fig. 4.4), since at injection only light from the undulator is available (500 nm to 800 nm) and at high energy more SR power is available in the NUV region, a good compromise for the choice of a fixed wavelength for interferometric measurement at both energies was found to be $\sim 550\ \text{nm}$.

In addition, in order to find the optimum visibility value, the uncertainty on the

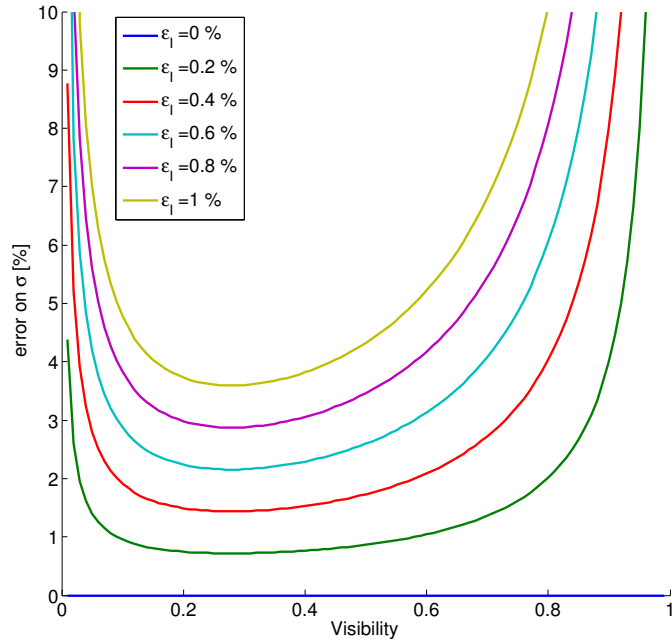


Figure 4.29: Relative error on the beam size determination in function of the visibility, calculated for different values of error on the measured pixel intensity.

beam size calculation (ϵ_σ) due to the error on the determination of the intensity of the CCD pixel (ϵ_I) was taken into account. Such an error is obtained from an error propagation of Eq. 4.7 and 4.9:

$$\epsilon_\sigma = -\epsilon_I \cdot \frac{\left(1 + \frac{1}{V}\right)}{\ln(V)} \quad (4.11)$$

This is graphically presented in Fig. 4.29, where ϵ_σ is calculated for different pixel intensity error values. A typical value of this error for the camera planned to be used is $\sim 0.6\%$ ¹. Nevertheless, this value is easily subject to increase when coupled to an intensifier, where in the process of the light conversion, additional errors are introduced.

The presence of an optimum range of visibilities (around $V=0.35$) where the error is

¹Since the photons detection by the CCD is a statistical process, the deviation in intensity (the number of photons recorded) found for each image follows the well known Poisson distribution. Considered to be the noise associated with the image ("shot noise"), the deviation will be plus or minus the square root of the signal intensity measured [74].

minimized, is clear.

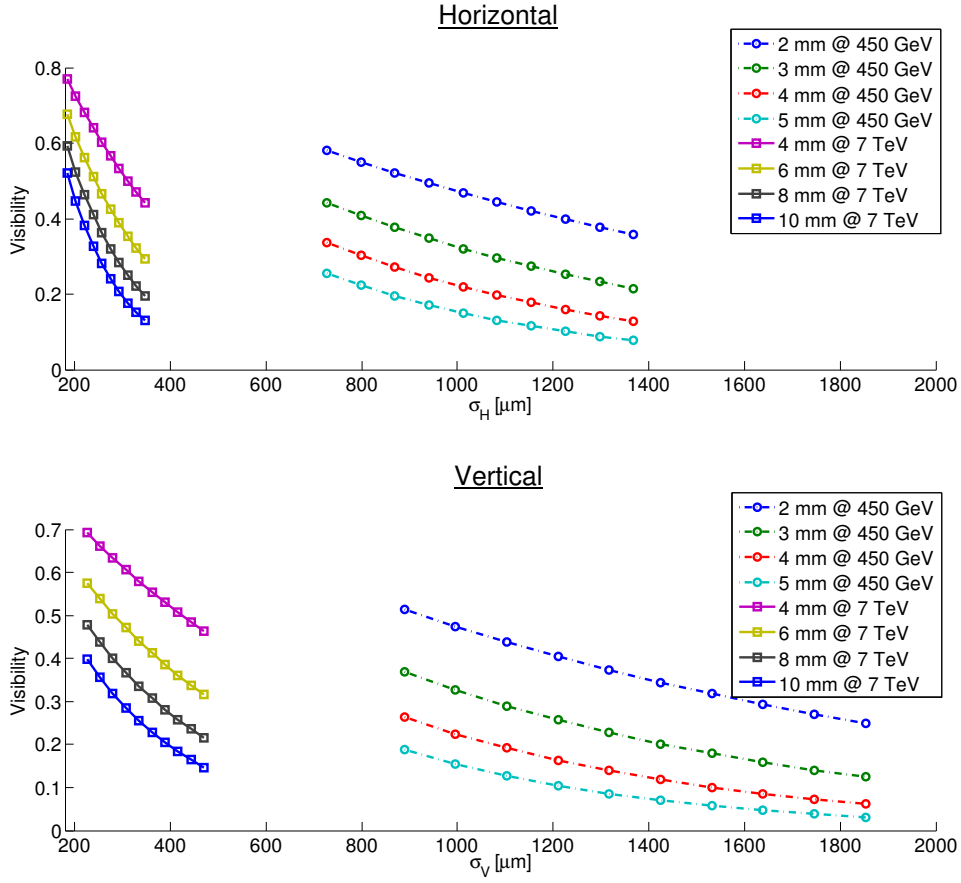


Figure 4.30: Interferometry fringe visibility as function of the beam size for various slit separation, shown for beam sizes corresponding to the emittance range of 2 to 5 μm at 450 GeV and 7 TeV.

Then, the optimum configuration of slit separation to be used compatibly with the range of the typical LHC emittance at both energies (450 GeV and 7 TeV) can be identified. Actually, Fig. 4.30, plotting the fringes visibility as function of the beam size for various slit separation, indicates $D_{INJ} \simeq 5\text{ mm}$ and $D_{FT} \simeq 10\text{ mm}$ as the optimal values respectively for injection and flattop energy.

In order to keep the error bars on the size measurement below the 5% level, rather than measuring the visibility according to Eq. 4.7, it is recommended to extract the value of $|\Gamma|$ from fitting Eq. 4.8 to the interferogram.

4.5.1 Simulated performance

For a typical interferometry system, sketched in Fig. 4.31, simulations were carried out to probe whether SR interferometry would allow calculation of the beam size by probing the spatial coherence of the light, checking the applicability of Van Cittert–Zernike theorem in its modified version for synchrotron radiation [48] for the LHC case.

In the following only the horizontal beam size¹ measurement is discussed, since it features the additional complexity of the non-uniform intensity distribution across the slits and the depth of field effect. Furthermore, the technique to calculate the interference pattern for finite size beam, explained in Section 4.1.3, was applied.

It has to be noted that in the following, only the horizontal² polarization of the SR will be used, since the polarization mix leads to a reduction of the visibility independent of the beam size variation.

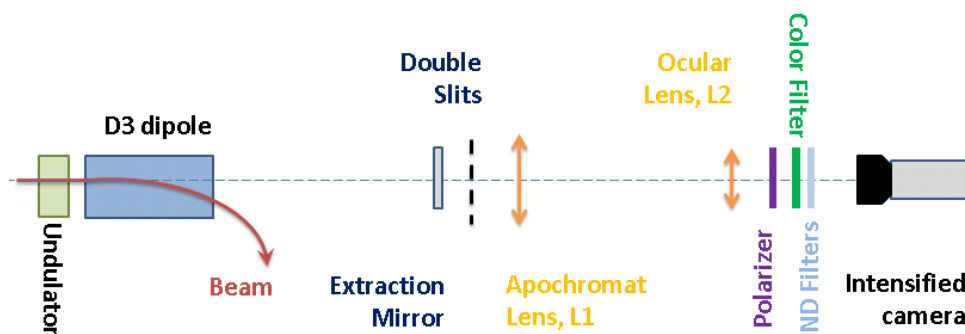


Figure 4.31: Typical optical system used for SR interferometry measurements.

Injection energy

The interference pattern of the sampled SR wavefront from a filament beam at the location of the camera was simulated for a double slit separation of 5 mm and width of 1 mm. As expected from Eq. 4.9 a maximum visibility is observed, as shown in

¹In proton machines and in particular the LHC, round beams are accelerated, whereas the horizontal and vertical normalized emittances are theoretically equal at injection.

²The choice of the horizontal polarization rather than the vertical one is mainly motivated by the intensity difference of the two.

Fig. 4.32.

Due to the small aperture (slits) of the interferometry system, different macro-

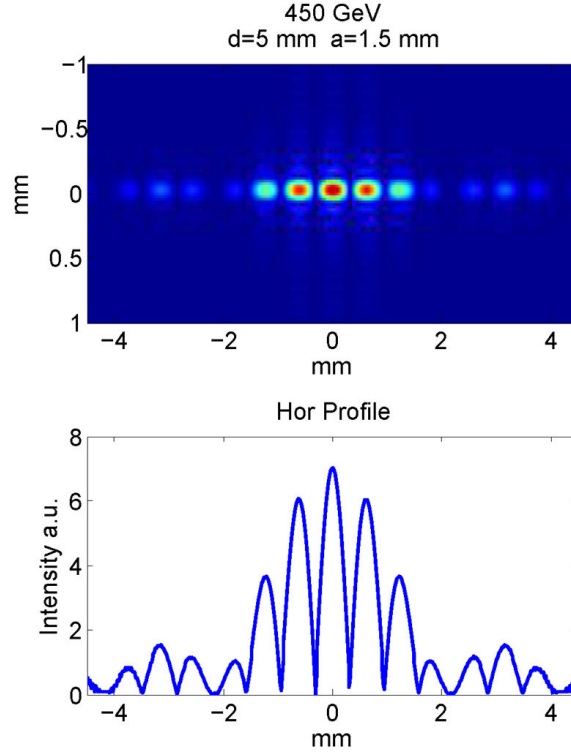


Figure 4.32: Interferometer LSF at 450 GeV at 550 nm, simulated for a slit separation 5 mm and 1 mm width.

particles in the phase space feature different LSF¹. Therefore, contrarily to the imaging technique, where the LSF is enough to characterize the system, the interferometry pattern in the image plane of a FBS can not be obtained by a simple convolution of the LSF with the beam distribution.

For this reason, as earlier explained, the "Reconstruction by extrapolation" technique will be used. Figure 4.33 shows the horizontal phase space of the protons at 450 GeV. Few reference macro-particles are selected and the corresponding LSFs were simulated. Some of the results are plotted in Fig. 4.34. Qualitatively, a dependency of the intensity and position of the fringe maximum on the position of the macro particle

¹A small intensity imbalance over the slits, caused by the variation of the SR cone direction, leads to a different visibility

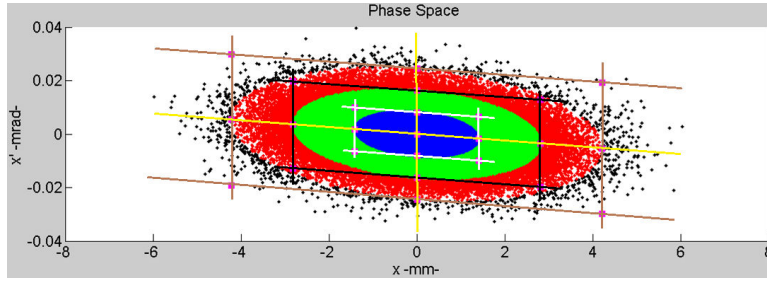


Figure 4.33: Reference macro-particles chosen from the horizontal phase space of the proton beam at 450 GeV.

in the phase space could be observed. In fact, as shown in Fig. 4.34, a linear fit describes the relative translation of the interferogram centroid tr_i while a parabolic fit was found suitable to describe the relative change of its intensity through an attenuation factor Att_i .

The resulting numerical model:

$$I_{part_i}(x) = Att_i \cdot I_{part_0}(x - tr_i) \quad (4.12)$$

allows predicting the SR intensity distribution I_{part_i} of every particle in phase space, where Att_i and tr_i are obtained for each particle based on its position and angle.

By populating the phase space with 10^5 protons uniformly distributed, the total interferometry pattern is obtained by summing the single interferograms weighted by beam size dependent weight functions.

The resulting interference fringes are shown for different beam sizes in Fig. 4.35.

The difference between the visibility change as function of the beam size, extracted from the simulation, and the theoretical values, calculated using Eq. 4.9, resulted to be smaller than 2%, as shown in Fig. 4.36. Such a good agreement is very important, since it validates this BFS technique, giving more confidence in its application for the high energy case.

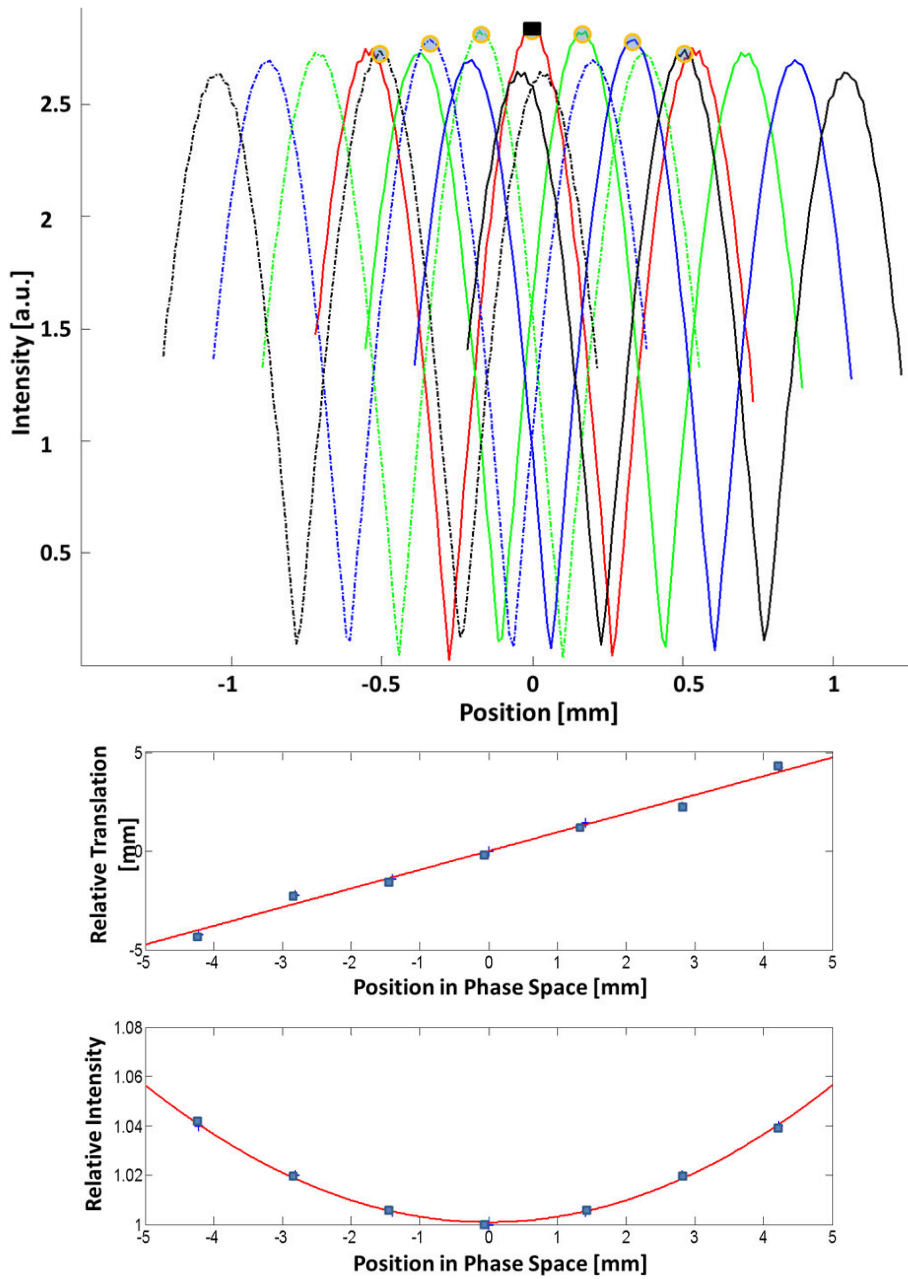


Figure 4.34: Interferogram of 7 reference particles at 450 GeV (top plot) showing a qualitative dependency of the pattern centroid with the position and angle of the macro-particle. A numerical model is found describing such a relation via a linear and a parabolic dependency as shown in the bottom plots.

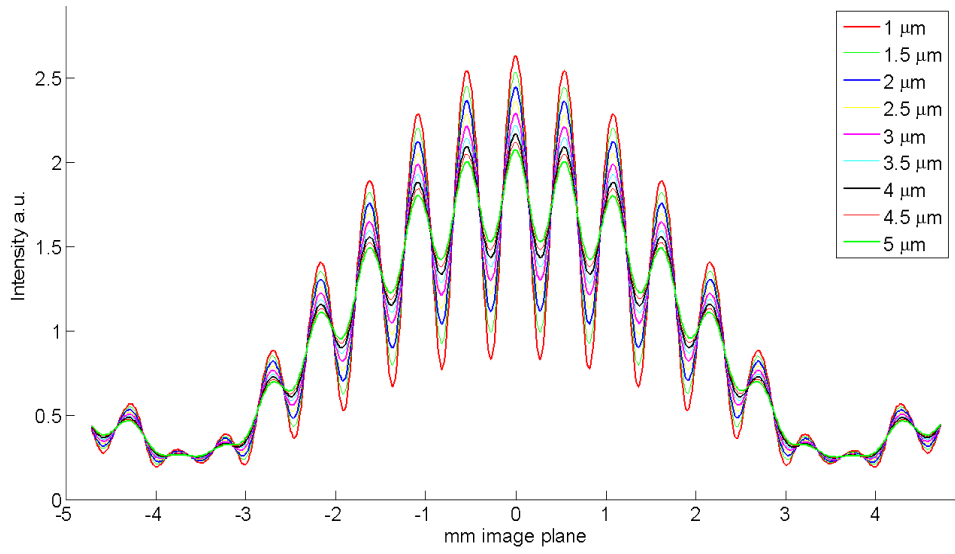


Figure 4.35: Interference fringes corresponding to different beam normalized emittances at 450 GeV in the LHC.

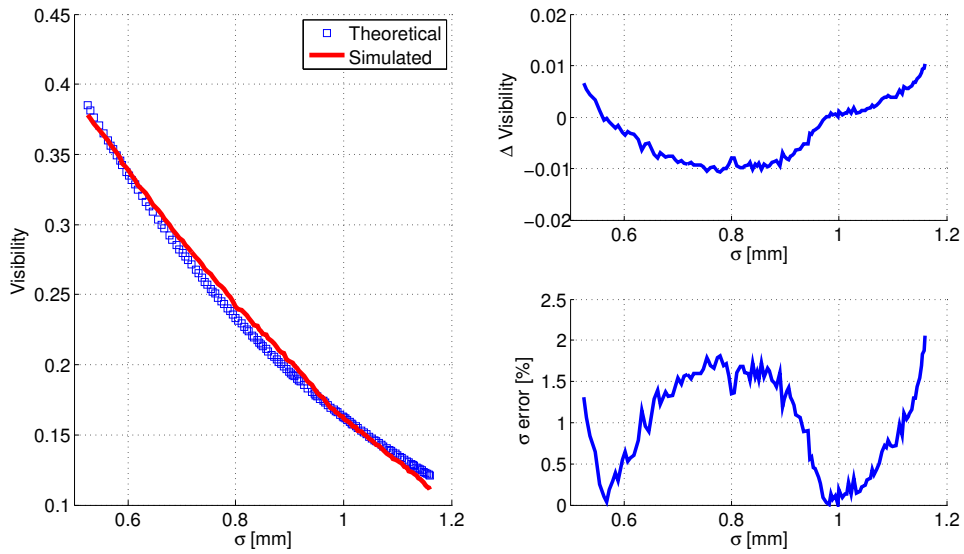


Figure 4.36: Comparison of the simulated visibility variation in function of the beam size with respect to the theoretic predictions (left plot). The absolute discrepancy is calculated (upper right plot) to be < 0.01 leading to an error in terms of beam size determination $< 2\%$.

Flattop energy

The interference pattern at 7 TeV, shown in Fig. 4.37, is expected to be substantially different from the one at 450 GeV. This is due to the different longitudinal extension of the source (60 cm undulator, ~ 4 m dipole), that results in a reduction of visibility at 7 TeV because of the incoherent depth of field effect.

In literature [48], this effect is quantified and the fringes visibility is corrected by the integration over the beam orbit:

$$\Gamma' = \iint \frac{2 \cdot \sqrt{I_1(\psi) \cdot I_2(\psi)}}{I_1(\psi) + I_2(\psi)} \cdot f[x - \rho \{1 - \cos(\psi)\}, \psi] \cdot g(\psi) \cdot \exp\left(-ikD \frac{x}{R_0}\right) d\psi dx \quad (4.13)$$

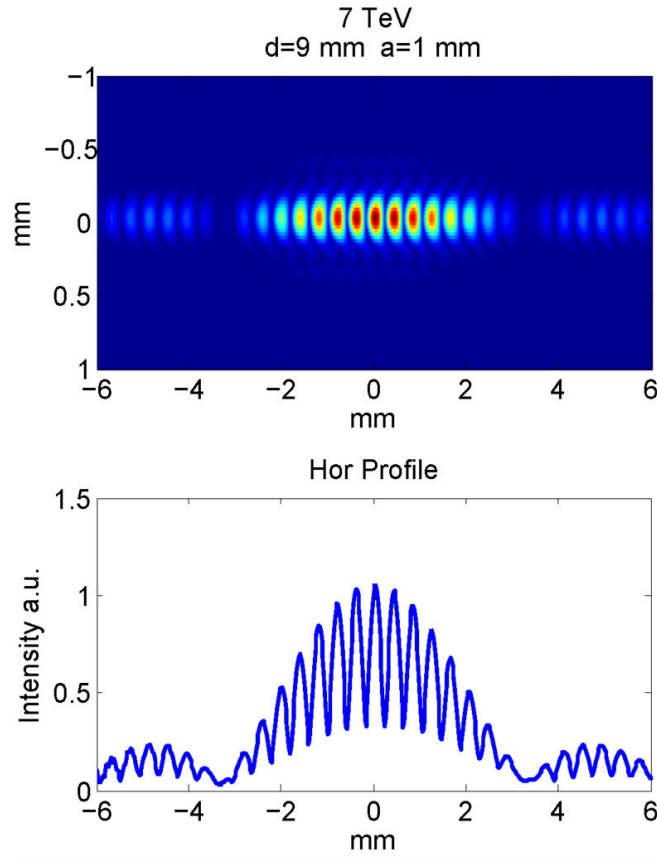


Figure 4.37: Interferometer LSF at 7 TeV at 550 nm, simulated for a slit separation 9 mm and 1 mm width.

with ψ being the bend angle in the dipole. This integration incorporates as well the intrinsic intensity imbalance, at each position in the orbit, caused by the finite opening angle of the SR and its direction change. However, Eq. 4.13 results limited for the LHC case since an additional factor has to be taken into account: the intensity imbalance originating from the edge effect. Approximation formulae for its calculation are not useful in this case, since the expected visibility is strictly related to the exact intensity illuminating both slits.

For this reason, simulating a FBS scenario was carried out. No numerical model predicting the LSF of every particle in the phase space was found, therefore the “Weighted uniform phase space sampling” technique was used.

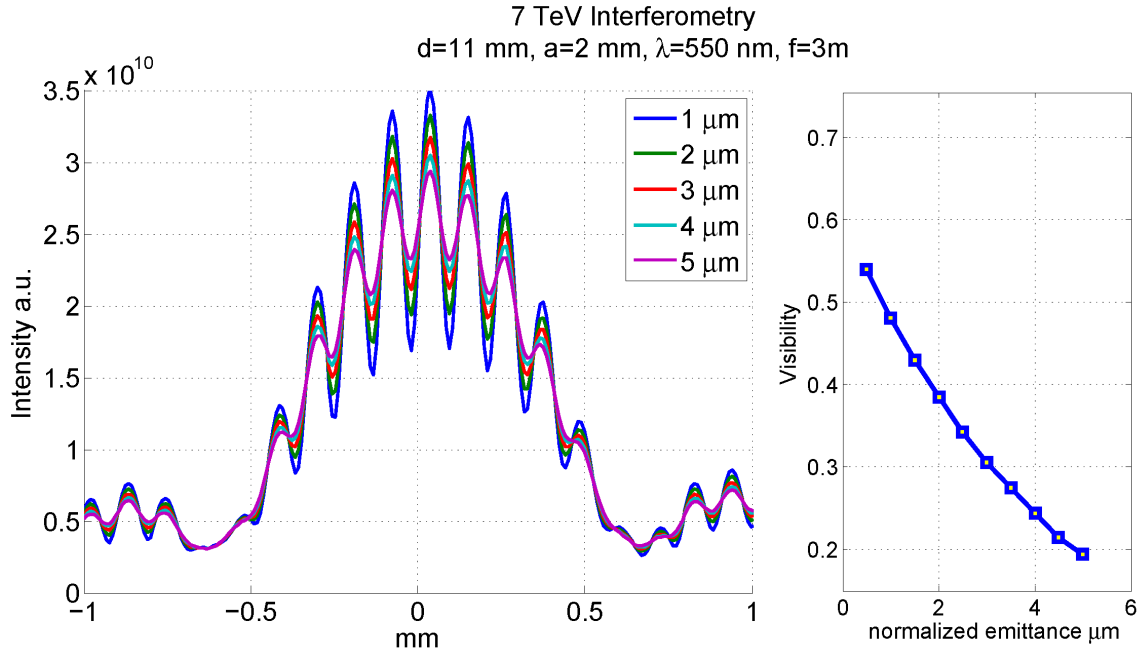


Figure 4.38: Interference fringes corresponding to different beam normalized emittances at 7 TeV in the LHC (for a slit separation 11 mm and width 2 mm) are shown in the left plot. The obtained curve mapping the visibility change in function of the emittance is given in the right plot.

The finite response of the interferometer of various beam sizes have been studied by summing the LSF of ~ 500 simulated macro-particles, weighted accordingly to the 2D multivariate normal distribution fitting the beam emittance. The resulting

interference patterns are shown in Fig. 4.38, where a calibration curve is obtained mapping the measured fringes visibility to the corresponding beam size.

4.5.2 Error sources and corrections

In addition to the error on the determination of the intensity of the CCD pixel (ϵ_I) (Eq. 4.11), other phenomena could result in a fringe visibility variation, not related directly to the beam size. On one hand, some (the floor vibration, beam jitter and detector non-linearity) could be neglected due to the stability of the machine and the performing digital CCD to be used in the “gated mode” over few turns of the LHC. On the other hand, other important factors need to be quantified and eventually corrected.

Chromatic effect correction

Equation 4.8 does not take into account the finite spectral acceptance of the interferometer, and assumes a monochromatic light. In practice, the wavelength is selected using a narrow band pass filter with a central frequency of 540 nm and a FWHM width ~ 10 nm.

For a different slit separation, the relative error committed when neglecting the *quasi-monochromatic* nature of the observed pattern is shown for various beam sizes in Fig. 4.39. However, the visibility reduction due to chromatic effects can be modeled as shown in Fig. 4.40, from which, given a beam size, a visibility adjustment (slit separation dependent) has to be applied before extracting the beam size itself. For the LHC case the correction is very small, but can become relevant for measuring smaller beam sizes (as will be shown in 5.3).

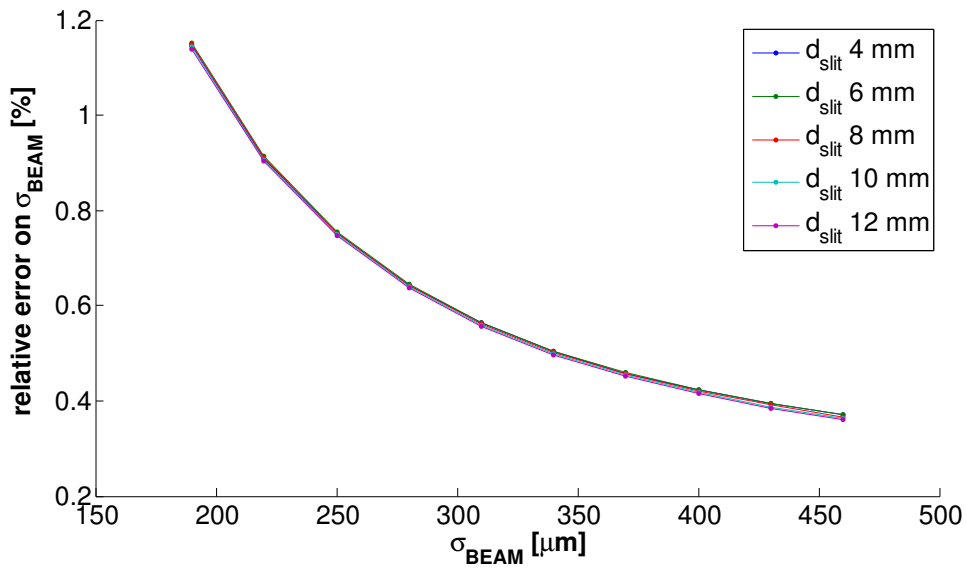


Figure 4.39: Relative error on beam size determination in function of the beam size (for different slits separation) when neglecting the finite spectral width of the color filter.

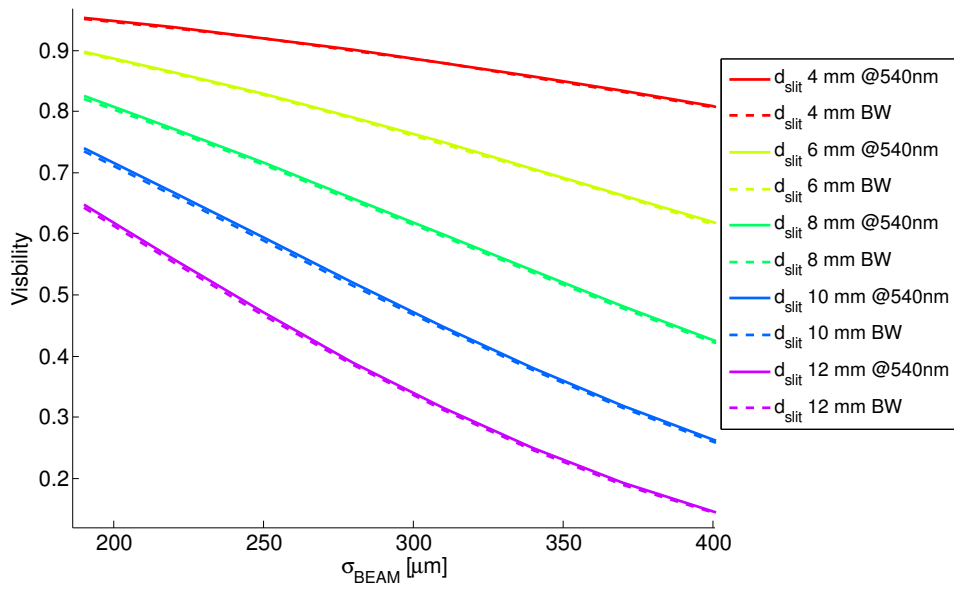


Figure 4.40: Visibility variation in function of beam size when assuming monochromatic light (solid line) or a quasi-monochromatic light (dashed line).

Apparent and real slit separation

As depicted in Fig. 4.41, any deformations of the extraction mirror, yield to an apparent double slit separation d_{meas} different from the effective d_0 .

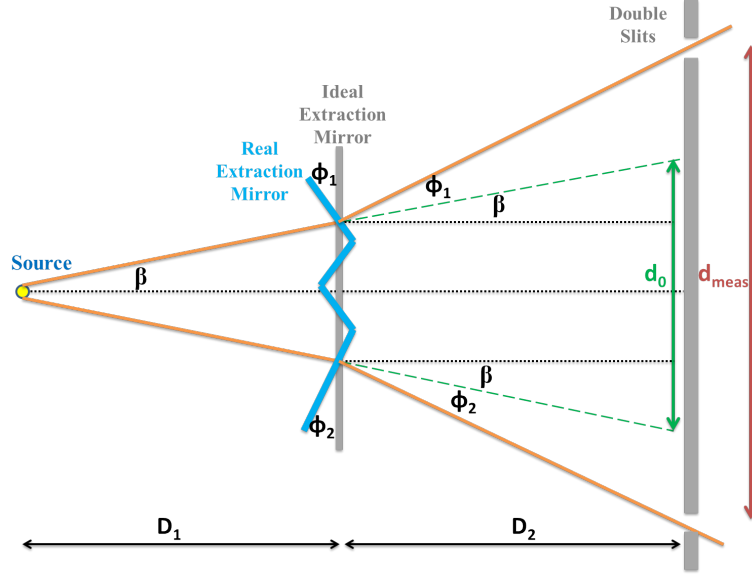


Figure 4.41: Sketch showing the effect of the extraction mirror surface deformation (Φ_1 , Φ_2) on the apparent slit separation.

The apparent slit separation depends on the distance from the source to the extraction mirror D_1 , the distance from the mirror to the double slits D_2 and on the surface tilt (Φ_1 and Φ_2) and it can be expressed as:

$$d_{meas} = 2D_1 \frac{d_0}{2(D_1 + D_2)} + D_2 \left[\tan \left(\text{atan} \left(\frac{d_0}{2(D_1 + D_2)} \right) + \Phi_1 \right) + \tan \left(\text{atan} \left(\frac{d_0}{2(D_1 + D_2)} \right) + \Phi_2 \right) \right] \quad (4.14)$$

where $d_0 = 2(D_1 + D_2)\tan(\beta)$.

This can be a severe limitation for the SR interferometer, since errors on the determination of the slit separation reflects directly into errors on determination of the beam size in Eq. 4.9. It follows that measuring the mirror surface deformations is of extreme importance.

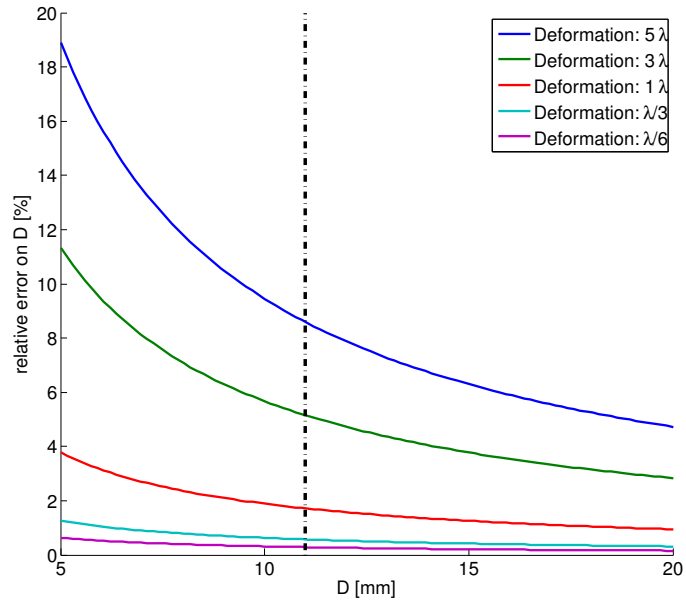


Figure 4.42: Relative error on the slit separation determination (and respectively on the beam size inferred value) for different separations, plotted for various deformations of the extraction mirror surface.

Figure 4.42 graphically represents Eq. 4.14, showing the error contribution from different deformations ($\Phi_1 = \Phi_2$). Even though the resulting error is within few percents at the operational separation of $D \sim 11$ mm, a space on the optical bench of the BSRT will be dedicated to measuring the mirror surface deformation via the "Hartmann-Mask technique" described in details in Chapter 8.

4.6 SPS source characterisation

The SR intensity distribution on the SPS extraction mirror at top energy (450 GeV) is shown in Fig. 4.43 for different wavelengths within the detectable range (200 – 800 nm). A clear interference pattern is shown across the wavelengths, resulting from the interference of the SR emitted from the consecutive magnet edges spaced by ~ 50 cm as described in Section 3.2.

In addition, Fig. 4.44 shows the calculated extracted power spectrum (integrated over the area of the extraction mirror) of the visible edge radiation. The simulations were carried out only for 3 energies along the SPS ramp (270, 405 and 450 GeV) for which the rise of the magnetic field of the bends, fundamental input for the simulation, were provided¹. The calculations show that the SR is mainly concentrated above 500 nm, giving a hint that the optical system must be optimized for near-infrared operation. The SPS SR intensity spectrum is compared to the spectrum of the SR emitted from the undulator in the LHC at injection energy in the left plot of Fig. 4.44. The right plot shows a comparison with the light emitted by the same bunch passing through the LHC undulator at injection resulting in very similar total extracted power at the SPS flattop.

It is relevant to note that the experience with the LHC undulator radiation, using the a similar optical system proposed for the SPS, has shown that, for these light intensities, it is possible to measure a single pilot bunch ($5 \cdot 10^9$ protons) in a single turn [75].

The total SPS SR energy per turn extracted at 270, 405 and 450 GeV, by integrating the SR spectrum over the detectable range, is plotted in Fig. 4.44. A linear trend is observed in the plane (proton Energy| $_{GeV}$, SR Energy| $_{dB}$) with a slope ~ 0.0165 , resulting in a scaling of the the total extracted SR with E_{GeV}^{13} . In addition, Fig. 4.45 shows the light intensity integrated over all the range 200–800 nm on the extraction mirror. The width of both horizontal and vertical distributions is ~ 10 mm at a distance of ~ 14 m from the source, thus corresponding to a smaller opening angle than the classical $1/\gamma$ by a factor of ~ 2.5 .

¹The magnetic description used is obtained from the OPERA ®software and compared to magnetic measurements carried out by experts.

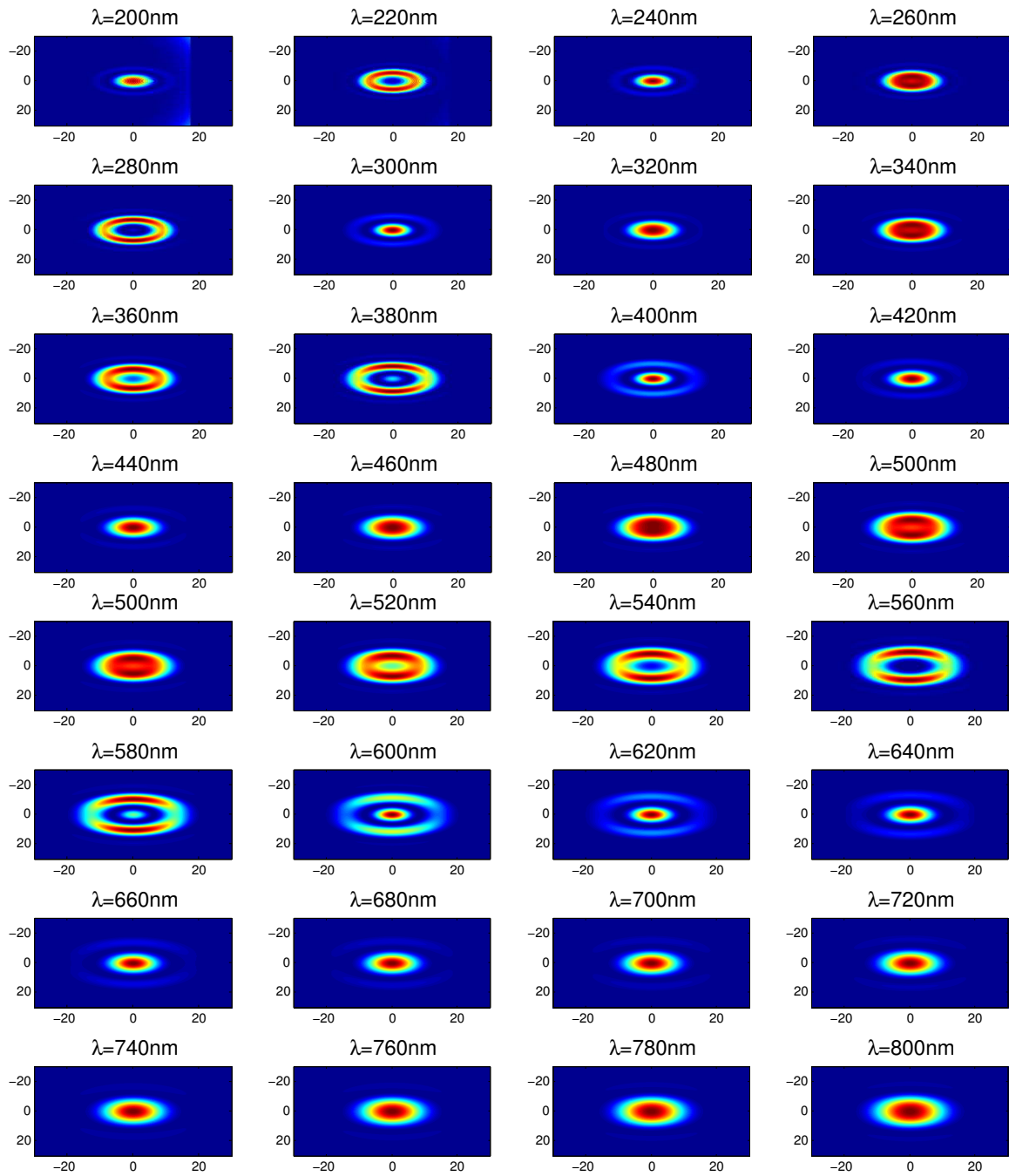


Figure 4.43: SR intensity distribution (a.u.) on the SPS extraction mirror at top energy (450 GeV) for several wavelengths covering the detectable range (200– 800 nm).

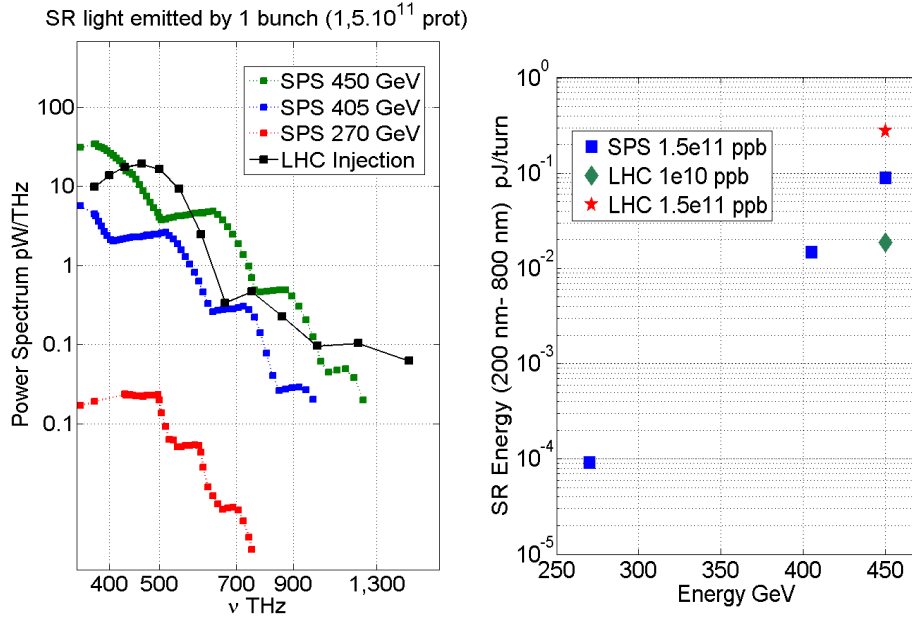


Figure 4.44: On one hand SR power spectrum, integrated over the extraction mirror area, is shown for 3 energies (270, 405, 450 GeV). Additionally, the LHC power spectrum emitted by the undulator is shown for comparison (left). On the other hand, the integrated energy per turn over the detectable range in function of the beam energy is shown in the right plot.

4.7 Performance of the SPS SR imaging system

As described in Section 3.2.3, a two stage focusing optical system based on apochromat lenses is proposed for SR imaging in the SPS.

The system features 3 silver protected mirrors, that direct the light to the optical bench. Then, an apochromat lens of focal $f_1 = 800$ mm is used to form an intermediate image, zoomed later with an ocular lens of focal length $f_2 = 18$ mm forming the final image on the intensified gated CCD described in Section 3.1.4. The optical elements light transmission, convoluted with the sensitivity of the type-N cathode mounted on the CCD, gives the final system spectral sensitivity, shown in Fig. 4.46. Accordingly, the convolution of the simulated LSF at different wavelength with the system sensitivity results in the total LSF of the monitor, shown in Fig. 4.47, while focusing in the center of the gap between the two magnets. A Gaussian fit is ap-

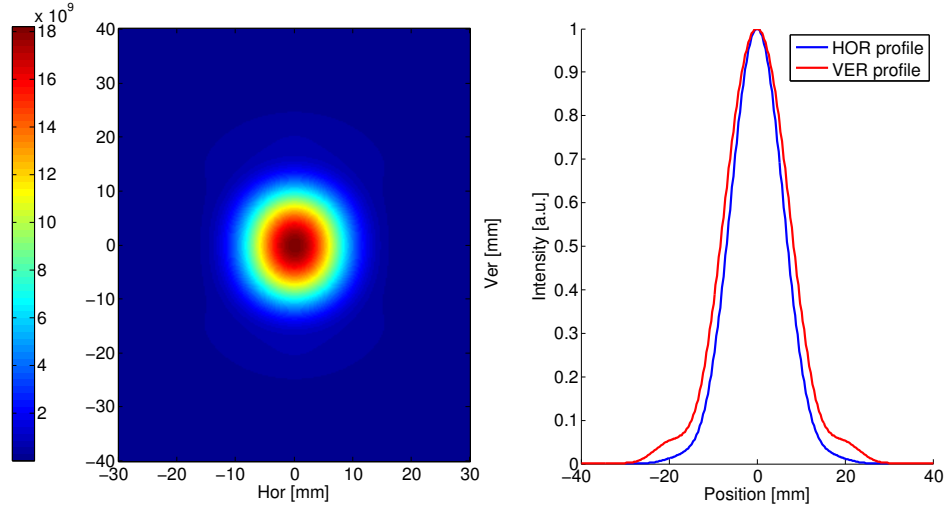


Figure 4.45: SR intensity distribution on the extraction mirror emitted by a filament beam in the range of 200– 800 nm.

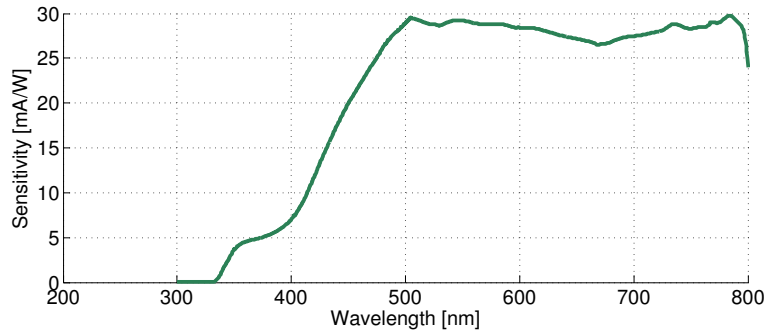


Figure 4.46: Sensitivity of the SPS imaging system obtained as a convolution of the detector’s sensitivity and the transmission of the optical system.

plied to the obtained horizontal and vertical LSF, resulting in a width of 211 μm and 205 μm respectively.

Such an approximation, was checked through the effective σ_{LSF} , earlier introduced in Section 4.3.1. Assuming typical normalized emittances (1.5 μm – 5 μm), the LSF was convoluted with various beam sizes and the effective σ_{LSF} is extracted according to the quadrature correction of Eq. 4.4. The results are shown in Fig. 4.48, where a slight dependency on the beam size is observed. By choosing the mean values

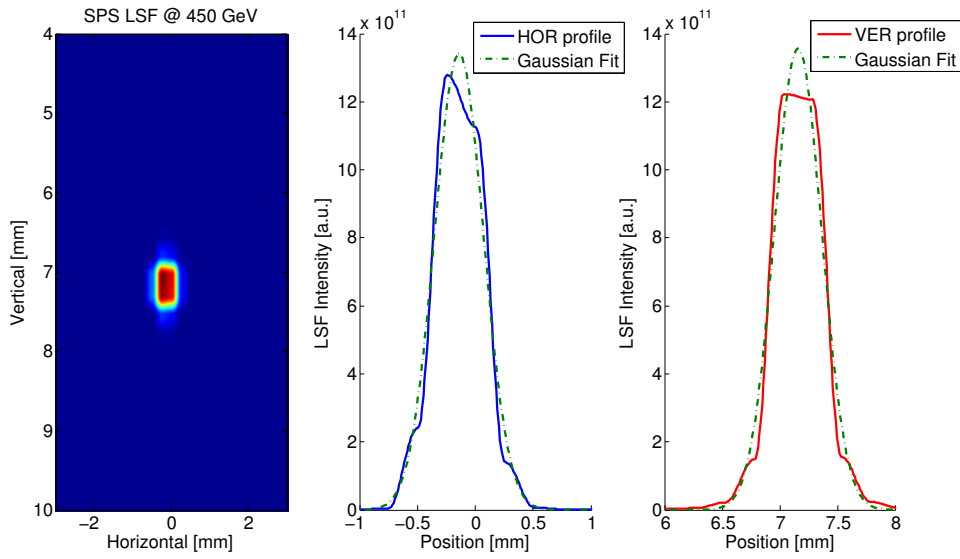


Figure 4.47: Total LSF of the SPS imaging system at 450 GeV integrated over the detectable range, convoluted with the system sensitivity.

($\sigma_{LSFH}=219\ \mu\text{m}$ and $\sigma_{LSFV}=209\ \mu\text{m}$) as the quadratic correction factors to be used over all the beam size ranges, the maximum error committed, $\epsilon_{\sigma_{LSF}}$, amounts to $\sim 1.75\%$ in the horizontal plane and $\sim 1\%$ in the vertical. According to Eq. 4.6, both will result in a sub-percent beam size measurement error.

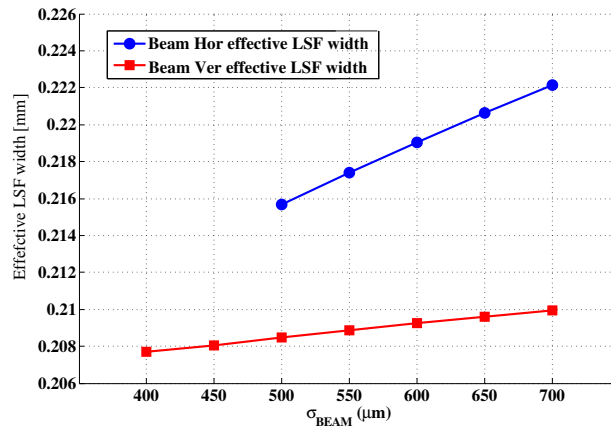


Figure 4.48: SPS horizontal and vertical effective σ_{LSF} in function of the beam size at 450 GeV.

Chapter 5

Beam Measurements

The core experimental part of this thesis work consisted in beam based measurements at the CERN SPS and LHC accelerators and at the ALBA synchrotron radiation source in Barcelona, Spain.

Concerning the SR source characterization in the SPS and the LHC, dedicated experiments were carried out to validate SRW simulations, reported in Chapter 4, either qualitatively (LHC) and quantitatively (SPS).

Considering the SR imaging in the LHC, experiments aimed at first to validate the LSF simulations described in Chapter 4, thus assessing the performance of the upgrades, described in Chapter 3, that the SR monitors at CERN went through. To estimate their relative and absolute accuracy, the LHC systems' results were then compared to the wire scanner monitors (that are considered as a reference) and the beam sizes de-convoluted from the LHC luminosity measurements.

At the ALBA synchrotron, a series of interferometry measurements were taken in order to validate the simulations described in Chapter 4 for the LHC case.

5.1 SR source observations

5.1.1 SPS

Following the refurbishment of the SR monitor in the SPS, observations of the extracted light from the first proton beams injected in the ring in October 2014, after

the CERN complex Long Shutdown, are presented in this section.

By the mean of the gated intensified Proxitronic camera described in Section 3.1.4, light emitted from 1 out of 12 bunches accelerated in the SPS up to 450 GeV was observed. The experimental conditions can be summarized as:

- mean bunch intensity $\sim 10^{11}$ protons;
- no neutral density or bandpass filter used;
- CCD acquisition at 50 Hz and intensifier gating at ~ 200 Hz, therefore every CCD frame images 4 SPS turns of the proton bunch;
- intensifier voltage set to a "safe" value, corresponding to a gain allowing the measurement of the maximum light intensity emitted at top energy, avoiding the CCD saturation.

Under these conditions, the signal to noise ratio was enough to allow profile measurement starting from the energy of 385 GeV. Figure 5.1 presents snapshots of the imaged SR during the ramp; it is worth noting that the light spot position on the CCD reflects directly (through the system magnification) the beam displacement since no automatic steering mechanism to compensate for any source shift was available.

The optical system was qualified in terms of focus and magnification using the dedicated calibration target BSRF. The magnification was measured by analysing the acquired target images, while performing a scan of the focusing lens position and the CCD position. This was possible after developing a dedicated (off-line) software capable of analyzing the acquired target image (Fig. 5.2a) and calculating the corresponding CCD pixel size in the object plane for several lens and camera positions, as plotted in Fig. 5.2b. For the nominal (focusing between the two edges) lens and CCD position, as by design in Zemax, the measured magnifications were found to be 0.0671 in the horizontal and 0.0733 in the vertical plane.

In addition to the qualitative intensity observation, an attempt to validate quantitatively the simulated SR intensity was carried out. The intensity was calculated by integrating the fitted Gaussian profile of the CCD frames acquired at 25 Hz, corresponding to a momentum increase of ~ 3 GeV per frame. The results are presented in Fig. 5.3, where the intensity was obtained by integration over both the horizontal

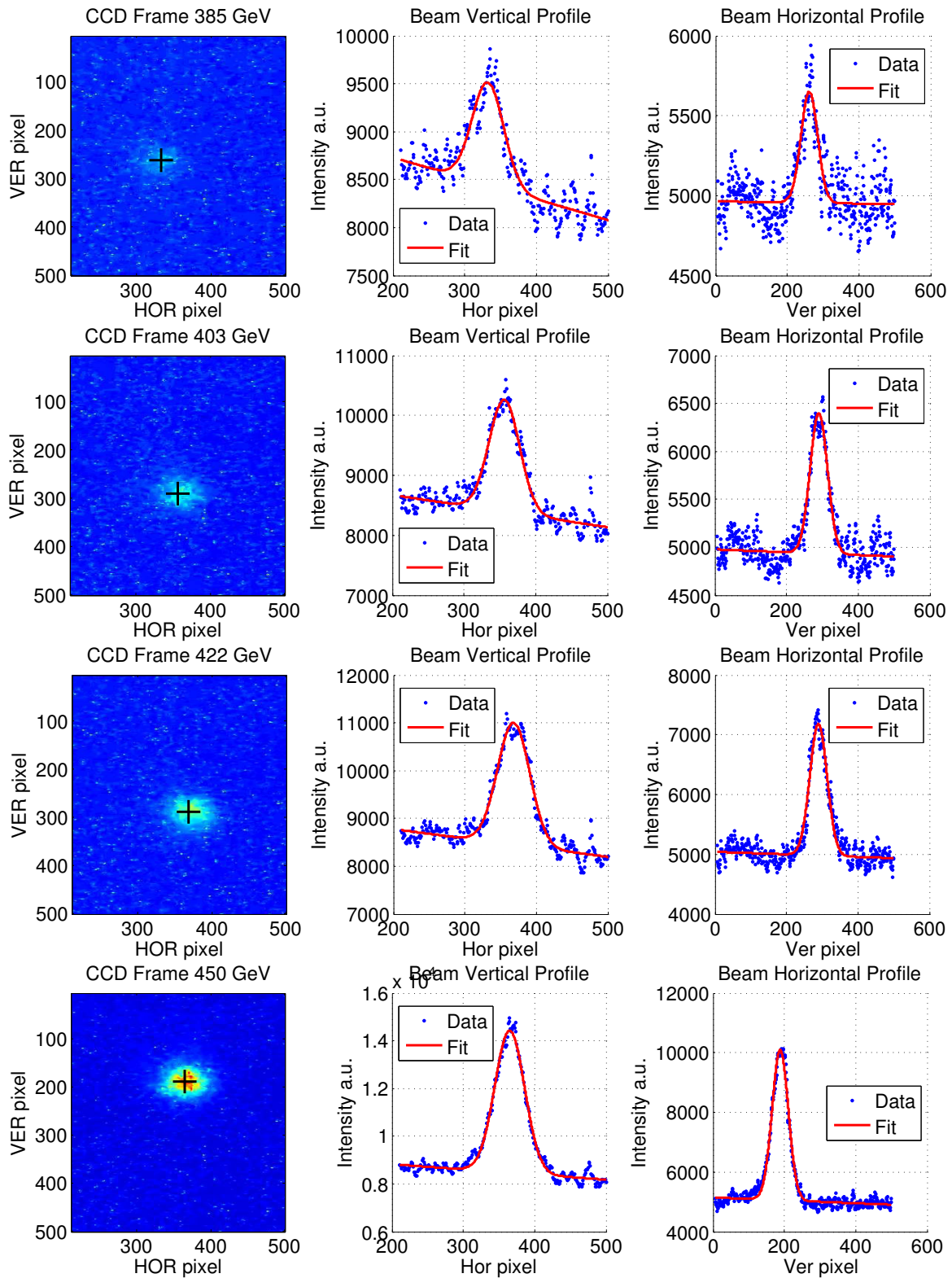
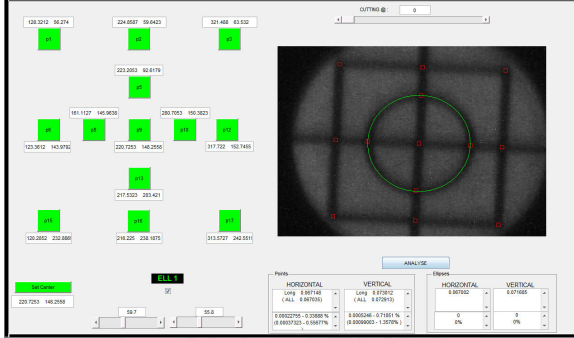
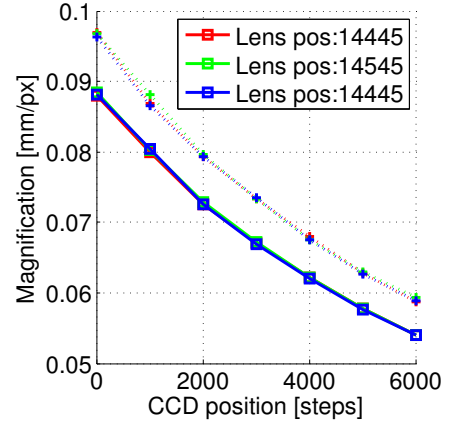


Figure 5.1: Imaged SPS SR light for a bunch of $\sim 10^{11}$ protons over 4 SPS turns along the energy ramp.



(a) Automated software calculating the magnification of captured SPS target images.



(b) Horizontal and vertical magnification of the SPS imaging system for different zoom configurations.

Figure 5.2: Calibration of the SPS imaging system.

(blue curve) and the vertical (red curve) measured profiles. The shaded areas represents the standard deviations of the plotted means over several ramps.

The dashed vertical line delimits the end of the ramp and the start of the short flat-top at 450 GeV lasting ~ 0.5 s, the dotted vertical line corresponds to the energy of 400 GeV.

Comparing the energy dependence of the extracted SR intensity with what simulated in Section 4.6, a best fit (black curve) of the measured intensity increase indicates a dependency on γ^{11} found to be in a reasonable agreement with the simulated behaviour following γ^{13} .

At 450 GeV the horizontal blue line corresponds to $I_{meas@450}$, the mean measured light intensity on the CCD (in arbitrary units). Based on Section 4.6, g is defined as the ratio between the simulated SPS source light intensity at 450 GeV ($I_{sim@450}$) and 400 GeV ($I_{sim@400}$). Consequently, this ratio is applied to $I_{meas@450}$ and the value $g \cdot I_{meas@450}$ (green horizontal line) is compared to the measured value $I_{meas@400}$. This comparison validates in term of relative SR light the source simulations presented in Chapter 4. The agreement is found to be within $\sim 15\%$.

Another set of measurements was dedicated to determine the lowest energy during the ramp when imaging is possible. This was done by setting the intensifier gain

close to its maximum value and turning off the detector before the end of the ramp, avoiding its saturation. The machine was filled with a total intensity of $\sim 2 \cdot 10^{12}$ protons and the camera was set to accumulate, in every frame, the SR from the total beam integrated over 4 turns of the accelerator. As shown in Fig. 5.4, profiles were reconstructed and fitted already at the energy of ~ 290 GeV.

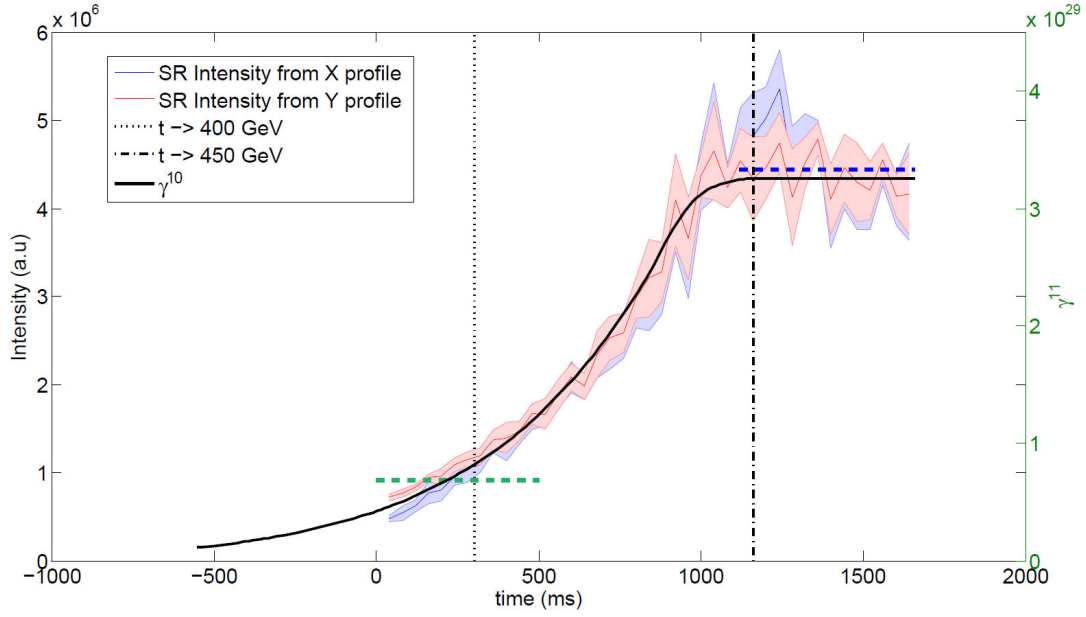


Figure 5.3: Measured SR intensity emitted by a bunch of 10^{11} protons over 4 turns during the SPS energy ramp.

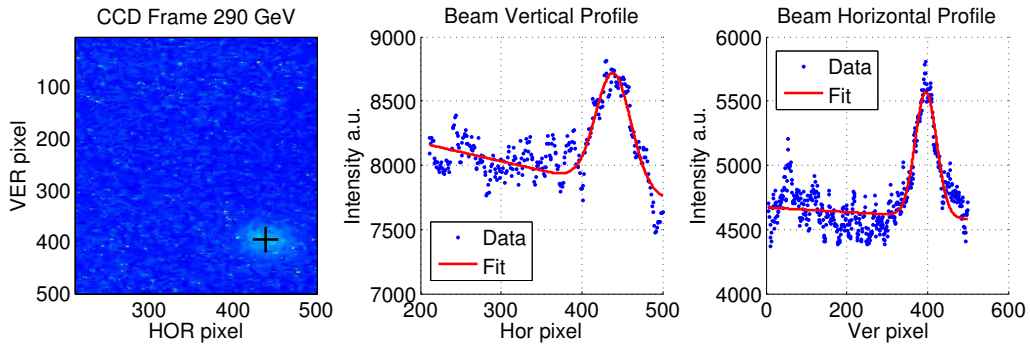


Figure 5.4: Imaged SPS SR light of 24 bunches at the Energy of 290 GeV integrated over 4 SPS turns.

5.1.2 LHC

In this section, only a qualitative observation of the LHC SR sources is presented, whereas quantitative comparison of the source with respect to the simulations can be found in [75].

Following the BSRT steering problems described in Chapter 6.2.1, an additional CCD was installed on the optical bench. Mounted on a translation stage, during the extraction mirror monitoring, the CCD was moved in the SR beam path, intercepting the light just after the steering mirror. The extraction mirror deteriorated coating shown in Fig. 6.7c, caused by the beam induced heating, acted as a light diffuser allowing the CCD to image the light distribution on the extraction mirror itself through the steering mirror.

Since the mirror is located at 26 m from the SR source, this light intensity distribution corresponds to the SR angular distribution simulated in Chapter 4.

In order to compare snapshots from this monitoring CCD to the simulations, the latter have to be convoluted with the spectral acceptance of the extraction-steering mirrors and of the CCD detector (see Fig. 5.5). The experiment result is shown in

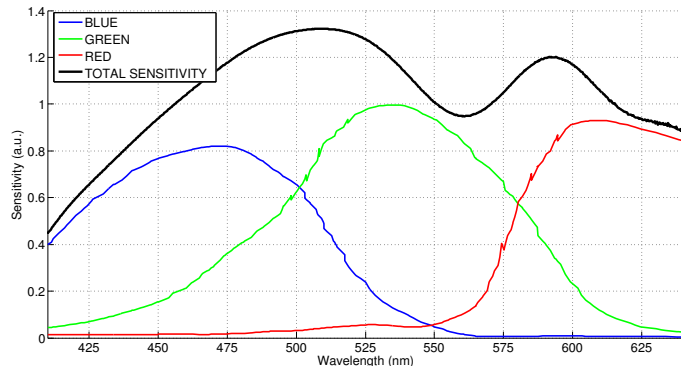


Figure 5.5: Spectral sensitivity of the LHC extraction mirror monitoring CCD [5].

Fig. 5.6 at particular energies within the LHC ramp, where the visible SR characteristics radically changes and its source shifts from the undulator to the dipole.

The qualitative agreement between observations and simulations is remarkable. The

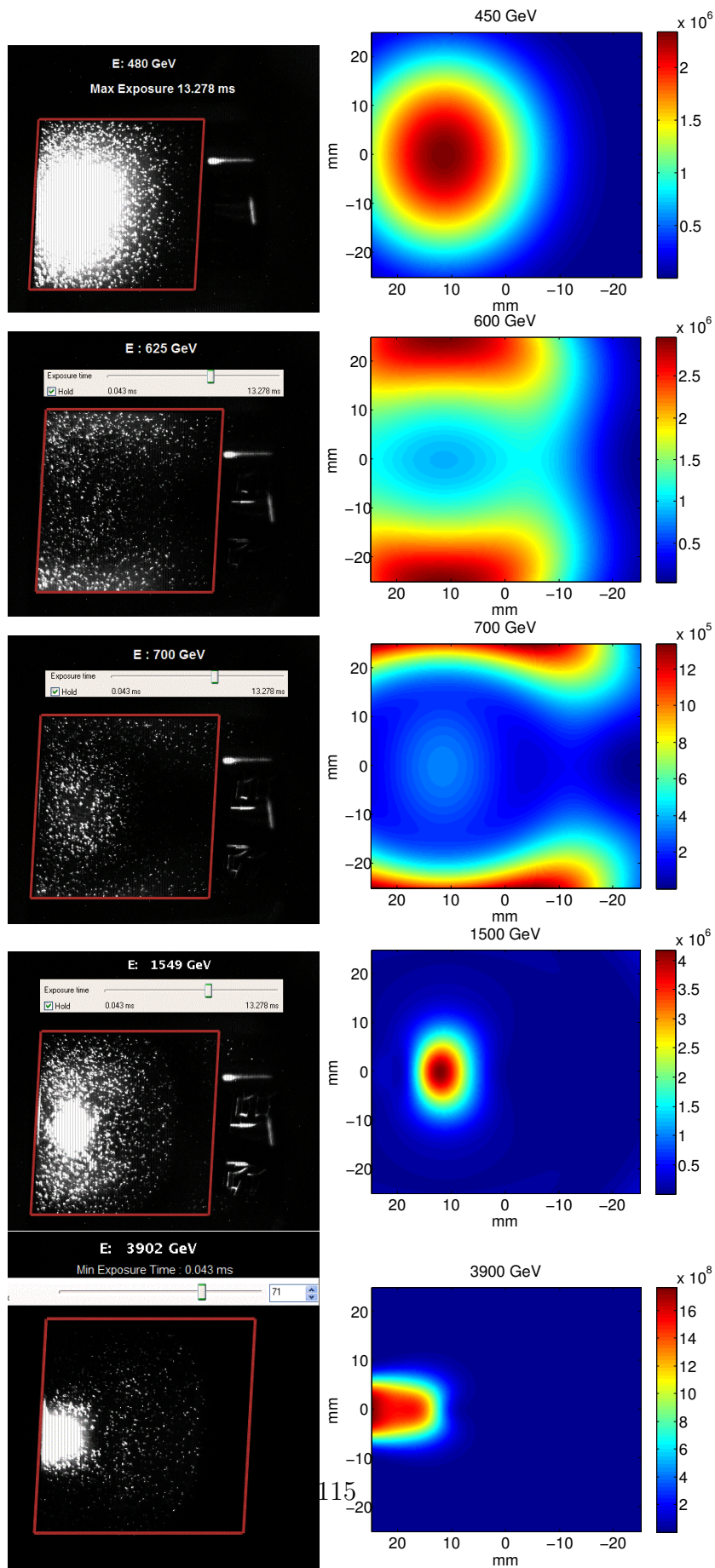


Figure 5.6: Measured SR light distribution (left plots) at the extraction mirror (delimited by the red rectangle) compared to the simulated SR intensity (right plots).

systematic light reduction in the proximity of the extraction mirror borders, observed especially around 500 and 600 GeV, is due to the limited angular acceptance of the objective lens mounted on the CCD.

5.2 Characterization of the LHC imaging system

This section is meant to summarize the LHC beam size measurements based on imaging, concentrating on the various techniques that allowed characterizing the system resolution and accuracy. Most of the studies were carried out on the first telescope version based on reflective optics that was operational until the end of 2012.

Then such studies allowed assessing the overall improvement of the system understanding and calibration after installing the new proposed refractive optics based system and the technique for best validating it (i.e. with the lowest error).

The optical systems will be qualified in terms of magnification and resolution by identifying the corresponding LSF. The measured resolution will be compared to the predicted resolutions computed using the simulation kit discussed in Chapter 4. Few examples of LHC fills will be presented, showing the effectiveness of the instrument calibration for different ranges of beam sizes, bench marked with the LHC wire scanners and the luminosity detectors of ATLAS and CMS.

5.2.1 Magnification measurements

The imaging system magnification dictates the conversion of CCD pixel into mm in the object plane. It has been predicted by the optics simulations using Zemax where the full BSRT system is modelled. However, additional techniques were implemented and used to experimentally determine the magnification.

Calibration target

Half of the BSRT optical bench, as mentioned in Chapter 3.1.3, hosts a calibration line. The incoherently retro illuminated target, shown in Fig. 5.7, is installed at the start of this calibration path. A set of mirrors allows the light, through multiple passes across the table, to reach the optical system with the same length as the SR

path from the undulator.

The accuracy of this technique is limited by the fact that the in-vacuum extraction mirror and the first mirror on the bench are not included in the calibration path, for which the measured magnification does not take into account any wavefront deformation introduced by these two elements.

For the reflective optical system, where the delay trombone was used to compensate

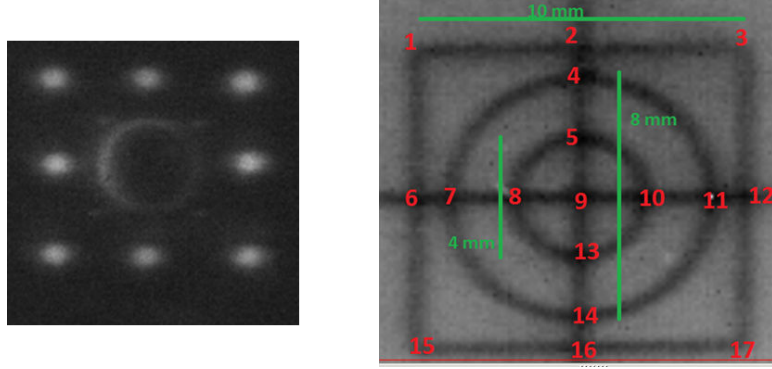


Figure 5.7: Beam 1 (right) and Beam 2 (left) resolution targets used for magnification measurement.

for the source shift (from the undulator to the dipole), the imaging of the target was enough to calculate the magnification for both energy scenarios (injection and flattop energy). The measurement results are summarized in Tab. 5.1. The errors represent the statistical error obtained averaging over several target images.

		K [mm/px]	$\delta\mathbf{K}/\mathbf{K}$ [%]
BEAM 1	Hor	0.1037	1.5
	VER	0.1113	2.1
BEAM 2	Hor	0.1121	2.6
	VER	0.1223	3.2

Table 5.1: Measured Magnifications using the calibration targets.

Contrarily, the refractive optical system, as it is conceived, features two different

magnifications depending whether the SR source is the undulator or the dipole and therefore a fixed calibration target is not enough to characterize the system.

Orbit bumps

This technique relies on shifting the beam position (hence the SR source) applying a "4 correctors" closed orbit bump, as shown in Fig. 5.8, that also indicates the location of the synchrotron radiation sources and other transverse profile monitors. The beam displacements at the BSRT source (undulator/Dipole D3) are obtained by the extrapolation of the beam position measured by the closest three Beam Position Monitors (squares in Fig. 5.8). At different camera positions (translation stage TS in Fig. 5.9), the calibration factors [mm/px] are obtained as the slope of the linear fit of the light centroid shift as function of the proton beam displacement, as shown in Fig. 5.10. This results in the linear law giving the optical system magnification for all CCD positions:

$$K_{x,y} = p \cdot TS + q \quad (5.1)$$

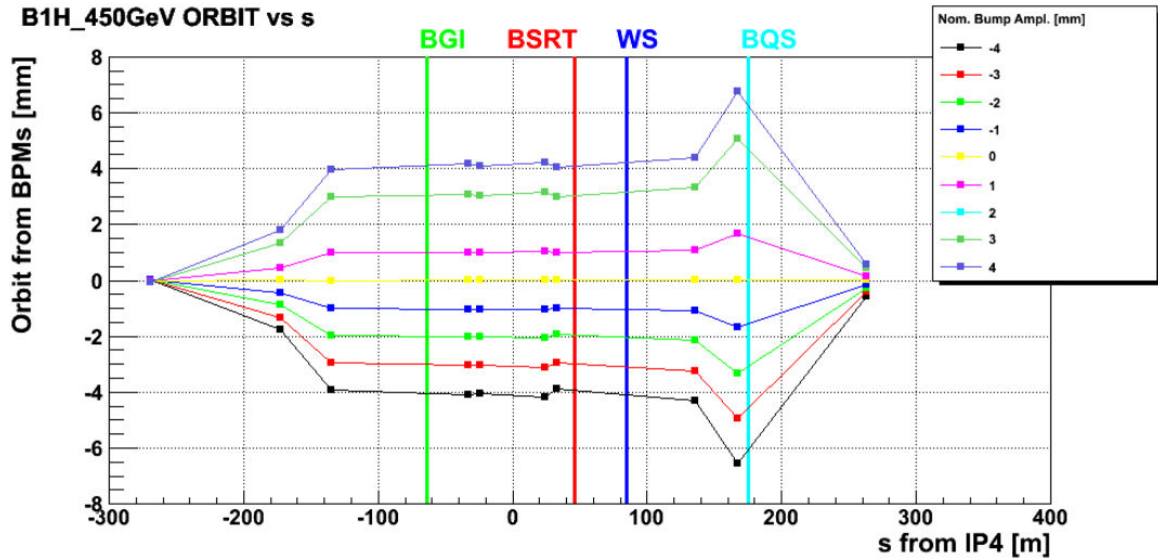


Figure 5.8: Beam orbit as measured by the Beam Position Monitors (BPMs) at the location of different profile monitors while applying closed orbit bumps of different amplitudes [6].

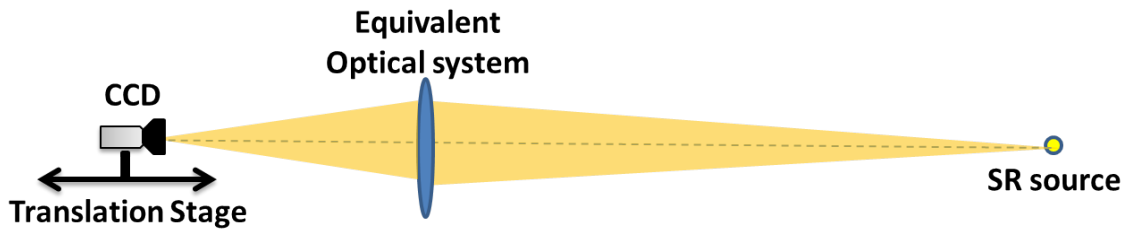


Figure 5.9: Schematic of the BSRT optical system, where at each bump amplitude the camera has been moved from end of the translation stage to the other to measure the magnification at every camera position.

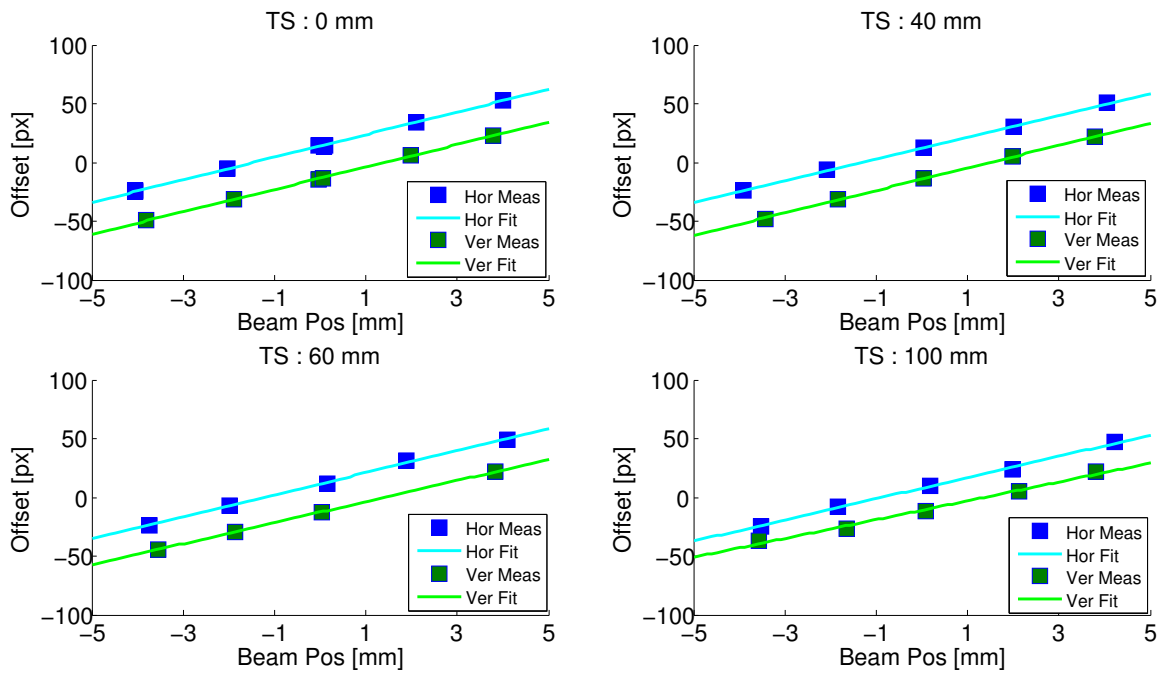


Figure 5.10: SR centroid on the CCD shift with respect to the beam transverse displacement at different camera positions (0, 40, 60 and 100 mm).

where TS is the camera position, $K_{x,y}$ the horizontal/vertical magnification and p, q the linear regression parameters, as shown in Fig. 5.11.

By evaluating Eq. 5.1 for $TS=50$ mm, calculated to be the nominal focus position of the system [53], the nominal calibration is extracted and summarized in Tab. 5.2.

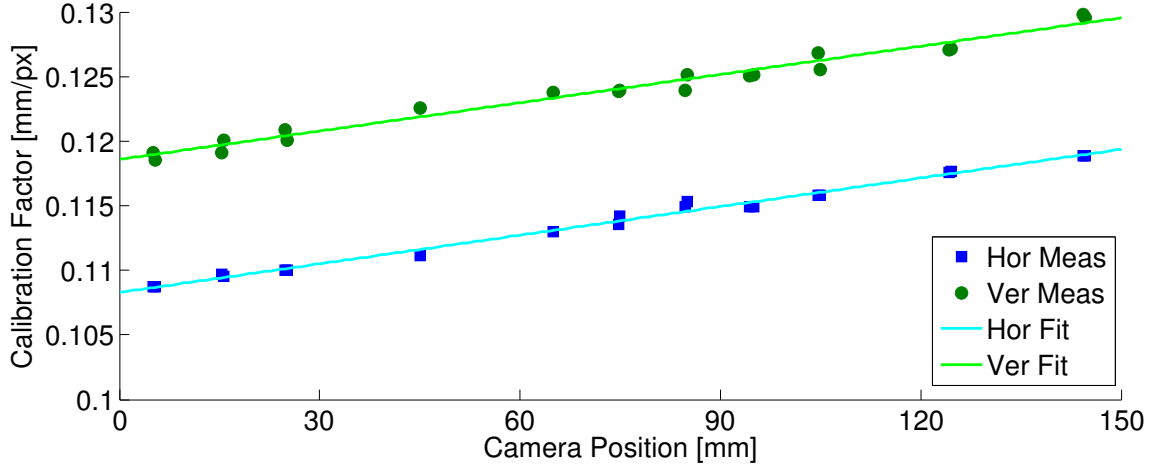


Figure 5.11: Horizontal and vertical measured magnifications at different CCD position.

		K [mm/px]	$\delta\mathbf{K}/\mathbf{K}$ [%]
BEAM 1	Hor	0.988	1.2
	VER	0.0994	0.9
BEAM 2	Hor	0.1062	1.35
	VER	0.1112	1.05

Table 5.2: Measured magnifications using the Orbit Bumps evaluated at the CCD focus position: $TS=50$ mm.

5.2.2 Cross-calibration with Wire Scanners (WS)

Complementary to the magnification measurement, the WS, reference instrument for emittance measurement in the LHC, were used to calibrate the BSRT, thus experimentally measuring its resolution and accuracy.

For the same beam passing through different locations in the accelerator and in the absence of beam perturbations in between, the emittance conservation law yields the following relationship:

$$\sigma_{BSRT}^2 = \beta_{ratio} \cdot \sigma_{WS}^2 \quad (5.2)$$

with σ_{WS} being the measured beam size by the WS, σ_{BSRT} the expected beam size at the BSRT source (Undulator/Dipole) and $\beta_{ratio} = \frac{\beta_{BSRT}}{\beta_{WS}}$ the ratio of the optical functions at the two monitors. Assuming Gaussian beam sizes and a Gaussian instrument resolution σ_{LSF} , the beam size measured by the BSRT can be expressed as:

$$\sigma_{BSRT_{meas}}^2 = \sigma_{BSRT}^2 + \sigma_{LSF}^2 \quad (5.3)$$

where $\sigma_{BSRT_{meas}}$ is obtained by applying the measured magnification:

$$\sigma_{BSRT_{meas}} = K \cdot \sigma_{BSRT_{meas_{pixel}}} \quad [object \text{ mm}] \quad (5.4)$$

The quadratic correction to be applied to the instruments measurements, σ_{LSF} (the resolution), is the result of the convolution of the broadening caused by light diffraction, the depth of field in the dipole and eventual aberrations (chromatic, geometric, flatness...). It can be expressed by:

$$\sigma_{LSF} = \sqrt{\sigma_{BSRT_{meas}}^2 - \beta_{ratio} \cdot \sigma_{WS}^2} \quad [object \text{ mm}] \quad (5.5)$$

Figure 5.12 presents the calibration results, where the measured quadratic corrections, summarized in Tab. 5.3, are applied to the measured emittances by the BSRT (grey) to find the best agreement with the emittances measured by the WS (red).

The measured resolution differs by at least a factor 3 from what the theoretical values predicted for the reflective optics imaging system in Chapter 4.3.1 ($\sigma_{LSFH} \sim 300 \mu\text{m}$

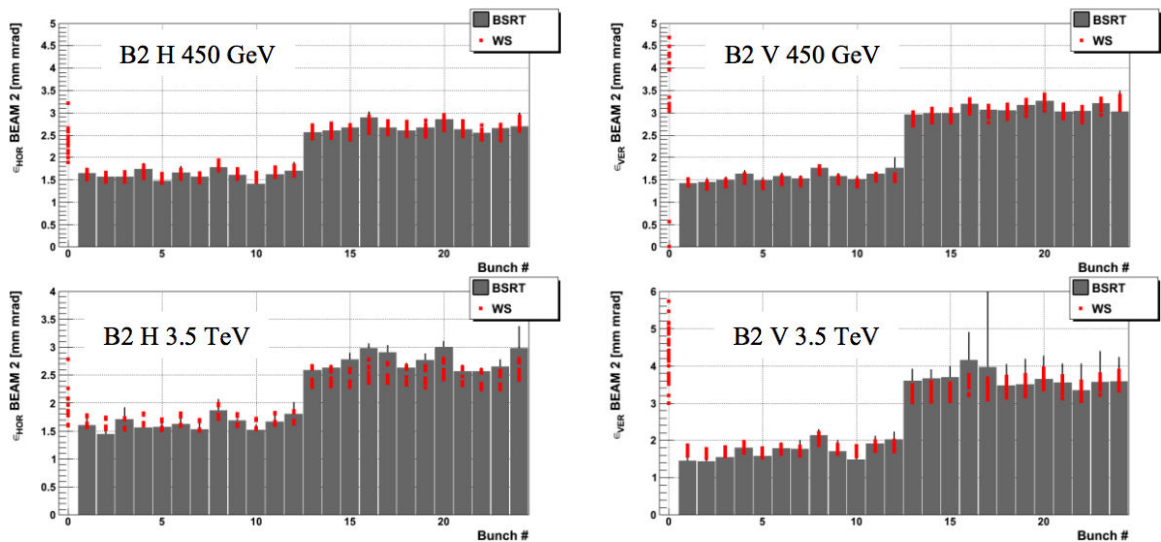


Figure 5.12: Bunch by bunch normalized emittances measured by WS (red) and BSRT (grey histogram) during the cross calibration period at injection energy (450 GeV) and 3.5 TeV.

		σ_{LSF} [object mm]
<i>Injection</i>	Hor	0.9
	VER	1.1
<i>Flattop</i>	Hor	0.6
	VER	0.7

Table 5.3: Measured calibration factors, σ_{LSF} , of the BSRT in its version based on focusing mirrors, at injection and flattop energy.

and $\sigma_{LSF_H} \sim 220 \mu\text{m}$). This can only partially be explained by the fact that the simulations for top energy do not include chromatic aberrations¹, optical surface imperfections and light cutting due to the limited optical elements apertures.

In addition, it is worth noting that the relative error on the magnification measurement (deriving from the uncertainties of p and q parameters in Eq. 5.1) induces an error in the LSF width determination.

¹ In presence of reflective optics only, the only source for chromatic aberrations could be caused by the dispersion in the viewport, that is supposed to be very small due to the normal incidence of the SR.

An approximated relation can be obtained by applying the error propagation technique to Eq. 5.5:

$$\epsilon_{\sigma_c [mm]} = \epsilon_K \cdot \left(K^2 \cdot \frac{\sigma_{BSRT_{meas [pixel]}^2}}{\sigma_c^2 [mm]} \right) \quad (5.6)$$

with ϵ_K being the relative error of the measured magnification and $\epsilon_{\sigma_c [mm]}$ the relative error of the obtained resolution. For nominal values of the normalized emittance and expected resolution ($\varepsilon = 3 \mu\text{m}$, $\sigma_{LSF [mm]} \sim 250 \mu\text{m}$), this approximation yields an error amplification factor equivalent to ~ 30 for small magnification errors. The extent of its validity is checked in Fig. 5.13, where the numerical error propagation (blue curve) is compared to the analytical first order propagation (Eq. 5.6 in black). It is observed that the approximation holds up to $\epsilon_K < 2\%$.

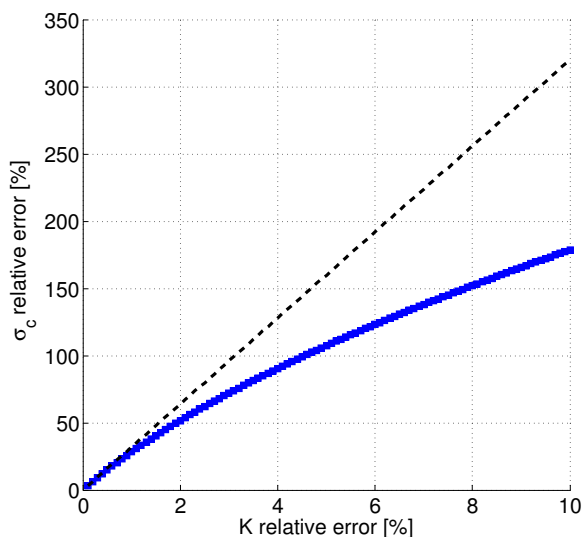


Figure 5.13: Induced error on the LSF width determination by error on the magnification measurement (blue). The black curve is a first order approximation of $\frac{\partial \epsilon_{\sigma_c}}{\partial \epsilon_K}$

In order to reduce the uncertainty on the measured system resolution (hence on the measured beam size), an alternative calibration technique, not relying on the measured magnification, is proposed. It consists of extracting both the magnification and the resolution (σ_{LSF}) from the cross-calibration procedure with the WS.

By combining Eqs .5.4 and 5.5, the following expression is obtained:

$$K \cdot \left(\sigma_{BSRT_{meas}[px]}^2 - \sigma_{LSF[px]}^2 \right) = \beta_{ratio} \cdot \sigma_{WS[mm]}^2 \quad (5.7)$$

that can be expressed in the following form:

$$\sigma_{BSRT_{meas}[px]}^2 = \left(\frac{\beta_{ratio}}{K} \right) \sigma_{WS[mm]}^2 + \sigma_{LSF[px]}^2 \quad (5.8)$$

The slope and offset of a linear regression in terms of $\sigma_{BSRT_{meas}[px]}^2$ and $\sigma_{WS[mm]}^2$ allows deriving the values of K and $\sigma_{PSF[px]}$.

This alternative technique, as shown in Fig. 5.14, was applied to check the validity of the early measured resolution reported in Tab. 5.3. The horizontal plane at injection energy (450 GeV) was considered in this example and the resulting resolution ($\sigma_{LSF} \simeq 0.7$ mm) was found to differ by $\sim 20\%$ from the initially measured value (0.9 mm with the first technique). Moreover, the obtained resolution with the new technique features an error of $\sim 17\%$ (derived from the confidence interval on the fitted intercept), being smaller than what shown in Fig. 5.13 with the first method ($\sim 30\%$).

Nevertheless, the measured LSF resulted to be again larger than what expected from simulations. The reason for this difference was traced down to the system alignment, strongly affected by the eight movable mirrors of the delay line presented in Fig. 4.11, and to the degradation of the extraction mirror coating as discussed in details in Chapter 6.

In order to improve the accuracy of this calibration technique, a wide range of emittances should be used along with a high number of measured samples during the process. Also a good knowledge of the machine optics¹ is required.

Since this last technique yields a better characterization of the system (lower errors), it was adopted to study the performance of the new optical system (based on refractive lenses) installed in September 2012. Unfortunately, the switch of the optical system took place at the time that the extraction mirrors were exchanged.

¹The knowledge of the machine optics at the source of the monitors location is of crucial importance. Therefore, a measurement campaign of the β function at the BSRT and WS was carried out, and the results are reported in Chapter 7.

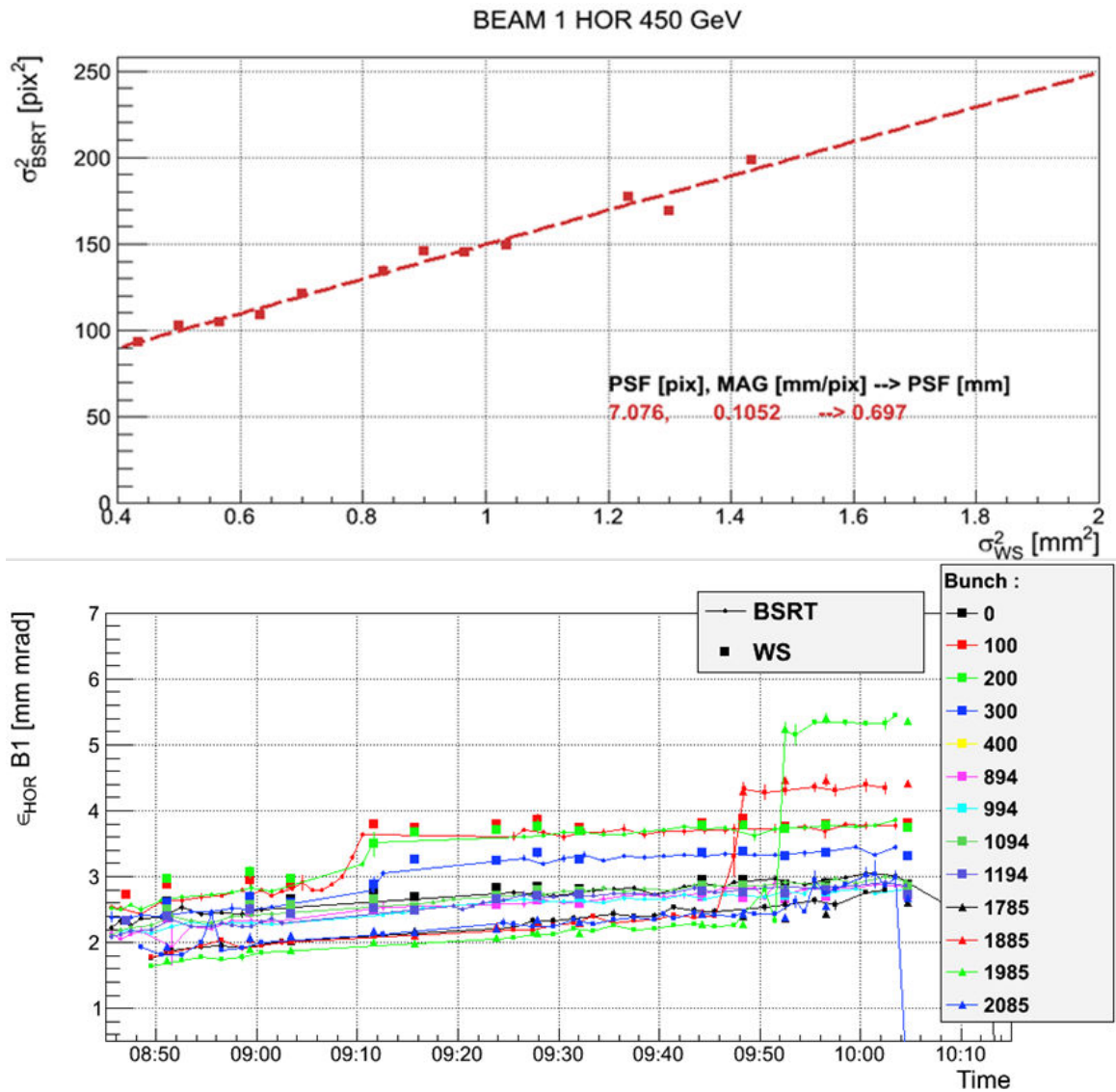


Figure 5.14: Beam-based calibration technique to obtain experimentally the magnification and the LSF width of the BSRT optical system through a cross calibration with the WS measurements. The regression coefficients obtained in the top plot are applied in the bottom plot obtaining the normalized emittance evolution as measured by the BSRT and WS.

Thus, no fair comparison is available between the reflective and the refractive optics. The magnification and resolution found for the new optics are summarized in Tab. 5.4 and found to be in a good agreement with the simulations, especially for the high energy case.

Energy [GeV]	Plane	K [mm/px]	$\sigma_{LSF_{meas}}$ [mm]	$\sigma_{LSF_{sim}}$ [mm]
<i>Injection</i>	H	0.0451	0.36	0.33
	V	0.0486	0.38	0.3
<i>FlatTop</i>	H	0.0532	0.39	0.37
	V	0.0589	0.35	0.32

Table 5.4: Properties of BSRT optical system in its lenses based version: measured magnification and resolution 450 GeV and 4 TeV compared to simulations.

A further validation of the measured magnification and LSF is shown in Fig. 5.15 and 5.16, where the emittance evolution as measured by the BSRT in an LHC fill is compared to the WS measurements. LHC fills 3215 and 3216 were chosen since they were dedicated to machine optics studies in which important emittance variations (more than factor 3) were expected. The calibration resulted to be stable and reliable, over a significant range of emittances.

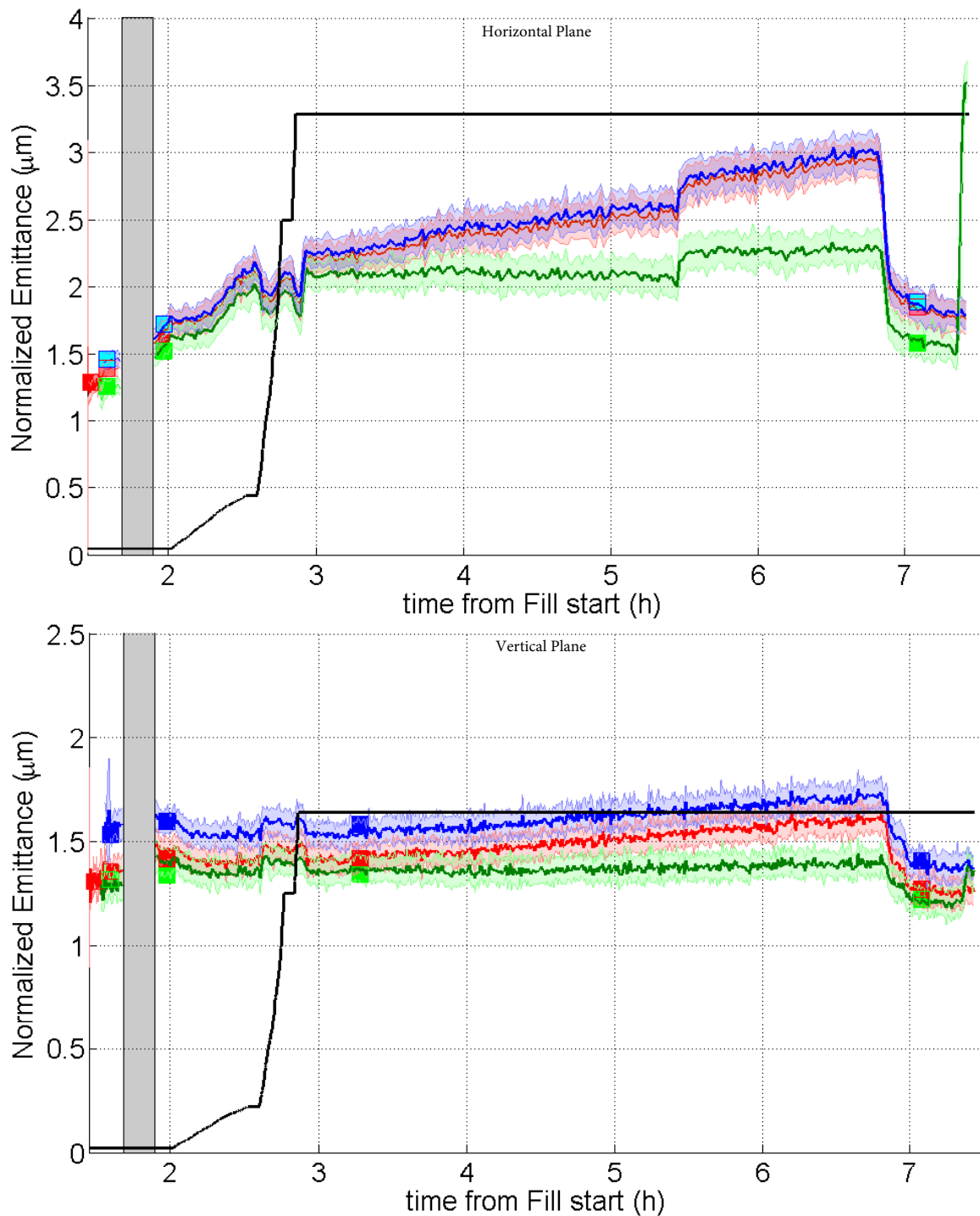


Figure 5.15: Normalized emittance evolution for 3 different bunches in the LHC fill 3215 as measured by BSRT (line) and WS (square). The measurements are carried out at 450 GeV (left of the grey vertical band) and 4 TeV (right of the vertical grey band). The additional black curves represent the increase of the optical function at the collision point (a.u.) and is not of interest to our studies.

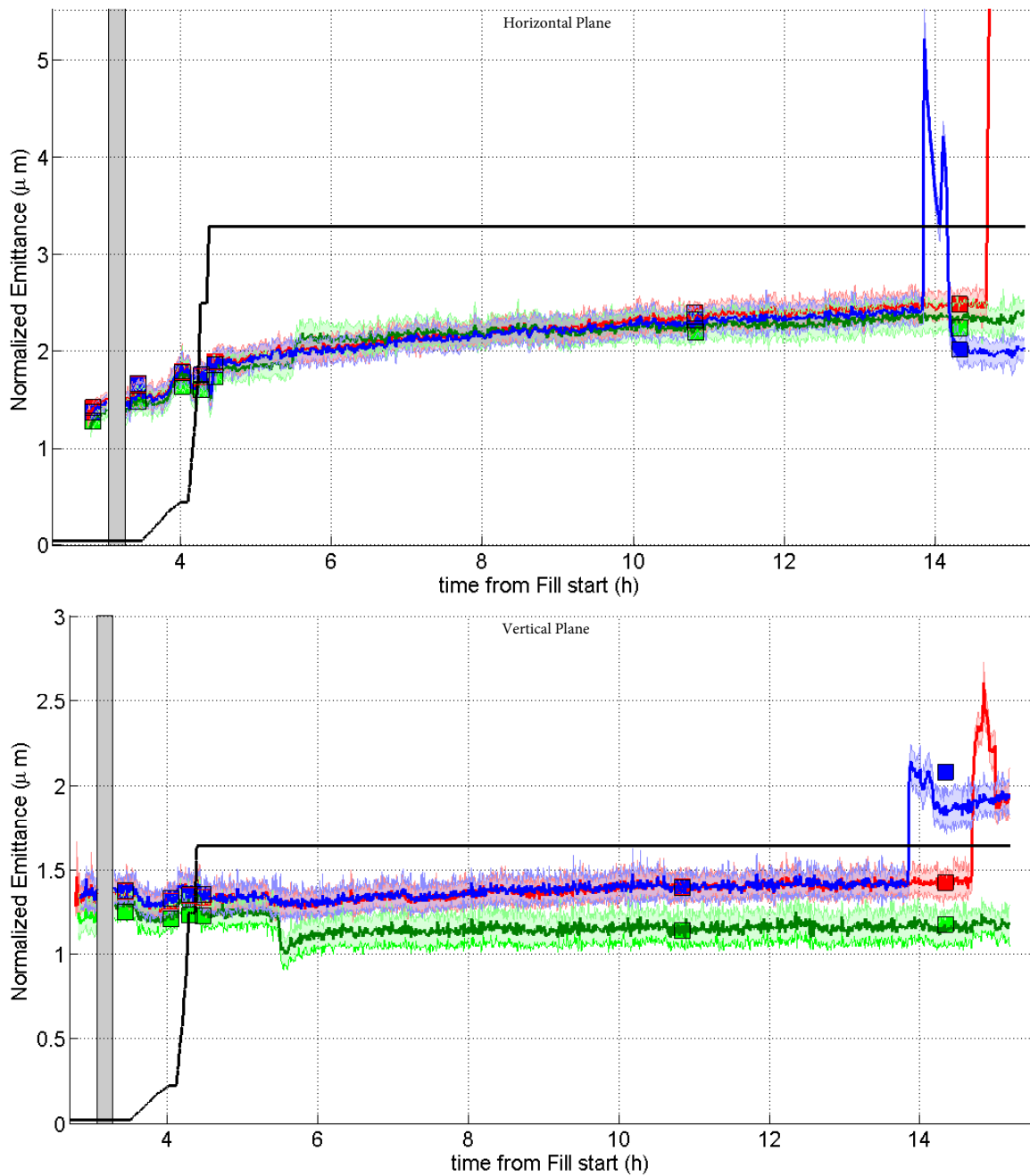


Figure 5.16: Normalized emittance evolution for 3 different bunches in the LHC fill 3216 as measured by BSRT (line) and WS (square). The measurements are carried out at 450 GeV (left of the grey vertical band) and 4 TeV (right of the vertical grey band). The additional black curves represent the increase of the optical function at the collision point (a.u.) and is not of interest to our studies.

5.2.3 Cross-calibration with luminosity measurements

Recalling the definitions of Chapter 1.2.5, the collider luminosity $\mathcal{L}(t)$ can be approximated as:

$$\mathcal{L}(t) = \mathcal{L}_0(t) \cdot CA(t) \quad (5.9)$$

with

$$\mathcal{L}_0(t) = f \frac{N_1(t) \cdot N_2(t)}{2\pi\beta^* \sqrt{(\epsilon_{x_1} + \epsilon_{x_2}) \cdot (\epsilon_{y_1} + \epsilon_{y_2})}} \quad (5.10)$$

$$CA(t) = \frac{1}{\sqrt{1 + \left(\frac{\sqrt{\sigma_{s_1}^2 + \sigma_{s_2}^2}}{\sqrt{\sigma_{x_1}^2 + \sigma_{x_2}^2}} \tan\left(\frac{\phi}{2}\right) \right)^2}} \quad (5.11)$$

where \mathcal{L}_0 is the nominal luminosity of the two colliding “head-on” (no transverse offset at the collision point) counter-rotating beams, $N_{1,2}(t)$ are the beam intensities, β^* the betatron function at the collision point, $\epsilon_{x,y}(t)$ the transverse emittances, $\sigma_s(t)$ the bunch length, $\sigma_{x,y}(t)$ the transverse beam sizes at the interaction point and ϕ the crossing angle.

The factor CA accounts for a luminosity reduction from the head-on to the crossing angle (as occurs in the LHC) case (whereas other geometrical correction factors are neglected here).

The luminosity can be calculated from the transverse emittance measured at the profile monitors locations and compared to the direct luminosity measurements continuously performed by the collision detectors.

LHC fill 2201 was chosen for this comparison, since it featured only 1 bunch per beam, brought into collisions at the energy of 3.5 TeV. The WS-BSRT calibration was checked by applying the measured LSF width reported in Tab. 5.4 as a correction, and the agreement between the two monitors is shown in Fig. 5.17.

Figure 5.18 compares the evolution of the calculated luminosity $\mathcal{L}(t)$ to the measured one by the LHC experiments ATLAS (green) and CMS (blue). A systematic difference is found between the two experiments measurements and above all between the measured luminosity and the one inferred from the beam measurements (emittance,

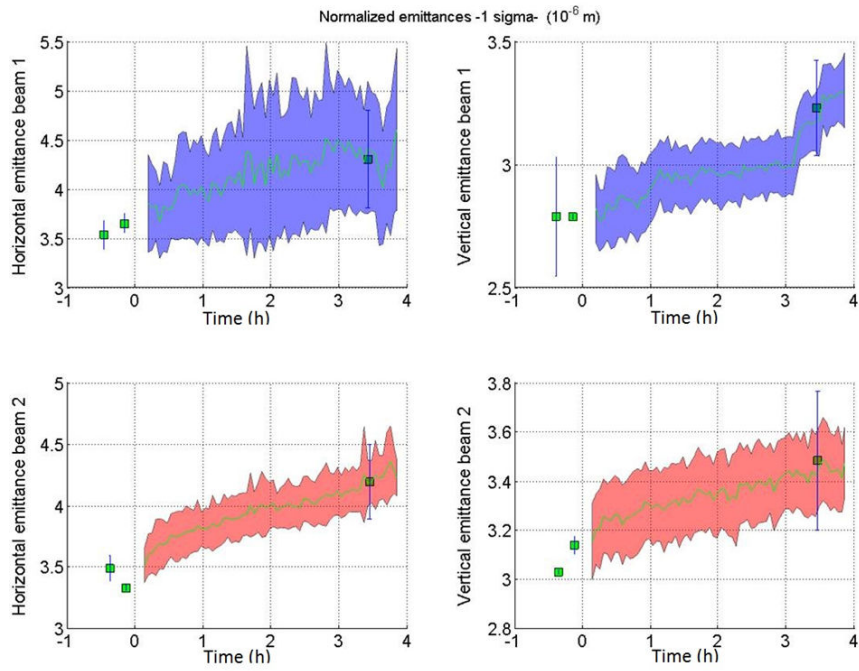


Figure 5.17: Normalized emittances evolution during the BSRT-WS cross calibration for the LHC Fill 2201.

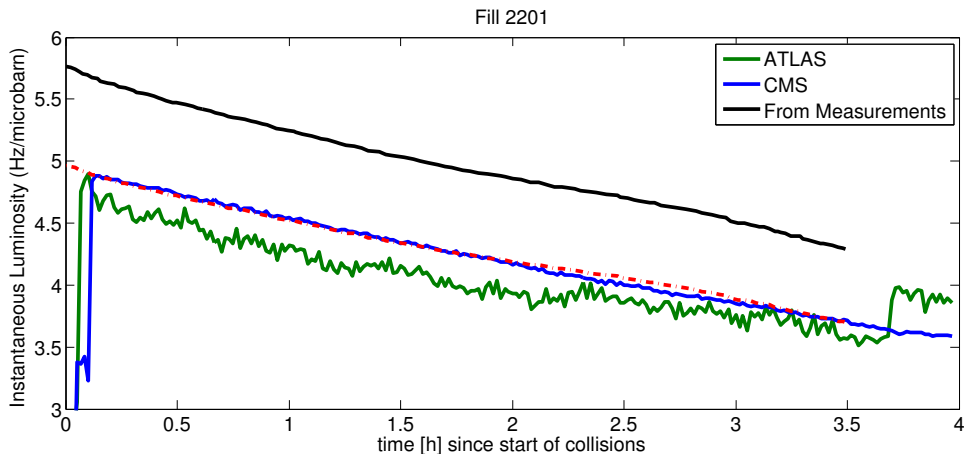


Figure 5.18: Evolution of the measured instantaneous luminosity measured by ATLAS and CMS compared to the computed luminosity computed from the measured beam parameters. The red dotted curve is obtained by scaling the black curve to be compared with the luminosity measurements.

bunch length and intensity). Such a difference could well be explained by a luminosity reduction (w.r.t. to the estimation of Eq. 5.9) due to transverse beam offsets at the collision points and to (known) uncertainties on the β^* knowledge. Such effects are difficult to quantify (that is why luminosity measurements via emittance measurements are normally not considered as reliable) and can be by definition different at different collision points, thus explaining the measured luminosities difference. Simply shifting the luminosity inferred from the beam parameters results in the red dotted curve in the plot and in a remarkable relative agreement with the CMS measurement.

The BSRTs were also used to monitor the beam size during the calibrations of the luminosity detectors with the Van Der Meer (VDM) scans technique [76]; an example is given in Fig. 5.19, where the emittance evolution measured by the BSRT is shown during a VDM scan in LHC fill 3311. These kind of SR measurements have been recognised as a very powerful tool for monitoring the emittance increase correlation with the bunch collision patterns (i.e. number of collisions per bunch per IP).

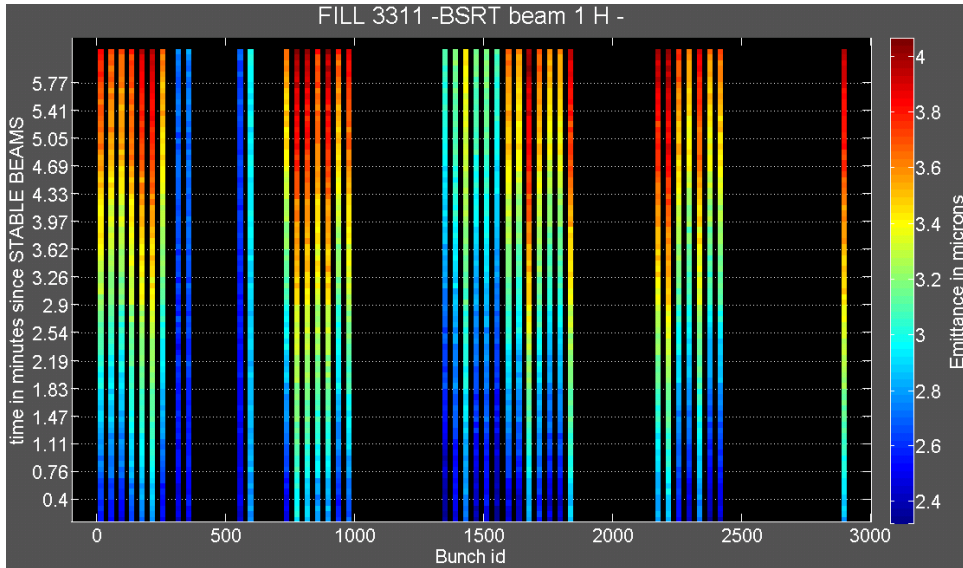


Figure 5.19: Normalized emittance evolution as measured by the BSRT during a luminosity calibration fill in the LHC.

5.2.4 LHC SR imaging summary

Two alternative techniques were described for experimentally measuring the characteristics of the BSRT optical system.

The first consists in measuring separately the system magnification and resolution:

- the magnification was measured by the mean of an external calibration target or by inducing a source displacement in the system by the mean of orbit bumps;
- the LSF width was then obtained as the quadratic correction applied to the beam size measured by the BSRT, that minimizes the difference between the emittance measured by the BSRT and WS.

The second consists in applying a linear regression to the square of the BSRT measured beam sizes versus the square of the WS measured ones. The regression parameters are directly related to the magnification and σ_{LSF} . This method claims a lower error on the LSF width determination. Therefore it was adopted to evaluate the resolution of the new LHC optical system (based on lenses) as well.

The LSF measured for reflective optics was found to be always greater to what simulated in Chapter 4. Additionally, with the gradual increase of the LHC total intensity in 2012 (and the consequent degradation of the light extraction system, see Chapter 6), the calibration coefficients resulting from the BSRT-WS cross calibration were found to be unstable and very often increasing. The deteriorated extraction monitor was found to be the main source of additional aberrations in the system, that are not included in the simulations.

Contrarily, the LSF measured for the new optical system based on lenses, after the installation of the new extraction mirror, was found to be very close (within 10 %) to the simulated values.

With the new optics, the measured magnification and PSF were validated by cross-calibrating BSRT and WS over several fills and emittance ranges, that evidenced a remarkable absolute and relative agreement between the two instrument types. The relative monitor accuracy was also confirmed by comparing the LHC experiments luminosity data with the luminosity inferred from the beam size measurements.

5.3 Interferometry at ALBA

In the framework of a CERN-CELLS¹ collaboration, a series of interferometry measurements were taken at the ALBA synchrotron. This section presents the measurement setup and results, including the use of the correction algorithm proposed in Chapter 4, successfully applied to extract the horizontal beam size value.

ALBA is a 3rd generation Synchrotron Light facility. The 3 GeV electron beam energy is achieved by combining a Linear ACcelerator (LINAC) and a low-emittance, full-energy BOOSTER placed in the same tunnel as the STORAGE RING. ALBA's 270 m perimeter has 17 straight sections designed to host the insertion devices for the SR production [77].

In a dedicated diagnostics line, transverse beam size measurements are carried out in parallel by the x-ray pinhole technique and the visible SR interferometer [78]. The first uses the x-ray part of the SR produced by a dipole, while the second technique uses the visible light coming from another bending dipole *BM01*. Table 5.5 lists the main beam parameters at both monitors. The visible SR light is extracted 8.63 m

Parameter	Interferometry	Pinhole Camera
Hor beam size [μm]	54.2	57.2
Ver beam size [μm]	23.8	28.3
Beam energy [GeV]		3
Bending radius [m]		7.05

Table 5.5: Beam and machine parameters at the location of the ALBA profile monitor sources [78].

downstream by an "in-vacuum" mirror. To avoid its exposure to the hard x-rays (emitted within a narrower cone than the visible SR), that potentially could alter its characteristics, the extraction mirror bottom edge is set at 6 mm from the beam orbit plane. Therefore, only the upper lobe of the emitted SR is extracted and sent to an optical table through 6 in air mirrors, as shown in Fig. 5.20. On the optical

¹Consortium for the Construction, Equipping and Exploitation of the Synchrotron Light Source (CELLS), Cerdanyola del Valls, Barcelona, Spain, <https://www.cells.es/>

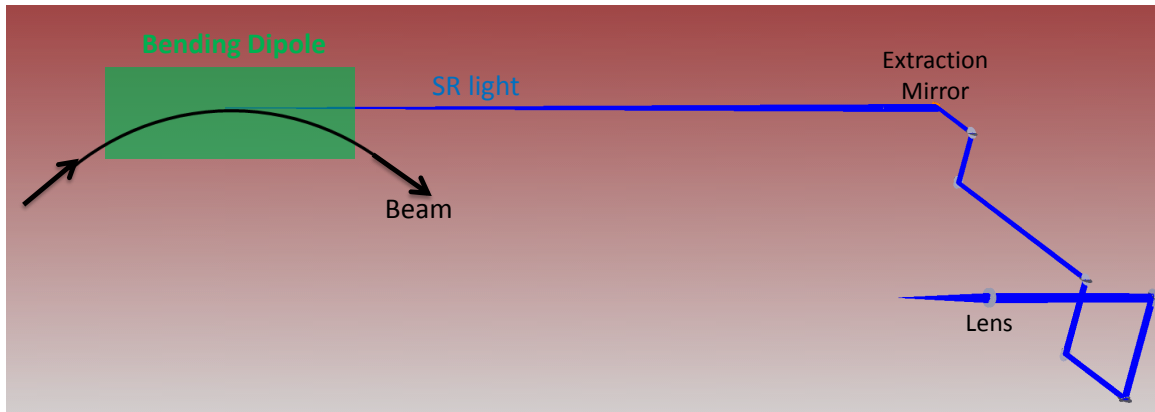


Figure 5.20: Sketch of SR optical path at ALBA from its source (bending dipole *BM01*) to the optical bench.

table, a double slit system was installed, allowing to vary the slit separation (from ~ 3 mm to ~ 40 mm) while keeping its width to ~ 1 mm. The double slit is followed by an apochromat lens with focal length of 500 mm that forms an intermediate image of the interferogram. The latter is then zoomed by the mean of an ocular lens with the equivalent focal length of 18 mm to suit the resolution ($3.75 \mu\text{m} \times 3.75 \mu\text{m}$) of the CCD installed in its image plane. Just after the zoom lens, a narrow bandpass filter (440 nm), presented in Fig. 5.21, followed by a linear polarizer (Glan-Taylor type), is used to select only the horizontal polarization of the incoming SR. Particular atten-

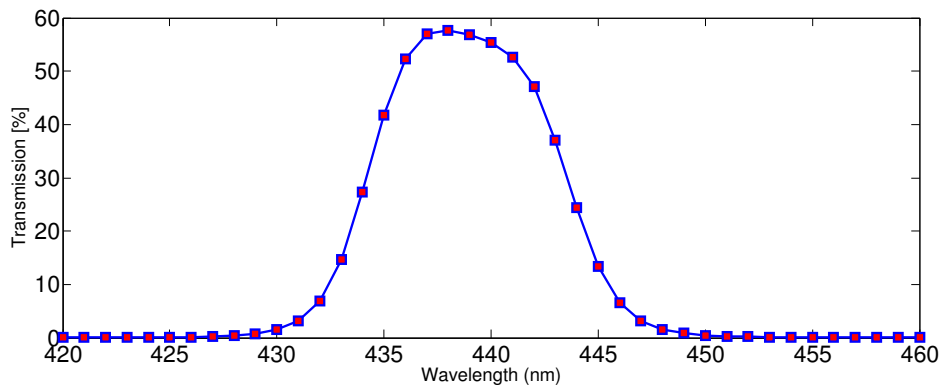


Figure 5.21: Color bandpass filter used in the interferometry setup at ALBA.

tion was dedicated to positioning the CCD in the image plane of the focusing system (imaging the SR source) and finding the suitable magnification needed to resolve the interference fringes on the CCD. In addition, selecting only the horizontal polarization was of interest, since mixing two polarizations leads to a washout of the observed visibility, thus falsifying the beam size measurements.

The experiment consisted in acquiring several CCD images (each with 15 ms exposure time) for every slit separation. Figure 5.22 shows the vertical projection of the interference fringes¹ for different slit separations, ranging from 8 to 32 mm. The profiles are then fitted using Eq. 2.48, reported here again for the sake of clarity:

$$I(x) = I_0 \left[\text{sinc} \left(\frac{2\pi a}{\lambda_0 R} x \right) \right]^2 \cdot \left\{ 1 + |\Gamma| \cos \left(\frac{2\pi D}{\lambda_0 R} x + \phi \right) \right\}$$

with a the half of the single slit width, D the separation between the two slits, λ_0 the wavelength of observation, I_0 the sum of the incoherent intensities from both slits, ϕ an arbitrary phase, R the distance from the lens to the detector plane and Γ the first order degree of mutual spatial coherence.

Qualitatively, the number of fringes increases with the slit separation and the visibility $|\Gamma|$ decreases.

As described in 2.3.2, assuming a Gaussian beam in the horizontal plane, the beam size σ_x can be calculated as

$$\sigma_x = \frac{\lambda_0 S}{2\pi\sigma_v} \quad (5.12)$$

where S ($=15.532$ m in this case) is the distance between the SR source and the double slit, and σ_v ($=21.5$ mm in this case) is the Gaussian fit of the visibility as function of the slit separation. This resulted in $\sigma_x = 50.6 \mu\text{m}$, but, as evident in Fig. 5.23, the poor fit quality confirmed the need to apply further corrections to disentangle the effect of the beam size on the fringes visibility from the one of additional effects such as the depth of field, chromatic effects and the slit calibration.

¹Raw data of the CCD acquisition are kindly provided by L. Torino

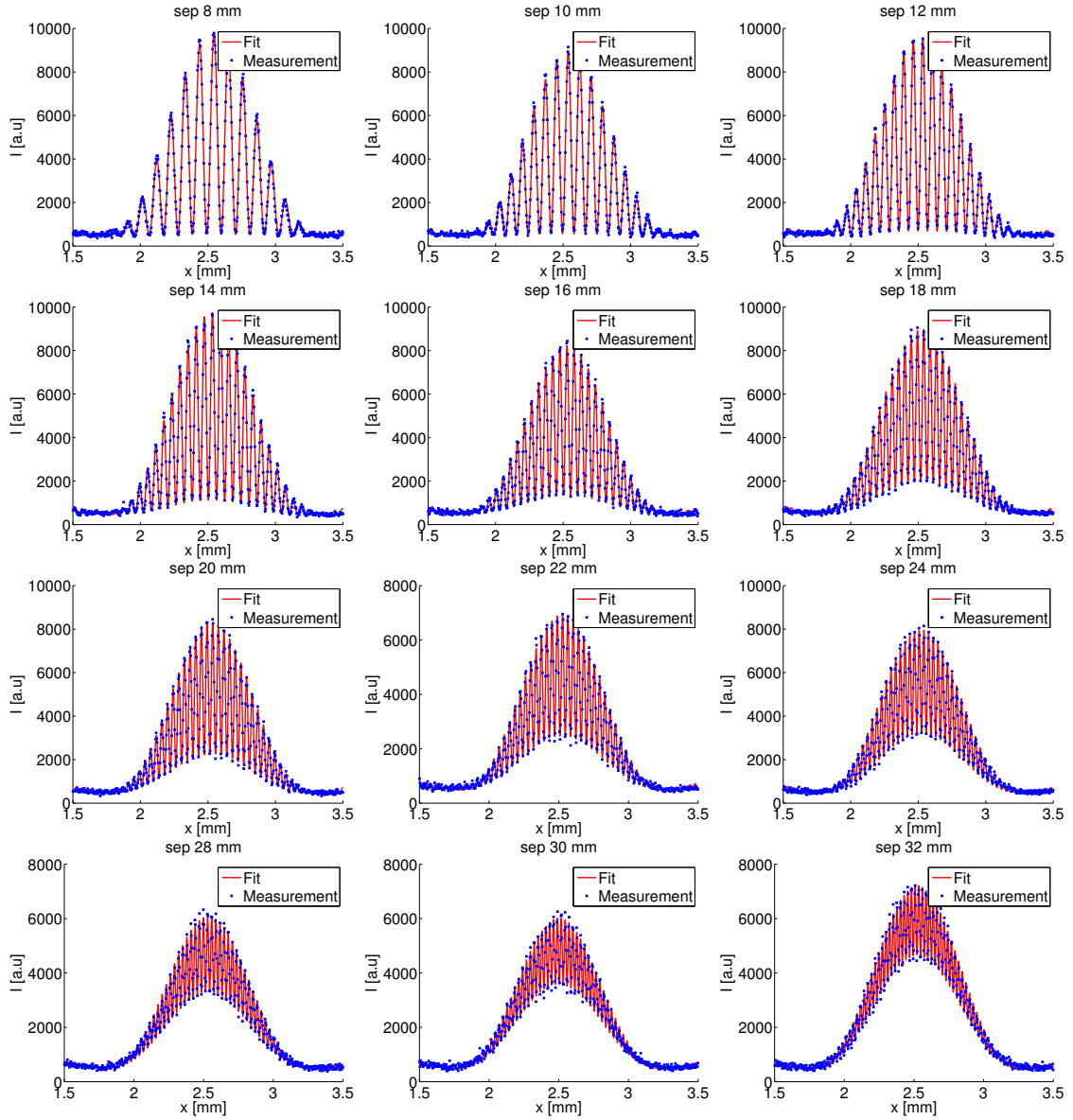


Figure 5.22: Vertical projection of the interference fringes of the ALBA beam size interferometer for different slit separations, ranging from 8 to 32 mm. Experimental data is shown in blue, while the fit according to Eq. 2.48 is shown in red.

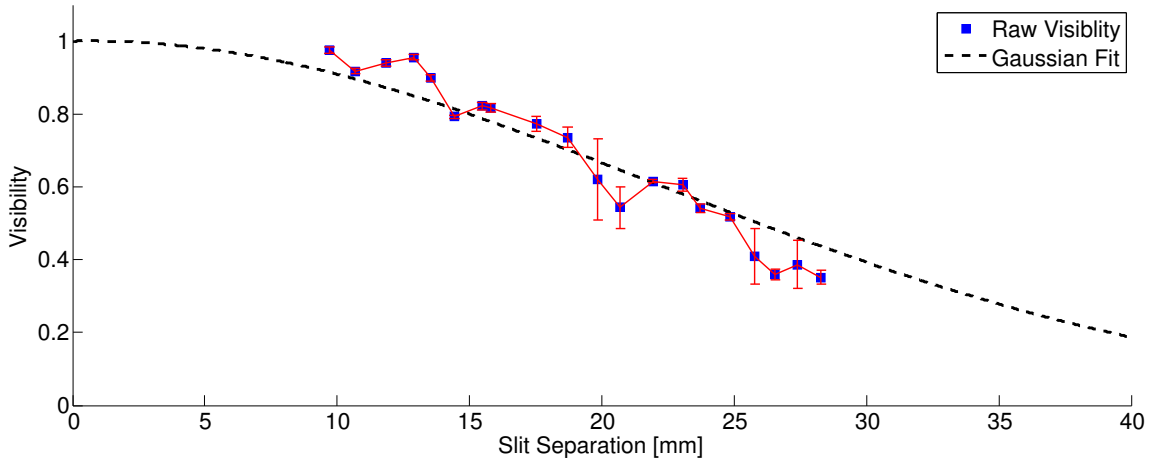


Figure 5.23: Measured fringe visibility during the slits separation scan from 9 to 28 mm, fitted by Gaussian distribution.

5.3.1 Corrections

Chromatic effect correction

It is worth noting that Eq. 2.48 does not take into account the finite spectral acceptance of the interferometer and assumes a monochromatic light. For a different slit separation, the relative error committed when neglecting the *quasi-monochromatic* nature of the observed pattern is shown for various beam sizes in Fig. 5.24. The visibility reduction due to chromatic effects can be modeled as shown in Fig. 5.25, from which, given a beam size, a visibility adjustment (slit separation dependent) has to be applied before extracting the beam size itself.

Depth of field correction

Even though the ALBA dipole bending radius (7 m) is small with respect to the LHC (6 km), when running the simulations presented in Chapter 4 for the ALBA case, a depth of field (DOF) effect is observed. This incoherent depth of field is responsible for a visibility reduction and thus an overestimation of the measured beam size. Such an effect is presented in Fig. 5.26, where the observed discrepancy between the expected visibility with or without DOF effect increases with the slit separation and

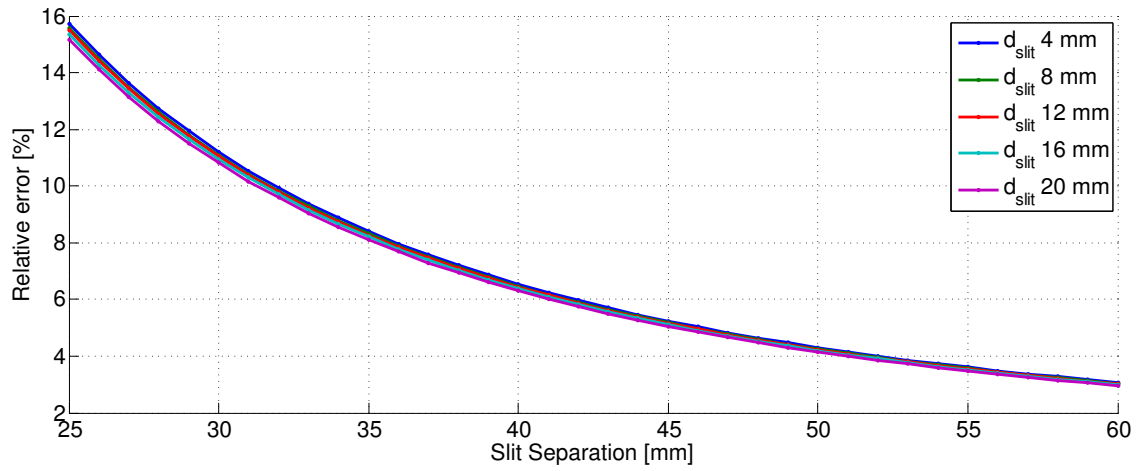


Figure 5.24: Relative error introduced by neglecting the finite bandpass of the color filter assuming monochromatic light for different beam size and slit separation.

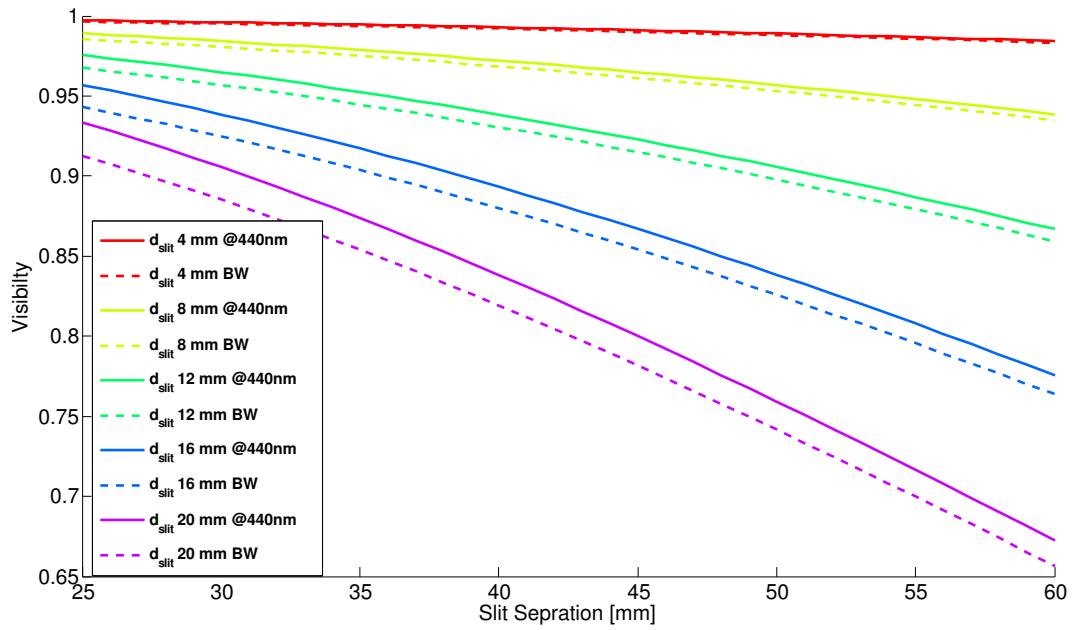


Figure 5.25: Visibility reduction due to chromatic effects for different beam sizes and slit separations.

decreases with the beam size.

Also in this case, for a given beam size, a visibility adjustment (slit separation dependent) has to be applied before extracting the beam size.

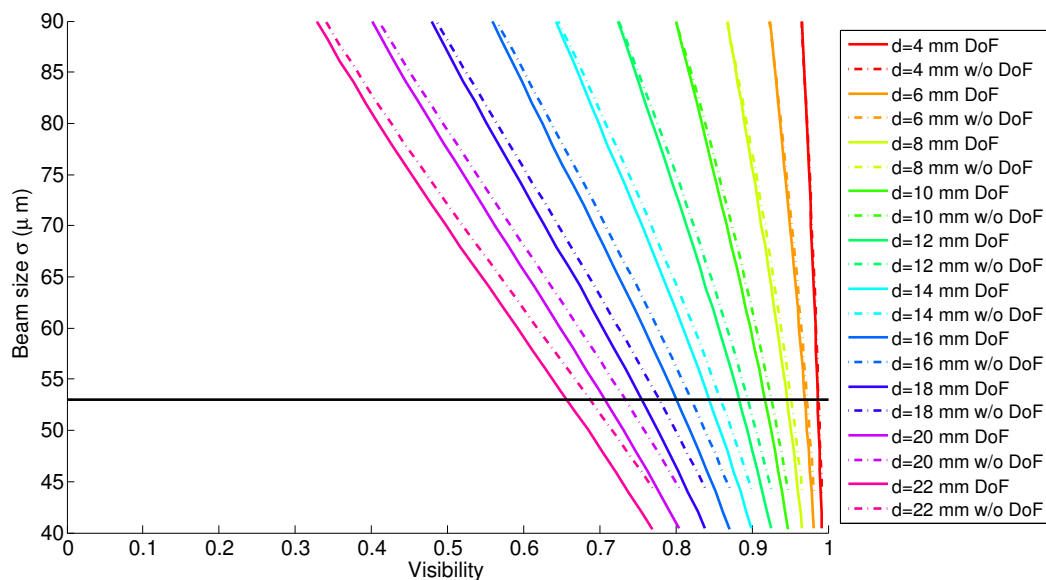


Figure 5.26: Incoherent depth of field effect on the interference fringes visibility for different slit separations and beam sizes.

Slit calibration

In addition to the amplitude correction to be applied to the raw data of Fig. 5.23, a horizontal correction is also needed. This comes from any deformation of the extraction mirror, yielding to a (different from theoretical) effective double slit separation. At ALBA, this effect is amplified by the lever arm (8 m) from the extraction mirror to the double slit.

According to the flatness measurement carried out at ALBA via the Hartmann Mask technique, that will be described in Chapter 8, the extraction mirror resulted to be deformed in the order of few wavelengths (550 nm) in the central region of interest [79]. In particular, deformations of 3λ and 8λ were used for the mirror regions of interest, sending photons to the right and left slit respectively. Figure 5.27 shows:

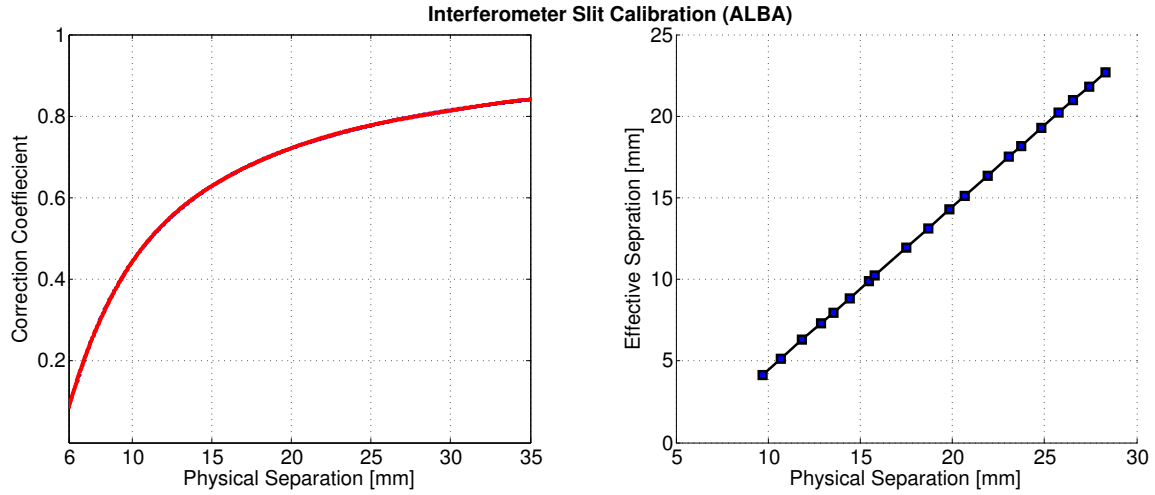


Figure 5.27: Interferometer double slit calibration to be applied to the physically measured slit separation $D_{physical}$ to obtain the effective separation $D_{effective}$.

Left plot: the correction factor α to be applied to the measured slit separation in order to obtain the effective separation according to:

$$D_{effective} = \alpha \cdot D_{physical} \quad (5.13)$$

Right plot: the effective separation $D_{effective}$ to be used at the place of the mechanical separation $D_{physical}$.

Correction algorithm and results

Finally, the correction algorithm to be applied to $V(D)$ curve consists in the following steps:

1. applying the slit separation correction to obtain $V(D_{effective})$;
2. identifying an initial set of possible beam sizes (based on the nominal machine optics and beam parameter) for ALBA, ranging from $45 \mu\text{m}$ to $60 \mu\text{m}$ by a step of $1 \mu\text{m}$;
3. for every beam size σ_{x0} within that range:

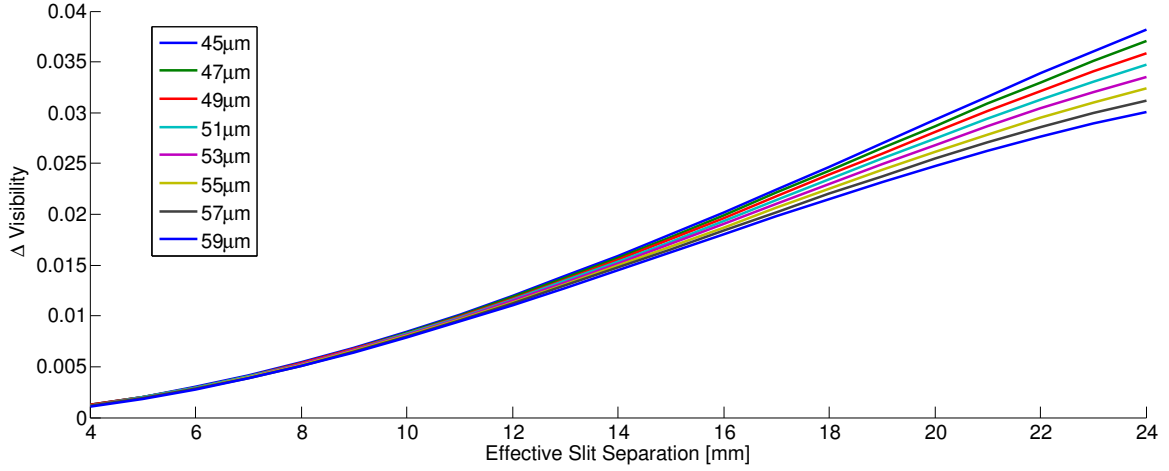


Figure 5.28: An example of visibility corrections (chromatic correction and DOF) to be applied for a given set of beam sizes ranging from 45 μm to 59 μm .

- correcting the curve $V(D_{effective})$ by applying the corresponding increase of visibility (derived from chromatic correction and DOF correction) for each slit separation (as shown in Fig. 5.28);
 - applying a Gaussian fit to each of the obtained curve $V_{corrected}(D_{effective})|_{\sigma_{x_0}}$ and determining the beam size $\sigma_{FIT_{x_0}}$, using Eq. 5.12;
 - evaluating the discrepancy $\Delta = (\sigma_{x_0} - \sigma_{FIT_{x_0}})^2$.
4. finding the minimum m_0 of the the curve $\Delta(\sigma_{x_0})$;
 5. repeat from step 2, narrowing the beam sizes range to probe around σ_{x_m} corresponding to m_0 , the minimum found in the previous step.

By iterating this procedure, the desired resolution of 0.1 μm is easily reached. Figure 5.28 shows the corrections to be applied for different beam sizes following step 2 of the correction algorithm and the final correction to Fig. 5.23 after 3 iterations are presented in Fig. 5.29. The red curve stands for the initial raw data $V(D)$, while the green one is the corrected data after applying the chromatic and incoherent depth of field correction (blue) and the slit separation calibration. A Gaussian fit (in black) indicates its width: 27.93 mm, with a high R-square¹ (0.9681), corresponding

¹ In statistics, the coefficient of determination [80], denoted R^2 and pronounced R squared, is a number that indicates how well data fit a statistical model sometimes simply a line or curve. The

to 55.1 μm beam size.

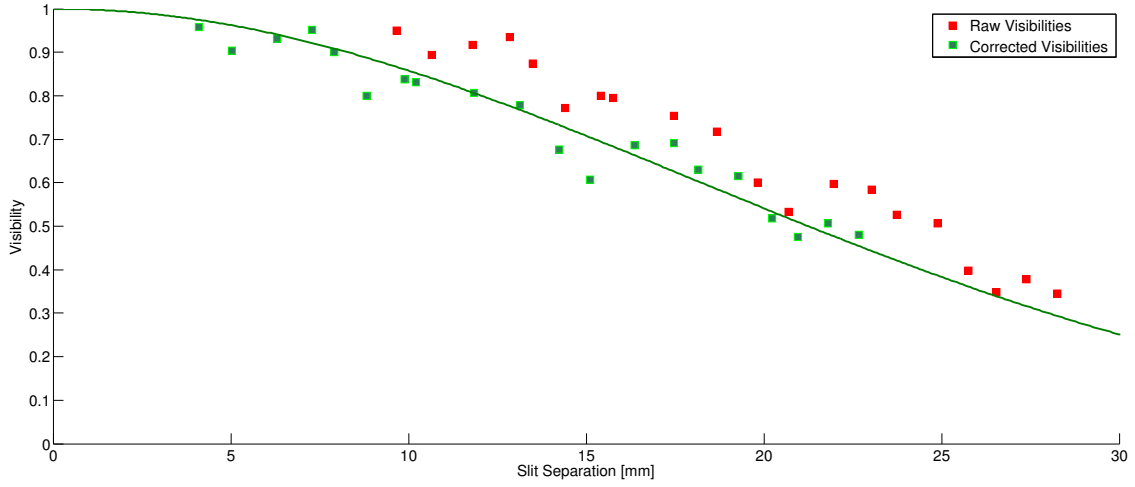


Figure 5.29: Fringe visibility change with respect to the slit separation before (red) and after (green) applying the correction algorithm.

A good agreement is found with the expected beam size (see Tab. 5.5), thus confirming the validity of the applied corrections; however it is worth mentioning that plans are ongoing at ALBA to shield the optical path (the 6 in air mirrors) to avoid perturbations and additional broadening of the measured beam size due to air turbulence and fluctuations, hence more reliable measurements should be possible in the near future.

most general definition of the coefficient of determination is: $R^2 = 1 - \frac{\sum_i (y_i - f_i)^2}{\sum_i (y_i - \bar{y})^2}$ with $\bar{y} = \frac{1}{n} \sum_{i=1}^n y_i$, being the mean over n observations of the data sets y_i each of which has an associated modelled value f_i .

Chapter 6

RF Heating in the LHC Light Extraction System

During the LHC Run I the accuracy, availability and reliability of the SR monitors were highly affected by the heating of the light extraction mirror. This caused the reflective coating degradation and eventually the failure of one mirror support. The appearance of this issue during the daily operation with beam in 2012 motivated the request for dedicated machine development periods to study the problem in detail.

Such studies allowed to trace back the heating to electromagnetic coupling between the circulating beam and the light extraction system, for which characterizing the induced wake fields and the so-called *beam coupling impedance* of the structure became a must.

In the following the beam coupling impedance concept is explained and the technique used to characterize it in the laboratory is described. The results of the laboratory experiments will be compared to numerical simulations carried out in parallel by the RF experts. This ended up in a new mechanical design which is expected to be almost immune to electromagnetic coupling.

6.1 Longitudinal wake fields, potentials and coupling impedance

Beside the magnets (dipoles, quadrupoles, sextupoles...) and the RF cavities, another source of EM fields in the accelerator is the beam itself. The beam induced electric and magnetic fields are denoted as *wake fields* [81, 82]; these self-induced wake fields represent the scattered fields excited by the beam interacting with the accelerator devices (beam pipe, cavities, collimators, beam diagnostics, etc.). These fields can drive the beam unstable, a behaviour which may culminate in partial or total beam loss.

Wake fields depend on the beam charge distribution, therefore by knowing what is the effect of a single charge (i.e. the Green's function), the fields produced by any charge distribution is reconstructed by a convolution of the Green's function with the actual current distribution. The fields created by a point charge act back on the charge itself and on any other charge in the beam. In the following, we therefore focus our attention on the source charge q_0 , and on a test-charge q , assuming that both are moving with the same constant velocity $v = \beta c$ on trajectories parallel to the axis. The Lorentz force applied on the test charge is:

$$F = q [E_z \vec{z} + (E_x - vB_y) \vec{x} + (E_y + vB_x) \vec{y}] = F_{\parallel} + F_{\perp} \quad (6.1)$$

where \vec{E} , \vec{B} are the fields generated by q_0 .

Thus, there can be two effects on the test charge:

- a change of its energy given by the work done by the longitudinal force along the structure of length l

$$U = \int_0^l F_{\parallel} ds \quad (6.2)$$

- a transverse deflecting kick

$$M = \int_0^l F_{\perp} ds \quad (6.3)$$

The longitudinal wake potential w_{\parallel} is defined normalizing U by the charges, with a minus sign meaning that the test charge loses energy when the wake is positive:

$$w_{\parallel} = -\frac{U}{q_0q} [V/C] \quad (6.4)$$

In linear accelerators, the concept of wake fields in the time domain is more common, while in circular accelerator, due to the intrinsic periodicity, the frequency domain approach is preferred; the longitudinal coupling impedance Z_{\parallel} is defined as the spectrum of the point charge longitudinal wake function:

$$Z_{\parallel}(\omega; r, r_q) = \frac{1}{v} \int_{-\infty}^{+\infty} W_{\parallel}(s; r, r_q) e^{-i\omega \frac{s}{v}} ds \quad [\Omega] \quad (6.5)$$

The coupling impedance contains all the information about electromagnetic coupling, just as the corresponding wake field.

As already mentioned, the coupling can originate from any vacuum chamber wall discontinuity, for instance needed to accommodate cavities or diagnostic instruments. The longitudinal coupling impedance can be split in two types according to the effective range of the wake fields:

- the *broadband impedance* corresponds to fast decay wake fields and thus to a short effective range (shorter than few RF bucket lengths). Typically this type of wake field can only be seen by particles in the same bunch and are transparent to the trailing bunches;
- the *narrow-band impedance* corresponds to a long range wake effect affecting trailing bunches. It is usually excited in RF cavities (or trapped modes) and is dominated by high quality factor, Q , resonant modes of the cavity itself.

The machine impedance is a function of the angular frequency ω , and it is often maximum at the resonance frequencies of cavity-like objects. A charge crossing such resonant structures, excites the fundamental and Higher Order Modes (HOM) where each mode can be treated as an electric RLC circuit (Fig. 6.1) loaded by an impulsive current I charging the capacitor with a voltage $V_0 = Cq_0$ that decays oscillating and producing a current flow in the resistor and the inductance [7, 83]. The general

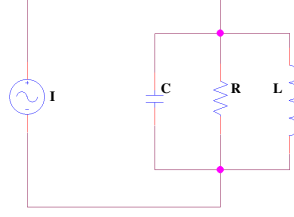


Figure 6.1: RLC circuit.

differential equation of RLC systems is :

$$\ddot{V} + \frac{1}{RC}\dot{V} + \frac{1}{LC}V = \frac{1}{C}\dot{I} \quad (6.6)$$

where R is the shunt impedance, C and L being the capacitance and inductance of the equivalent circuit. Its solution is described by a damped oscillator:

$$V(t) = V_0 e^{-\Gamma t} \left[\cos(\bar{\omega}t) - \frac{\Gamma}{\bar{\omega}} \sin(\bar{\omega}t) \right] \quad (6.7)$$

where $\omega^2 = 1/LC$ and $\Gamma = 1/2RC$ For $z = ct$ with $z > 0$ being behind the charge, the expression of the resulting wake potential (wake potential of a resonant HOM in cavity-like structures) is:

$$w_{\parallel}(z) = -\frac{V(z)}{q_0} = w_0 e^{-\Gamma z/c} \left[\cos\left(\frac{\bar{\omega}z}{c}\right) - \frac{\Gamma}{\bar{\omega}} \sin\left(\frac{\bar{\omega}z}{c}\right) \right] \quad (6.8)$$

If the aforementioned circuit is excited by an oscillating current ($I = I_0 e^{j\omega t}$), finding a solution of the type $V = V_0 e^{j\omega t}$ allows evaluating the impedance of the resonator:

$$Z(\omega) = \frac{V_0}{I_0} = Z_r(\omega) + j Z_i(\omega) = R \frac{1 - iQ \frac{\omega^2 - \omega_r^2}{\omega \omega_r}}{1 + \left(Q \frac{\omega^2 - \omega_r^2}{\omega \omega_r} \right)^2} \quad (6.9)$$

As stated in Eq. 6.9, generally $Z(\omega)$ is complex because V_0 is not in phase with the excitation I_0 ; Fig. 6.2 shows $Z_r(\omega)$ and $Z_i(\omega)$ of a resonator.

Moreover, the real part of the impedance $Z_r(\omega)$ can be thought as the power spectrum of the energy loss. In fact, the power lost P_{loss} by the beam is derived from the convolution of the impedance $Z_r(\omega)$ (a characteristic of the structure itself) with the

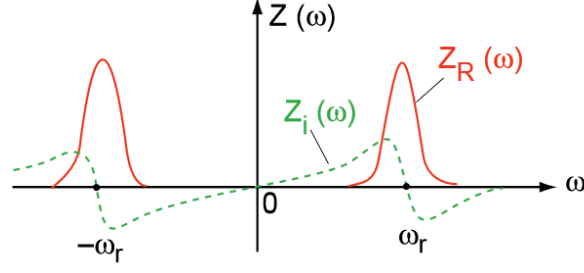


Figure 6.2: Real and imaginary parts of impedance Z of a resonator [7].

beam spectrum (a property of the beam itself, indicating the beam power at each frequency that it contains). In more details, for a beam composed of M equi-spaced equi-populated bunches of N_b protons travelling in the aperture of an accelerator equipment of longitudinal impedance Z_{long} , P_{loss} is expressed as [84]:

$$P_{loss} = 2(eMN_b f_{rev})^2 \left(\sum_{p=1}^{\infty} \text{Re} [Z_{long}(2\pi p M f_{rev})] \cdot \text{Powerspectrum}(2\pi p M f_{rev}) \right) \quad (6.10)$$

where e is the proton charge, f_{rev} the revolution frequency, $\text{Powerspectrum}(f)$ the power spectrum of the bunch as a function of frequency.

In the case of a narrow-band resonance, the impedance can be simplified near the resonant frequency f_r to:

$$Z(\omega) \approx R \frac{1 - i2Q \frac{\Delta\omega}{\omega_r}}{1 + \left(2Q \frac{\Delta\omega}{\omega_r}\right)^2} \quad (6.11)$$

and P_{loss} would reduce to:

$$P_{loss} = (eMN_b f_{rev})^2 \cdot \text{Re} [Z_{long}(f_r)] \cdot \text{Powerspectrum}(f_r) \quad (6.12)$$

The high quality factor Q resonance features a low damping rate: once the beam has induced a signal into the structure, it will oscillate during many machine turns, memorizing the fields induced during many passages of all bunches (multi-bunch effects). The converse is true for a broad-band cavity-like structure: Q is low, the damping rate is large, the induced fields collapse rapidly and are not memorized long enough to have repercussions on subsequent bunches, but only on the bunch itself

(single-bunch effects).

6.2 Beam observations

As introduced above, during the LHC Run I, the overall performance of the SR imaging system was dominated by the gradual deterioration of the extraction mirror which was not easy to identify. The continuous variation of the correction factors (described in Chapter 5) observed in 2012 evidenced that the calibration with respect to the WS was not stable and had to be rechecked often.

6.2.1 SR steering drift

A first indication of the problem was found by studying the stability of the incoming SR angle at the entrance of the optical system. By design the extracted light is directed to the optical table with a 90 degrees tilt on a 3 inches motorized mirror, which is meant to center the focused light on the camera following the proton beam orbit displacement (expected to be in the order of few hundreds of microns). However, when the LHC started to be operated above a certain beam intensity, the steering mirror horizontal tilt to be applied was found to continuously drift, as shown in Fig. 6.3. This was totally un-correlated to any beam orbit change. To evaluate the absolute value of this tilt, the actuator steps were calibrated to the corresponding angular value as explained in Fig. 6.4. The image displacement on the camera (ΔImage) caused by a Δsteps of the actuator, corresponds to a virtual displacement of the source ($\Delta\text{VirtualObject}$) after accounting for the magnification M of the optical system (represented by the equivalent lens f). Therefore, the angular tilt of the steering mirror to be applied to re-center the image results to be:

$$\beta \approx \frac{1}{M} \frac{\Delta\text{Image}}{d} = \frac{\Delta\text{VirtualObject}}{d} \quad (6.13)$$

where d is the distance between the mirror and the source. The calculated steering mirror angular tilt was found to be greater than one degree and excluded any corresponding beam orbit displacement. This indicated the deformation of the extraction

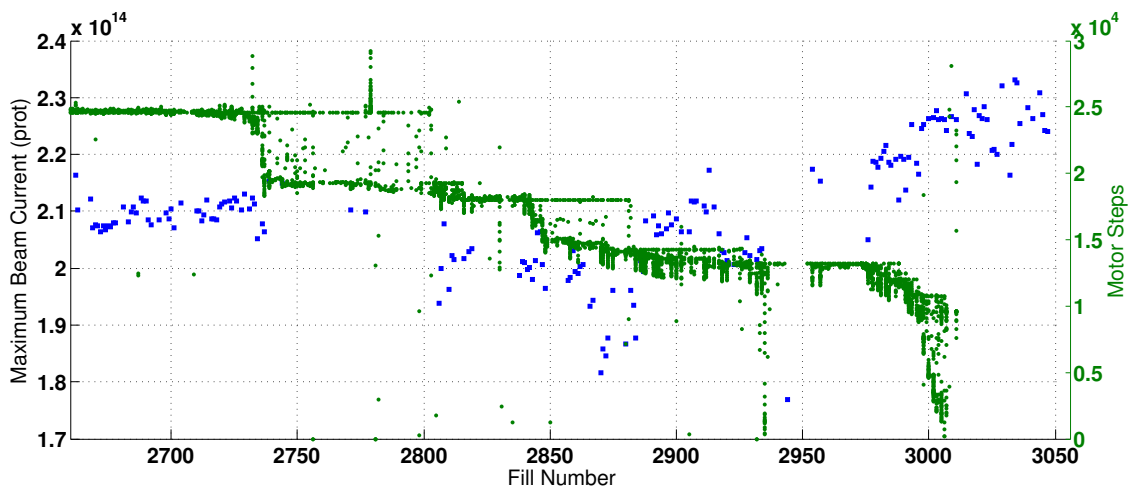


Figure 6.3: Correlation between the horizontal steering mirror motor position that was set for centering the SR on the camera (green) and the peak beam intensity per fill (blue).

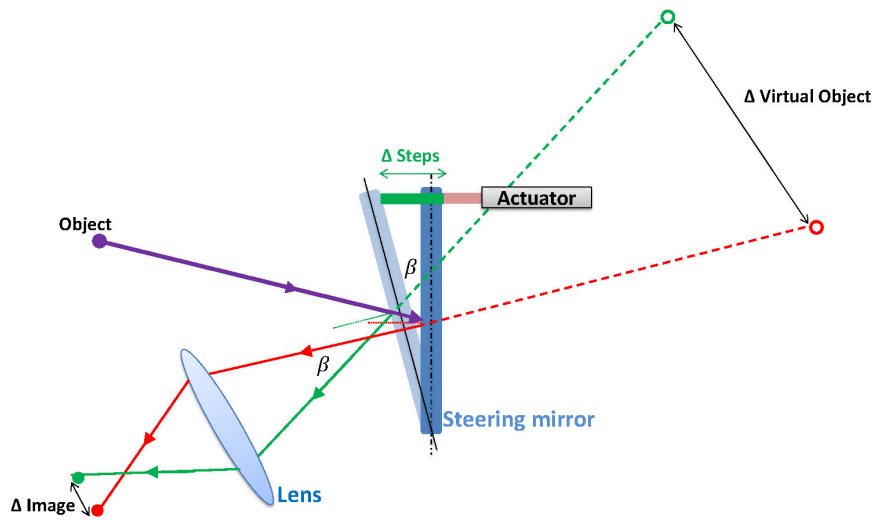


Figure 6.4: Sketch to explain the conversion of the steering mirror motor steps into the corresponding displacement of the light source (see text).

mirror (only element between the source and the steering mirror).

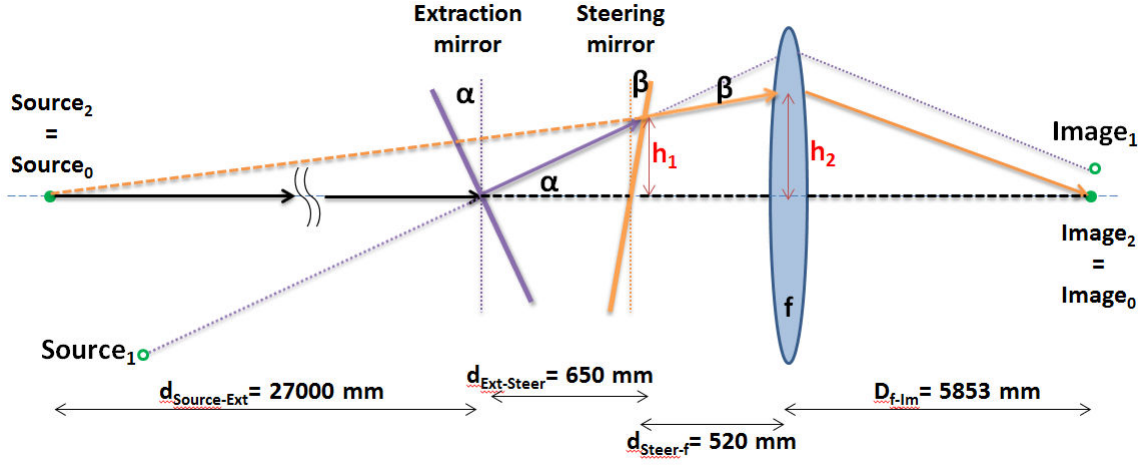


Figure 6.5: Schematics showing the steering mirror as a tool to compensate beam displacements and extraction mirror tilts for the case the LHC BSRT optical system parameters.

Referring to Fig. 6.5, the tilt of the extraction mirror can be estimated by solving the following equation:

$$\alpha - \arcsin\left(\frac{d_{\text{Extraction-Steering}} \cdot \sin(\alpha)}{d_{\text{Source-Steering}}}\right) - \beta = 0 \quad (6.14)$$

that is derived assuming that a perfect correction of an extraction mirror tilt is such that the corrected ray reaches the lens with the same angle of a direct ray originated from the source. As a result, the calculated steering mirror and the corresponding extraction mirror tilt angles are shown in Fig. 6.6, evidencing the drift in time measured in terms of motor steps (see Fig. 6.3).

6.2.2 Extraction mirror support failure and coating deterioration

The horizontal steering mirror settings plotted in Fig. 6.3 refer to several months of LHC physics fills (from July to August 2012). During this period one can identify at least two sub-periods (fills from 2740 to 2800 and from 2850 to 2875) in which at

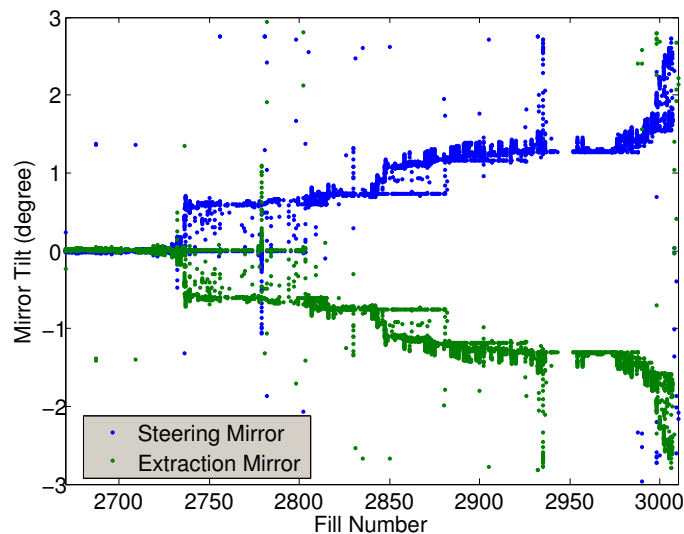


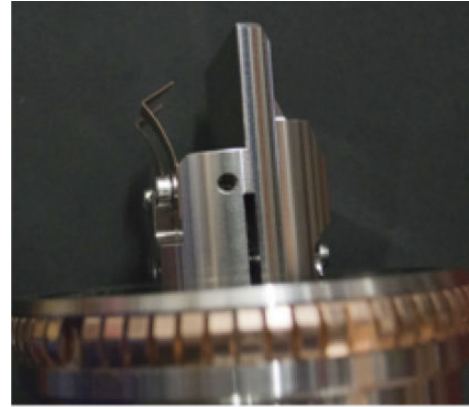
Figure 6.6: Estimated extraction mirror (blue) tilt with respect to the steering mirror tilt (green) deduced from the motor steps.

every re-fill of the LHC the steering mirror went back to the position of the previous fill. Assuming the light extraction system heating during each fill and cooling in between fills (with no beam), this means that the mirror support was suffering elastic deformations. However, the abrupt change of the initial steering at around fill 2800, fill 2875 and then the constant drift after fill 2975 evidences the occurrence of a plastic deformation. Indeed, the absence of green dots between fill 3010 and 3050 corresponds to a major failure of the mirror holder at the end of August 2012, that was followed by the system removal for inspection. As shown in Fig. 6.7, the elastic clamps designed to hold the mirror were found permanently deformed and the mirror reflective coating highly degraded.

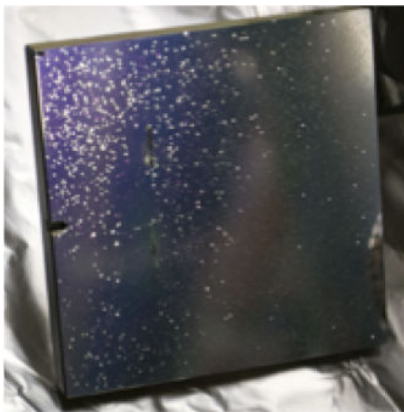
All this refers to the mirror originally chosen for the SR imaging, consisting of a silicon bulk covered with a dielectric reflective coating. Following the system failure due to heating, other mirror types were tested in order to investigate the best option to minimize the heating effects with the present tank design, while ensuring enough reflectivity:



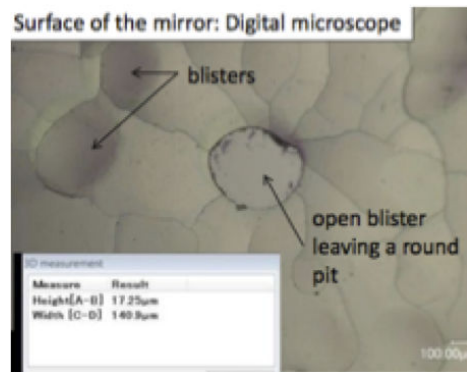
(a) Mirror as assembled before installation



(b) Holding clamps as found after the system removal



(c) Evidence of mirror coating degradation



(d) Mirror inspection at the microscope, evidencing the coating blisters

Figure 6.7: Outcome of the visual and microscopic inspection of the light extraction system after its removal in August 2012.

-
- A silicon bulk, uncoated mirror showed a similar heating (as measured with temperature probes outside the BSRT tank and observed during the MW oven tests mentioned below), and resulted to be unusable for imaging, given the distorted recorded images.
 - A glass bulk, metallic coated mirror resulted in a reduced heating effect at low beam intensities, but suffered coating deformation (evidenced by the beam spot image deformation) at high intensities.
 - A glass bulk, dielectric coated mirror resulted in a reduced heating (w.r.t. the original silicon bulk, dielectric coated mirror) and did not show any coating deformation according to the recorded images, also at high beam intensity.

This last mirror type was then chosen for the last part of the LHC Run I.

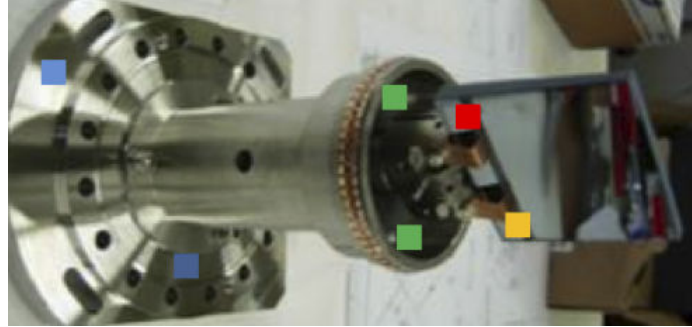
6.2.3 Temperature monitoring

After the light extraction system failure described above and the mirror type change, it was decided to equip one of the light extraction systems with in-vacuum temperature probes (see Fig. 6.8a) in order to monitor the heating with different beam conditions. During the normal LHC operation for physics, these probes evidenced a systematic heating build up for total beam intensities above a threshold of about 10^{13} protons. The heating resulted to be independent of beam energy, thus excluding the direct deposition of SR power on the structure as the heating cause (SR power increased with energy). This was also confirmed by simulations.

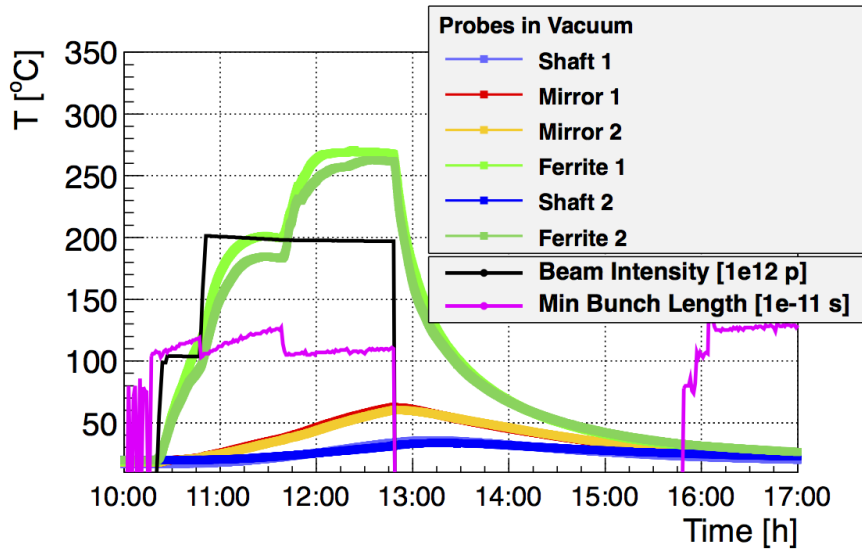
At this stage, the other candidate as heating source was electromagnetic power carried by the charged beam and coupled to the light extraction structure.

Indeed, any equipment installed in the accelerator can be characterized by its longitudinal and transverse impedance, but the real electromagnetic power that couples to the structure depends on the beam intensity (e.g. for it increases linearly with the number of bunches and quadratically with the intensity per bunch), the beam frequency spectrum and the envelope of which is defined by the longitudinal bunch length. In particular, shortening the bunch length in time results in extending the frequency beam spectrum. During a dedicated LHC study period it was possible to change in a controlled way the beam intensity and the longitudinal bunch length [85].

As shown in Fig. 6.8b, the experiment resulted in a heating very clearly correlated to the intensity variation (for a constant bunch length) and to the bunch length variation (for a constant beam intensity). The probes close to the ferrite (TT2-111R) located at the base of the mirror support to damp resonances, reached $\sim 270^\circ\text{C}$ (the ferrite Curie temperature is estimated to be $\sim 350^\circ\text{C}$). The heat is irradiated from the ferrite to the mirror and the mirror shaft.



(a)



(b)

Figure 6.8: (a) Location of the six in-vacuum temperature probes (square markers with color code corresponding to the plot below) as installed in one of the light extraction systems and (b) temperature profiles during a dedicated machine development period with varying beam intensity and longitudinal bunch length.

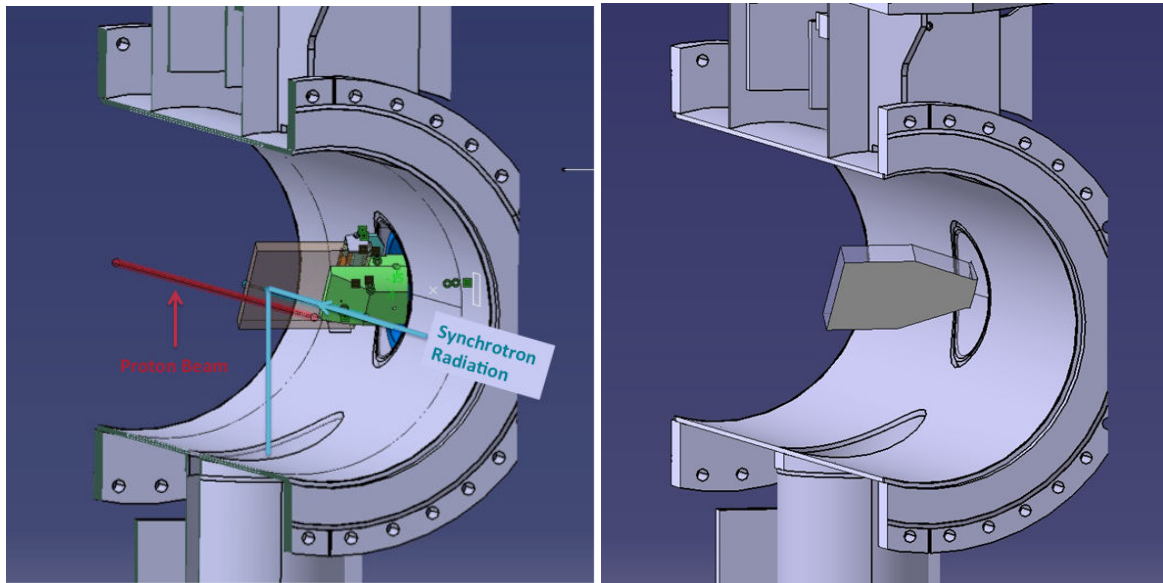
6.3 Light extraction system re-design

Overcoming the heating issues presented in Section 6.2.2, implied an alternative design of the SR extraction system, less prone to beam RF coupling. The different alternatives were constrained by the need for keeping the existing vacuum vessel in order not to affect the LHC schedule, keeping the distance from the mirror edge to the beam fixed and not reducing its area in order to not lose SR intensity. Moreover it was desirable to avoid the need of HOM damping materials, (e.g. ferrites). The different design options resulted to be:

- a system identical to the existing (see Figs. 6.8a and 6.9a), replacing the metallic elements after the RF fingers (all the parts seen by the beam) by ceramic (Macor[®]¹),
- a new design with a longer mirror inserted through a slit into the beam-pipe, where the mirror holder and shaft are completely hidden (see Figs. 6.13 and 6.9b).

These two options have been compared to the old design at first by means of EM simulations in order to estimate the improvements in terms of EM coupling. The simulations [8] were based on 3D models of the BSRT light extraction system excited by a nominal LHC bunch (50 mm RMS length, 17 nC charge), analyzed in time domain with the CST Particle Studio Wake field[®] solver [87]. The simulations implied the use of the Finite Elements Method (FEM) to numerically model the geometries. The wake field analysis was carried out for the two geometries shown in (Fig. 6.9a and 6.9b), corresponding to pre-LS1 and post-LS1 configurations. The wake was simulated along 50 m, discretizing the structure in equidistant 1.3 mm 35.10^6 hexahedral mesh cells omitting screws, pins and the mirror coating and simplifying the springs contact. The boundaries in the transverse directions were set to electric and "WaveGuides" ports were used as open boundaries in the longitudinal direction for better energy absorption. The wake response has then been converted in longitudinal impedance as function of frequency, via FFT transformations. The results are shown

¹Macor[®] is the trademark for a machineable glass-ceramic developed and sold by Corning Inc. Macor is made up of fluorphlogopite mica in a borosilicate glass matrix. Its composition is roughly: 46% silica (SiO₂) 17% magnesium oxide (MgO) 16% aluminium oxide (Al₂O₃) 10% potassium oxide (K₂O) 7% boron trioxide (B₂O₃) 4% fluorine (F) [86]



(a) Old system, simulated (and then measured in the laboratory) with metallic and ceramic holder materials

(b) New system, only metallic

Figure 6.9: 3D models of the old and new light extraction systems (courtesy of W. Andreazza).

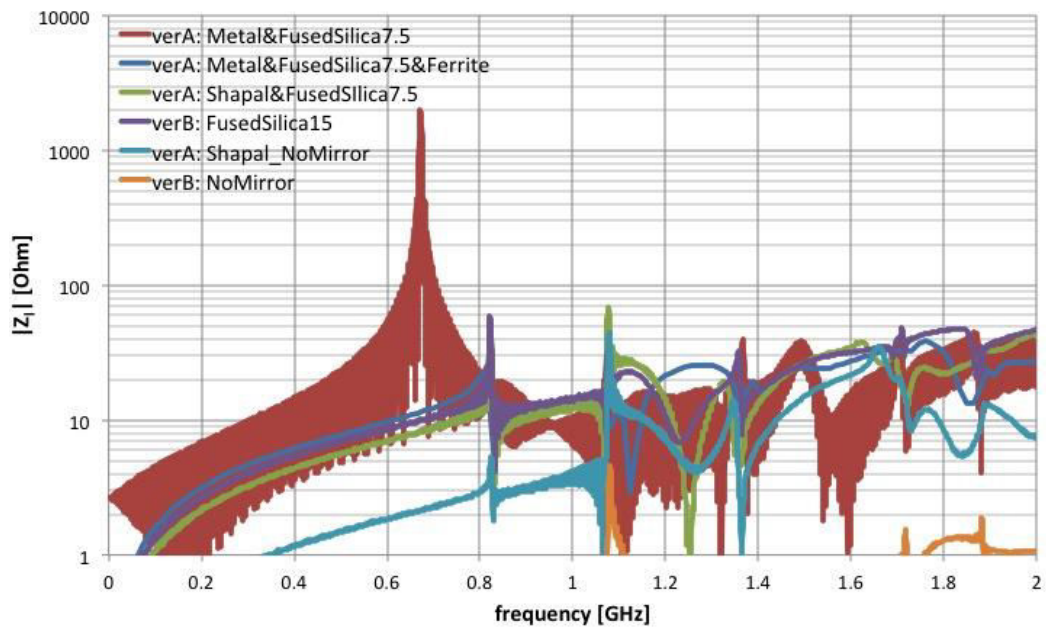


Figure 6.10: Simulated Longitudinal impedance by the mean of CST comparing different combinations of mirror holder materials [8].

in Fig. 6.10, that compares the magnitude of the longitudinal wake impedance for the different configurations. These results have been cross-checked with *eigen mode solvers* directly in frequency domain, via the ACE3P Omega3P suite [88].

Despite the relative confidence in the simulation results, the need for laboratory measurements resulted from the difficulty (/impossibility) of simulating, in reasonable computing times, the effect of thin layers of coating and small pieces (screws, pins and springs contact) in the complex geometry of this big tank. Moreover, modeling the effect of ferrites as RF absorbers can be very difficult.

6.4 Coupling impedance laboratory measurements

This section presents a bench measurement technique for coupling impedance characterization and its application to to the BSRT tanks.

6.4.1 Stretched wire technique

The coaxial wire method has been in use for more than four decades for impedance and loss factor determination on the bench because of the ease with which the measurements may be carried out. Since it was first proposed by Sands and Rees in 1974 it undertook several revisions in technique especially the ones proposed by Gluckstern and Vaccaro [89, 90, 91, 92]. Its principle relies on the similarity between the field pattern generated by a current passing through a wire in a coaxial structure and the wake fields left by a bunch passing through the structure. In fact, a moving charged particle produces an electromagnetic field in an arc transverse to its direction of motion, where the angle of the arc opening is proportional to $1/\gamma$. Therefore the field pattern generated by an ultra-relativistic particle, is entirely perpendicular to the direction of motion and can be expressed by:

$$E_r(r, \omega) = Z_0 H_\phi(r, \omega) = \frac{Z_0 q}{2\pi r} e^{-j\frac{\omega}{c}z} \quad (6.15)$$

This expression is similar to the one for a TEM (Transverse Electrical and Magnetic) mode propagated by a short electrical pulse sent along a conductive wire along the

same path of the particle:

$$E_r(r, \omega) = Z_0 H_\phi(r, \omega) = Z_0 \frac{\text{const}}{r} e^{-j\frac{\omega}{c}z} \quad (6.16)$$

This technique uses the substitution method: a signal is propagated from one end of the device under test (DUT) and recorded on the other end, thus giving the scattering parameter S_{21} , which is a measurement of the EM power transmitted along the structure.

Then the DUT is replaced by a smooth beam-pipe, the reference pipe (REF), and the measurement repeated. From simple transmission line theory, it is possible to

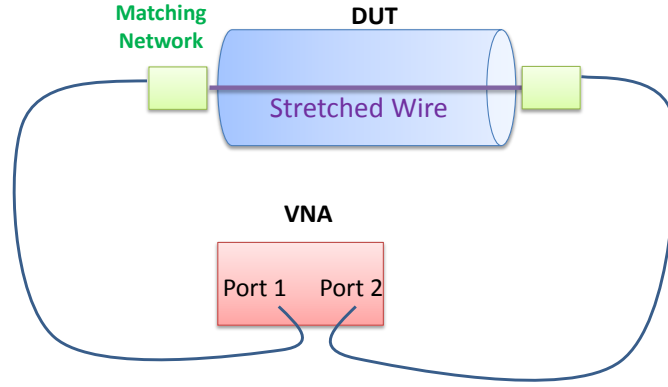


Figure 6.11: Stretched Wire technique for coupling impedance measurement.

derive a relationship between the longitudinal distributed coupling impedance of the DUT Z_{\parallel} and the ratio of transmission parameters, S_{21} , of the DUT and a reference structure [93]:

$$Z_{\parallel} = -2Z_c \ln \left(\frac{S_{21,\text{DUT}}}{S_{21,\text{REF}}} \right) \left[1 + j \frac{\ln \left(\frac{S_{21,\text{DUT}}}{S_{21,\text{REF}}} \right)}{2\Theta} \right] \quad (6.17)$$

where L and $\Theta = 2\pi \frac{L}{\lambda}$ are the mechanical and the normalised electric lengths of the device and Z_c is the characteristic impedance calculated as a coaxial line approximation:

$$Z_c = \frac{Z_0}{2\pi} \ln \left(\frac{d_{\text{TANK}}}{d_{\text{WIRE}}} \right) \quad (6.18)$$

with $Z_0 = 120\pi [\Omega]$ being the free space impedance and d_{TANK} , d_{WIRE} respectively the inner diameter of the DUT and the diameter of the stretched wire.

In the experimental setup shown in Fig. 6.11, the external circuit (i.e. VNA, cables, transition between connections...) is electrically matched to the characteristic impedance of the coaxial line inside the DUT through a matching network either by adding a resistive network between the DUT and the external circuit or by a physical tapering.

It is worth noting that the “wire measurements” on cavities (expected resonances with high Q) are in general not recommended due to the strong mode perturbation caused by the presence of the wire itself [94].

6.4.2 Experimental results

For the laboratory experiments, a spare BSRT tank (Fig. 6.12) was used. A metallic wire of 500 μm diameter was installed along the tank axis with a horizontal transverse offset of 11 mm, thus reproducing the beam trajectory. The measurements were performed at first on the bare (empty) tank (acting as the reference) and then on the tank equipped with the following extraction mirror designs:

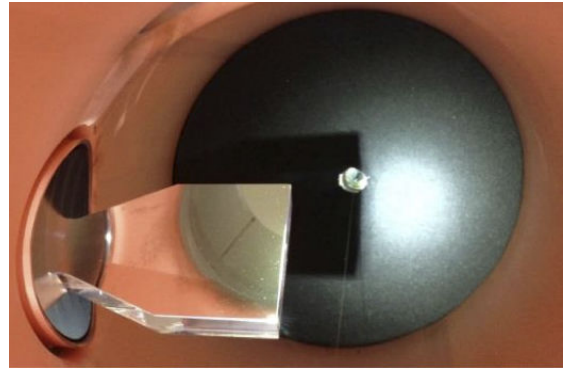
- old (metallic) (see Fig. 6.9a)
- new metallic (see Figs. 6.9b and 6.13)
- new ceramic (see Fig. 6.14).



Figure 6.12: Laboratory setup for wire measurements.



(a)



(b)

Figure 6.13: New Design of the extraction mirror, on the measurement bench. To be noted the absence of the cavity-like shape created by the mirror holder in the old design.



Figure 6.14: Alternative holder design, based on the initial metallic holder, except that all the parts seen by the beam were replaced by ceramic.

The characteristic impedance of the empty tank was estimated using Eq. 6.18 and was found to be $\sim 360 \Omega$,

Knowing the characteristic impedance of the VNA and associated cables to be $Z_{c_0} = 50 \Omega$, a matching resistor was added in series just before the DUT to resistively match the characteristic impedance (as seen by the DUT) of the VNA and associated measurement setup to that of the DUT. The series resistance is simply calculated by $R_s = Z_c - Z_{c_0} = 310 \Omega$. However also a 10 dB attenuator was used as shown in Fig. 6.15 to reduce the effect of reflections from the mismatch between the VNA and the resistor. However, this matching is (partially) effective only for frequencies $< 1 \text{ GHz}$ and the high frequency matching was realized by a disk made out of 50 mm thick microwave absorbing foam [95].

Figure 6.16 compares the matching for a reference beam tube with and without absorbing foam when measuring the bare BSRT tank (600 mm long, 213 mm diameter). The foam effect at high frequencies is efficient, whereas, as expected, at low frequencies the matching with lumped resistors is not perfect. The first step for qualifying the stretched wire setup was to crosscheck its results with the EM simulations discussed above in the simple case of no mirror (i.e. mirror holder only) and no ferrites. For this, a series of transmission measurements (in terms of S_{21} scattering parameters) were carried out for different metallic mirror holder offsets w.r.t. the wire. Figure 6.17 shows the center frequencies and the correspondent attenuation of the main resonance located around 700 MHz for the different distances (where Holder Pos=60 mm is the nominal position when in operation) . The agreement between the wire measurement and the simulations is found to be within $\pm 10 \%$. The second set of measurements aimed at checking the effect of different mirror materials while



Figure 6.15: Matching Network for the "stretched wire" technique composed of attenuators, matching resistor and absorbing foam.

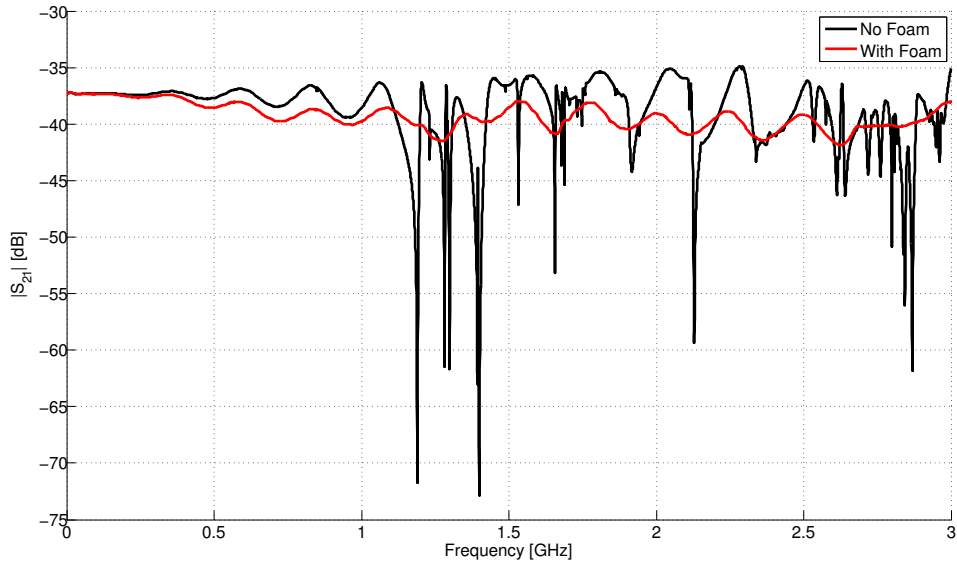


Figure 6.16: Empty Tank reference S_{21} measurement with (red) and without (black) the absorbing foam used for matching at high frequencies.

maintaining the same extraction system (metallic holder). Figure 6.18 presents the measured S_{21} parameters for the following setups:

- inserting a bare metallic holder with no mirror mounted and no ferrites installed (black),
- mounting on the metallic holder respectively three types of mirrors (SI bulk + dielectric coating, glass bulk + metallic coating, glass bulk + dielectric coating).

In both cases the mirror edge was set at the nominal distance (20 mm from wire/beam). The Si bulk mirror with dielectric coating (in operation till 2012) and the glass bulk mirror with metallic coating (red and blue curve in the figure) result in a very similar S_{21} values. Both manifest a significant attenuation (~ 7 dB) around 550 MHz with fairly high Q value and several dips ~ 2 dB around 1.3, 1.5 and 1.7 GHz. Contrarily, the dielectric coating on the glass bulk mirror (green curve) introduces a smaller perturbation in the structure whereas the highest resonance observed around 700 MHz is very similar to the one observed with the bare metallic holder (black).

As a result of these measurements, the beam observations are confirmed since the

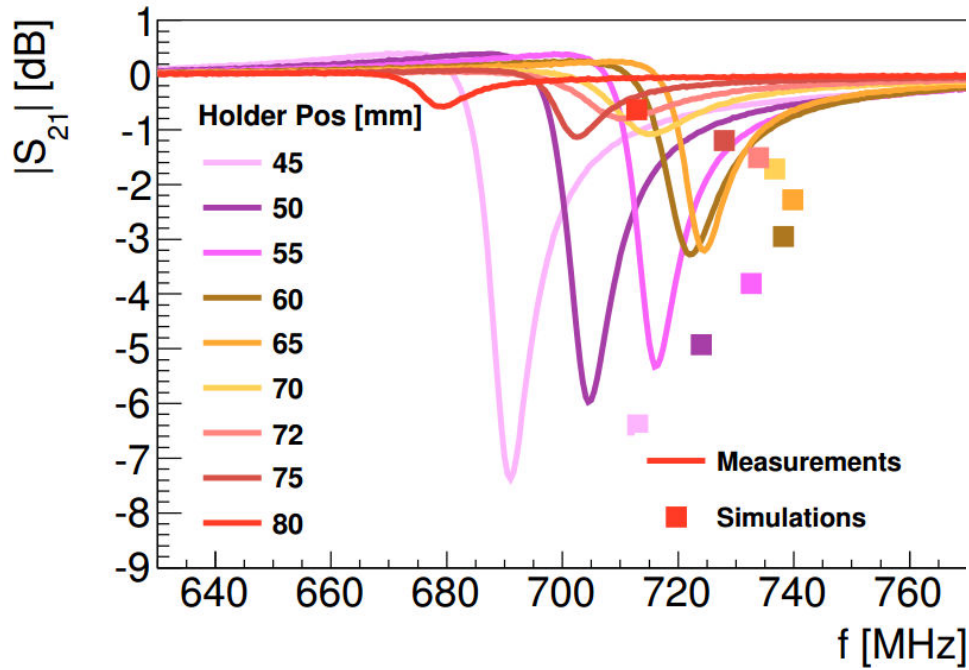


Figure 6.17: Transmission measurement compared to simulations for the metallic holder with no mirror installed and no ferrites, at different distances from the beam (60 mm being the nominal position).

glass mirror with dielectric coating showed no sign of heating. In the following, this mirror will be used for the validation of the different proposals of mirror holders.

Finally, the measured S_{21} for the two new proposals has been compared to the one of the initial design, as shown in Fig. 6.19. Both proposals result in a significant improvement, as for frequencies <1 GHz, the maximum attenuation is found to be less than 1 dB around 800 MHz.

Even though the ceramic setup features smaller attenuation and eventually less heating with respect to the new fully metallic proposed holder, the latter is considered to be the best option due the fragility of the Macor®holder and the consequent risks for its use under continuous thermal cycles.

In conclusion, the final new design consists of the combination of the modified metallic holder coupled to a longer glass bulk mirror coated with reflective dielectric layer. Fig. 6.20 shows the comparison of the initially installed extraction system

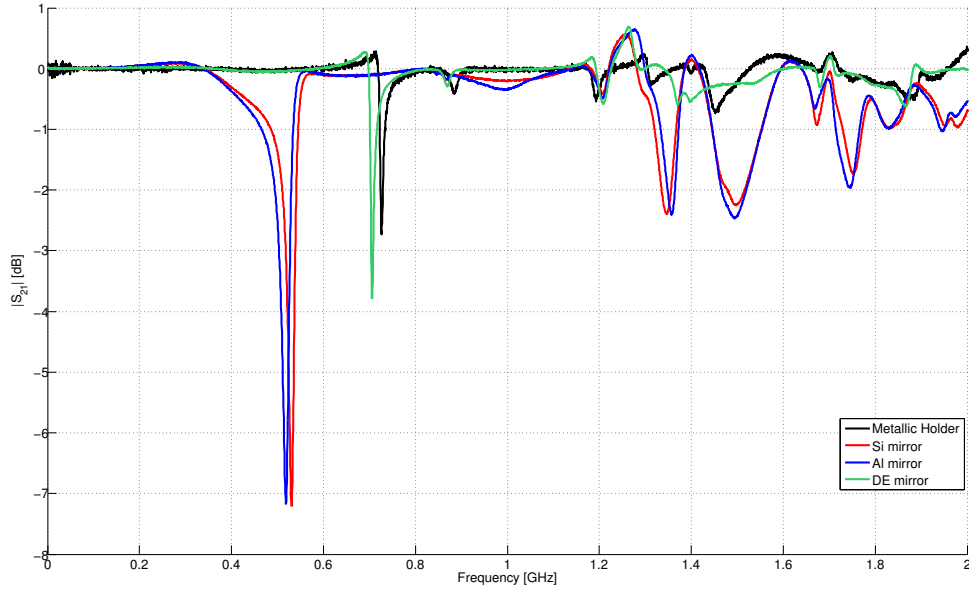


Figure 6.18: Measured scattering parameter S_{21} via stretched wire technique comparing, at the nominal distance (20 mm from wire/beam), the effect of inserting the metallic mirror holder with no mirror mounted and no ferrites installed (black) with the configuration with three different types of mirrors.

in operation since 2012 (black), and the extraction system installed during LS1 for 2015 operation (red). To be noticed that the 2012 setup includes also the ferrites responsible for the observed attenuation broadening and peak reduction.

Using Eq. 6.17, the corresponding longitudinal coupling impedance is calculated and shown in Fig. 6.21. Consequently, according to Eq. 6.10, the power coupled from the beam to the extraction system, can be calculated. The LHC beam power spectrum was measured [84] with 50 ns bunch spacing (see Fig. 6.22). It can be seen that the power spectrum consisted of sharp harmonics (blue, separated by the inverse of the time bunch spacing, in this case 20 MHz line spacing originates from 50 ns bunch spacing) contained in a multi-lobe envelope (green, with width determined by the bunch length). In the calculations, in order to be immune to eventual shifts of the notches in the spectrum due to the energy change in the machine, the red line will be used in the power loss calculations as an overestimation of the power spectrum of the beam. Figure 6.23, shows for both configurations (2012 vs. 2015) the power lost

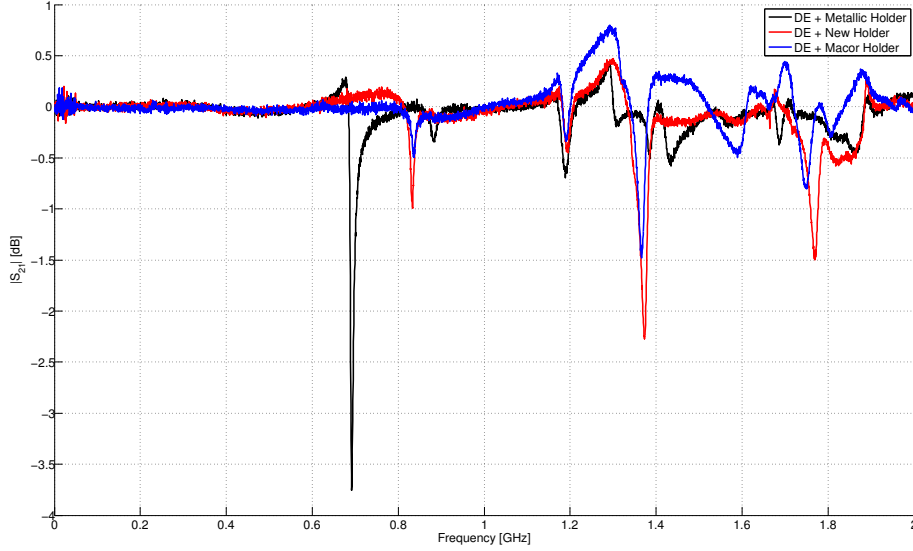


Figure 6.19: Measured scattering Parameter S_{21} for different mirror holders via the stretched wire technique were compared. The glass mirror with dielectric coating was mounted on the three mirror holders (old metallic in black, new ceramic in blue and the new modified metallic in red) and positioned at the nominal distance (20 mm from wire/beam).

in the structure when the circulating beam consists in 2808 bunches (nominal LHC filled with bunches spaces by 25 ns), each populated by $1.3 \cdot 10^{11}$ protons. On one hand, the total power lost in the pre-LS1 system amounts to ~ 36 W. On the other hand, it reaches ~ 10 W in the post-LS1 system.

However, as it was already pointed out in Fig. 6.18, by comparing S_{21} in absence of a mirror and after installing the glass mirror with dielectric coating, the difference consists mainly in an additional attenuation around 700 MHz and 1.4 GHz. Therefore it is justified considering only the integrated power loss around these frequencies as the power absorbed by the mirror. This integration has been performed using the power loss spectrum shown in the lower plot of Fig. 6.23, that yields a power loss in the glass bulk of ~ 4 W in the worst case where in the NB approximation (Eq. 6.12), the impedance couples fully with a line of the beam spectrum.

Based on the calculations above, it is possible to get a first approximation of the equilibrium temperature reached by the extraction mirror in operation. The

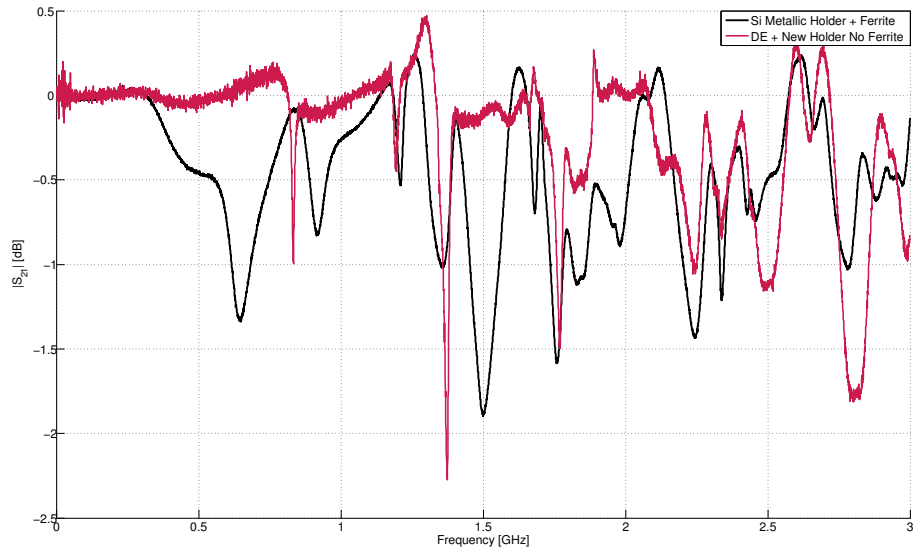


Figure 6.20: Measured scattering Parameter S_{21} via stretched wire technique, comparing original BSRT extraction system (silicon bulk mirror mounted on metallic holder with ferrites) in black and the new design for after LS1 operation (glass mirror with dielectric coating mounted on a modified metallic holder without ferrites) in red.

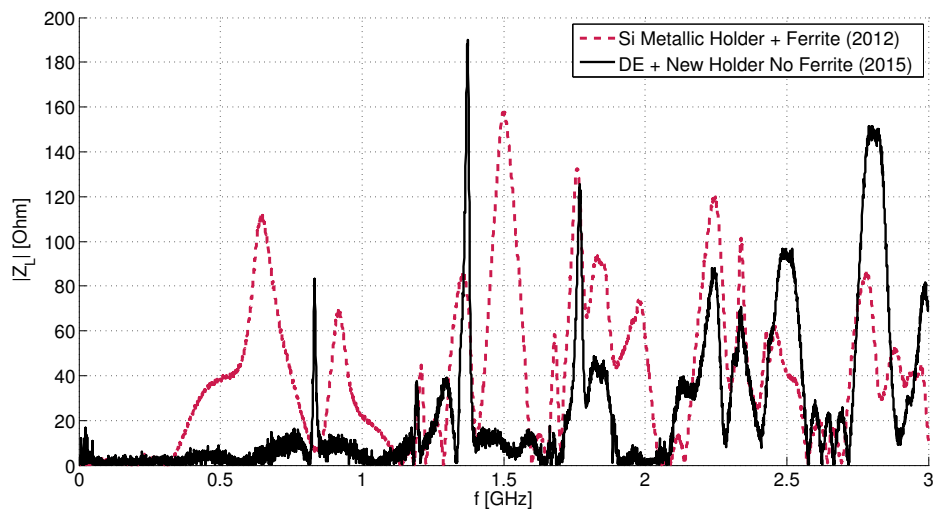


Figure 6.21: Calculated coupling impedance Z_L of the initially installed extraction system (2012 in black) and the newly designed and installed system (2015 in red).

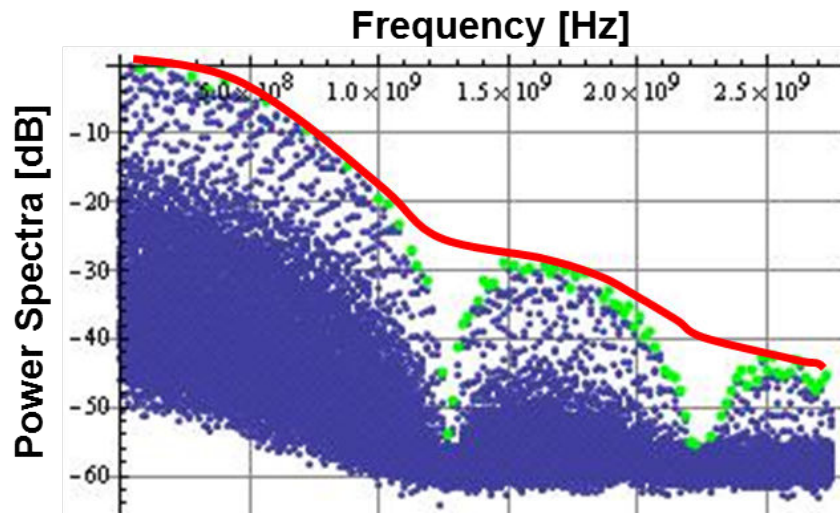


Figure 6.22: LHC beam spectra measured during proton fill 2261 at injection energy (blue). The green dots reveal the peaks and used only for visual purpose. The red line is an envelope of the lobes higher peaks [9].

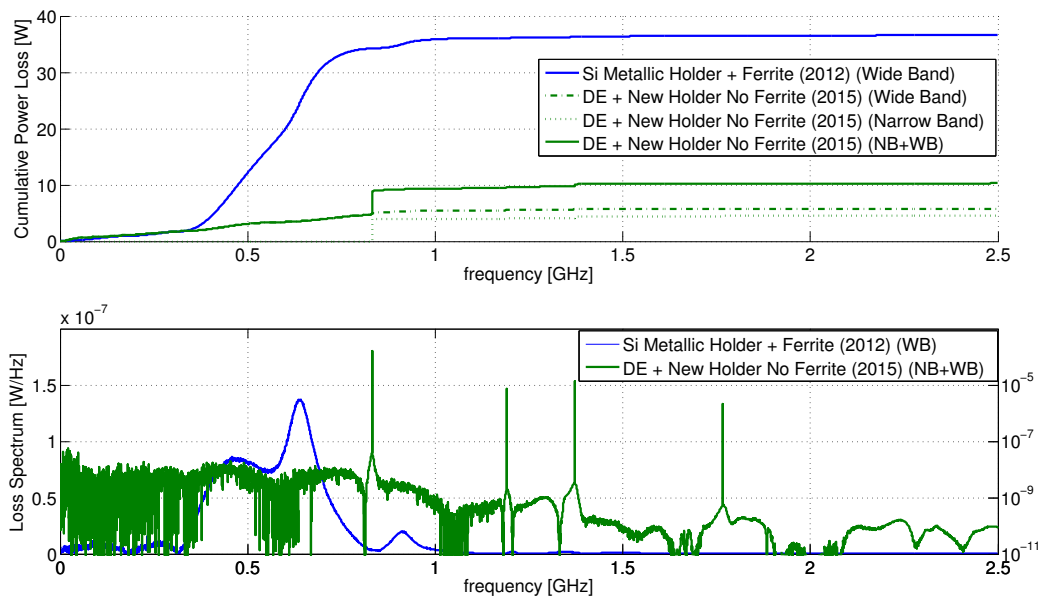


Figure 6.23: Power lost in the two versions of the SR extraction system (2012 (pre-LS1) in blue and 2015n (post-LS1) in green). The upper plot shows the cumulative power lost in Watt, while the lower plot shows the power loss spectrum in Watt/Hz.

approximation relies on the very pessimistic hypothesis that all the power lost by the beam is absorbed by the glass mirror. Moreover, the cooling is assumed to be possible only by radiation, since convection is ruled out in LHC ultra vacuum conditions and conduction is ineffective due to the very limited contacts between the mirror and its holder. Under these assumptions, the final temperature reached can be computed referring to the black body radiation equilibrium [96]:

$$T_{eq} = \left(\frac{P_{abs}}{\epsilon \cdot \sigma_B \cdot S} + T_{amb}^4 \right)^{\frac{1}{4}} - 273 \quad (6.19)$$

where T_{amb} , T_{eq} are respectively the ambient temperature and the reached equilibrium temperature of the mirror after absorbing the power P_{abs} and radiating via "black body" radiation from a total surface S . In addition, $\sigma_B = 5.67 \cdot 10^{-8} \text{ Wm}^{-2}\text{K}^4$ is the StefanBoltzmann constant and ϵ is the mirror emissivity considered 0.7 for coated glass¹.

The resulting mirror equilibrium temperature in the post-LS1 extraction system, as calculated by Eq. 6.19, amounts to $\sim 90^\circ\text{C}$. This temperature is reached in about two hour [97] with a small temperature gradient. Accordingly, the mirror will be heated uniformly and no important distortions are expected.

A good agreement was found between the EM simulations and the laboratory measurements in terms of wake fields, impedance and power loss. This reinforces the confidence in the effectiveness of the longer glass mirror with dielectric coating proposal in terms of reduced beam coupling and heating.

Furthermore, investigations are carried out by the mean of more accurate EM simulations (higher level of modeled details, increased number of meshes). Even though it implies longer simulation time and higher computational load, it allows a detailed study of the first resonance merit factor Q . It is a final confirmation needed for validating this new design since, as already stated, "wire measurements" results would be compromised by the presence of very narrow resonances with high Q values.

¹Considered to be a good approximation since only one side of the glass bulk is coated.

Chapter 7

From Beam Size to Beam Emittance: Optical Functions

An accurate measurement of the beta function at the location of a beam size monitor is necessary for the determination of the beam emittance, expressed as:

$$\varepsilon_{n_{x,y}} = \frac{\gamma\beta}{\beta_{x,y}} \left[\sigma_{x,y}^2 - \left[D_{x,y} \cdot \left(\frac{\Delta p}{p} \right) \right]^2 \right] \quad (7.1)$$

where $\sigma_{x,y}$ is the beam size measured by the monitor, $\beta_{x,y}$, $D_{x,y}$ are respectively the machine betatron and dispersion functions, p is the average particle momentum and Δp is the particle momentum distribution standard deviation.

The error propagation from $\beta_{x,y}$, $\sigma_{x,y}$, $D_{x,y}$, $\frac{\Delta p}{p}$ to the overall relative error on the emittance can be approximated in the case of small perturbations as:

$$\begin{aligned} \epsilon_{\varepsilon_{x,y}} &= \frac{\Delta\varepsilon_{x,y}}{\varepsilon_{x,y}} \\ &= \frac{1}{\varepsilon_{x,y}} \left[\left| \frac{\partial\varepsilon_{x,y}}{\partial\beta_{x,y}} \right| |\Delta\beta_{x,y}| + \left| \frac{\partial\varepsilon_{x,y}}{\partial\sigma_{x,y}} \right| |\Delta\sigma_{x,y}| + \left| \frac{\partial\varepsilon_{x,y}}{\partial D_{x,y}} \right| |\Delta D_{x,y}| + \left| \frac{\partial\varepsilon_{x,y}}{\partial \frac{\Delta p}{p}} \right| \left| \Delta \frac{\Delta p}{p} \right| \right] \end{aligned} \quad (7.2)$$

where:

$$\begin{aligned}
\frac{\partial \epsilon_{x,y}}{\partial \beta_{x,y}} &= -\gamma\beta \left[\sigma_{x,y}^2 - \left(D_{x,y} \frac{\Delta p}{p} \right)^2 \right] \frac{1}{\beta_{x,y}^2} \\
\frac{\partial \epsilon_{x,y}}{\partial \sigma_{x,y}} &= 2 \frac{\gamma\beta}{\beta_{x,y}} \sigma_{x,y} \\
\frac{\partial \epsilon_{x,y}}{\partial D_{x,y}} &= \frac{\partial \epsilon_{x,y}}{\partial \frac{\Delta p}{p}} = -2 \frac{\gamma\beta}{\beta_{x,y}} D_{x,y} \left(\frac{\Delta p}{p} \right)
\end{aligned} \tag{7.3}$$

Therefore, the uncertainty on the emittance determination $\epsilon_{\epsilon_{x,y}}$ is expressed in terms of errors on the beam size measurement $\epsilon_{\sigma_{x,y}}$, the momentum spread $\epsilon_{\frac{\Delta p}{p}}$ and the optical function $\epsilon_{\beta_{x,y}}, \epsilon_{D_{x,y}}$:

$$\epsilon_{\epsilon_{x,y}} = \epsilon_{\beta_{x,y}} + \frac{2 \left[(\sigma_{x,y})^2 \epsilon_{\sigma_{x,y}} + \left(\frac{\Delta p}{p} D_{x,y} \right)^2 \epsilon_{D_{x,y}} + \left(D_{x,y} \left(\frac{\Delta p}{p} \right)^2 \right) \epsilon_{\frac{\Delta p}{p}} \right]}{\sigma_{x,y}^2 - \left(D_{x,y} \frac{\Delta p}{p} \right)^2} \tag{7.4}$$

Since for the LHC case $D_{x,y} \ll 1$, Eq. 7.4 reduces to:

$$\epsilon_{\epsilon_{x,y}} = \epsilon_{\beta_{x,y}} + 2 \epsilon_{\sigma_{x,y}} \tag{7.5}$$

Given that the errors on the betatron functions $\beta_{x,y}$ at the monitors linearly sum up to the errors on the beam size measurement itself, in order to reduce the overall uncertainty, it is desirable to have the best knowledge possible of the betatron function. The standard techniques used at LHC to monitor the betatron function deviation from the the accelerator model [98] are specially designed for measurements in the superconducting arcs and are not optimized for precise measurements in the straight section IR4, where most of the profile monitors sit. For this reason, during the LHC Machine Development (MD) periods in 2012, a total of eight hours of the beam instrumentation studies time was dedicated for the first time to the betatron function measurements at the location of the transverse profile monitors (BSRT, WS and BGI) in IR4 via the K-modulation method, explained in the next section.

7.1 K-modulation

The K-modulation technique concept is shown in Fig. 7.1. The value of the mean betatron function at a quadrupole location is directly obtainable by modulating the gradient of the quadrupole and measuring the consequent betatron tune modulation.

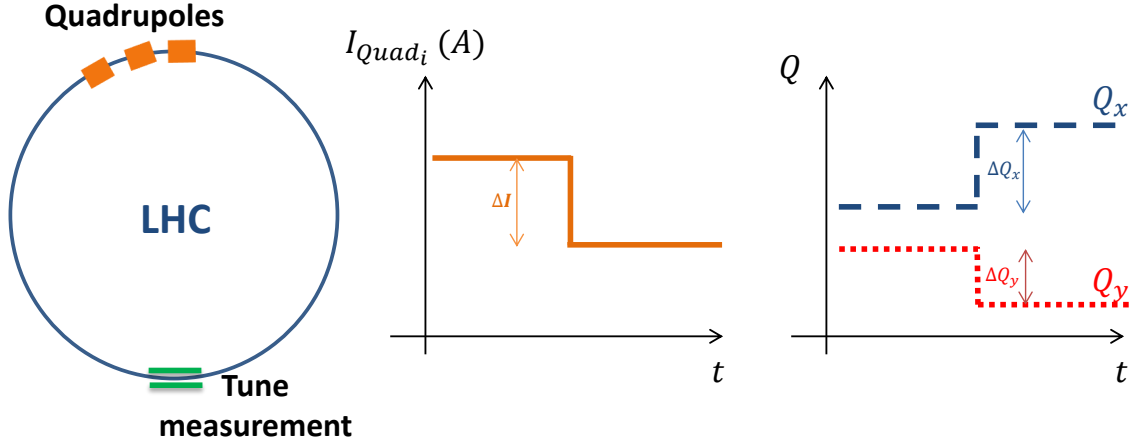


Figure 7.1: K-modulation working principle.

The underlying physics can be obtained from the One Turn Map (OTM) concept explained in the following section.

7.1.1 Measurement technique

The beam transport matrix introduced in 1.2.4 is defined as:

$$M(s_1|s_2) = \begin{pmatrix} \sqrt{\frac{\beta_2}{\beta_1}} (\cos\varphi_{21} + \alpha_1 \sin\varphi_{21}) & \sqrt{\beta_2\beta_1} \sin\varphi_{21} \\ -\frac{1+\alpha_1\alpha_2}{\sqrt{\beta_2\beta_1}} \sin\varphi_{21} + \frac{\alpha_1-\alpha_2}{\sqrt{\beta_2\beta_1}} \cos\varphi_{21} & \sqrt{\frac{\beta_1}{\beta_2}} (\cos\varphi_{21} - \alpha_2 \sin\varphi_{21}) \end{pmatrix} = \begin{pmatrix} S & C \\ S' & C' \end{pmatrix} \quad (7.6)$$

The OTM matrix (M_{otm}) is the particular case of the beam transport matrix when considering a full turn around the machine (i.e. $s_2 = s_1$ and phase advance $\varphi_{1turn} = 2\pi Q$):

$$M_{otm} = \begin{pmatrix} \cos(2\pi Q_{x,y}) + \alpha_{x,y} \sin(2\pi Q_{x,y}) & \beta_{x,y} \sin(2\pi Q_{x,y}) \\ -\gamma_{x,y} \sin(2\pi Q_{x,y}) & \cos(2\pi Q_{x,y}) - \alpha_{x,y} \sin(2\pi Q_{x,y}) \end{pmatrix} \quad (7.7)$$

with its trace:

$$\text{tr}(M_{otm}) = 2 \cos(2\pi Q_{x,y}) \quad (7.8)$$

The quadrupole excitation is expressed as (in thin lens approximation):

$$\Delta K = l_q \cdot \frac{B_T}{(B\rho) a} \quad (7.9)$$

with l_q being the effective magnetic length of the quadrupole, B_T and a respectively the pole-tip field and radius and $(B\rho)$ the magnetic rigidity. Such an excitation represents a perturbation of the M_{otm} resulting in a new turn map given by:

$$\begin{aligned} M_{otm_{fin}} &= M_{otm_{old}} \cdot M_{perturbation} \\ &= M_{otm_{old}} \cdot \begin{pmatrix} 1 & 0 \\ -(\pm\Delta K) & 1 \end{pmatrix} \end{aligned} \quad (7.10)$$

A relation between the tune Q_{fin} before and Q_{old} after the excitation, is obtained by expressing the traces of the matrices of the right and left hand side of Eq. 7.10 as:

$$\begin{aligned} 2 \cos(2\pi Q_{fin_{x,y}}) &= 2 \cos(2\pi (Q_{old_{x,y}} + \Delta Q_{x,y})) \\ &= 2 \cos(2\pi Q_{old_{x,y}}) - \beta_{x,y} (\pm\Delta K) \sin(2\pi Q_{old_{x,y}}) \end{aligned} \quad (7.11)$$

Solving for $\beta_{x,y}$, we obtain:

$$\beta_{x,y} = \pm \frac{2}{\Delta K} [\cot(2\pi Q_{ini_{x,y}}) \{1 - \cos(2\pi \Delta Q_{x,y})\} + \sin(2\pi \Delta Q_{x,y})] \quad (7.12)$$

When the tunes $Q_{x,y}$ are far from the integer and half integer resonances and the observed variation $\Delta Q_{x,y}$ is small, Eq. 7.12 is approximated by [99]:

$$\beta_{x,y} \approx 4\pi \frac{\Delta Q_{x,y}}{\Delta K} \quad (7.13)$$

7.1.2 Experimental results

In the IR4 region of the LHC, housing the beam size monitors (BSRT, BGI, WS), the individually powered quadrupoles listed in Tab. 7.1 were chosen for this study; their position with respect to the WS and the BSRT light sources (undulator and bending dipole D3) are shown in Fig. 7.2. The measurements were carried out at injection energy (450 GeV) and flattop energy (4 TeV) with injection optics and repeated with the squeezed optics¹. Even though by design the optics in IR4 is static and in principle invariant, spurious changes to the betatron and dispersion function propagated from neighbouring IPs are not to be excluded.

Modulated Quadrupoles	
BEAM 1	BEAM 2
MQ.5R4.B1	MQ.5R4.B2
MQ.6R4.B1	MQ.5L4.B2
MQ.7R4.B1	MQ.6L4.B2
MQ.5L4.B1	

Table 7.1: List of the modulated Quadrupoles in both beams.

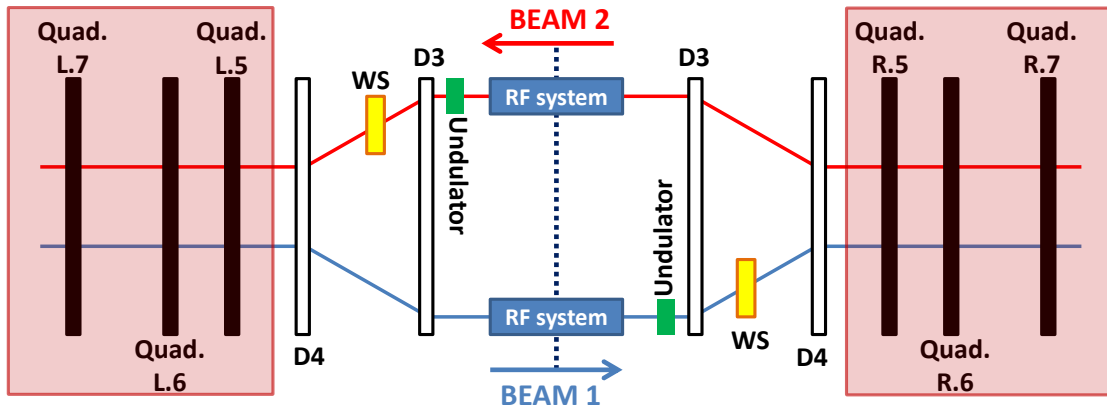


Figure 7.2: Schematics of IR4 showing the quadrupoles IP4

¹Squeezed and Un-squeezed optics refer to the β^* value at the collision point IPs ranging from 10 m before the squeeze down to 65 cm at collision.

The LHC tune measurement relies on the diode-based base-band-tune (BBQ) technique [100]. In order to have a clean Q measurement from the BBQ, even at flat-top, the machine was operated at the design injection tunes ($Q_x = 0.28, Q_y = 0.31$), the coupling was minimized and the orbit was optimized. The magnetic strength of each of the quadrupoles listed above was modulated separately, by applying sub-Amperes trims to the current (maximum overall current change $\sim 2 A$ equivalent to an overall change of $k \sim 10^4 m^{-1}$).

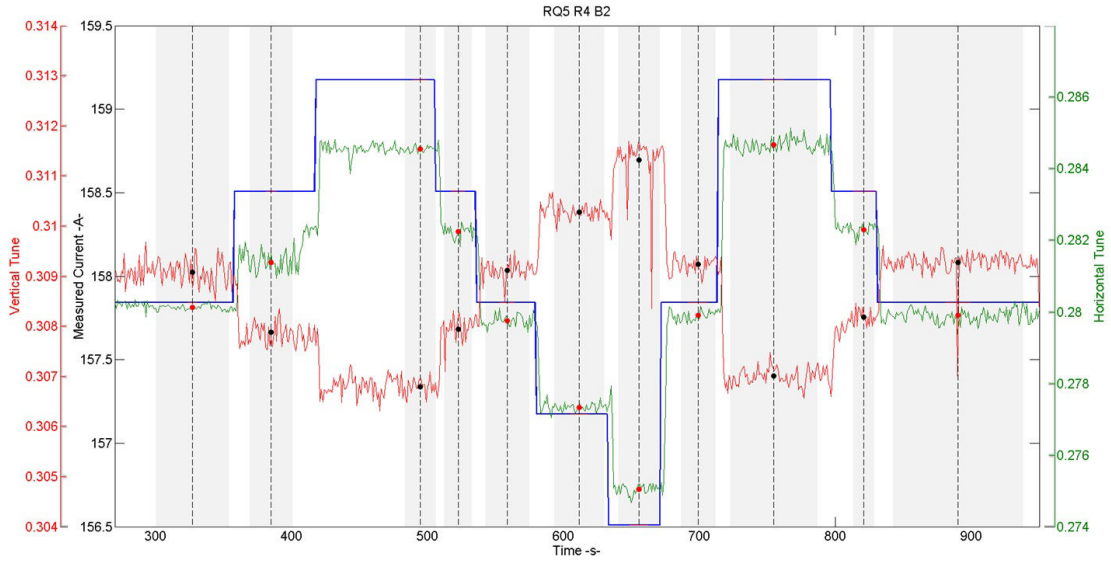


Figure 7.3: K-modulation applied for RQ5.R4.B2; the blue curve denotes the current trims applied to the quadrupole and the green and red curve shows respectively the horizontal and vertical resulting tune changes.

An example result is given in Fig. 7.3 where the current trims are shown for the quadrupole $MQ.5R4.B2$ in blue and the corresponding tune changes (H and V) are shown respectively in green and red. To reduce the statistical fluctuations of the BBQ measurements, at least 15 seconds were spent at each modulation step. Since the maximum resulting tune change from the nominal value was $\sim 5 \cdot 10^{-2}$ in both planes, the approximation in Eq. 7.13 was found suitable since the maximum error would be $< 0.07\%$ as shown in Fig. 7.4.

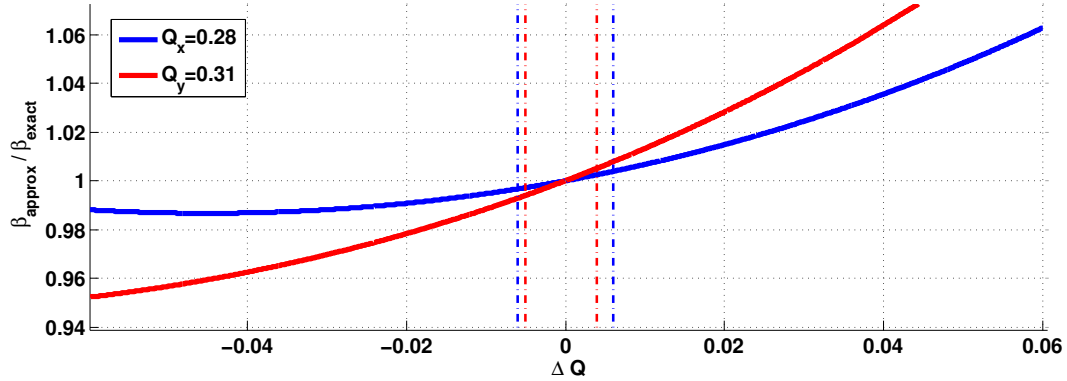


Figure 7.4: Validation of the approximation in Eq. 7.13 for the LHC parameters. The blue and red curves denote respectively the relative error introduced by the approximation in function on the induced tune change for the horizontal and vertical tune working points (0.28 and 0.31)

Therefore, the mean value of the betatron function at the excited quadrupole can be expressed in terms of the quadrupole current I variation as follows:

$$\beta_{x,y} = 4\pi \cdot \frac{\Delta Q_{x,y}}{\Delta I} \cdot \frac{\Delta I}{\Delta K} \quad (7.14)$$

The clear correlation between Q and I is shown in Fig. 7.5. Linear fits were applied to the data sets and the β s were calculated according to Eq. 7.14 from the resulting angular coefficients ($\Delta Q/\Delta I$) together with the transfer function of each quadrupole ($\Delta I/\Delta K$ ¹) shown in Tab. 7.2.

Due to noisy tune measurements during the study of the quadrupole $MQ.5L4.B1$, the resulting β s in both planes were omitted.

The measured β s are shown in Tab. 7.3 and 7.4, along with the errors on the measurements, which are dominated by the uncertainty on the measured tune. These values can also be compared to the predicted values by the LHC model calculated using the software Methodical Accelerator Design (Mad-X), a scripting language used for describing particle accelerators, simulating beam dynamics and optimizing beam

¹Measured values of $\Delta I/\Delta K$ are obtained from the LHC Software Architecture (LSA) [101]

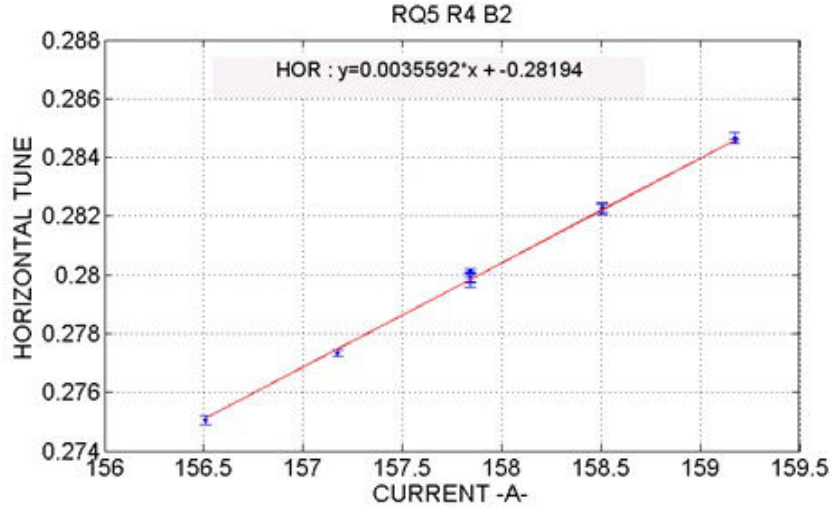


Figure 7.5: Correlation between the current steps set to the quadrupole RQ5.R4.B2 and the measured tune in the horizontal plane for Beam 2. A Linear regression is applied (red curve) and summarized by the line equation on the top.

Linear angular coefficients
 $\Delta I / \Delta K$ (10^4)
interpolated from LSA

	MQ.5R4.B1	-3.332
BEAM 1	MQ.6R4.B1	3.346
	MQ.7R4.B1	-4.083
	MQ.5R4.B2	3.33
BEAM 2	MQ.5L4.B2	-3.324
	MQ.6L4.B2	-3.323

Table 7.2: Linear angular coefficients $\Delta I / \Delta K$ for the studied quadrupoles as interpolated from LSA .

optics [102]. The disagreement varies from few % to a maximum of 9%. The theoretical and measured betatron functions for Beam 1 are also shown in Fig. 7.6 together with the IR4 optical layout.

		<i>MQ.5R4.B1</i>	<i>MQ.6R4.B1</i>	<i>MQ.7R4.B1</i>	<i>MQ.5L4.B1</i>	
Beam 1	MODEL	Horizontal	186.0524	493.0379	74.1019	467.335
		Vertical	430.9873	131.8243	122.9628	163.701
	K-MODULATION	Horizontal	195.6675 $\pm(20.95\ 10.7\%)$	520.6486 $\pm(6.89\ 1.32\%)$	73.0126 $\pm(5.96\ 8.16\%)$	
		Vertical	445.392 $\pm(16.52\ 3.71\%)$	137.033 $\pm(12.02\ 8.77\%)$	133.6981 $\pm(3.43\ 2.57\%)$	
	Difference (Mad vs K-MOD)	Horizontal	5.17 %	5.6 %	1.47 %	
		Vertical	3.34 %	3.95 %	8.73 %	

Table 7.3: Summary of the measured β s in both planes for Beam 1 modulated quadrupoles, compared to the LHC model.

		MQ.5R4.B2	MQ.5L4.B2	MQ.6L4.B2	
Beam 2	MODEL	Horizontal	444.8336	150.7804	409.876
		Vertical	210.7991	509.1754	179.2128
	K-MODULATION	Horizontal	438.0847 $\pm(25.54\ 5.8\%)$	156.3988 $\pm(17.26\ 11.04\%)$	430.435 $\pm(5.76\ 1.33\%)$
		Vertical	208.3149 $\pm(13.1897\ 6.33\%)$	527.2172 $\pm(16.22\ 3.07\%)$	182.923 $\pm(7.02\ 3.83\%)$
	Difference (Mad vs K-MOD)	Horizontal	1.52 %	3.7 %	5 %
		Vertical	1.18 %	3.54 %	2 %

Table 7.4: Summary of the measured β in both planes for beam 2 modulated quadrupoles, with respect to the predicted ones from Mad-X.

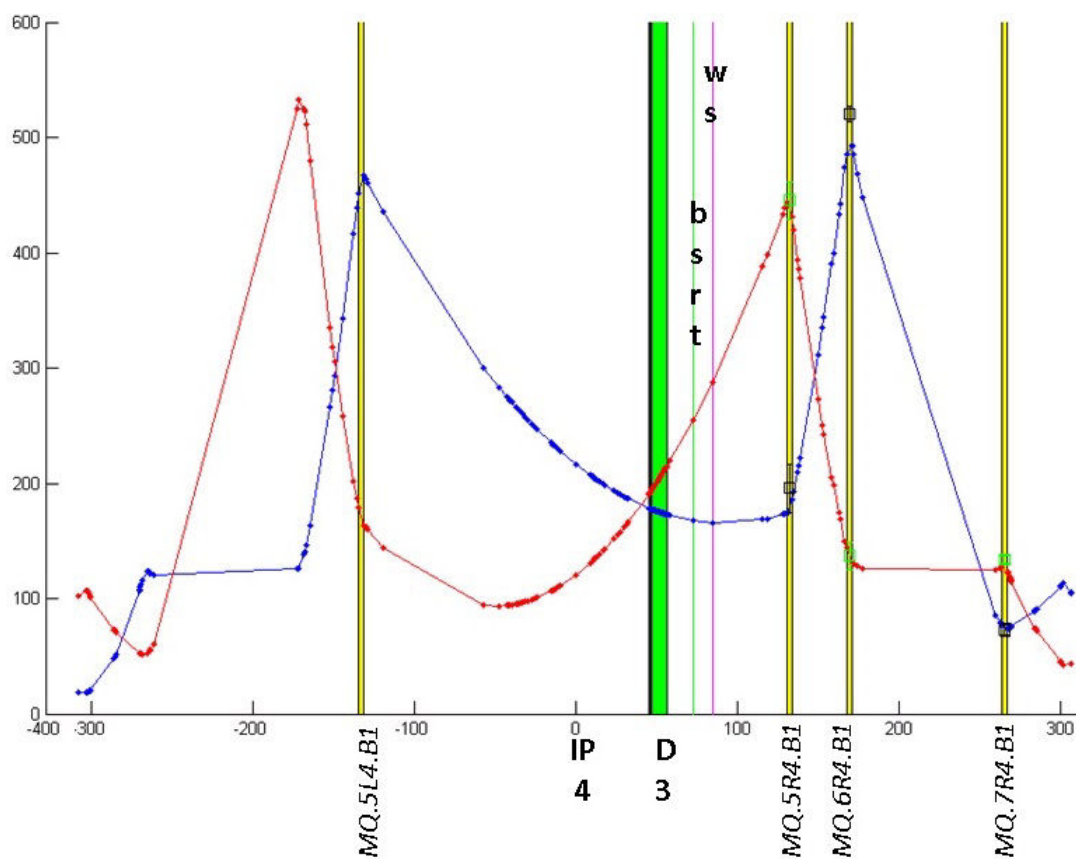


Figure 7.6: IR4 optical Layout for Beam 1 showing β_x in blue and β_y in red and the measured β s via K-modulation in black (horizontal) and green (vertical). The green and purple vertical bands denote the beam size monitors (WS and BSRT source) while the yellow ones represent the modulated quadrupoles.

7.2 β transport to beam size monitors

Since the interest in these measurements is to predict the β s at the SR source (Undulator and D3 Dipole) and the WS, transporting the measured β values from the quadrupoles location is needed. Two alternative approaches were adopted: analytically and numerically by the mean of the Mad-X software.

7.2.1 Analytical transport

This approach is based on the betatron function measurement at two quadrupoles locations and the knowledge of the nominal Twiss parameters at the two quadrupoles and a profile monitor location. The Twiss parameters can be transported as:

$$\begin{pmatrix} \beta \\ \alpha \\ \gamma \end{pmatrix}_{final} = T_{final-initial} \cdot \begin{pmatrix} \beta \\ \alpha \\ \gamma \end{pmatrix}_{initial} \quad (7.15)$$

where:

$$T_{final-initial} = \begin{pmatrix} C^2 & -2SC & S^2 \\ -CC' & SC' + S'C & -SS' \\ C'^2 & -2S'C' & S'^2 \end{pmatrix} \quad (7.16)$$

with S, C, S' and C' defined in Eq. 7.6. For example, considering the transport from *MQ.5R4.B1* to the undulator “*UND*” and then from *MQ.5R4.B1* to *MQ.6R4.B1* (see Fig. 7.7) and using Eq. 7.16 gives the following set of equations:

$$\begin{cases} \beta_{UND} = a_{UND-5}\beta_5 + b_{UND-5}\alpha_5 + c_{UND-5}\gamma_5 \\ \beta_6 = a_{6-5}\beta_5 + b_{6-5}\alpha_5 + c_{6-5}\gamma_5 \\ \gamma_5 = \frac{1+\alpha_5^2}{\beta_5} \end{cases} \quad (7.17)$$

where a, b and c are the elements of the first line of the corresponding Twiss transport matrix T . The first two equations reduces to the following expression of the second order in γ_5 :

$$c_{65}^2\gamma_5^2 + (2a_{65}c_{65}\beta_5 - 2c_{65}\beta_6 - b_{65}^2\beta_5)\gamma_5 + (b_{65}^2 + (a_{65}\beta_5 - \beta_6)^2) = 0 \quad (7.18)$$

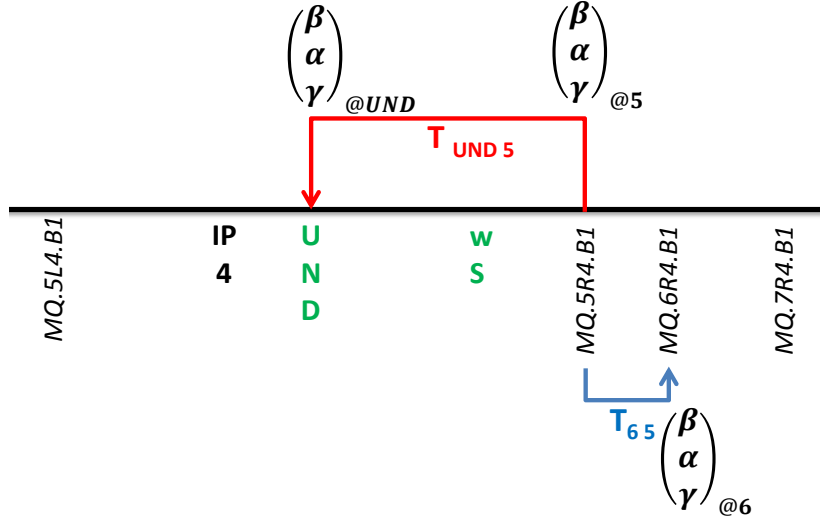


Figure 7.7: Schematics explaining the analytical transport of the measured β s at the quadrupoles via K-modulation to the beam size monitors.

that, combined with the third equation and solving for α_5 , results in:

$$\begin{cases} \alpha_{5,1,2} = \pm \sqrt{\beta_5 \gamma_{5_1} - 1} = \pm \alpha_{5_A} \\ \alpha_{5,3,4} = \pm \sqrt{\beta_5 \gamma_{5_2} - 1} = \pm \alpha_{5_B} \end{cases} \quad (7.19)$$

These four solutions can be substituted back into the first of Eqs. 7.17 to give four solutions for β_{UND} :

$$\begin{cases} \beta_{UND_{1,2}} = a_{UND-5} \beta_5 \pm b_{UND-5} \alpha_{5_A} + c_{UND-5} \frac{1 + \alpha_{5_A}^2}{\beta_5} \\ \beta_{UND_{3,4}} = a_{UND-5} \beta_5 \pm b_{UND-5} \alpha_{5_B} + c_{UND-5} \frac{1 + \alpha_{5_B}^2}{\beta_5} \end{cases} \quad (7.20)$$

Out of these four solutions, only one turns out to be within a realistic range and is considered as the transport result.

In addition, a Monte Carlo (MC) approach was implemented to define an error bar bounding the propagated β s. The method consisted of:

- iteratively assigning the quadrupole measured β s randomly from a Gaussian distribution centered around the measured value with a standard deviation derived

from the statistical error of the measurement;

- defining the error of the propagated value at the beam size monitor as the RMS standard deviation of the resulting Gaussian distribution

7.2.2 Mad-X transport

This approach to transport the measured quadrupoles β s to the monitors location is based on the matching module in Mad-X. The transport principle is shown in Fig. 7.8.

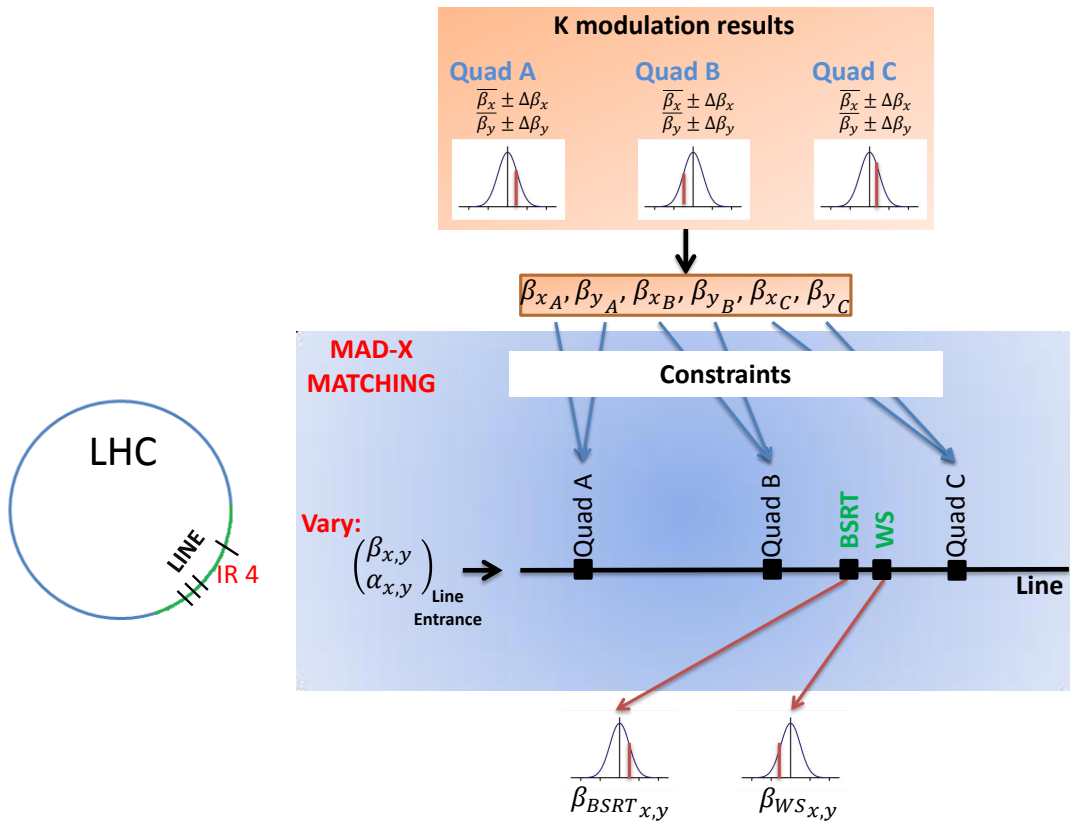


Figure 7.8: Schematics explaining the transport of the measured β s at the quadrupoles via K-modulation to the beam size monitors via the matching module in Mad-X.

The portion of accelerator including the profile monitors locations (around the LHC IR4) is extracted from the Mad-X LHC sequence and given as input to the Mad-X. The matching module is designed to calculate the best optics parameters along

the accelerator sub-sequence by varying a number of user-defined variables while respecting some constraints (e.g. measured betatron functions at the quadrupoles) and match the nominal optics at the beginning of the sub-sequence.

Depending on the problem scenario (typically defined by the number of constraints, the number of variables and the desired tolerances), different matching methods (minimizing algorithms), can be used in this module [103]:

- LMDIF: Fast Gradient Minimisation,
- MIGRAD: Gradient Minimisation,
- SIMPLEX: Simplex Minimisation,
- JACOBIAN: Newton Minimisation.

In the following both "LMDIF" and "SIMPLEX" minimizations were adopted for crosschecks; the results agreed within 1 %.

In this case, the β functions measured via K-modulation at the quadrupoles are used as constraints (three quadrupoles, 6 constraints), $\beta_{x,y}$ and $\alpha_{x,y}$ act as input variables (4 variables). At each iteration, the constraints are assigned randomly from a Gaussian distribution centered around the measured value with a standard deviation derived from the statistical error of the measurement. The solution is given when a set of inputs ($\bar{\beta}_{x,y_0}$ and $\bar{\alpha}_{x,y_0}$) propagated via Mad-X in the line, is found to minimize a penalty function that is null when the mean¹ β propagated in the quadrupoles are equal to the K-modulation measurements. A Gaussian fit is then applied to the distribution of the β propagated to the Undulator, dipole D3 and WS giving the mean value and the error of the transport. This transport approach was developed and implemented in an elaborated software architecture using Python, Matlab and Mad-X.

¹An external python library, PyMad [REF], is used to perform averaging and saving of the optical functions

7.2.3 Results

Both the transport techniques presented above gave consistent results. However the propagation using the matching technique, is considered more accurate since the measurements at all the quadrupoles are used simultaneously for the transport, whereas the analytical technique relies on pairs of quadrupoles for each transport. A summary of the β s propagated to the SR sources and the WS is given in Tab. 7.5, 7.6 and 7.7 for 450 GeV and 4 TeV (before and after β^* squeeze), where the k-modulation and transport results are compared to the LHC model predicted by Mad-X and to the standard (*Beta-beating*) [104, 105] measurements routinely carried out by the LHC Optics Team.

BEAM 1		MODEL	Beta-beating	Best Analytical	matching
WS	X	165.484	158.83 \pm 13 %	181.2 \pm 6.45 %	183.7 \pm 11.5%
	Y	287.814	280.99 \pm 12.3%	287.1 \pm 4.22 %	286.9 \pm 3.34%
Undulator	X	178.144	174.93 \pm 13.2%	199.9 \pm 9.75 %	196.8 \pm 13.3%
	Y	192.094	188.1 \pm 22.1%	189 \pm 4.94 %	187.5 \pm 3.24%

BEAM 2		MODEL	Beta-beating	Best Analytical	matching
WS	X	123.512	126.43 \pm 9.5%	124.2 \pm 2.04%	125.3 \pm 4.05%
	Y	404.551	418.95 \pm 8.5%	424.7 \pm 3.33%	412.9 \pm 2.78%
Undulator	X	127.535	129.3 \pm 16.2%	126.5 \pm 3 %	172.7 \pm 2.82%
	Y	332.832	344.02 \pm 7.4%	354 \pm 2.72 %	351.2 \pm 4.2%

Table 7.5: Summary of the transported β s measured via K-modulation at 450 GeV to the SR source and WS, with respect to the predicted ones from Mad-X and the measured ones by the optics team.

These calculated values became practically the reference for emittance calculations in the LHC. Figure 7.9 shows an example where using the β predicted by the model, unphysical normalized emittance shrinking (since no beam losses were measured) was observed at 4 TeV with respect to 450 GeV (blue curve). Contrarily, by using the

BEAM 1		MODEL	Beta-beating	Best Analytical	matching
WS	X	165.484	151.7 ± 12.1%	159.2 ± 6.45%	173.3±12%
	Y	287.814	292.0 ± 10.68%	288.2 ± 10.9%	284 ± 6.8%
Undulator	X	172.967	158.7 ± 8.76%	165.4 ± 5.35%	177.3 ± 12%
	Y	214.595	209.5 ± 0.75%	207.5 ± 3.1%	213 ± 11 %

BEAM 2		MODEL	Beta-beating	Best Analytical	matching
WS	X	123.512	122.9 ± 2.75%	118.7 ± 4.2%	117 ± 8%
	Y	404.551	451.0 ± 23.11%	438.7 ± 4.1%	435.1 ± 3.2%
Undulator	X	127.090	124.9 ± 11.87%	122.1 ± 6.2%	125.1 ± 8.4%
	Y	334.613	381.1 ± 23.37%	358.8 ± 3.9%	355.8 ± 2.5%

Table 7.6: Summary of the transported β measured via K-modulation at 7 TeV before squeeze to the SR source and WS, with respect to the predicted ones from MADX and the measured ones by the optics team.

measured β s via K-modulation in the calculation (red curve), an emittance increase is observed. However, no information can be extracted about when the emittance growth takes place during the ramp since, in the grey-shaded area corresponding to the energy ramp, the optical functions were not measured. In Fig. 7.9, a linear interpolation between the measured values at injection and flattop is used at each energy to calculate the β . Nevertheless, future tests for K-modulation measurements during the ramp are planned in the LHC after the restart [106], where an accurate knowledge of the optical functions spurious changes during the ramp is necessary for the emittance measurement.

BEAM 1		MODEL	Beta-beating	Best Analytical	matching
WS	X	165.484	151.7 ± 12.1%	159.2 ± 6.45%	173.3±12%
	Y	287.814	292.0 ± 10.68%	288.2 ± 10.9%	284 ± 6.8%
Undulator	X	172.967	158.7 ± 8.76%	165.4 ± 5.35%	177.3 ± 12%
	Y	214.595	209.5 ± 0.75%	207.5 ± 3.1%	213 ± 11 %

BEAM 2		MODEL	Beta-beating	Best Analytical	matching
WS	X	123.512	122.9 ± 2.75%	118.7 ± 4.2%	117 ± 8%
	Y	404.551	451.0 ± 23.11%	438.7 ± 4.1%	435.1 ± 3.2%
Undulator	X	127.090	124.9 ± 11.87%	122.1 ± 6.2%	125.1 ± 8.4%
	Y	334.613	381.1 ± 23.37%	358.8 ± 3.9%	355.8 ± 2.5%

Table 7.7: Summary of the transported β measured via K-modulation at 7 TeV after squeeze to the SR source and WS, with respect to the predicted ones from Mad-X and the measured ones by the optics team.

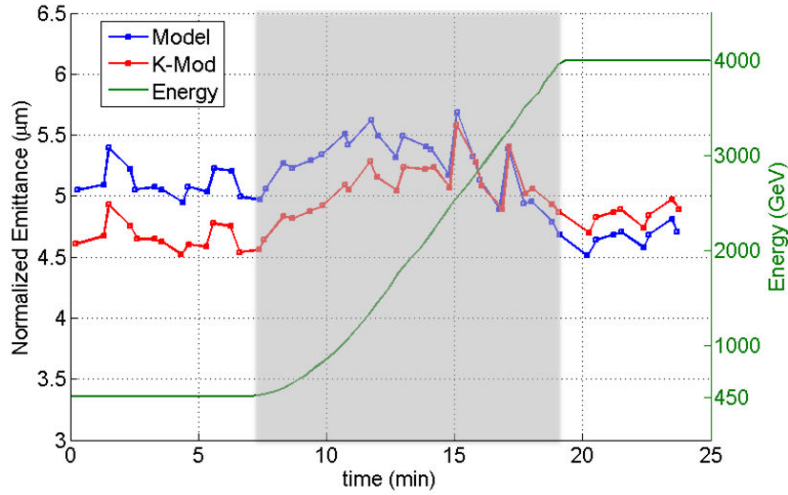


Figure 7.9: LHC beam 1 mean normalized horizontal emittance evolution, in fill 2778, calculated using the model predicted β (blue) and the measured β via K-modulation at the SR monitors location.

Chapter 8

New SR Optical System for the LHC

The studies presented in Chapters 4 and 5 resulted in the conceptual design and development of an improved optical system layout for the LHC monitors. The new system layout and the new optical elements, that are being installed at the moment of writing, is described in detail in this chapter.

External calibration line

The calibration studies discussed in Chapter 5 showed a clear difference between the measured magnification using the calibration target and the orbit bumps. As stated earlier, the difference could be explained by the fact that the extraction and the steering mirrors are not included in the calibration light path (from the target to the CCD) installed on the optical bench.

Therefore, an external calibration line was designed to replace the internal calibration line described in Section 3.1.3. The new line will include all the optical elements (extraction mirror, viewport and steering mirror) in the calibration path, thus freeing half of the optical bench for other measuring lines, as shown in Fig. 8.2.

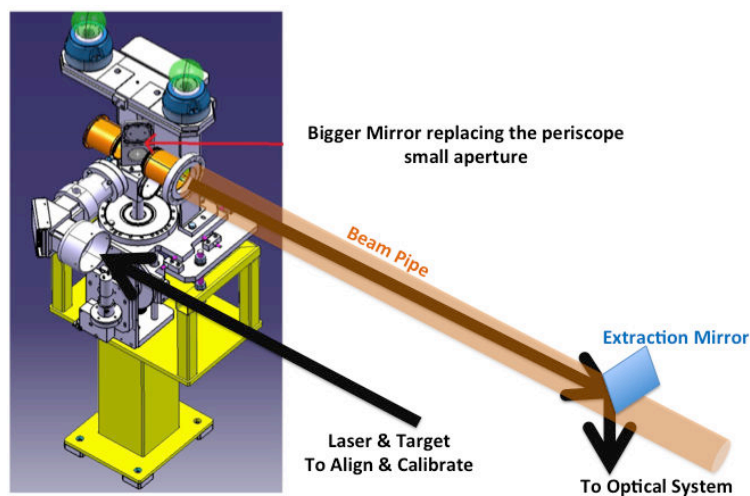


Figure 8.1: New external calibration line installed in the LHC (Courtesy: A. Goldblatt).

Upgraded imaging system

Since the resolution studies presented in Chapter 4 highlighted the advantage of shifting the imaging working point to a lower wavelength (250 nm), an additional set of lenses (F1, F2), that are optimized for near ultra violet wavelengths will be installed in parallel to the existing lenses optimized for the injection operation where the SR light is available only around 600 nm. The switching between the two sets of lenses is energy dependent and should take place at around 2 TeV as mentioned in Section 4.25.

Interferometry setup

As discussed in Chapter 4, a SR interferometer was studied as an alternative to direct imaging for the LHC beam size measurements. The system will replace the internal calibration line (green area in fig.8.2).

The interferometry line will be used in parallel to the normal imaging operation by inserting a motorized “50/50” (R/T) parallel plates splitter, or in alternative to the imaging, by replacing the splitter by a full 3” mirror.

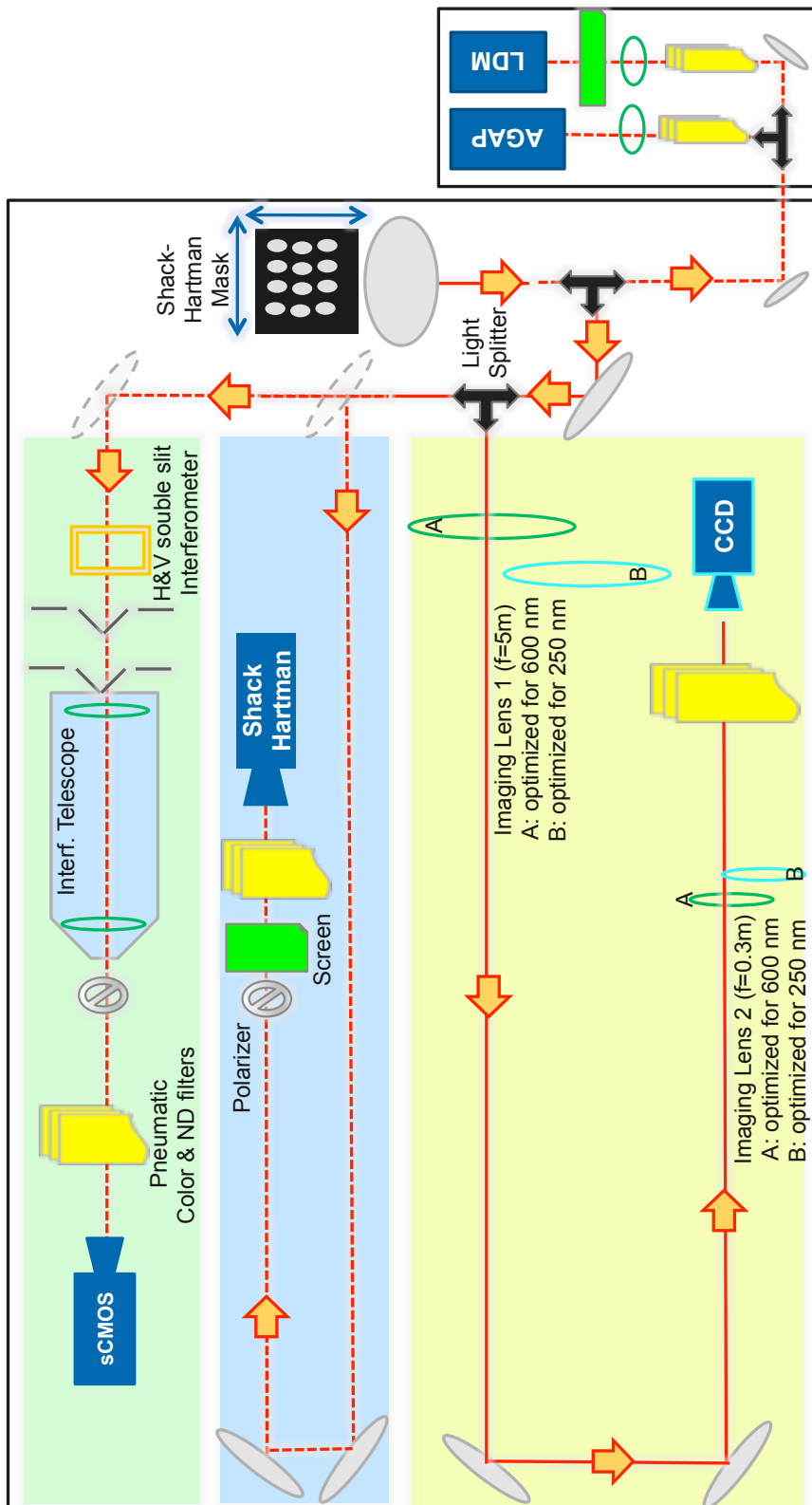


Figure 8.2: New optical bench layout for post-LS1 operation, featuring the imaging line, the interferometry line and the wavefront distortion measurement line.

The interferometry line, shown in more details in Fig. 8.3, features two fully motorized double slit systems (horizontal and vertical) as shown in Fig. 8.4. It is followed by a “Takahashi” [107] telescope, that consists in an apochromat 100 mm diameter lens followed by an ocular lens mounted on a translation stage to achieve a variable zoom. The detector will consist in a digital camera (“Andor” [108] sCMOS) is installed, preceded by a set of neutral density filters and linear polarizer mounted on rotational stage.

The double slit systems can be completely retracted, thus allowing normal imaging at $\lambda = 450$ nm in parallel to the original imaging system (yellow area in Fig.8.2) operating at $\lambda = 250$ nm. Moreover, by inserting both slits together, a 2D interferometer is

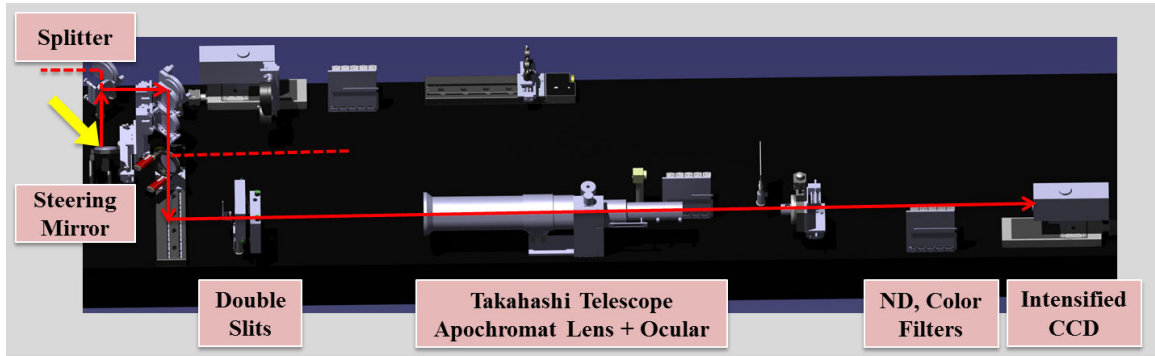


Figure 8.3: Sketch of the interferometry line to be installed in the LHC (Courtesy: A. Goldblatt).

planned for testing. It allows measuring both horizontal and vertical beam sizes at once. In fact, by superimposing the horizontal to the vertical slits, a pattern of 4 squares is obtained. The squares are at the edges of the rectangle defined by the separations of the first and second set of double slit, D_1 and D_2 respectively. Figure 8.5 presents the LSF of the system, corresponding to the central particle within the phase space, obtained via the simulation tool described in Chapter 4. The projections of the 2D interferogram is compared with the projected LSFs of two single interferometers (H and V) in Fig. 8.6.

The very good agreement obtained is a hint, that the two planes can be treated

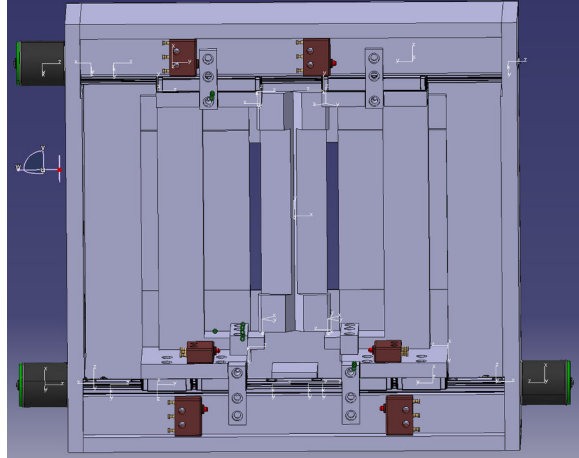


Figure 8.4: Motorized double slits system to be used for the interferometry line in the LHC (Courtesy: A. Goldblatt).

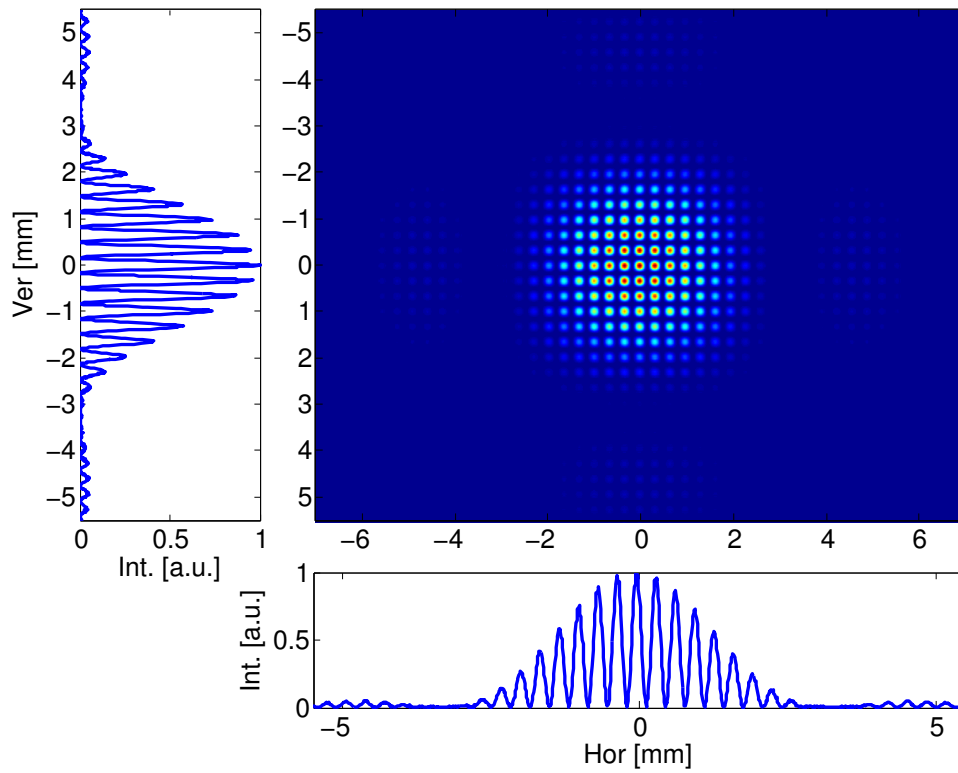


Figure 8.5: LSF of two double slits system at $D_1 = D_2 = 11$ mm at $\lambda = 550$ nm, with the corresponding horizontal and vertical projections.

separately, and if the intensity reduction is acceptable¹, simultaneous measurements of both planes are feasible.

Finally, a simulation probing eventual effects of the drift space between the two slits

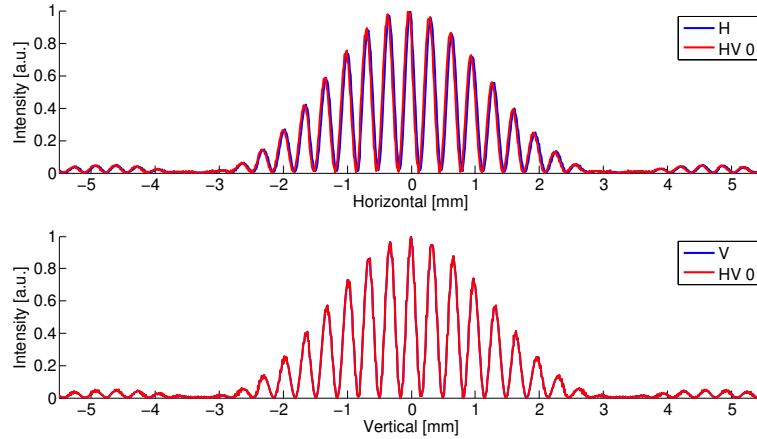


Figure 8.6: Comparing 2D interferometer LSF with separate 1D interferometer respectively in the horizontal and vertical plane.

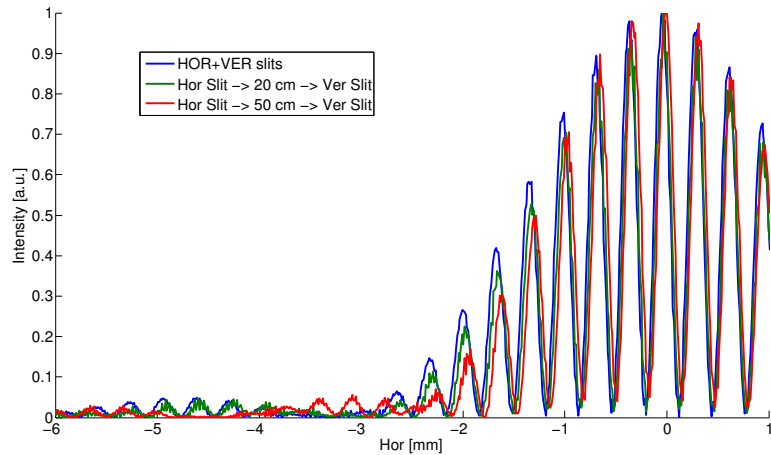


Figure 8.7: LSF of various 2D interferometers obtained by varying the drift space between the single sets of double slits.

on the measured visibility was carried out. In fact, due to mechanical constraints,

¹The intensity reduction can be fairly approximated by the reduction of the slits aperture area from the 1D to the 2D case.

a minimum space between the two sets of slits of about $\sim 10\text{--}15\text{ cm}$ is required. As shown in Fig.8.7, for a distance $<20\text{ cm}$, the error on the visibility determination results to be $<3\%$. This small error is considered to be acceptable, therefore no further modeling of this effect is needed.

Online monitoring of extraction mirror flatness.

Even though the new SR extraction system was found less prone to beam induced heating, thermocouples are installed in the proximity of the extraction mirror allowing an on line monitoring of eventual temperature rising.

Since additional aberrations introduced in the system by the heating of the extraction mirror could be a severe limitation to the imaging system resolution and compromise the interferometric beam size measurements, a system monitoring eventual wavefront distortion will be installed. It consists in the implementation of the

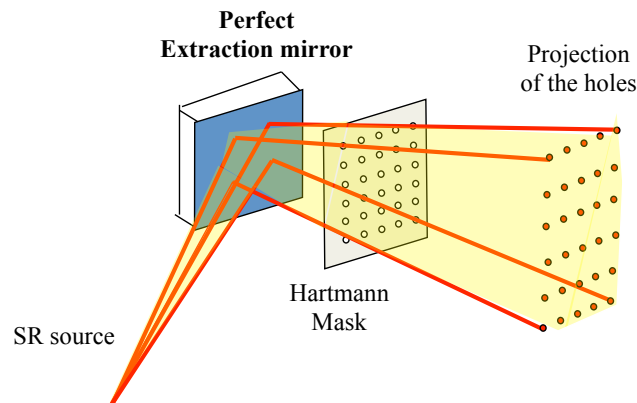


Figure 8.8: Hartmann-mask Setup.

“Hartmann–Mask” described in [109, 110]. The technique is presented in Fig. 8.8, where a square array screen, an opaque screen filled with a regular pattern of holes, is used to sample the incoming SR wavefront from the extraction mirror. The principle laying behind is the following:

- the proton beam, due to its small size, is considered as a point source illuminating the extraction mirror;

-
- since SR is a directive light (confined within a cone of $1/\gamma$ opening), when passing through a hole on the Hartmann-mask, a well-defined underlying area on the mirror is sampled;
 - these traversing rays are tracked up to a ground glass diffuser;
 - the projected holes on the diffuser are imaged on a CCD evaluating eventual shift of the centroid position with respect to a defined nominal position (corresponding to a flat mirror);
 - eventual tilt of the sampled part of the extraction mirror are computed from the measured displacement.

A sketch of the working principle is shown in Fig. 8.9.

In order to preserve an unambiguous correspondence between the hole position on the mask and the sampled area on the mirror, the Hartman-mask has to be installed as close as possible to the extraction mirror. To fulfill this requirement without installing an in vacuum element, the mask will be placed as close as possible to the viewport, at about 50 cm from the extraction mirror, which is still acceptable [109]. In addition, the distance between the mask and the diffusive screen on which the holes are projected sets the minimum wavefront distortion the instrument can measure. According to the optical table layout, and the available space (blue area in Fig. 8.2), it was decided to set this distance to 6 m. Assuming that the holes projection position on the diffuser can be estimated with a resolution of $\sim 50 \mu\text{m}$ using the CCD, the system would reach a wavefront deformation detection in the order of $\lambda/10$ according to Eq.8.1 and 8.2.

$$\alpha_{\min} = \text{atan} \left(\frac{\text{resol}_{\text{CCD}}}{\text{dist}_{\text{Mask-Screen}}} \right) \quad (8.1)$$

$$\text{Resol} = \text{dist}_{\text{holes}} \cdot \sin(\alpha_{\min}) \quad (8.2)$$

where α_{\min} is the minimum detectable angular deformation on the extraction mirror, $\text{resol}_{\text{CCD}}$ is the CCD resolution, $\text{dist}_{\text{Mask-Screen}}$ is the distance between the Hartman-mask and the diffusive screen and $\text{dist}_{\text{holes}}$ is the distance between adjacent hole on the mask.

Moreover, the holes pattern on the Hartmann-mask has to be carefully studied. The

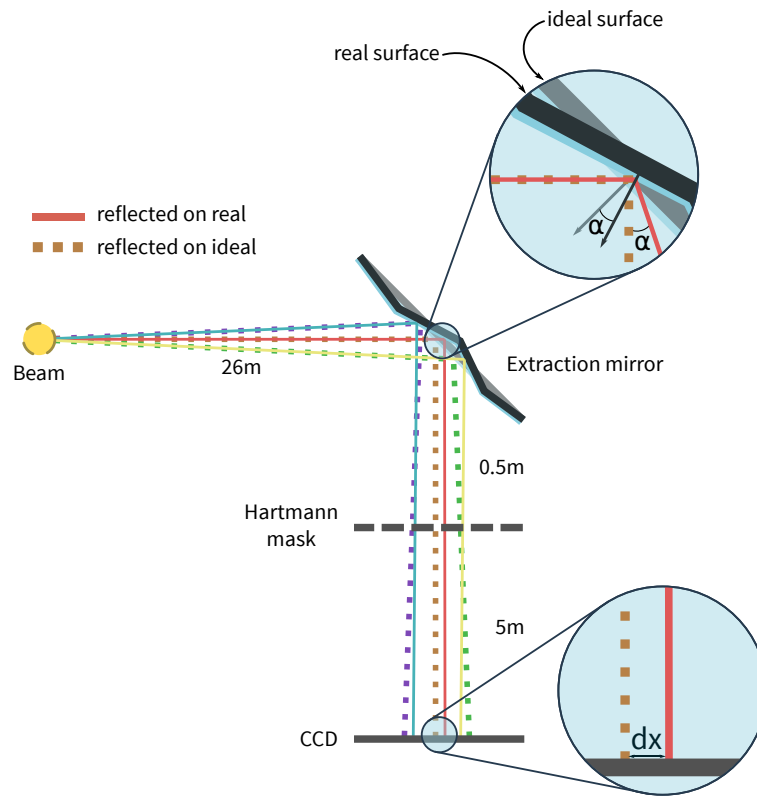


Figure 8.9: Hartmann-mask working principle.

hole diameter should be sufficiently small to allow accurate measurement by reducing the sampled area on the extraction mirror. However, very small holes lead to a wide diffraction pattern on the observation screen, so that two adjacent holes projections would overlap. Figure 8.10 presents the diffraction pattern of the incoming SR light at 7 TeV and $\lambda=550$ nm, for different hole diameter at different distances between the mask and the diffusive screen.

Based on all these considerations, the Hartman-mask to be installed is finally chosen to be a mask with a matrix (8x8) holes spaced by 7 mm and 1.5 mm diameter each. It will be installed at 0.5 m from the extraction mirror and mounted on motorized (x,y) translation stages to allow continuous sampling of the extraction mirror.

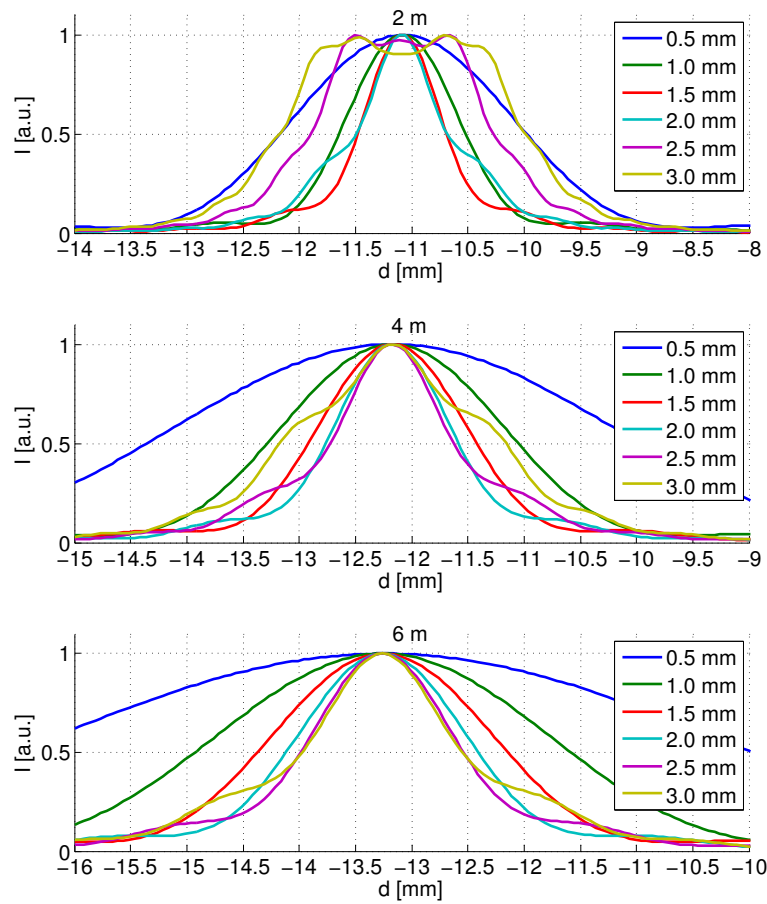


Figure 8.10: Diffraction pattern of the SR light passing through different Hartman-mask hole diameter at different distances from the extraction mirror.

Conclusions

The thesis work documented in this report focused on the design, development, characterization and optimization of the CERN SR-based beam size monitors. Such studies were based on a comprehensive set of theoretical calculations, numerical simulations and experiments.

A powerful simulation tool has been developed combining conventional softwares for synchrotron radiation simulation and optics design, thus allowing the description of an SR monitor from its source up to the detector.

This resulted in an exhaustive description of the SR source, confirmed by direct observations, and a detailed performance studies of the operational SR imaging monitor in the LHC. The simulations of this imaging monitor based on reflective optics featured a horizontal resolution of $\sim 300 \mu\text{m}$ and a vertical resolution of $\sim 200 \mu\text{m}$, almost constant with beam energy. Different techniques for experimentally validating the system were applied, such as cross-calibrations with the wire scanners at low intensity (that are considered as a reference) and direct comparison with beam sizes de-convoluted from the LHC luminosity measurements.

However, the obtained resolution was found broadened by a almost a factor three. The reason for this worsening mainly originated from the deteriorated SR extraction mirror, source of important aberrations in the system.

Moreover, an accurate analysis of the optical system design indicated a strong relation between possible misalignment and aperture reduction of the system with the resolution worsening.

Therefore, it was decided to develop a new optical system to overcome this limitation. The choice of refractive optics resulted in a simplified system with the drawback of being prone to additional chromatic aberrations and lenses imperfections, for which

its simulated resolution was found higher than its predecessor: $\sim 350\ \mu\text{m}$ at injection energy, $\sim 380\ \mu\text{m}$ at 4 TeV and $\sim 410\ \mu\text{m}$ at 7 TeV.

However, the simplified optical layout (combined to an improved extraction mirror coating) resulted in measured resolutions agreeing within 10% with the simulated ones, thus representing in a significant improvement with respect to the old system.

All this was achieved before the LHC long shutdown (LS1), at a maximum beam energy of 4 TeV. In 2015, with the further increase of the beam energy to 7 TeV the beam sizes to be measured will decrease down to $\sim 190\ \mu\text{m}$. In this conditions, the SR imaging technique was found at its limits of applicability since the error on the beam size determination is proportional to the ratio of the system resolution and the measured beam size.

Therefore, various solutions were probed to improve the system's performance (choice of one light polarization, reducing depth of field effect by applying slits) but the only effective solution found was to reduce the imaging wavelength from 400 nm down to 250 nm.

Indeed, at this new working point, the system has been re-qualified and its resolution checked along the energy ramp, allowing continuous beam size measurement up to 7 TeV with a resolution of $\sim 350\ \mu\text{m}$ (at high energy).

In parallel to reducing the diffraction contribution to the resolution broadening, the extraction mirror, found as the main sources of aberrations in the system was redesigned. The system's failure was caused by the EM coupling with the beam's fields that led to overheating and deterioration of the coating. A new system's geometry featuring a smoother transition in the beam pipe was qualified in terms of longitudinal coupling impedance via the stretched wire technique. A comparison with the older system was carried out and resulted in a reduction of the total power dissipated in the extraction system by at least a factor of four.

A new, non-diffraction limited, SR-based monitor based on double slit interferometry was designed as well as an alternative method to the direct imaging. Its principle is based on the direct relation between the interferogram fringes visibility and the beam size.

This dependency is guaranteed by the Van Cittert–Zernike theorem for an equally illuminated slits and a negligible longitudinal extension of the source. The existing

modification of such a theorem developed for its application to the SR case resulted not applicable to the LHC case where an overlap of the SR sources along the ramp changes radically the source characteristics.

However, a set of extensive simulations allowed obtaining a calibration curve mapping the fringes visibility to the beam size. The simulations also accounted for the intensity imbalance on the slits and the big longitudinal extension of the source. For the injection energy, where the Van Cittert–Zernike theorem is applicable, such a calibration curve showed an agreement with the analytical estimations of better than 5%. The results were validated during the commissioning of the SR interferometer at the ALBA light source in Barcelona.

Since the beam emittance is the physical quantity of interest in the performance analysis of the LHC, determining the optical functions at the SR monitors is as relevant as measuring the beam size. The “K-modulation” method for the optical function determination was applied for the first time in the LHC IR4, where most of the profile monitors sit.

The β s, at all the standalone quadrupoles, were measured and via two different propagation algorithms (analytical and matching) the β s at the BSRT and the WS were obtained. Compared to the design optics, a discrepancy $< 10\%$ was observed, confirming the beta beating results carried out in all the ring, and the uncertainty at the beam size monitors was reduced significantly. This led to a better characterization in terms of magnification and resolution of the BSRT.

In order to continuously monitor the brightness of the SPS beams to the LHC, a monitor capable of measuring the beam size at extraction is required. Up to now the SPS has relied on the use of wire scanners, but this technique is limited by the wire breakage when used with high brightness beams. Since, a profile monitor based on synchrotron light could solve both of these issues, the refurbishment of the SPS SR monitor and the design of a new imaging system was studied during this thesis work. The optical system, based on refractive optics (very similar to the LHC imaging system), optimized for infrared operation was designed following simulations characterizing the SR source, defined as the light emitted from bending dipoles edges. The first beams circulating in the SPS after the LS1 were used to verify the alignment, the magnification and the transmission of the monitor. Source intensity simulations across the energy ramp were found in line with the measurements (discrepancy

<15 %).

The system resolution at 450 GeV was estimated to be very similar for both planes, $\sim 215 \mu\text{m}$. Beam measurements are planned soon to crosscheck these simulations.

Appendix

A Derivation of the SR spatial distribution emitted by relativistic charges on circular orbit

Recalling Eq. 2.27, the total radiated SR power in the relativistic case can be expressed by:

$$P_{\text{TOT}} = \frac{e^2 c}{6\pi\epsilon_0(m_0c^2)^2} \left(\frac{d\vec{p}}{d\tau} \right)^2 \quad (3)$$

that for the case of a circular acceleration in a bending dipole ($\frac{d\vec{v}}{d\tau} \perp \vec{v}$), reduces to:

$$P_{\text{TOT}} = \frac{e^2 c \gamma^2}{6\pi\epsilon_0(m_0c^2)^2} \left(\frac{d\vec{p}}{dt} \right)^2 \quad (4)$$

It is worth noting that in a circular trajectory with the radius ρ , a change of the orbit angle $d\alpha$ causes a momentum variation $dp = p d\alpha$. The latter could also be expressed by:

$$\frac{dp}{dt} = p\omega = \frac{pv}{\rho} = \frac{E}{\rho} \quad (5)$$

Therefore by substituting $\gamma = E/m_0c^2$ in Eq. 4, the dependency of the radiated power on the particle energy E is obtained:

$$P_{\text{TOT}} = \frac{e^2 c}{6\pi\epsilon_0(m_0c^2)^4} \frac{E^4}{\rho^2} \quad (6)$$

By inserting the obtained Poynting vector at the radiated time (Eq. 2.15) in the expression of the total radiation power per unit solid angle (Eq. 2.17), the latter

becomes:

$$\frac{dP}{d\Omega} = \frac{1}{c\mu_0} \vec{E}^2 (1 + \vec{n}\vec{\beta}) R^2 \quad (7)$$

By using the electric field expression (Eq. 2.16), the radiation power distribution can be expressed as follows:

$$\begin{aligned} \frac{dP}{d\Omega} &= \frac{1}{c\mu_0} \frac{e^2}{(4\pi\epsilon_0)^2} \frac{1}{c^2 a^6} \cdot \left\{ \vec{R} \times \left[(\vec{R} + \vec{\beta}R) \times \dot{\vec{\beta}} \right] \right\}^2 (1 + \vec{n}\vec{\beta}) R^2 \\ &= \frac{1}{c\mu_0} \frac{e^2}{(4\pi\epsilon_0)^2} \frac{R^5}{c^2 a^5} \left\{ \vec{n} \times \left[(\vec{n} + \vec{\beta}) \times \dot{\vec{\beta}} \right] \right\}^2 \end{aligned} \quad (8)$$

Recalling the reference coordinates system K^* , introduced in Chapter 2:

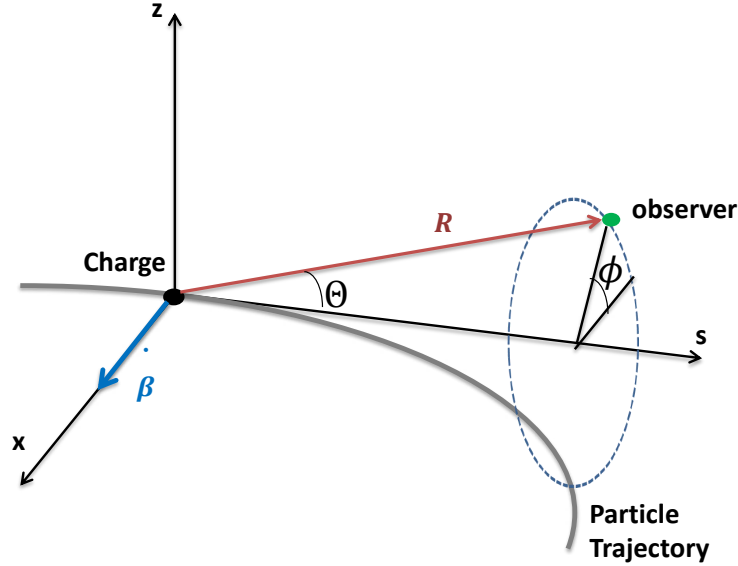


Figure 11: The geometry used for the treatment of synchrotron radiation, featuring K^* as coordinate system moving along the trajectory.

In K^* , the vector position \vec{R} , pointing from the observer to the moving particle, and its unit vector are given by

$$\vec{R} = -R \begin{pmatrix} \sin \Theta \cos \phi \\ \sin \Theta \sin \phi \\ \cos \Theta \end{pmatrix} \quad (9)$$

$$\vec{n} = \begin{pmatrix} -\sin \Theta \cos \phi \\ -\sin \Theta \sin \phi \\ -\cos \Theta \end{pmatrix} \quad (10)$$

The Lorentz force \vec{F} of an electron traveling along a trajectory in a magnet is then expressed by:

$$\vec{F} = -e\vec{v} \times \vec{B} = -e \begin{pmatrix} -vB_z \\ 0 \\ 0 \end{pmatrix} = \gamma m_0 \dot{\vec{v}} \quad (11)$$

By the nature of the particle circular motion, we recall that: $\vec{v} = \begin{pmatrix} 0 \\ 0 \\ v \end{pmatrix}$, $\dot{\vec{v}} =$

$$\begin{pmatrix} \dot{v}_x \\ 0 \\ 0 \end{pmatrix} \text{ and } \vec{B} = \begin{pmatrix} 0 \\ B_z \\ 0 \end{pmatrix}. \text{ Therefore: } \gamma m_0 \dot{v}_x = evB_z = ec\beta B_z.$$

The bending radius of a trajectory in a magnet can be evaluated according to:

$$\frac{1}{\rho} = \frac{e}{p} B_z = \frac{eB_z}{\gamma m_0 v} \Rightarrow B_z = \frac{\gamma m_0 v}{e\rho} \quad (12)$$

and the transverse acceleration of the particle becomes:

$$\dot{v}_x = \frac{c^2 \beta^2}{\rho} \quad (13)$$

obtaining finally:

$$\vec{\beta} = \frac{\vec{v}}{c} = \begin{pmatrix} 0 \\ 0 \\ v/c \end{pmatrix} \quad (14)$$

and

$$\dot{\vec{\beta}} = \begin{pmatrix} \dot{v}/c \\ 0 \\ 0 \end{pmatrix} = \begin{pmatrix} (c\beta^2)/\rho \\ 0 \\ 0 \end{pmatrix} \quad (15)$$

By using the mathematical identity:

$$\left\{ \vec{n} \times \left(\left[\vec{n} + \vec{\beta} \right] \times \dot{\vec{\beta}} \right) \right\} = \left(\vec{n} + \vec{\beta} \right) \left(\vec{n} \dot{\vec{\beta}} \right) - \dot{\vec{\beta}} \left(1 + \vec{n} \vec{\beta} \right) \quad (16)$$

and recalling a :

$$a = R \left(1 + \vec{n} \vec{\beta} \right) = R (1 - \beta \cos \Theta) \quad (17)$$

the radiated power per unit solid angle is finally obtained:

$$\frac{dP}{d\Omega} = \frac{1}{c^3 \mu_0} \frac{e^4}{(4\pi\epsilon_0)^2} \frac{\beta^4 (\beta^2 - 1) \sin^2 \Theta \cos^2 \phi + (1 - \beta \cos \Theta)^2}{\rho^2 (1 - \beta \cos \Theta)^5} \quad (18)$$

References

- [1] “CERN official webpage.” www.cern.ch/about. v, 5, 6
- [2] K. Wille, “Synchrotron radiation,” *Joint Universities Accelerator School, Lecture Notes*, 2012. v, 25, 27, 30, 31, 32
- [3] “HPFS Fused Silica Standard Grade.” http://www.corning.com/docs/specialtymaterials/pisheets/H0607_hpfs_Standard_ProductSheet.pdf. vi, 47, 48
- [4] “ProxiVision, High Resolution Low Light Cameras.” <http://www.proxivision.de>. vi, 52, 54
- [5] “IDS, ueye.” <http://en.ids-imaging.com/>. xi, 114
- [6] D. Belohrad, A. Boccardi, E. Bravin, E. Calvo, B. Dehning, J. Emery, M. Favier, J. Gras, A. Guerrero, A. Jeff, T. Lefevre, A. Rabiller, F. Roncarolo, M. Sapinski, L. Soby, and R. Steinhagen, “BI MD studies on June 29th 2011. Beam Instrumentation,” Aug 2011. xi, 118
- [7] K. Schindl, “Instabilities,” *CERN, Geneva, Switzerland*, 2006. xiii, 145, 147
- [8] F. Caspers, A. Goldblatt, A. Nosych, F. Roncarolo, G. Trad, C. Völlinger, and M. Wendt, “The LHC Synchrotron Light Monitor (BSRT),” Tech. Rep. CERN-ACC-SLIDES-2014-0049, CERN, Geneva, Apr 2014. xiv, 155, 156
- [9] B. Salvant, R. Jones, O. Aberle, G. Arduini, T. Mastoridis, M. Garlasche, O. Berrig, M. Zerlauth, L. Lari, E. Shaposhnikova, *et al.*, “Update on beam induced RF heating in the LHC,” in *Proc. of the IPAC 2013, Shanghai, China*. xv, 167

-
- [10] “1984 Nobel Prize in physics.” http://www.nobelprize.org/nobel_prizes/physics/laureates/1984/. 7
- [11] E. Gschwendtner, T. Bohl, C. Bracco, A. Butterworth, S. Cippiccia, S. Doebert, V. Fedosseev, E. Feldbaumer, C. Hessler, W. Hofle, M. Martyanov, M. Meddahi, J. Osborne, A. Pardons, A. Petrenko, and H. Vincke, “The AWAKE experimental facility at CERN,” in *Proc. of IPAC 2014, Dresden, Germany*. 7
- [12] O. Brüning, P. Collier, P. Lebrun, S. Myers, R. Ostojic, J. Poole, and P. Proudlock, *LHC design report (Volume I, The LHC Main Ring)*. CERN, Geneva, Switzerland, 2004. 7, 42
- [13] K. Foraz, *LS1 general planning and strategy for the LHC, LHC injectors*. CERN, Geneva, Switzerland, 2012. 7
- [14] “The top ten large hadron collider world records.” <http://www.guinnessworldrecords.com/news/2012/7/higgs-boson-discovery-the-top-ten-lhc-world-records-43350/>. 7
- [15] G. Aad, T. Abajyan, B. Abbott, J. Abdallah, S. Abdel Khalek, A. Abdelalim, O. Abdinov, R. Aben, B. Abi, M. Abolins, *et al.*, “Observation of a new particle in the search for the Standard Model Higgs boson with the ATLAS detector at the LHC,” *Physics Letters B*, vol. 716, no. 1, pp. 1–29, 2012. 7
- [16] S. Chatrchyan, V. Khachatryan, A. M. Sirunyan, A. Tumasyan, W. Adam, E. Aguilo, T. Bergauer, M. Dragicevic, J. Erö, C. Fabjan, *et al.*, “Observation of a new boson at a mass of 125 GeV with the CMS experiment at the LHC,” *Physics Letters B*, vol. 716, no. 1, pp. 30–61, 2012. 7
- [17] “2013 Nobel Prize in physics.” http://www.nobelprize.org/nobel_prizes/physics/laureates/2013/. 7
- [18] H. Wiedemann, *Particle accelerator physics*, vol. 1. Springer, 2003. 9
- [19] G. W. Hill, “On the part of the motion of the lunar perigee which is a function of the mean motions of the sun and moon,” *Acta mathematica*, vol. 8, no. 1, pp. 1–36, 1886. 11

-
- [20] K. Wille, *The physics of particle accelerators: an introduction*. Oxford: Oxford Univ. Press, 2000. [15](#)
- [21] W. Herr and B. Muratori, *Concept of luminosity*. CERN, Geneva, Switzerland, 2006. [16](#)
- [22] S. Burger, A. Ravni, F. Roncarolo, R. Sautier, E. Bravin, A. Boccardi, and A. Goldblatt, “Turn by Turn Profile Monitors for the CERN SPS and LHC,” in *Proc. of IBIC 2013, Oxford, UK*. [17](#)
- [23] M. Sapinski, W. Andreatza, B. Dehning, A. Guerrero, M. Patecki, and R. Versteegen, “The first experience with LHC beam gas ionization monitor,” Tech. Rep. CERN-ATS-2012-286, CERN, Geneva, Switzerland, Oct 2012. [17](#)
- [24] J. Bosser, J. Camas, L. Evans, G. Ferioli, R. Hopkins, J. Mann, and O. Olsen, “Transverse emittance measurement with a rapid wire scanner at the CERN SPS,” *Nuclear Instruments and Methods in Physics Research Section A: Accelerators, Spectrometers, Detectors and Associated Equipment*, vol. 235, no. 3, pp. 475–480, 1985. [18](#)
- [25] M. Sapinski and T. Kroyer, “Operational limits of wire scanners on LHC beam,” in *Proc. of the Beam Instrumentation Workshop, Lake Tahoe, California*, 2008. [19](#)
- [26] F. Méot, L. Ponce, J. Bosser, and R. Jung, “Diagnostics with synchrotron radiation of the LHC proton beams,” in *Proc. of the European Particle Accelerator Conference, Paris, France*, pp. 1945–1947, 2002. [19](#)
- [27] *Lawrence Berkeley National Laboratory, X-ray Data Booklet*. University of California, Berkeley, California, second edition, 2006. [21](#)
- [28] P. Lagassé, L. Goldman, A. Hobson, and S. R. Norton, *The Columbia Encyclopedia*. Columbia University Press New York, 2000. [21](#)
- [29] J. D. Jackson and J. D. Jackson, *Classical electrodynamics*, vol. 3. Wiley New York etc., 1962. [22](#), [27](#), [28](#)

-
- [30] J. Larmor, “A Dynamical Theory of the Electric and Luminiferous medium. Part III. Relations with Material Media.,” *Proceedings of the Royal Society of London*, vol. 61, no. 369-377, pp. 272–285, 1897. [28](#)
- [31] A. Hofmann, T. Ericson, and P. Y. Landshoff, *The physics of synchrotron radiation*. Cambridge University Press Cambridge, UK, 2004. [29](#)
- [32] R. Bartolini, “Synchrotron radiation,” *Joint Universities Accelerator School, Lecture Notes*, 2013. [29](#)
- [33] R. Coisson, “On synchrotron radiation in non-uniform magnetic fields,” *Optics Communications*, vol. 22, no. 2, pp. 135–137, 1977. [32](#), [56](#)
- [34] R. Coisson, “Angular-spectral distribution and polarization of synchrotron radiation from a ”short” magnet,” *Physical Review A*, vol. 20, no. 2, p. 524, 1979. [32](#)
- [35] H. Onuki and P. Elleaume, *Undulators, wigglers and their applications*. CRC Press, 2003. [33](#), [35](#)
- [36] F. Méot, *Mesure de profils par rayonnement onduleur des faisceaux de protons et d’antiprotons*. PhD thesis, Grenoble, Université Joseph Fourier, CERN, Geneva, Switzerland, 1981. Presented on 30 Oct 1981. [33](#)
- [37] L. Cadet-Ponce and R. Jung, *Diagnostic par rayonnement synchrotron des faisceaux de protons du LHC*. PhD thesis, Grenoble, INP, CERN, Geneva, Switzerland, 2002. Presented on 10 Oct 2002. [35](#), [45](#), [51](#)
- [38] S. Takano *et al.*, “Beam diagnostics with synchrotron radiation in light sources,” *Proc. of IPAC 2010*, pp. 2392–2396. [35](#)
- [39] G. Kube, “Review of synchrotron radiation based diagnostics for transverse profile measurements,” in *Proc. of DIPAC 2007*. [35](#)
- [40] M. Born and E. Wolf, *Principles of optics: electromagnetic theory of propagation, interference and diffraction of light*. CUP Archive, 1999. [36](#), [39](#)
- [41] M. Griot, “optics Guide 4,” 1988. [36](#)

-
- [42] G. Kube, “Theory of optical reconstruction for synchrotron light sources.” 9th DITANET Topical Workshop on NON-Invasive Beam Size Measurement for High Brightness Proton and Heavy Ion, 2013. [37](#)
- [43] M. Masaki and S. Takano, “Diffraction Limited Resolution of a Synchrotron Radiation Beam Profile Monitor.,” *Japan Synchrotron Radiation Research Institute SPring-8, Kamigori, Ako-gun, Hyogo 678-12, Japan*. [37](#)
- [44] G. Kube, R. Fischer, C. Wiebers, and K. Wittenburg, “Detailed resolution studies of the synchrotron radiation profile monitor for the HERA electron beam,” in *Proc. of DIPAC 2005, Lyon, France*, vol. 5, p. 202, 2005. [37](#)
- [45] J. A. Clarke, “A review of optical diagnostics techniques for beam profile measurements,” in *Proc. of EPAC 1994*. [37](#)
- [46] A. Hofmann and F. Meot, “Optical resolution of beam cross-section measurements by means of synchrotron radiation,” *Nuclear Instruments and Methods in Physics Research*, vol. 203, no. 1, pp. 483–493, 1982. [37](#)
- [47] W. Hossack, “Modern Optics-Topic 2: Scalar Diffraction,” *Lecture Notes, School of Physics University of Edinburgh*, 1998. [37](#)
- [48] T. Mitsuhashi, “Beam profile and size measurement by SR interferometers,” *Beam Measurement*, pp. 399–427, 1998. [39](#), [93](#), [98](#)
- [49] R. Maccaferri, D. Tommasini, R. Jung, W. Venturini-Delsolaro, and M. Facchini, “The 5 T superconducting undulator for the LHC synchrotron radiation profile monitor,” in *Proc. of EPAC 2004, Lucerne, Switzerland*. [45](#)
- [50] A. Jeff, C. Welsch, and A. Boccardi, *A Longitudinal Density Monitor for the LHC*. PhD thesis, Liverpool University. Presented 11 Dec 2012. [46](#), [65](#)
- [51] J. B. Jeanneret and R. Ostokic, “Geometrical acceptance in LHC version 5.0,” tech. rep., CERN-LHC-Project-Note-111, 1997. [46](#)
- [52] F. Roncarolo, J.-P. Perroud, and B. D. Dehning, *Accuracy of the Transverse Emittance Measurements of the CERN Large Hadron Collider*. PhD thesis, LPHE, Lausanne, 2005. Presented 2005. [49](#)

-
- [53] A. S. Fisher, “Expected Performance of the LHC Synchrotron-light Telescope (BSRT) and Abort-Gap Monitor (BSRA),” tech. rep., 2010. 49, 51, 80, 120
- [54] T. Lefevre, S. B. Pedersen, A. Boccardi, E. Bravin, A. Goldblatt, A. Jeff, A. Fisher, and F. Roncarolo, “First Operation of the Abort Gap Monitors for LHC,” in *Proc. of IPAC 2010, Kyoto, Japan*. 51
- [55] A. Jeff, A. Boccardi, E. Bravin, A. Fisher, T. Lefevre, A. Rabiller, F. Roncarolo, and C. Welsch, “First results of the LHC longitudinal density monitor,” *Nuclear Instruments and Methods in Physics Research Section A: Accelerators, Spectrometers, Detectors and Associated Equipment*, vol. 659, no. 1, pp. 549–556, 2011. 51
- [56] A. Goldblatt, E. Bravin, F. Roncarolo, and G. Trad, “Design and Performance of the Upgraded LHC Synchrotron Light Monitor,” in *Proc. of IBIC 2013, Oxford, UK*. 51
- [57] “How an Image Intensifier Tube Works.” <http://www.photonis.com/en/content/102-nightvision-how-it-works>. 53
- [58] R. Bossart, J. Bosser, L. Burnod, R. Coisson, E. d’Amico, A. Hofmann, and J. Mann, “Observation of visible synchrotron radiation emitted by a high-energy proton beam at the edge of a magnetic field,” *Nuclear Instruments and Methods*, vol. 164, no. 2, pp. 375–380, 1979. 55
- [59] R. Bossart, J. Bosser, L. Burnod, E. d’Amico, G. Ferioli, J. Mann, and F. Meot, “Proton beam profile measurements with synchrotron light,” *Nuclear Instruments and Methods*, vol. 184, no. 2, pp. 349–357, 1981. 55
- [60] “The RCA Ultricon and SIT Camera Tubes.” [http://archive.org/stream/RcaUltriconSITCameraTubes/RcaUltriconSITCameraTubes\\$_\\$djvu.txt](http://archive.org/stream/RcaUltriconSITCameraTubes/RcaUltriconSITCameraTubes$_$djvu.txt). 55
- [61] R. Garoby, S. Gilardoni, B. Goddard, K. Hanke, M. Meddahi, and M. Vretenar, “Plans for the upgrade of the LHC injectors,” Sep 2011. 55
- [62] G. Trad, E. Bravin, A. Goldblatt, S. Mazzoni, and F. Roncarolo, “A novel approach to synchrotron radiation simulation,” in *Proc. of IPAC 2014, Dresden, Germany*. 59

-
- [63] “1984 Nobel Prize in physics.” http://www.nobelprize.org/nobel_prizes/physics/laureates/1984/. 60
- [64] O. Chubar, “Precise computation of electron-beam radiation in nonuniform magnetic fields as a tool for beam diagnostics,” *Review of scientific instruments*, vol. 66, no. 2, pp. 1872–1874, 1995. 60
- [65] O. Chubar and P. Elleaume, “Accurate and efficient computation of synchrotron radiation in the near field region,” in *Proc. of the EPAC 1998, Stockholm, Sweden*, pp. 1177–1179, 1998. 60
- [66] E. Zemax, “Software For Optical System Design, Zemax Development Corporation.” 60
- [67] Mathworks, “The Language For Technical Computing, Matlab.” 60
- [68] Wavemetrics, “Technical graphing and data analysis software.” 60
- [69] J. Goodman, *Introduction to Fourier optics*. McGraw-Hill, 2008. 61
- [70] G. N. Lawrence, “Optical modeling,” in *Applied Optics and Optical Engineering, Volume XI*, vol. 11, p. 125, 1992. 61
- [71] *Zemax User’s Manual, Radiant Zemax, LLC*. July, 2011. 62
- [72] J. Burke, S. Garg, M. Kailashnath, V. Kertesz, B. R. Kumar, S. Lakshmi, J. Lakshminarayana, S. Mishra, A. R. Rao, P. K. Tamanna, *et al.*, “Dynamic data exchange server,” June 1998. US Patent 5,764,155. 62
- [73] D. M. Sykora and M. L. Holmes, “Dynamic measurements using a Fizeau interferometer,” in *SPIE Optical Metrology*, pp. 80821R–80821R, International Society for Optics and Photonics, 2011. 83
- [74] C. McFee, “Types of noise in a CCD.” 91
- [75] T. Lefevre, E. Bravin, G. Burtin, A. Fisher, A. Goldblatt, A. Guerrero, A. Jeff, and F. Roncarolo, “First beam measurements with the LHC synchrotron light monitors,” in *Proc. of IPAC 2010, Kyoto, Japan*. 104, 114

-
- [76] S. White, R. Alemany-Fernandez, M. Lamont, and H. Burkhardt, “First luminosity scans in the LHC,” in *Proc. of IPAC 2010, Kyoto, Japan*. 131
- [77] “ALBA.” <https://www.cells.es/en/about/welcome>, 2014. 133
- [78] U. Iriso, L. Torino, and T. M. KEK, “First transverse beam size measurements using interferometry at ALBA,” 2013. 133
- [79] U. Iriso, L. Torino, and T. M. KEK, “Beam size measurements using synchrotron radiation interferometry at ALBA,” 2014. 139
- [80] “Coefficient of determination — Wikipedia, the free encyclopedia.” http://en.wikipedia.org/w/index.php?title=Coefficient_of_determination&oldid=634608541. 141
- [81] L. Palumbo, V. G. Vaccaro, and M. Zobov, “Wake fields and impedance,” *Arxiv preprint physics/0309023*, 2003. 144
- [82] R. M. Jones, “HOM mitigation,” *Lecture Note: CERN Accelerator School, Ebeltoft, Denmark*, 2010. 144
- [83] M. Ferrario, L. Palumbo, and M. Migliorati, “Wake fields and instabilities in linear accelerators,” 2006. 145
- [84] E. Métral *et al.*, “Beam-induced heating / bunch length / RF and lessons for 2012,” in *LHC Performance Workshop, Chamonix*, 2012. 147, 164
- [85] T. Baer, E. Bravin, A. Boccardi, S. Burger, E. Calvo, B. Dehning, J. Emery, M. Gasior, A. Guerrero, R. Jones, T. Lefevre, J. Gras, A. Rabiller, F. Roncarolo, M. Sapinski, R. Steinhagen, and G. Trad, “BI MD studies on April 22nd 2012 (LHC MD-1),” Jul 2012. 153
- [86] “Macor, Machinable glass ceramic.” <http://psec.uchicago.edu/ceramics/MACOR%20Data%20Sheet.pdf>. 155
- [87] C. M. Studio, “Computer Simulation Technology,” *GmbH, Darmstadt, Germany*, 2014. 155

-
- [88] K. Ko, N. Folwell, L. Ge, A. Guetz, L. Lee, Z. Li, C. Ng, E. Prudencio, G. Schussman, R. Uplenchwar, *et al.*, “Advances in electromagnetic modelling through high performance computing,” *Physica C: Superconductivity*, vol. 441, no. 1, pp. 258–262, 2006. 157
- [89] M. Sands, J. R. Rees, *et al.*, “A bench measurement of the energy loss of a stored beam to a cavity,” tech. rep., Stanford Linear Accelerator Center (United States). Funding organisation: US Department of Energy (United States), 2005. 157
- [90] V. G. Vaccaro, “Coupling impedance measurements: an improved wire method,” Tech. Rep. INFN-TC-94-023, INFN, Rome, Nov 1994. 157
- [91] A. W. Chao, K. H. Mess, M. Tigner, and F. Zimmermann, “Handbook of accelerator physics and engineering,” *Handbook of Accelerator Physics and Engineering (2nd Edition)*. Edited by Chao Alexander Wu *et al.* Published by World Scientific Publishing Co. Pte. Ltd., 2013. ISBN# 9789814415859, vol. 1, 2013. 157
- [92] F. Caspers and A. Mostacci, “History and development of bench measurement techniques for impedance evaluation,” Tech. Rep. CERN-ACC-SLIDES-2014-0048, CERN, Geneva, Apr 2014. 157
- [93] E. Jensen, “An improved log-formula for homogeneously distributed impedance,” Tech. Rep. CERN-PS-RF-NOTE-2000-001, CERN, Geneva, Jan 2000. 158
- [94] M. Masullo, V. Vaccaro, M. Panniello, *et al.*, “The stretched wire method: A comparative analysis performed by means of the mode matching technique,” *LINAC’10*, 2010. 159
- [95] F. Caspers. private communication. 161
- [96] G. Elert, “Blackbody radiation, The Physics Hypertextbook.” <http://physics.info/planck/>. 168
- [97] E. Bravin. private communication. 168

REFERENCES

- [98] R. Tomas, M. Kuhn, J. Coello, S. White, Y. Levinsen, T. Persson, P. Skowronski, V. Maier, N. Magnin, T. Bach, *et al.*, “Prospects for the LHC optics measurements and corrections at higher energy,” in *Proc. of IPAC 2014, Dresden, Germany*. 170
- [99] M. G. Minty and F. Zimmermann, *Measurement and control of charged particle beams*. Springer, 2003. 172
- [100] R. J. Steinhagen, “Performance and LHC beam stability issue related to Q/Q’ diagnostics and feedback systems,” 2010. 174
- [101] C. Roderick and R. Billen, “The LSA database to drive the accelerator settings,” Tech. Rep. CERN-ATS-2009-100, CERN, Geneva, Nov 2009. 175
- [102] H. Grote and F. Schmidt, “MAD-X: an upgrade from MAD8,” in *Proc. of the 2003 Particle Accelerator Conference*, vol. 5, pp. 3497–3499, IEEE, 2003. 177
- [103] R. de Maria, F. Schmidt, P. K. Skowronski, *et al.*, “Advances in matching with mad-x,” in *Proc. of ICAP 2006, Chamonix, France*. 182
- [104] M. Aiba, A. Morita, J. Wenninger, M. Giovannozzi, R. Calaga, G. Vanbavinckhove, A. Franchi, V. Kain, and R. Tomás, “First beta-beating measurement in the LHC,” in *Proc. of PAC09, Vancouver, BC, Canada*. 183
- [105] R. Tomás, Y. Papaphilippou, S. D. Fartoukh, F. Zimmermann, R. Calaga, A. Franchi, M. Giovannozzi, O. S. Brüning, and S. Peggs, “Procedures and accuracy estimates for beta-beat correction in the LHC,” in *Proc. of EPAC 2006, Edinburgh, Scotland*. 183
- [106] M. Kuhn, B. Dehning, V. Kain, R. Tomas, and G. Trad, “New Tools for K-Modulation in the LHC,” in *Proc. of IPAC 2014, Dresden, German*. 184
- [107] “Takahashi TSA-120 refractor triple super Apochromat telescope.” <http://www.takahashi-europe.com/en/TSA-120.specifications.php>. 189
- [108] “Zyla sCMOS - Andor, an Oxford Instruments Company.” http://www.andor.com/pdfs/specifications/Andor_Zyla_sCMOS_Specifications.pdf. 189

REFERENCES

- [109] T. Mitsuhashi and M. Tadano, “Measurement of Wavefront Distortion Caused by thermal Deformation of Sr Extraction Mirror Based On Hartmann Screen Test and Its Application for Calibration of SR interferormter,” in *Proc. of the Second Asian Particle Accelerator Conference, Beijing. China, 2001*. [192](#), [193](#)
- [110] J. Chen, K. Ye, and Y. Leng, “Hartmann screen and wavefront sensor system for extracting mirror at ssrf,” [192](#)